Relationship between water transfer and plastic deformation : the case study of quartzites

Lucille Nègre

UNIVERSITÉ D'ORLÉANS

ÉCOLE DOCTORALE Énergie, Matériaux et Sciences de la Terre et de l'Univers

Institut des Sciences de la Terre d'Orléans

THÈSE présentée par :

Lucille NEGRE

soutenue le : **05 juillet 2021**

pour obtenir le grade de : **Docteur de l'Université d'Orléans**

Discipline/Spécialité : Sciences de la Terre et de l'Univers

Relationship between water transfer and plastic deformation: the case study of quartzites

THÈSE dirigée par :

STÜNITZ Holger	Professeur, Université d'Orléans
RAIMBOURG Hugues	Maître de conférences, Université d'Orléans

RAPPORTEURS :

TREPMANN Claudia	Professeur, Ludwig-Maximilians University (Munich)
BYSTRICKY Micha	Maître de conférences, Université de Toulouse

---

JURY :

BYSTRICKY Micha	Maître de conférences, Université de Toulouse
PRECIGOUT Jacques	Ingénieur de recherche, Université d'Orléans
RAIMBOURG Hugues	Maître de conférences, Université d'Orléans
ROSENBERG Claudio	Professeur, Sorbonne Université
STIPP Michael	Professeur, Martin Luther University (Halle-Wittenberg)
STÜNITZ Holger	Professeur, Université d'Orléans
TREPMANN Claudia	Professeur, Ludwig-Maximilians University (Munich)

Table of contents

I. Introduction: general context

This first chapter introduces the main context of the thesis, including general aspects and work from previous studies.

Some aspects of the general scientific state of knowledge that still are not well understood are discussed at the end.

The general organisation of the manuscript is then presented.

I.1. Tectonic and geodynamic context

Earth's movements include phenomena that are observable at human time scale such as earthquakes but also more global and slower phenomena such as plate tectonics in general. Plate tectonics consist of the movement of more or less rigid lithospheric plates (consisting of upper mantle and crust) on the underlying and weaker asthenospheric mantle with zones of deformation localisation along relatively narrow plate boundary zones. The movements responsible for plate tectonics are governed by the rheology (or mechanical properties) of the lithospheric plates, depending on various parameters (temperature, pressure, mineral and chemical compositions, grain size, stress conditions, …).

The rheology of the lithosphere is characterized by constitutive equations and commonly described by strength envelopes showing the strength of the rock as a function of depth (e.g., Kohlstedt et al., 1995). At shallow depth, the deformation behaviour is brittle (frictional sliding) with an increase in strength with depth. Then, when the temperature is high enough to allow plastic flow, the deformation becomes viscous and occurs at lower stress with a decrease as a function of temperature. The change in deformation regime occurs during a transitional zone (brittle-viscous (or -plastic) transition), when the stress necessary for plastic flow is about equal to the effective confining pressure (Goetze's criterion).

Earth's rheology is currently described by three models (e.g review by Burgmann and Dresen, 2008) based on food analogies (Figure I.1). The rheological models (strength envelopes) are layered due to change in composition with depth: the crust is modelled using quartz and feldspar flow laws, whereas for the mantle olivine is used.

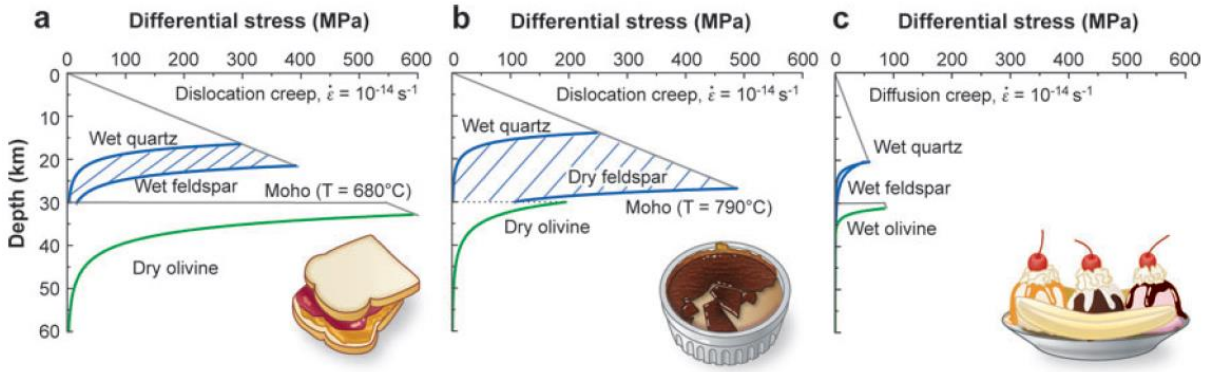

Figure I.1. Models for lithosphere strength as a function of differential stress and depth: (a) jelly sandwich, (b), crème brûlée and (c) banana split, from Burgmann and Dresen (2008).

For the upper crust, the three models present a frictional strength increasing with pressure and depth. For the two first models, the frictional behaviour follows the Byerlee's law (with or without hydrostatic fluid pressure) whereas the third one considers high pore fluid pressure, resulting in a steeper slope (lower differential stress with pressure). Then, as pressure and temperature conditions increase with depth, creep processes are activated and the strength decrease (brittle-viscous transition) as a result of change in the dominant deformation mechanism.

The "jelly sandwich" model assumes weak middle and lower crust between strong upper crust and mantle. For the "crème brûlée" model the crust is dry and strong whereas the mantle is

weak due to presence of fluids. The “banana split model” considers weakening processes reducing the strength of the lithosphere along the plate boundaries.

At different levels, it has been widely observed and described that in nature the deformation localises at different scales, from kilometres (plate boundaries) to micrometres (thin sections) (e.g., Passchier and Trouw, 2005). The localisation of deformation is a fundamental process described as controlling the deformation of lithosphere. The presence of multiple deformation mechanisms (grain size reduction, dynamic recrystallization, …) depending on several factors such as temperature and pressure conditions, strain rate, chemical composition, mineral assemblages, presence of fluids, … leads to the formation of weakened shear zones.

One of the tools that is available to characterize the mechanical behaviour of minerals and rocks is the experimental deformation. It allows to explore the deformation processes acting at controlled laboratory conditions (pressure, temperature, strain rate, force, …) on known materials. The apparatus currently available allow to explore the range of pressure and temperature encountered in the Earth’s lithosphere and establish constitutive laws describing the mechanical behaviour of rocks.

The experimental scale is obviously limited by the size of the samples that can be supported by the apparatus in order to apply representative pressures and temperatures. In addition to the size limitation there is a time limitation with the slowest rates applied in laboratory (commonly 10^{-7} s^{-1}) being several orders of magnitude faster than natural rates (10^{-12} – 10^{-14} s^{-1}).

As the experimental data are obtained under limited conditions, applications to geodynamic scale require large extrapolations. Elaboration of scaling laws is needed to link the short time scale available for laboratory studies to the long duration of geodynamic processes operating in the lithosphere. However, laboratory experiments are fundamental to understand the Earth’s deformation.

I.2. Crust rheology (quartz as a proxy)

The plate tectonics processes are controlled by the mechanical properties of the Earth’s mantle and crust. While the mechanical properties of the mantle are commonly described using olivine, those of the crust can be monitored using quartz, which is one of the most abundant mineral in crustal rocks.

Quartz is one of the minerals in the Earth’s continental crust, that is most commonly involved in deformation processes, so that understanding its mechanical behaviour is of great importance to model the deformation of the lithosphere and particularly the ductile middle crust (e.g., Burgmann and Dresen, 2008).

It is commonly assumed that the strength of the upper crust (brittle) is controlled by friction, regardless of the rock composition (Byerlee, 1968; Kohlstedt et al., 1995). With increasing depth (i.e., increase in the temperature and pressure conditions) and crossing of the brittle-plastic transition, the crustal rheology is then controlled by the rheology of its constitutive minerals.

Although most rocks are composed of more than one mineral, studying the mechanical behaviour of individual minerals is required to model the rheology of polymineralic assemblies. Indeed, the calculation of polymineralic rheologies is based on the mechanical behaviour of the constituent phases (Kohlstedt et al., 1995), weighted by their relative proportions.

Because of the abundance of quartz-bearing rocks in the continental crust (along with feldspar), studying quartz (and quartzite) behaviour under varying conditions give clues to understand the deformation of the continental crust. Using quartz as a proxy allows to constrain geodynamic properties of the crust.

The continental crust is described as mainly composed of quartzo-feldspathic rocks (such as granite). Its mechanical behaviour is dependent on the pressure and temperature conditions (Figure I.2), from brittle fracturing for both minerals at low grade conditions to viscous flow at high grade conditions. For medium grade conditions quartz first deforms plastically (dislocation creep) and accommodates most of the deformation while plastic deformation of feldspar needs higher conditions to be reached (Passchier and Trouw, 2005).

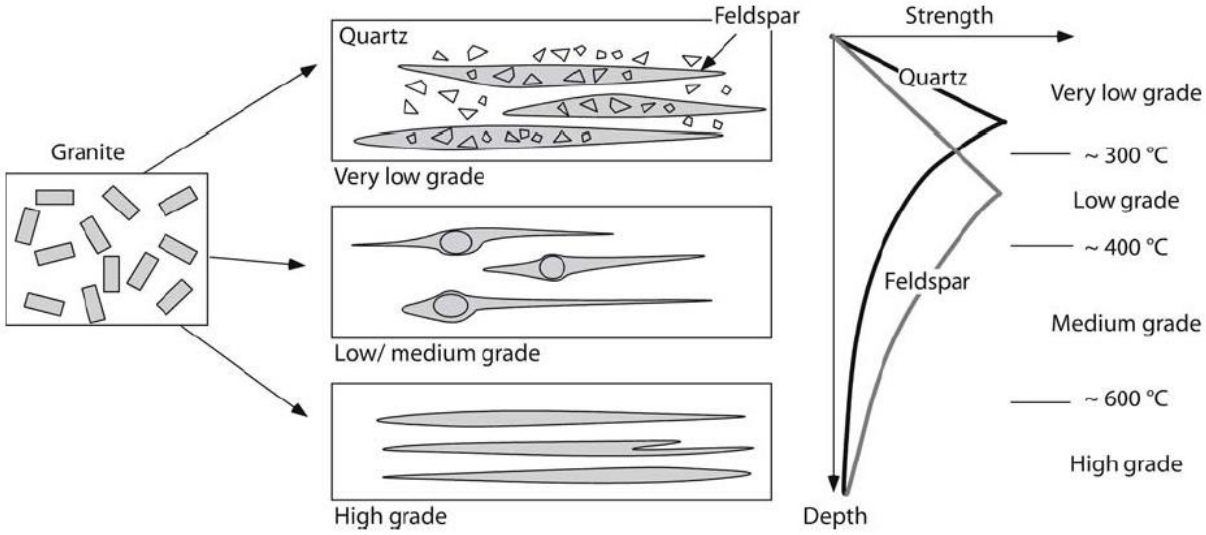

Figure I.2. Deformation behaviour of quartz-feldspar aggregates as a function of depth (P-T conditions), Passchier and Trouw (2005).

At geological strain rates (10^{-12} s^{-1}), the brittle-plastic transition for quartz occurs at lower temperatures than for feldspar. The quartz corresponds then to the fully ductile weak phase and accommodates the overall tectonic loading and acts as the viscously deformed matrix.

Even if the role of feldspar cannot be completely excluded to model the rheology of the crust, in a matter of system simplification, quartz, and in particular quartz aggregates, can be considered as a good proxy for understanding the deformation of continental crust.

Finally, it is worth noting that one great advantage of quartz is that there already exist abundant data.

I.3. Quartz characterization

Quartz is one of the most abundant minerals present in the Earth's continental crust. It is commonly observed in large amounts in a variety of rocks (igneous, metamorphic and

sedimentary). Because of its ubiquitous presence in the Earth's crust, the study of the quartz properties is of interest for many geological and mineralogical studies. As this mineral is used to model the rheology of the lithosphere, it is of great importance to experimentally constrain its mechanical behaviour.

Quartz is stable in different chemical systems and over a wide range of conditions (as observable into the P-T diagram, Figure I.3).

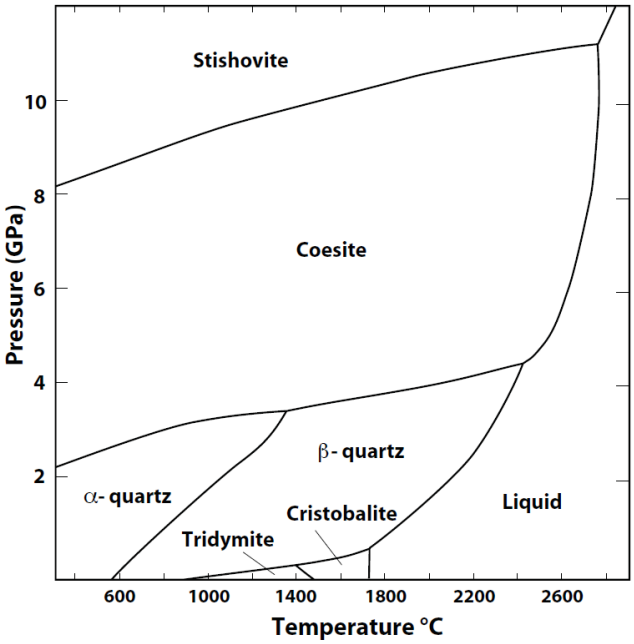

Figure I.3. Pressure - Temperature stability diagram for SiO_2 polymorphs.

The structural formula of quartz is SiO_2 in which the atoms are linked by strong covalent bonds. The mineral crystallizes in the trigonal system and is composed of SiO_4 tetrahedra in which all the four corners (composed of oxygen atoms) are shared with two other tetrahedra (in that way, one O atom is linked with two Si atoms and belongs to two tetrahedra). The tetrahedra form a continuous three-dimensional framework (helicoidal chains wrapping parallel to the c-axis) by polymerization that ensures electrical neutrality.

Due to its strong covalent bonds, the incorporation of trace elements (impurities) into quartz is limited. Depending on the physical and chemical (thermodynamic) growth conditions, quartz can incorporate some impurities into its lattice or in interstitial positions. The Si atoms can sometimes be substituted in the tetrahedral sites but due to the small ion radius of Si^{4+} and its high valence, these substitutions are rare. Substitutions by ions as Al^{3+}, Ga^{3+}, Fe^{3+}, Ge^{4+}, Ti^{4+} and P^{5+} have been reported, the most frequent one being Al^{3+} (common occurrence in the Earth's crust). However, as Al valence is 3+ but Si valence is 4+, a compensation of the electric charge is needed. The compensation can be ensured by various cations charged positively such as H^+, Li^+, Na^+, K^+, Cu^+, Ag^+, … incorporated interstitially.

Götze et al. (2001) proposed one example of the quartz structure including all the above-mentioned impurities (Figure I.4). Other defects such as silanol groups (Si-OH), oxygen vacancy (Si^+ … ^+Si), non-bridging oxygen (Si-O … O-Si), peroxy linkage (Si-O-O-Si) or radical (Si-O-O), … are also described as quartz lattice defects.

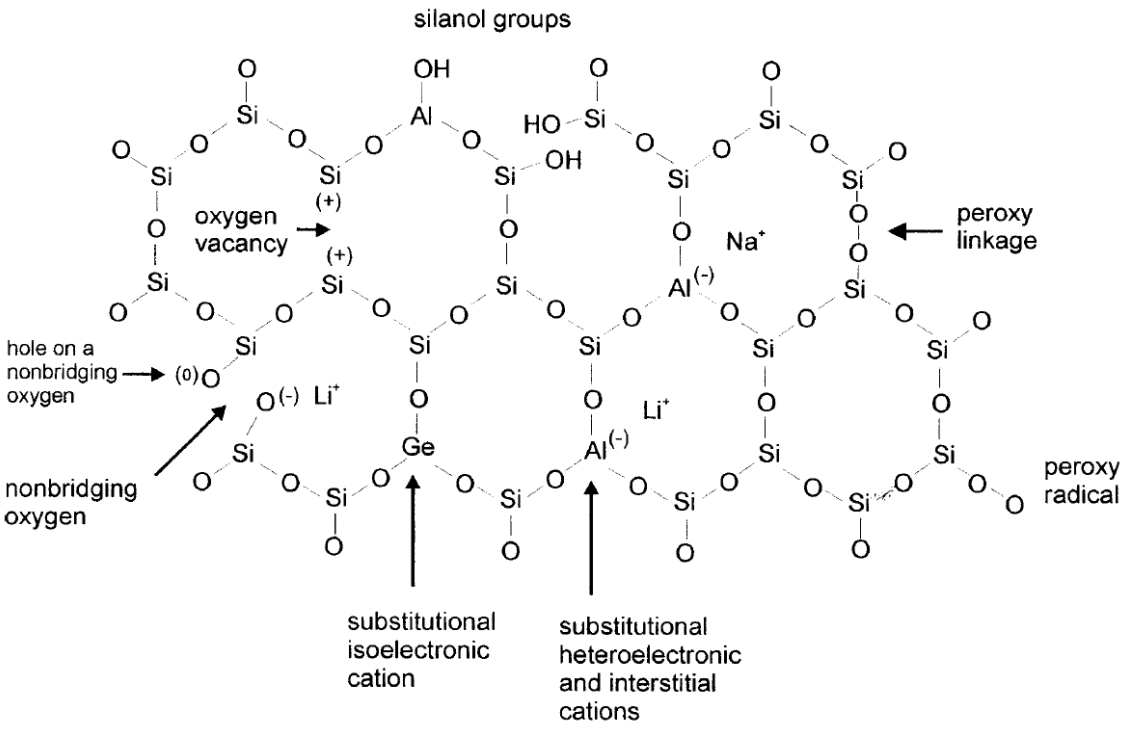

Figure I.4. Schema showing the most common lattice defects of quartz, from Götze et al. (2001).

I.4. Quartz deformation: water weakening

Quartz occurs in many different geodynamic environments and it is common to observe that quartz deformed plastically in natural samples. Evidence of plastic deformation affecting natural quartz are common such as the presence of undulose extinction, elongated grains, subgrains, recrystallized grains, ... making it one of the weak minerals in naturally deformed crustal rocks.

However, until the mid-60's, experiments failed to plastically deform dry quartz which was described as one of the strongest silicate minerals. Dry quartz typically does not deform plastically even at high temperatures (Griggs and Blacic, 1965) and responds to high applied stresses by fracturing (brittle mechanisms). The study of Griggs and Blacic (1965) challenged this point of view as the two authors observed that the presence of H_2O weakened the quartz, making it possible to deform in a ductile way. Deforming single crystals of Brazilian quartz at elevated temperatures (700 – 900 °C) and pressures (1000 – 1500 MPa), they observed that samples for which talc was used as confining medium were far weaker (200 – 400 MPa) compared to those deformed in dry conditions (> 2000 MPa, Figure I.5). They inferred that dehydration of the talc confining medium provided a source of H_2O which weakened the quartz.

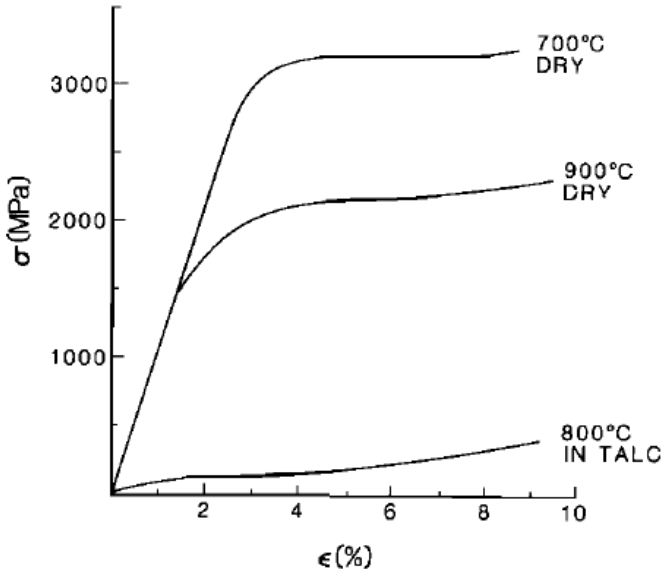

Figure I.5. Hydrolytic weakening as first observed by Griggs and Blacic (1965): stress – strain curves of single crystals deformed in talc assembly are almost more than 10 times weaker than crystals deformed in dry conditions. After Kronenberg et al. (1986).

Following the study of Griggs and Blacic (1965), a great number of research projects have studied different aspects and mechanisms involved in water weakening of quartz, all agreeing in the fact that the presence of H_2O into the quartz crystal lattice highly influences its strength (e.g., Jaoul et al., 1984; Kronenberg et al., 1986; Kronenberg and Wolf, 1990; Luan and Paterson, 1992; Kronenberg, 1994; Gleason and Tullis, 1995; Post et al., 1996; Post and Tullis, 1998; Stipp et al., 2006, and many others).

Griggs and Blacic (1965) and Griggs (1967) proposed that the hydrolization of Si-O bounds by H_2O was responsible for the water weakening (by easing the dislocation glide process). However, this process implied that H_2O was able to diffuse into the crystal lattice, which has been demonstrated to not be possible at experimental times scales (Kronenberg et al., 1986; Gerretsen et al., 1989). The diffusion of H_2O occurs at rates too slow to play a role in deformation experiments.

Moreover, the weakening of quartz is accompanied by a change in the deformation mechanisms, the recovery and recrystallization processes being promoted by water (Cordier and Doukhan, 1989; Tullis and Yund, 1989).

Different effects of H_2O weakening on quartz deformation have been reported, such as: promotion of dislocation nucleation, dislocation multiplication, dislocation slip and climb, diffusion, formation of subgrains, and recrystallization (bulge nucleation, subgrain rotation, grain boundary migration, grain boundary diffusion or grain boundary sliding, see review by Kronenberg (1994).

The complex role that water plays on quartz deformation and the potential multiple processes involved participates to the fact that deformation behaviour of quartz is not completely understood yet.

I.4.1. Deformation of quartz aggregates

Polycrystalline quartz deformation is well documented, both in natural (e.g., Kronenberg et al., 1990, 2020; Nakashima et al., 1995; Finch et al., 2016; Kilian et al., 2016) and experimental studies (e.g., Jaoul et al., 1984; Kronenberg and Tullis, 1984; Mainprice and Paterson, 1984; Hirth and Tullis, 1992; den Brok et al., 1994; Gleason and Tullis, 1995; Post and Tullis, 1998). As for the other minerals several factors can act on the deformation regime of quartz: deformation conditions such as temperature, pressure, strain rate (or displacement rate), applied force and chemical composition can influence quartz deformation.

For quartz aggregates, three dislocation creep regimes have been described by Hirth and Tullis (1992). These three regimes depend on temperature, strain rate and water conditions during deformation (Figure I.6). The definition of each regime is based on the deformation microstructures observed (which are the same within one regime) in conjunction with the characteristics of the mechanical behaviour. For each regime, distinctive microstructures can be identified because of the different mechanisms of dynamic recrystallization acting. The transition between the regimes is gradual and depends in the relative rates of grain boundary migration, dislocation climb and dislocation production.

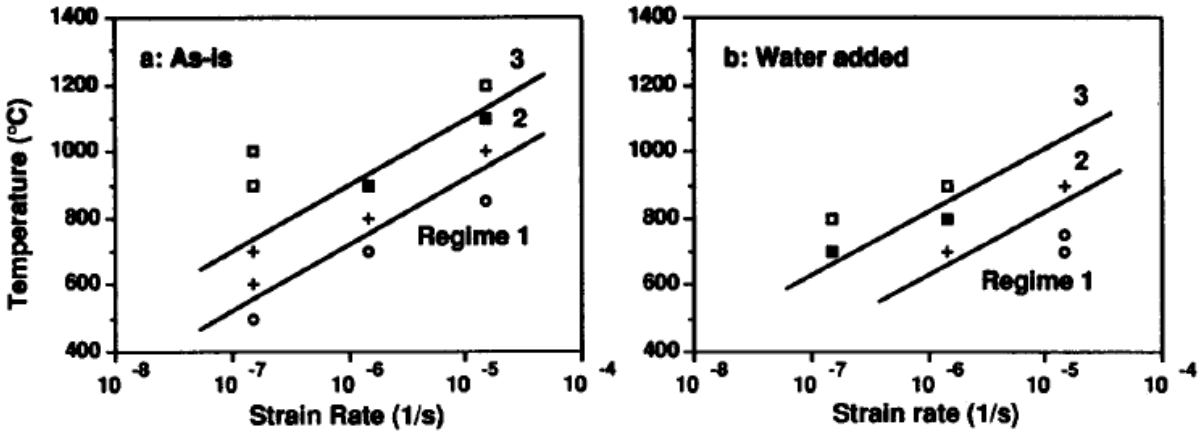

Figure I.6. Experimental conditions (temperature and strain rate) for the three dislocation creep regimes defined for quartz aggregates (Hirth and Tullis, 1992), deformed "as-is" (a) or with water added (b).

Deformation of quartz aggregates may depend on several parameters which can be varied and controlled in experimental studies: pressure, temperature, strain rate, grain size, and chemical composition. Experiments have been performed with and without added water ("as-is"). The addition of a trace amount of H_2O induces a lowering of the transitions between the three regimes (~100°C), the microstructures being the same within each regime, whatever the amount of H_2O available.

Effect of temperature

Temperature in an important factor to determinate deformation behaviour of quartz (fragile/ductile). The strength of quartz decreases with increasing temperature (Hirth and Tullis, 1992, 1994), the water weakening being thermally activated.

As noted by Kohlstedt et al. (1995), for experiments conducted on the plastic field, the temperature is frequently higher than expected in the lithosphere in order to obtain measurable strain rates.

Effect of strain rate

The deformation behaviour of quartz is also strongly dependent on the strain rate (Hirth and Tullis, 1992). As the strain rate increases, the quartz strength increases, too. Fast strain rates induce a hardening of the sample whereas with slow strain rates there is a decrease in the flow stress.

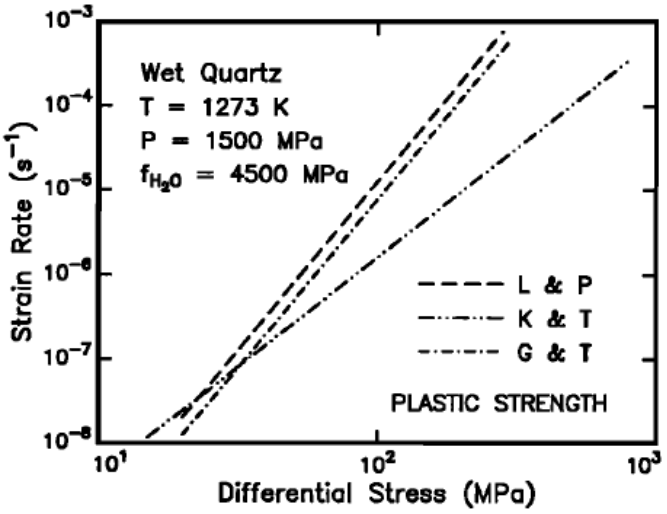

Figure I.7. Plot of strain rate as a function of differential stress for wet quartzite. The differential stress increases with the strain rate, Kohlstedt et al. (1995).

In laboratory experiments, as a matter of feasibility of the experiments, the strain rates used are usually several orders of magnitude faster than the ones encountered under natural geologic conditions (Kohlstedt et al., 1995).

Effect of grain size

In polycrystalline rocks, such as quartzite, the grain size is a crucial parameter impacting the strength. The active deformation mechanisms involved in the plastic deformation strongly depend on the aggregate grain size: larger grain sizes promoting deformation in the dislocation creep regime whereas for small grain sizes diffusion creep can be the dominant mechanism. Because of its high importance, the grain size (d) belongs to the parameters used in quartzite flow laws.

In addition to that, dynamic recrystallization leads to the formation of small grains and it has been hypothesized that there may occur a change in the deformation mechanism from dislocation creep to diffusion creep and grain boundary sliding because of the grain size reduction (Schmid, 1982).

The size of the recrystallized grains may also be used to determine the flow stress (piezometer). Thanks to experimental studies, Stipp and Tullis (2003) defined a piezometer relation $D = 10^{3.56\pm0.27} \times \sigma^{-1.26\pm0.13}$ for quartz deformed in the dislocation creep domain (regimes 2 and 3 from Hirth and Tullis (1992). This relation is applicable to naturally deformed rocks showing dynamic recrystallization microstructures.

Effect of pressure

At the elevated strain rates used in laboratory experiments, high confining pressures (> 10 MPa) are necessary to induce crystal plasticity in natural quartz aggregates The enhancing effect of confining pressure on the water weakening of quartz has been suggested by Paterson and Kekulawala (1979), Tullis et al. (1979), Blacic (1981) and Mainprice and Paterson (1984), speculating that pressure may positively affect the diffusive uptake of H_2O. However (as already pointed out above), the diffusion of H_2O into quartz at experimental times is too slow to be considered as an efficient process (Kronenberg et al., 1986; Gerretsen et al., 1989).

Kronenberg and Tullis (1984) have addressed the weakening effect of increasing confining pressure on the strength of quartzite in the presence of H_2O (Figure I.8). In their study, they show that the confining pressure strongly influences the strength of fine-grained wet quartz aggregates (3.6- 4.9 µm).

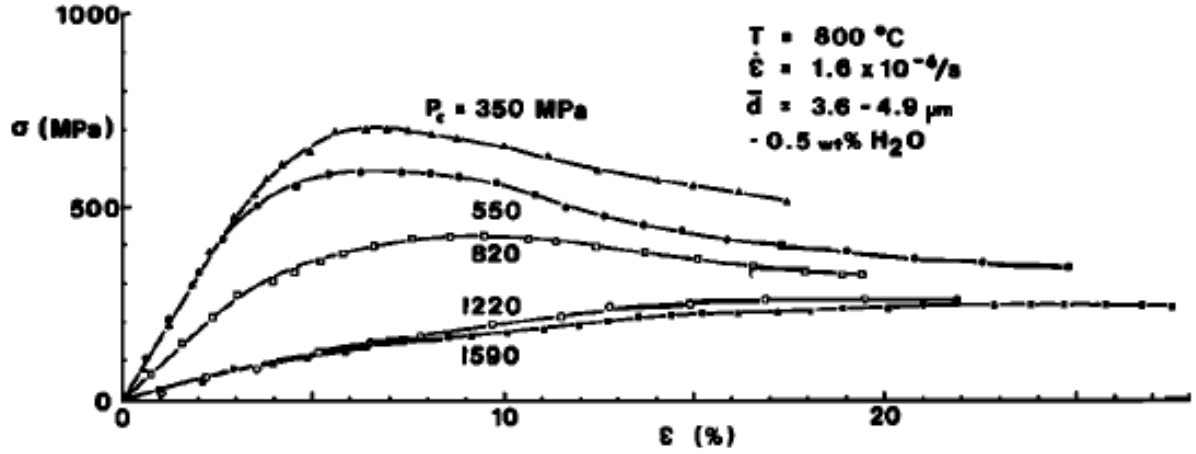

Figure I.8. Stress-strain curves showing the effect of confining pressure on the weakening of quartz aggregates (novaculites) with an inverse relationship between maximum deviatoric stress and confining pressure (Kronenberg and Tullis, 1984).

Tullis and Yund (1989) have presented a study of annealing deformed quartz crystals at different pressures in the presence of H2O and have shown that recovery and recrystallization are enhanced by higher pressures.

To account for both, H_2O and pressure effects, Kohlstedt et al. (1995) introduced the H_2O fugacity term (f_{H2O} in MPa) and its exponent (m) into the flow law: $\dot{\varepsilon} = A\,\sigma^n {f_{H2O}}^m \exp\left(\frac{-Q}{RT}\right)$, with $\dot{\varepsilon}$ the strain rate (s^{-1}), A the material constant, σ the differential stress (MPa), n the stress exponent, Q the activation energy ($kJ.mol^{-1}$), R the ideal gas constant ($J.K^{-1}.mol^{-1}$) and T the absolute temperature (K). This expression improved the applicability and consistency of quartz flow laws (Hirth et al., 2001; Holyoke and Kronenberg, 2013; Tokle et al., 2019) by correcting the strength for the effect of H_2O fugacity as a function of depth.

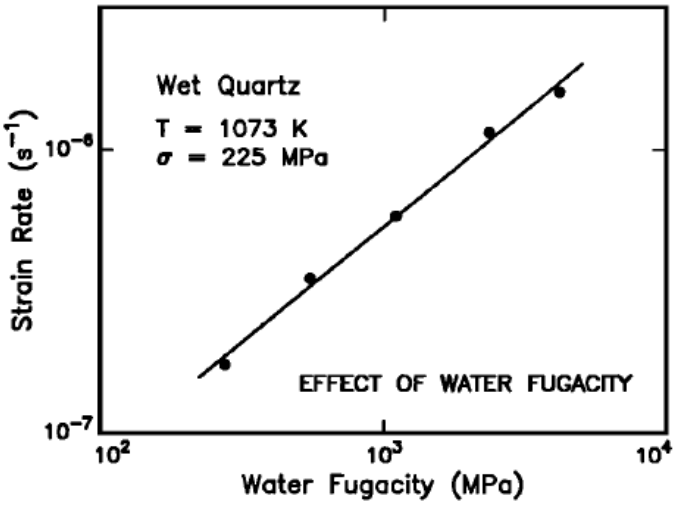

Figure I.9. Plot of strain rate as a function of H_2O fugacity for fine grained quartzites deformed in the dislocation creep regime (Kohlstedt et al., 1995).

Note: The fugacity is a thermodynamic parameter which corresponds to the expression of the difference between the real properties of a chemical species and its properties as a pure perfect gas. The fugacity coefficient of a chemical species is calculated from equations of state involving its activity and depends on the pressure and temperature.

The effect of H_2O fugacity (and not other fugacities such as hydrogen or oxygen) on flow strength was experimentally verified by Post et al. (1996). In addition to that, Chernak et al. (2009) conducted dislocation creep experiments on quartzite with varying H_2O fugacities (by changing the fluid composition, controlled by the presence of CO_2) without varying the confining pressure. Their results also show a weakening of the quartzite strength with increasing H_2O fugacity (Figure I.10).

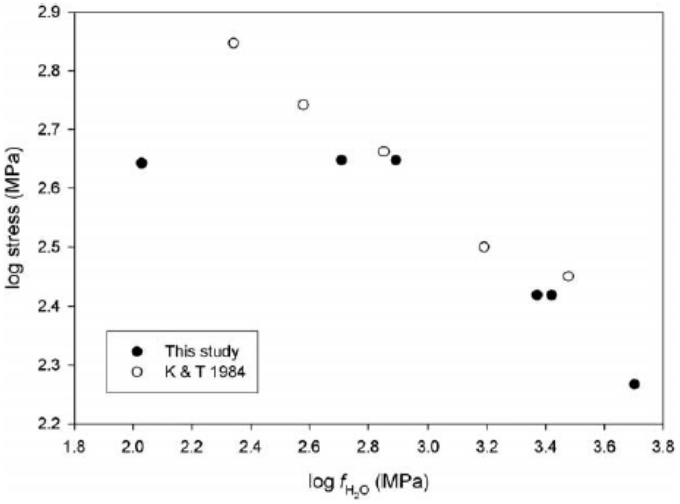

Figure I.10. The strength of quartzite decreases with increasing H_2O fugacity obtained by varying the confining pressure (data from Kronenberg and Tullis, 1984) or by varying the H_2O fugacity at constant confining pressure (Chernak et al., 2009).

Effect of the amount of water added

Several experimental studies investigated the deformation behaviour of quartz with different amounts of H_2O available (e.g., Jaoul et al., 1984; Post and Tullis, 1998; Stipp et al., 2006;

Chernak et al., 2009). Samples of quartzite were deformed vacuum-dried, as-is, or with added water (different quantities). When the H_2O content available to the samples increased, the strength of quartzite decreased (i.e., the weakening increased). This was also illustrated in the Figure I.6 (Hirth and Tullis, 1992) where the addition of trace amounts of H_2O induces a lowering of the transitions between the three dislocation creep regimes. With H_2O added, an increase in the recrystallized grain size is also observed (Stipp et al., 2006), consistent with the piezometer law for lower flow stress (Stipp and Tullis, 2003).

I.4.2. Flow laws for quartz

From experimental studies, it is possible to define the relationship between stress and strain. By varying the different conditions of deformation (temperature, pressure, strain rate and force) the flow law parameters can be defined (e.g., Luan and Paterson, 1992; Gleason and Tullis, 1995; Hirth et al., 2001; Rutter and Brodie, 2004a, 2004b; Tokle et al., 2019)

The general flow law for dislocation creep of quartz is: $\dot{\varepsilon} = A\,\sigma^n {f_{H2O}}^m \exp\left(\frac{-Q}{RT}\right)$ with $\dot{\varepsilon}$ the strain rate (s^{-1}), A the material constant, σ the stress (MPa), n the stress exponent, f_{H2O} the H_2O fugacity (MPa), m the H_2O fugacity exponent, Q the activation energy ($kJ.mol^{-1}$), R the ideal gas constant ($J.K^{-1}.mol^{-1}$) and T the absolute temperature (K).

There is a significant variation in the value of these parameters as a function of the studies, notably the value of the stress and H_2O fugacity exponents (n and m, respectively).

In studies of fine grained quartz material, Rutter and Brodie (2004a, 2004b) have determined stress exponents of n ≈ 3 and n ≈ 1 and have demonstrated grain size sensitive flow in quartz. These n-values are lower than previous values of n ≈ 4 for dislocation creep determined by Paterson and Luan (1990), Luan and Paterson (1992) and Gleason and Tullis (1995) and used by Hirth et al. (2001). Recently, Tokle et al. (2019) determined, from a compilation of experimental data on wet quartz aggregates, stress exponents of n ≈ 4 and n ≈ 2.7 depending on deformation conditions. For fine grained quartz aggregates, Fukuda et al. (2018) and Richter et al. (2018) have determined n-values of 1.7 to 1.9, respectively. These values were partly interpreted as a combination of dislocation and diffusion creep mechanisms, rheology associated with dislocation creep having stress exponent of n ≈ 3 whereas n ≈ 1 for rheology associated with solution transfer processes.

For the m-exponent, a value of m ≈ 1 is generally used (e.g., Luan and Paterson, 1992; Gleason and Tullis, 1995; Kohlstedt et al., 1995; Hirth et al., 2001; Fukuda et al., 2018; Tokle et al., 2019).

Deformation mechanism maps

Using the dislocation and diffusion creep flow laws (Hirth et al., 2001 and Rutter and Brodie, 2004a, respectively) deformation maps for wet quartz can be constructed (Figure I.11), allowing to predict the dominant deformation mechanism as a function of the grain size, temperature or differential stress.

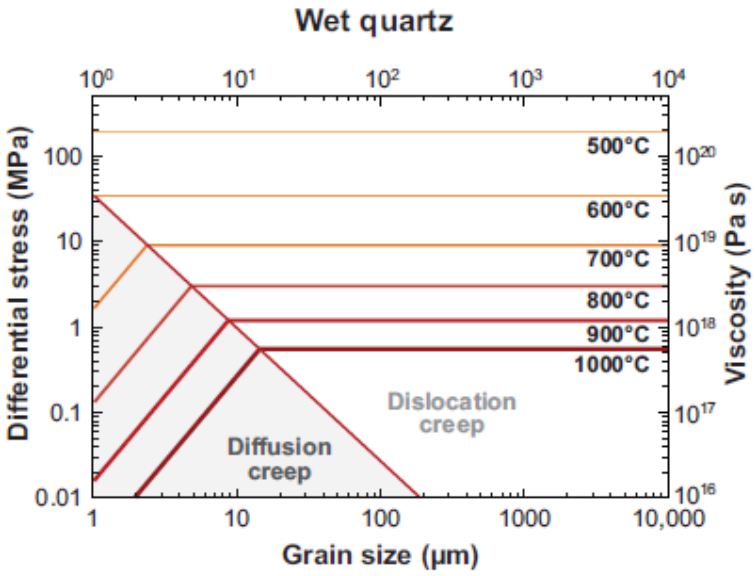

Figure I.11. Deformation mechanism map for wet quartz rheologies determined by Rutter and Brodie, 2004a, 2004b) for a strain rate of 10^{-12} s^{-1} (from Burgmann and Dresen (2008).

I.5. Water in quartz

As presented in the part I.4, the strength of quartz depends strongly on the presence of water (Griggs and Blacic, 1965). Although quartz is an anhydrous mineral (no H_2O included into its structural formulae) it is able to incorporate traces of water. Water is found to be present into quartz crystals and aggregates, in molecular form (H_2O) or as point defects (OH) (e.g., (Kats, 1962).

Molecular H_2O in natural quartz is found dissolved in the crystal lattice (structural water) or trapped within fluid inclusions and clusters (very small H_2O aggregates, Aines and Rossman, 1984; Kronenberg and Tullis, 1984; Kronenberg and Wolf, 1990; Kronenberg, 1994). Impurity-specific OH defects into quartz are found in various structural and defect sites (Kats, 1962).

H_2O content and speciation measurements

The H_2O content and the OH defects that are present into quartz can be qualitatively and quantitatively analysed by Fourier transform infrared spectroscopy (FTIR), this technique being particularly sensitive to water species. FTIR has been widely used to characterize H_2O in quartz aggregates, both on experimentally (e.g., Post and Tullis, 1998; Stipp et al., 2006; Gleason and DeSisto, 2008; Chernak et al., 2009) and naturally (e.g., Kronenberg et al., 1990; Kilian et al., 2016; Palazzin et al., 2018) deformed materials.

The infrared spectra recorded on quartz are composed of a broad absorption band centred at 3400 cm^{-1} representative for molecular H_2O and of thinner discrete bands in the 3000 – 3800 cm^{-1} range corresponding to OH points defects bound to the quartz structure (Kats, 1962; Aines and Rossman, 1984). The measurement of the broad absorption band area allows the quantification of the H_2O content of quartz (e.g., Paterson, 1982; Libowitzky and Rossman, 1997; Stipp et al., 2006).

Relationship between H_2O content and deformation of quartz

The water weakening of quartz has been correlated with the broad absorption band centred at 3400 cm^{-1} which corresponds to molecular H_2O and not to the discrete OH absorption bands (Kekulawala et al., 1978; Kronenberg et al., 1986; Gerretsen et al., 1989). Changes in the discrete absorption bands with deformation have also been reported (Kronenberg et al., 1986; Rovetta et al., 1986). For single natural quartz crystals, a positive relationship between the dislocation creep strength and the concentration and speciation of intragranular H_2O have been established (Kronenberg, 1994).

As described above (part I.4.1), the mechanical weakening of quartz depends on the amount of H_2O content of samples and on the externally available H_2O, a decrease in strength been observed when H_2O is added compared to vacuum-dried or as-is samples (Jaoul et al., 1984; Kronenberg and Tullis, 1984; Hirth and Tullis, 1992; den Brok et al., 1994; Post and Tullis, 1998; Stipp et al., 2006). However, it is not well understood how the H_2O added to the samples induces the weakening, the quartzite samples already containing enough H_2O to deform plastically as-is.

In addition to that, FTIR H_2O contents measurements of experimentally deformed quartz aggregates do not agree on the evolution of H_2O with deformation and about the quantity of H_2O needed. Kronenberg and Wolf (1990) and den Brok et al. (1994) did not find any change in intragranular H_2O contents of deformed samples compared starting material whereas Post and Tullis (1998) and Gleason and DeSisto (2008) found increased amounts and Stipp et al. (2006) and Palazzin et al. (2018) decreased amounts of H_2O.

Solubility and diffusion of H_2O in quartz

The H_2O weakening of quartz requires the infiltration of H_2O or OH into the grains. However, low solubility of H_2O into quartz (100 – 200 $H/10^6$ Si, Kekulawala et al., 1981; Gerretsen et al., 1989), corresponding to dry quartz in experiments, thus not plastically deformable) and low diffusion coefficients (10^{-10} to 10^{-12} $m^2.s^{-1}$, Kekulawala et al., 1981; Kronenberg et al., 1986; Rovetta et al., 1986) have been reported. These diffusion coefficients have been demonstrated to be incorrect, because the H_2O did not enter the crystals by diffusion but through cracks (Gerretsen et al., 1989). Then, fluid inclusions and water-related defects in quartz constitute excess H_2O compared to its low solubility, inferring that hydrolytic weakening as a disequilibrium process (Post and Tullis, 1998). In addition to that, due to the low H_2O diffusion coefficients, the diffusion of water-related species to attain equilibrium is not possible and cannot be considered as an effective mechanism for intragranular H_2O gain or loss at experimental times. The way that H_2O influences the strength of quartz is then still not understood.

Role of intergranular H_2O

In polycrystalline aggregates, the H_2O is found in both, inside the grains and along the grain boundaries. While quartzites deformed in presence of H_2O display evidence for intracrystalline dislocation creep deformation, the H_2O content present at grain boundaries may play a non-negligible role on the strength of quartz aggregates and on the weakening process. This is notably highlighted by the higher stresses observed for deformed vacuum-dried samples

compared to as-is and water-added samples (e.g., Jaoul et al., 1984; Hirth and Tullis, 1992; Post and Tullis, 1998; Stipp et al., 2006; Chernak et al., 2009).

The rates of diffusion along grain boundaries allow transport to be an effective process at experimental time scales (Farver and Yund, 1991a; Nakashima, 1995), however, as intragranular diffusion process are not, an equilibrium between intragranular and intergranular H_2O is not expected (Kronenberg, 1994). The grain boundary mediating-processes may then participate in the water weakening in quartz aggregates (Kronenberg and Tullis, 1984; Holyoke and Kronenberg, 2013).

Post et al. (1996) suggested that intergranular H_2O may also play a role in the weakening process, providing a source of fluid phase which may regulate the H_2O fugacity. The H_2O contained in the grain boundaries may enhance the rates of recovery in promoting recrystallization (Holyoke and Kronenberg, 2013) and solution transfer processes (den Brok and Spiers, 1991; den Brok et al., 1994) and then also participate in the weakening of quartz aggregates by the presence of H_2O.

I.6. Questions raised

Despite a long history of research since the early discovery of the effect of H_2O on quartz rheology by Griggs and Blacic (1965), many aspects of H_2O weakening in quartz are yet unresolved.

Effect of pressure on deformation of quartz natural aggregates in presence of H_2O

Considering the insights from the previous studies, one assessment that can be made is that even if the effect of pressure on deformation of quartz in the presence of H_2O had been demonstrated, its cause is still not very clear.

Kronenberg and Tullis (1984) have highlighted the weakening effect of pressure on the strength of wet quartz aggregates (Figure I.8). As their experiments have been carried out using fine grained novaculite (< 5 µm), and as this material has also been used in the experiments by Fukuda et al. (2018), who have concluded deformation by diffusion creep processes, it may be possible that the pressure dependence of deformation is related to the fine grained nature of the starting material. (Manning, 1994, 2018) established that the solubility of quartz increases non-linearly with increasing pressure, so that solution-precipitation processes may be expected to be enhanced at high pressures. Diffusion creep in the presence of H_2O will involve dissolution and precipitation and therefore is expected to be pressure dependent. The pressure dependence of quartz rheology could then arise from enhanced dissolution at higher pressures.

For this reason, the problem of pressure dependence of quartz deformation has been revisited by using a coarse grained quartzite (∼200 µm grain size) as starting material in order to diminish the potential role of diffusion creep processes and to test whether the dependence of quartz strength on pressure is the same as in fine grained material and to study the processes of weakening in more detail.

Several coaxial experiments were conducted on water-added quartzite samples and at different confining pressures ranging from 600 to 2000 MPa.

Evolution of H_2O content and speciation of natural quartz aggregates in the presence of H_2O

Alongside the pressure effect, the evolution of H_2O content during deformation is still not completely understood.

It is generally admitted that the mechanical properties of quartz depend critically on the presence of water, H_2O playing a great role in plastic deformation of quartz. Although a great number of studies have measured the H_2O contents of (naturally and experimentally) deformed samples, the redistribution of H_2O into the quartz aggregates during deformation is still subject to debate, both increasing and decreasing behaviours being reported. Moreover, the weakening effect may involve the participation (and redistribution) of H_2O into the quartz aggregate within and around the quartz crystal during deformation.

For this reason, the starting material and water-added samples experimentally deformed at different confining pressures have been studied using Fourier transform infrared spectroscopy in order to determine the content and distribution of H_2O before and after deformation. Thanks to the coarse grain size of the samples used, discrimination of the H_2O content in grain interiors and in the grain boundary region can be made.

The objectives of this thesis are:

(i) Specify the effect of confining pressure on the strength of coarse-grained quartz aggregates in the presence of H_2O, and explain its cause,

(ii) Study the distribution and speciation of H_2O in the grain interiors and grain boundary of deformed the samples.

I.7. Manuscript organisation

To answer the above-mentioned questions, the manuscript is divided into several chapters:

The first chapter (actual one, part 0) allowed to introduce the subject and define the objectives of the thesis.

The second chapter (part II) is dedicated to the presentation of the experimental and analytical methods used to assess the questions raised. The conditions of the analyses performed as well as the data treatment are also detailed.

The third chapter (part III) focuses on the mechanical and microstructural results obtained from the deformation experiments.

The fourth chapter (part IV) deals with the infrared measurements performed and the H_2O content evolution within the quartzite during the deformation.

The fifth chapter (part V) proposes a synthetized discussion, trying to gather the results obtained and discussed in the two previous chapter.

The sixth chapter (part VI) lists all the references used in the manuscript.

Finally, in the seventh chapter (part VII) additional data are collected.

II. Methodology

This chapter describes the experimental procedure and analytical methods used during this thesis work.

First, the Griggs type apparatuses used for the experiments and the related sample assembly are described. Following this, the experimental procedure and mechanical data treatment are presented.

Then, the different microstructural and analytical techniques used to study the samples are presented with their conditions of acquisition. Data treatments performed are also described for each method employed.

II.1. Experimental procedure

Deformation experiments consisted of coaxial shortening of natural quartzite samples from Tana, Norway (for the characterisation of the starting material, see the next chapter, part III.1). They have been performed using two Griggs-type apparatus: Tullis-modified apparatus at University of Tromsø (Norway) and new generation rig (Sanchez) at Institut des Sciences de la Terre d'Orléans (ISTO, France).

II.1.1. The Griggs-type apparatus (short description)

This part is based on the description of the Sanchez rig at Orléans Griggs lab made by Jacques Précigout (and available at: https://sites.google.com/site/jacquesprecigout/recherches/griggs-lab-en). More details about the apparatus can also be found in Précigout et al. (2018) and in Rybacki et al. (1998).

The Griggs-type apparatus consists of a specially designed piston-cylinder that allows deforming samples. It is a tri-axial apparatus with solid confining medium (NaCl here) where deformation experiments (in pure or simple shear) can be performed on various types of samples and at lithospheric pressures and temperatures conditions.

The general principle of deformation experiments is to impose to the sample a differential stress by applying a vertical force on the sample while an isostatic force (confining pressure) is maintained around it horizontally thanks to a confining medium.

Griggs-type apparatus has been first developed in the 60's (Griggs, 1967) and has then been improved by number of others (notably Tullis and Tullis, 1986 and Green and Borch, 1989) over the years. It consists of a metal frame constituted of three horizontal platens maintained together by four vertical columns (Figure II.1a).

The two forces (leading to confining pressure and to deformation) are exerted by two independent pistons. The first one (σ3 piston) applies an annular force on the confining medium (i.e., around the sample) whereas the second (σ1 piston) applies a vertical/axial force on the cylindrical piston and thus, the sample. The σ1 piston is positioned in the middle of the σ3 piston. They are made of tungsten carbide.

The pressure is exerted on the pistons by two regulated hydraulic pumps (rams). The confining pressure hydraulic ram is positioned on the central platen and the deformation actuator on the upper platen. The confining pressure ram is monitored by an oil pressure sensor and the deformation actuator by a load cell. In addition, the displacements of the two pistons are recorded by displacement transducers.

The sample to be deformed is contained inside an assembly, made of several pieces that need to be manufactured for each experiment (Figure II.1b and next section for the description of the different pieces of the sample assembly and how they are made).

During the experiment, this assembly is placed inside a pressure vessel (made of tungsten-carbide core inserted inside steel). The pressure vessel is placed on a base plate where the sample assembly lies on. This base-plate is perforated of two holes where thermocouples are

inserted and go off it in order to be connected to the temperature-controller system. The middle part of the base plate also allows the high voltage current to pass to the assembly (resistance graphite furnace) and heat the sample.

At the top of the pressure vessel, an end-load piston is placed. The two tungsten pistons (σ3 and σ1) are positioned at the middle of the end-load piston. These three pieces made the relay between the rams and the assembly and must be perfectly aligned.

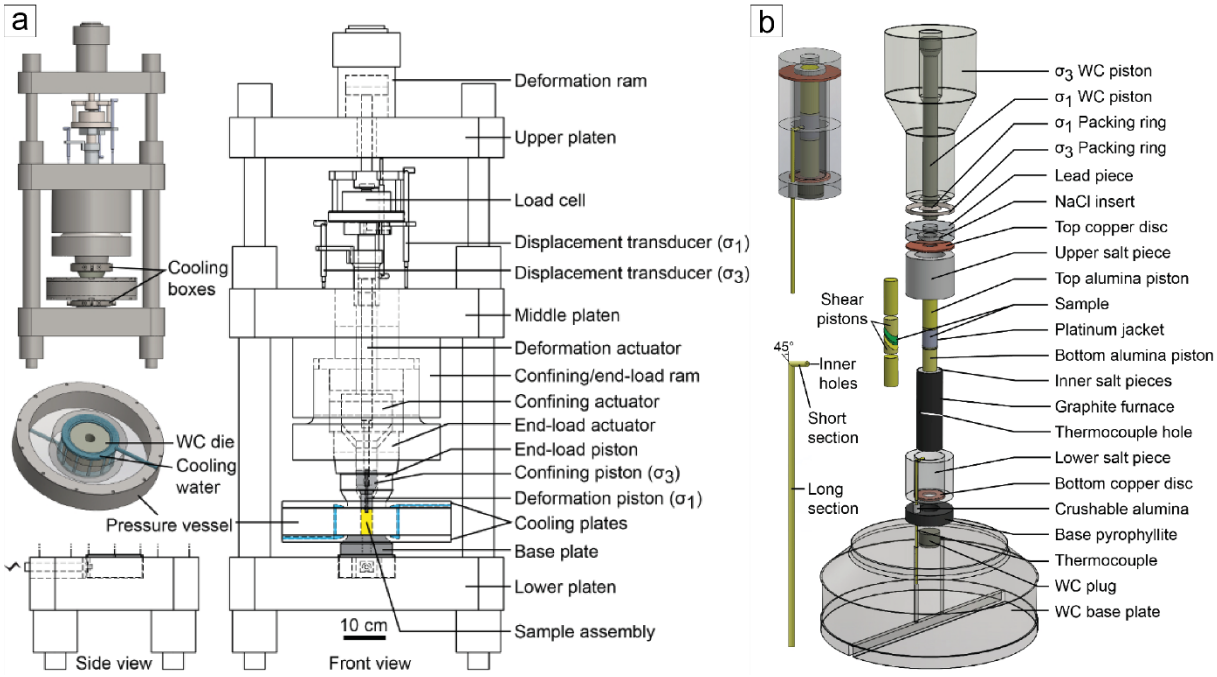

Figure II.1. Schematic drawings of (a) new generation Griggs-type apparatus at ISTO and (b) corresponding sample assembly. Images from Précigout et al. (2018).

While heating the assembly during the experiment, the base plate and the pressure vessel are cooled by water flowing in a cooling system that runs inside the steel part of the pressure vessel (from bottom to top). A silicon oil flow is also used to cool the confining pressure ram.

In the new Griggs-type Sanchez apparatus, all the parameters are servo-controlled and monitored from a computer that also records all the variables. This allows to maintain/regulate the confining pressure at the same value all experiment long while performing constant load or constant displacement deformation experiments.

II.1.2. The sample assembly

The sample assembly is composed of different pieces that need to be manufactured before each experiment. As more experiments have been performed in Orléans, the following section describes the sample assembly used for experiments performed with the Sanchez apparatus. You can find more details of the preparation procedure in Précigout et al. (2018).

For samples deformed in Tromsø, assemblies differ in size (smaller diameter and length) and use only one thermocouple. The general procedure and assembly making is almost the same. A detailed description can be found in Richter (2017).

The pieces constituting the assembly are shown in Figure II.2. The core of the assembly is the sample itself that is wrapped into a nickel foil weld sealed into a platinum jacket (composed of a tube and two cups). Two alumina pistons are inserted at each ends of the jacket. Then, a first layer of confining medium (NaCl salt) surrounds it. This is inserted inside a furnace then surrounded by a second layer of confining medium. One or two thermocouples pass through these layers in order to be in contact with the jacket. Two copper discs are added at each end. Finally, a piece of lead goes to the top while a ring pyrophyllite is put at the bottom.

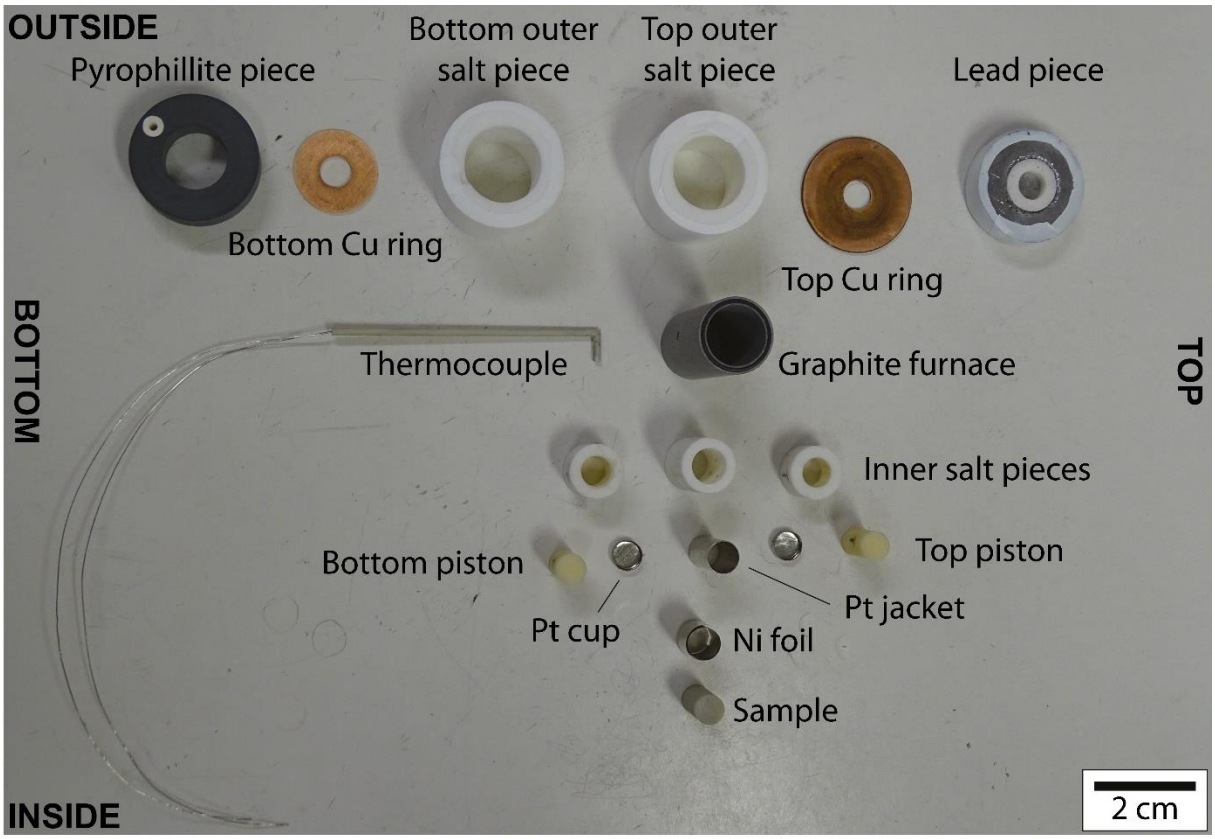

Figure II.2. Sample assembly "écorché" showing all the pieces that constitute it. These pieces go on the Tullis-modified Griggs apparatus.

The next sections describe in detail each part of the assembly and the corresponding photos are presented in the Appendix chapter (part VII.1: Figure VII.1 to Figure VII.17).

II.1.2.1. Sample

For coaxial deformation experiments, the samples consist of cylinders of natural quartzite that are cored into a block using a drill press. As the material seems isotropic at the scale considered, no particular preferential orientation was respected for the drilling. The cylinders diameter are ~6.35 mm for samples deformed in the conventional Griggs apparatus and ~8 mm for those deformed in the Sanchez apparatus.

The cored cylinders are cut with a diamond saw, 1-2 mm longer than the required length. The two ends are then ground flat, plane parallel, and to the right size (approximatively twice the diameter). This operation is done using a lathe machine tool equipped with a diamond rotating grinder tool. In order to ensure a better comparison between the samples, most of those deformed in Orleans had the same initial length (~15 mm).

Special care is needed during this operation as the sample ends have to be plane parallel (to ∼0.001 mm tolerance) to avoid its simple shearing during the deformation.

The sample is then dried in an oven at 110°C during ∼one day (20 – 25 hours) in order to remove surface water (and eventual water impregnated during machining, as water is used as lubricant during all the previous operations). After that, it is cooled to ambient temperature and weighted to calculate the amount of H_2O to be added.

Before being inserted into the jacket, the sample is wrapped into two layers of Nickel foil (0.025 mm thickness). This is made to avoid NaCl and C transfers to the sample through the Pt jacket during the experiment. The presence of Ni also allows buffering the oxygen fugacity.

The amount of distilled H_2O added represents 0.1 wt.% of the sample, that means that for 1 g of sample, 1 µL of distilled H_2O is added. This quantity is measured and added into the jacket using a calibrated pipette.

For two experiments (OR73 and OR76), no H_2O was added. They were just cooled and weighted before being wrapped into the Ni foil and directly inserted into the Pt jacket.

II.1.2.2. Jacket

The sample is weld sealed into a Platinum jacket (pure Pt). The jacket is composed of three parts: a Pt tube (8 mm diameter and 0.15 mm wall thickness) and two cups. The cups are made from discs cut with a metal puncher in a Pt foil (10 mm diameter and 0.15 mm thickness) that are embossed thanks to a special tool. They have an 8 mm base and ∼1 mm rim height. The Pt tube is cut ∼3 mm longer than the sample length.

The platinum jacket and cups need to be annealed at 900°C during ∼2 hours before being used, this is done using a high-temperature furnace. This annealing is necessary to prevent jacket failure during the experiment.

The first cup is then inserted at the bottom of the Pt tube. The extremities of the Pt tube and cups that are welded together need to fit really well and their surface to be plane. Pliers and metal file are used to adjust them and obtain flat ends. This allows the welding procedure to be easier and faster.

The weld is made under binoculars, using a TIG welder with argon as inert gas (from PUK brand) at 18% power and 10 ms. The quality of the weld needs to be carefully checked with the binoculars, in order to be sure that there is no hole.

Once the first cup is welded, the distilled H_2O is added at the bottom of the jacket. The sample (wrapped into the Ni foil) is inserted inside, and the second cup is put in place and immediately welded in order to limit the water loss.

Finally, the welds are gently flattened with pliers in order to allow the pistons to enter. Once the pistons are inserted, the welds are tightened around with the pliers to keep them in place and reduce the thickness of the welds.

II.1.2.3. Thermocouples

The temperature is monitored and regulated using S-type thermocouples. They are composed of two wires (of 0.25 mm diameter) inserted inside an insulating mullite tube (aluminium silicate $Al_6Si_2O_{13}$). One wire is made of Platinum (Pt pure) and the other of an alloy of Platinum and Rhodium (90%Pt – 10%Rh).

The two wires are cut to the right size (∼20 cm in Tromsø and ∼30 cm in Orléans) and welded together at one tip. The weld is then flattened with a plier and cut to obtain a flat, thin, and straight end.

The mullite sheath (1.5 mm external diameter) is perforated by two holes all along its length, allowing to insulate the two wires from each other and from the outside. It is made from two parts (one long of 76 mm and one short of 6 mm) that are cut flat at one end and at 45° at the other end. Once assembled together, the two parts at 45° will form a right angle that gives the thermocouple a "L" shape. At the flat end of the short part (the one in contact with the jacketed sample) a notch is made in order to receive the weld.

The wires are then inserted inside the mullite tubes (in the short then in the long one). The weld should fit perfectly inside the notch. At the junction, the wires are bended to form a 90° angle and the two mullite tubes are glued with ceramic glue. The notch is also filled with the same glue.

Note: the size of the long part of the mullite sheath depends on where we want to record temperature along the sample during the experiment. Here the thermocouples were positioned at the middle of the sample.

If they still are in good condition after the experiment, wires can be reused several times (until they are too short or too damaged). The thermocouples need to be tested before the experiment.

II.1.2.4. Alumina pistons

The pistons are positioned at the top and at the bottom of the jacketed sample, inside the cups and are made in alumina (Al_2O_3).

They are cut with a diamond saw (∼1-1.5 mm more than the desired length value) and plane parallelized (difference less than 2-3 µm) in the same manner than for the sample, using the lathe and the diamond tool under water flow.

Their lengths are calculated depending on the lengths of the sample, furnace and full assembly, taking into account that the sample should be positioned at the middle of the furnace.

The bottom piston length ($L_{P,inf}$) is calculated thanks to:

$$L_{P,inf} = L_{OSP,inf} - \frac{L_i + 2 \times t_{Pt}}{2} - c$$

with $L_{OSP,inf}$ the length of the outer bottom salt piece (24 mm), L_i the initial sample length (mm), t_{Pt} the Pt foil thickness (0.25 mm) and c the compaction of the assembly (1.7 mm).

The top piston length ($L_{P,sup}$) is then calculated with:

$$L_{P,sup} = L_F - L_{P,inf} - (L_i + 2 \times t_{Pt}) + 2$$

with L_F the length of the furnace (mm) and 2 the length of piston that should be higher than the furnace in order to go into the Cu disc and the bottom part of the lead piece at the top of the assembly.

Sometimes the diameter of the pistons needs to be rectified. This is done before cutting and parallelizing them, using the lathe and a special blade tool.

The pistons are inserted inside the cups of the platinum jacket. They have to fit well inside the welded cups and be aligned with the sample. They are tightened inside the welded cups thanks to a plier. The alignment of the jacketed sample and the alumina pistons should be done carefully in order to avoid asymmetrical deformation of the sample during the experiment.

II.1.2.5. Salt pieces

The confining medium consists of five salt pieces: three inner and two outers. The inner salt pieces take place around the sample and alumina pistons, inside the furnace. The outer salt pieces surround the furnace and are directly in contact with the pressure vessel.

All that pieces are made with sodium chloride (NaCl, 99.9% pure) that is first grinded into a ceramic mortar until it has the aspect of a fine powder. This salt powder is then weighted, mixed with addition of 1-2 drops of distilled H_2O and cold pressed into special moulds. The moulds used are specially adapted to the size of the sample assembly.

The three inner salt pieces are made with the same mould from 8 g of salt pressed at 6 tons during 30 s. The shape obtained consist of a hollow salt cylinder (~4 cm long).

The outer salt pieces are mould with the same tool, and both pressed at 14 tons during 30 s (the pressure has to be slowly released to avoid cracks). The bottom one is longer and made from 17.5 g whereas the top one needs 16.5 g of salt. The latter consist in a simple hollow cylinder while the former has a groove at its bottom inner part where the bottom Cu disc will take place.

Once all the pieces are made, they are let dry during at least one night at 110°C in a hoven. After that they can be adjusted to the right dimensions. The outer diameter of all pieces needs to be reduced with the lathe tool in order to allow them fitting inside the furnace (inner pieces, < 13 mm) or inside the pressure vessel (outer ones, < 26.9 mm).

The lengths and diameters of the inner salt pieces need to be adjusted to the pistons (for the top and bottom ones) or to the jacketed sample (middle one). The appropriate lengths are obtained by first cutting the salt inner pieces with the diamond saw (without water flow) and then rasping them with sandpaper. During this process, their ends must stay as flat as possible. The middle inner salt piece should measure the same length than the jacketed sample. The bottom and top inner salt pieces lengths are adjusted in order that the total inner salt length corresponds to the pyrophyllite furnace length.

The inner diameter of the top and bottom inner salt pieces is adjusted with sandpaper whereas for the middle inner salt piece, a bigger hole is obtained by drilling inside the piece (using once again the lathe machine) before using the sandpaper to adapt it.

The outer salt pieces lengths are adjusted by rasping them with sandpaper. The outer bottom should measure 24 mm whereas the top one should measure the pyrophyllite furnace length minus 24 mm (it is important that it does not exceed the graphite layer length that has to stick out). When rasping the salt ends, they should remain as flat and parallel as possible.

The inner diameter of the outer salt pieces should fit the furnace outer diameter, if it is not the case, sandpaper can be used.

It is important than the salt pieces lengths do not exceed the furnace pyrophyllite length to ensure a good contact between the graphite furnace layer and the top Cu disc.

In order to let the thermocouples, pass, two holes (1.7 mm diameter) are drilled all along the bottom outer salt piece, on opposite sides. At the top of these holes (on the inner top part of the bottom salt piece) perpendicular trenches are dug with a scalpel to receive the top short part (and corner) of the thermocouples. These trenches will then be continued with drills inside the furnace and the inner middle salt piece to allow the thermocouples to be near the jacket.

II.1.2.1. Furnace

The furnace is composed of three layers: one graphite layer between two pyrophyllite layers. It measures ~45.5 mm long. The graphite part is a little bit longer than the pyrophyllite ones in order to ensure a good contact with the top Cu disc and so on a homogeneous heating.

When the assembly is almost ready, the furnace (as well as the inner middle salt piece) is drilled to let the short thermocouples parts pass and be in contact with the sample. The drilling emplacement is determined thanks to the outer bottom salt piece (where trenches are made for the thermocouples).

During the experiment, a high voltage current is injected in the resistance furnace (graphite) from the bottom of the assembly (coming from the base plate). The increase in temperature of the furnace is obtained by Joule effect (up to 1300°C).

II.1.2.2. Lead piece

The lead piece sits at the very top of the assembly. Its role is to allow the pressure conditions to be attained without deforming the sample and to transmit the confining pressure from the confining piston (σ3) to the sample assembly (solid medium salt).

The lead piece is made from 50-55 g of lead (Pb) that is put to melt at 400°C in a furnace during ~30 min (the Pb fusion point is 327°C). The liquid lead is then poured inside a specially designed mould and pressed at 4 tons during ~30 seconds. The piece is then unmoulded, and the thickness of the central part measured (if the piece is not thick enough, i.e., < 3 mm, the moulding should be remade).

The outer diameter of the lead piece must be slightly adjusted in order to fit inside the pressure vessel (< 26.9 mm). This is done using the lathe and a special blade to have a regular aspect.

At the bottom of the lead piece a ring of salt is inserted. This ring is cut from the same salt tube than used for the inner salt pieces. It is grinded to the right thickness and its inner and diameter adjusted if necessary (the top of the top Al_2O_3 piston should fit inside). Once it has the good

dimensions (~2 mm thickness), it is inserted, and some lead is gently pushed around with a scalpel it in order to maintain it in place. This salt piece is necessary to maintain the top piston aligned vertically.

Finally, it has to be specified that special precautions must be taken when handling lead (at least use gloves and carefully washing hands after touching it).

II.1.2.3. Pyrophyllite piece

At the very bottom of the sample, there is an unfired pyrophyllite piece that consists into a thick disc. Two holes are drilled inside from either side to allow the passage for the thermocouples. Crushable magnesia tubes are inserted inside the drilled holes in order to maintain firmly the thermocouples without damaging them.

Both internal and external diameters must be checked (respectively with the tungsten plug and the pressure vessel) and adjusted using sandpaper if necessary.

II.1.2.4. Copper discs

At the top and at the bottom of the furnace, two copper discs are present. They allow the current to circulate into the furnace and so the heating of the sample assembly.

The top Cu disc is bigger than the bottom one and is positioned between the furnace and the lead piece. The bottom Cu disc is inserted inside a special groove at the bottom of the outer bottom salt piece.

No machining is needed for these two pieces. The inner diameter of the Cu discs should fit the diameter of the pistons. If it is not the case, they should be ground with the metal file.

II.1.2.5. Final steps

When all the pieces previously described are ready, the final step consists of drilling with the milling machine into the furnace and the middle inner salt piece two 2 mm holes in order to enable the passage of the thermocouples.

Once this is done, the assembly is built (without the top copper disc and the lead piece). Teflon (PTFE) is sprayed on the external face of the outer salt pieces and of the lead piece. This is done in order to isolate the pressure vessel and prevent it from rusting because of the salt that become corrosive. In addition to that, it allows the salt to glide against the metal and ease the insertion and then the removing of the assembly from the pressure vessel (reduces the friction between the assembly and the pressure vessel).

In Tromsø, Teflon tape is used instead of the PTFE spray. It is wrapped around the outer salt and the lead pieces.

At the very bottom of the assembly, a tungsten carbide cylinder is inserted inside the pyrophyllite piece. This piece supports the whole deformation column and allow the high-voltage current to pass from the base plate to the small copper disc and thus, the furnace.

Finally, the small and big packing rings, that will ensure the sealing/tightness between the lead piece and the pistons at the top, are cleaned and their top part grounded flat. This stage is

necessary in order to avoid lead leak during the experiment. The fit of the small packing ring with the σ1 piston is also checked.

The final assembly obtained after all these steps is shown in Figure II.3.

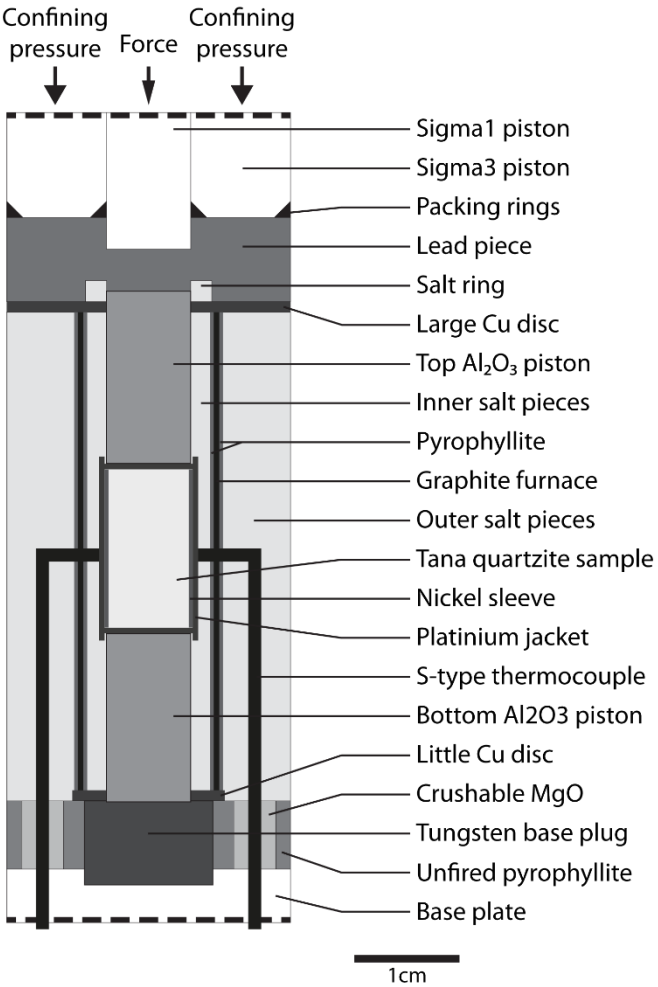

Figure II.3. Classical sample assembly used for deformation and hot-pressing experiments from 600 to 1500 MPa in the new generation Sanchez rig at ISTO (Orléans, France).

II.1.2.6. Adaptation of the pressure assembly to 2 GPa experiments

For deformation experiments at 2 GPa confining pressure, the sample assembly was slightly modified (Figure II.4). The top piston and top inner salt piece were separated into two parts (all plane-parallel) and a disc of compressed NaCl salt (of ~2.6 mm thickness and 13 mm diameter) was inserted in between. The disc was moulded from 0.7 g of powdered NaCl pressed at 4 tons for 30 seconds.

In this way, the deformation column was able to compact during acquiring the P-T conditions of the experiment (that require advancing a lot the pistons) without applying too much deviatoric stress on the sample.

Before the modification of the assembly, several experiments failed as the hit-point was reached during the pumping stage and the sample started to deform earlier than expected (OR45, OR50, OR54, OR56 and OR57). As the “hit-point” was not seen, the experiments were stopped, and the strengths curves could not be determined. The samples from these experiments were all deformed with different achieved strain.

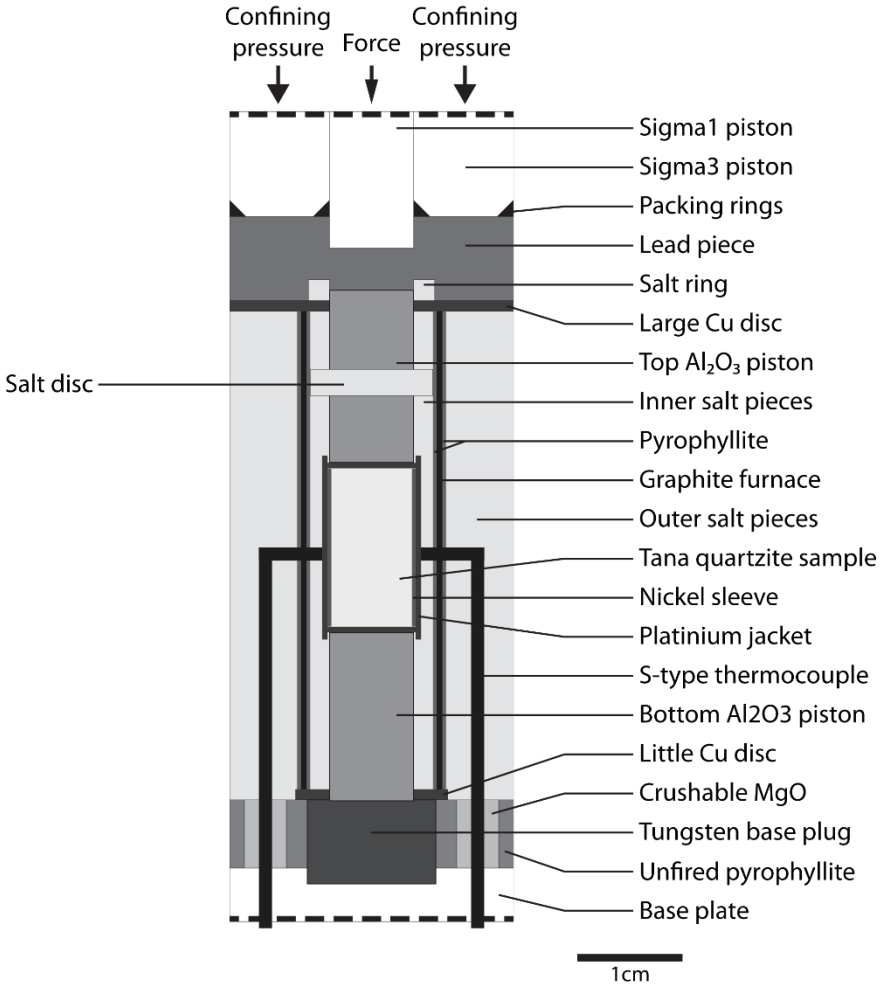

Figure II.4. Sample assembly adapted for experiments at 2 GPa: a salt disc is inserted at the middle of the top alumina piston. This modification allows the assembly to compact enough during the pressurization steps.

During the trials to perform experiments at 2 GPa, one experiment (OR56) was run at 10^{-5} s^{-1} in order to increase the resistance of the lead (expected to be low at these P-T conditions) and see the difference with the run-in curve and determine the hit-point. Unfortunately, this did not work, and the experiment had to be stopped after one day of deformation.

Previous other trials consisted in increasing the lead thickness (by adding an additional lead disc before the σ1 piston or by reducing the height of the rest of the assembly and increasing the weight of lead melted) or changing the pressurization steps.

II.1.3. Charging the assembly

Once the assembly is ready and sprayed with PTFE it is inserted inside the pressure vessel. For this purpose, an arbor press is used in order to suspend the pressure vessel above the base plate.

Before putting the assembly (that is quite fragile) inside the pressure vessel, it needs to be carefully aligned with the base plate (inside which the mullite sheaths of the thermocouples that stick out of the pyrophyllite will take place). The alignment is made with a steel cylinder of the same size and global shape than the assembly.

The sample assembly (without the top copper disc and the lead piece) is then inserted and an isolating sheet (Mylar) is placed between the base plate and the pressure vessel in order to isolate them (the high-voltage current that will be injected has to pass only within the sample assembly through the tungsten base plug). Special care is required when inserting the thermocouple mullite sheaths inside the corresponding base plate holes.

The base plate and the pressure vessel are then fixed together with clamps (that will be put away when the furnace with be started in order to insulate them from each other).

The top copper disc and lead piece can then be inserted at the top of the assembly and everything is maintained in place with the top bigger packing ring that is pushed into the pressure vessel. This packing ring makes a sealing between the σ3 piston and the pressure vessel.

The thermocouple wires are insulated all along and adaptors are connected (the Pt wire corresponds to the positive pole and the Pt-Rh the negative pole). For this operation, the pressure vessel is turned upside down.

Finally, the pistons are installed on the top of the pressure vessel. The end load contains the σ3 piston and the σ1 is inserted inside. As between the pressure vessel and the confining piston, a sealing is required between the force and confining piston. For this purpose, a small packing ring is inserted along the σ1 piston.

Once everything is ready, the whole assembly can be installed inside the apparatus.

II.1.4. Performing the experiment

Running one experiment with the apparatus is composed of several phases: the alignment of the pistons, the increase of pressure-temperature conditions until experiment conditions are attained, performing the experiment (deformation of hot-pressing) then quenching and finally removing the pressure vessel and then the assembly.

Alignment

Once the vessels are in the apparatus, the actuators (end-load, confining pressure and deformation) from the rig and the corresponding pistons on the pressure vessel need to be carefully aligned together.

For that purpose, the rig deformation piston is first advanced, and the alignment is made. Then the confining pressure and end-load pistons are advanced at their turn until they are in contact with their counterparts.

During this procedure, everything is controlled with the computer.

Variables recorded

During the experiments, several parameters are recorded to both follow the evolution of the experiment and then calculate the associated mechanical curves.

For the experiments performed on the Tullis-modified rig in Tromsø, the variables recorded during the experiment were the force, the confining pressure, and the displacement of the

deformation piston. These data were recorded on a chart paper (the electronic data recording did not work) in Volt units (that later were converted to other units).

For the experiments performed on the new-generation apparatus in Orléans, the computer monitoring allows to record the room temperature, the sample temperature, the displacements of the confining and deformation pistons, the pressures of the rams and the force. The variables are converted directly to σ1 and σ3 pressures, the differential stress and the differential piston displacements.

Heating and pressurization

Once everything is in contact, the confining pressure is increased to 50 MPa by alternatively advancing the σ3 and σ1 pistons. The σ3 piston is advanced of 10 MPa whereas the σ1 piston is only advanced in order to stay in contact with the lead.

When the 50 MPa are attained, the base plate and pressure vessel are detached, and the cooling systems started. The temperatures recorded by the thermocouples must be checked to be sure that they work. Once the expected temperature decrease happens, the furnace is started.

The temperature is first increased to 30°C, then to 100°C and 200°C without increasing the confining pressure (and so, moving the pistons) with a break at each level.

Then, the temperature and pressure are increased by alternatively starting the two pumps until the final P-T conditions are attained. The temperature was raised by steps of 100°C, at a rate of ~20°C per minute (45 minutes to go from 30 to 900°C). For the pressure, the steps depended on the final confining pressure to be reached. During these steps, it was important that the P-T conditions did not intersect the NaCl melting curve so that the confining medium stayed in the solid state. During pressurization, σ1 and σ3 pistons were alternatively advanced, respecting a maximum distance of 3 mm between the two in order to keep the small packing ring in place.

The last step before reaching the required conditions has to be an increase of the temperature (i.e., for us, the pressure conditions were attained at 800°C and then the temperature was increased to 900°C). The final pressurization step should consist in advancing the σ3 piston (not the σ1) trying to have a maximal distance (3 mm) between the two pistons. The σ1 piston should be as far as possible to obtain a smooth lead curve when starting the deformation.

Once the pressure and temperature conditions were attained, the experiment was left at conditions for one night. This allows the pressures to equilibrate but also to control that there is not lead leak (lead passing up the large packing ring, visible by a pressure drop).

Coaxial deformation experiments

First, the σ3 pump is set to regulate the oil flow to keep the confining pressure constant. Then the coaxial deformation at constant strain rate is started by giving the σ1 pump a constant oil flow to inject in order to constantly advance the deformation piston.

During the deformation stage, different phases can be identified on the differential stress curve while the σ1 piston advances (Figure II.5). First the force increases steeply because of the friction and then it adopts a gently sloping behaviour: this is the “run-in” curve through the

lead. This part must last a sufficient amount of time (that is why a certain thickness of lead is required). Then the slope increases steeply while the σ1 piston comes into contact with the top alumina piston: this is the "hit-point". The following phases correspond to the deformation of the sample with the loading curve until the curve typically flattens again. The identification of these phases is important for the monitoring of the experiment and the consecutive calculation of the mechanical data (see next section).

Note: because of friction effects, the loading curve does not constitute pure elastic behaviour of the sample at elevated temperatures, when the sample is weak. The slope of this curve is dependent of the sample strength and increases with the strength.

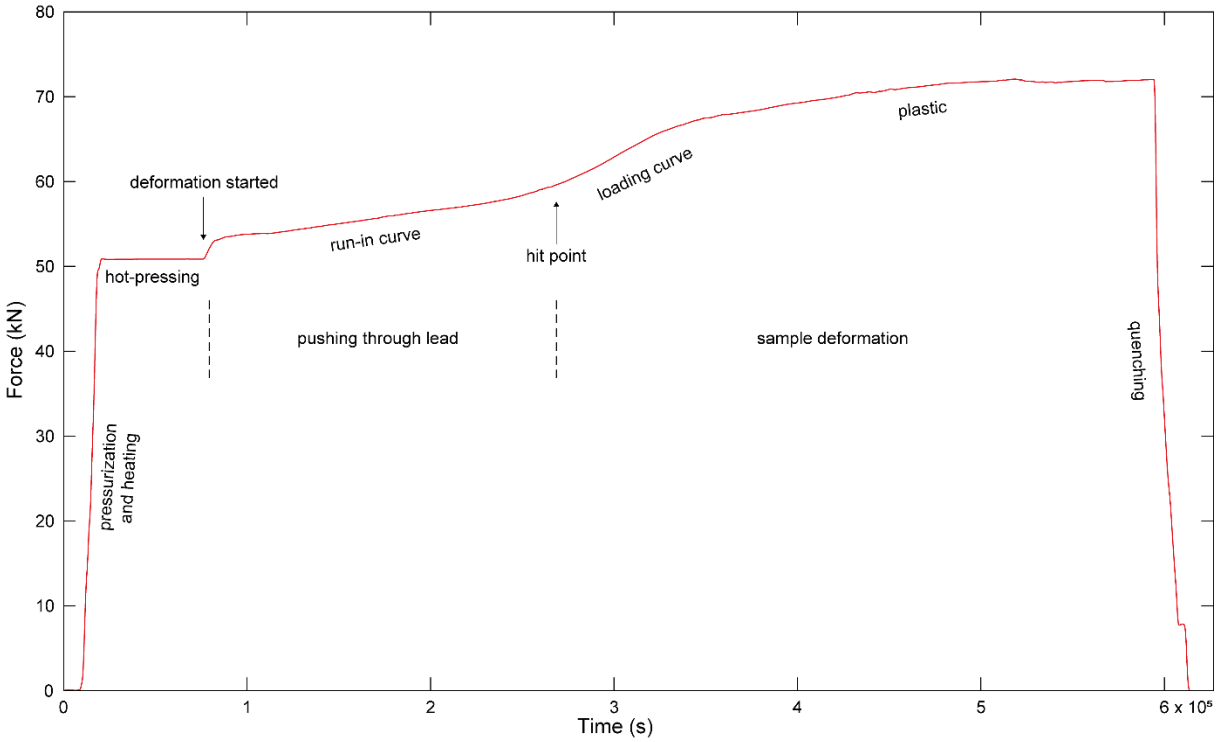

Figure II.5. Example of a force-time curve from sample OR32 with the different stages occurring during an experiment: heating and pressurization then hot-pressing, deformation and quenching. During the deformation two stages are visible: the run-in through the lead followed by the sample deformation. Figure adapted from Précigout et al. (2018).

For strain rate stepping experiments, the oil flow is changed in order to change the advancement of the σ1 piston and thus change the strain rate.

Hot-pressing experiments

For the hot-pressing experiments performed, once the conditions of pressure and temperature are attained, the samples were let in the apparatus during the same amount of time than the corresponding coaxial deformation experiments. During the whole time the pressure was regulated and maintained constant by the pumps.

Quenching

Once the expected amount of deformation or time is attained, the experiment is quenched. After stopping the deformation piston, the quenching consists of rapidly reducing the temperature to 200°C while both pistons are moved back, the σ1 deformation piston faster than the σ3 confining pressure piston. The temperature gradient imposed for the quenching is

of the order of 300°C per minute. The temperature is then hold to 200°C until the confining pressure reach 100 MPa.

When the differential stress reaches 100 – 150 MPa, the speed is reduced, and the two pistons are slowly moved back at the same rate (~5 MPa per minute). This differential of pressure is kept to avoid the formation of cracks ("unloading cracks", parallel to the piston). Then, when the confining pressure attains 100 MPa, the temperature is decrease to 30°C and the furnace and cooling systems are stopped. The pressure is then decreased to 0, the speed of the pistons being regulated in order they attain 0 MPa at the same time.

For hot-pressing experiments, the pistons are just moved back together at the same speed.

Removing the sample

When the pressure is zero, the pistons are moved back, and the vessels can be taking from the apparatus. The σ1, σ3, end-load pistons and base plate are put away and the pressure vessel is placed under the hydraulic press. The sample assembly is then extracted from the pressure vessel. Then everything is cleaned.

The assembly is then destroyed with pliers and scalpels in order to extract the sample. During this operation, it is required to keep the orientation of the sample (up or down) and the emplacement of the thermocouples.

II.1.5. Data treatment

The raw data recorded during experiments need to be corrected before being interpreted, this procedure is done using a MATLAB script written by Jacques Précigout (available at https://sites.google.com/site/jacquesprecigout/telechargements-downloads). This script is adapted from Pec et al. (2016) following the routines of Renée Heilbronner (available at https://micro.earth.unibas.ch).

The raw data from the experiments made in Tromsø consisted of the confining pressure, force and σ1 piston displacement traced on a chart paper. They have been read and translated from paper chart to text files (as 1 point every hour) to be read by the Matlab script. As these three variables were recorded in mV, they first needed to be converted to MPa, kN and mm, respectively. The conversion factors (for the Rig number 2) are $1\,mV = 251.6292 \times 10^{-3}\,MPa$ for the confining pressure, $1\,mV = 22.0344 \times 10^{-3}\,kN$ for the force and $1\,mV = 5.0431 \times 10^{-3}\,mm$ for the displacement.

Data from the experiments performed in Orléans were already in a numeric format. The raw data were converted from the recording software (Catman Easy AP, version 3.5) to Matlab readable data.

II.1.5.1. Hit point determination

The first step of the data treatment consists in determining the "hit-point". This virtual point corresponds to the point at which the deformation piston touches the alumina piston, i.e., the point at which the sample starts to deform. This point is defined as the zero sample differential stress and strain.

The hit-point is defined by curve-fitting as the intersection between the run-in curve through the lead and the subsequent loading curve of the sample (Figure II.6).

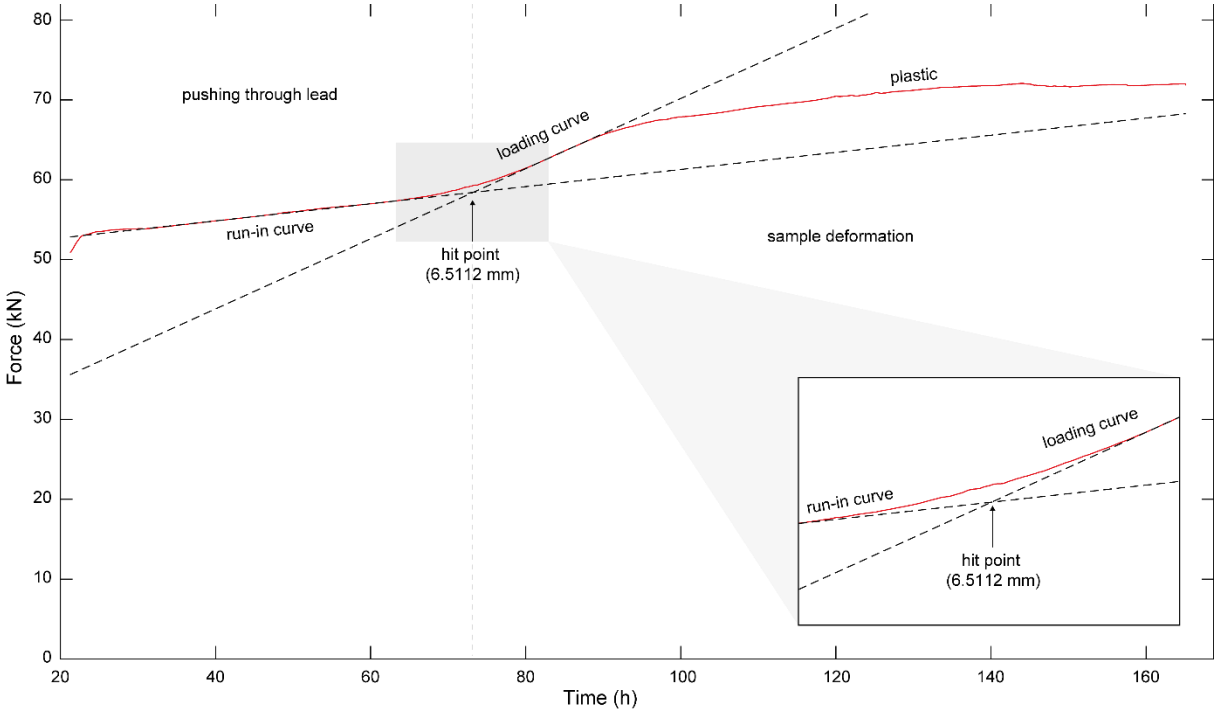

Figure II.6. Determination of the hit point by curve fitting (here for sample OR32). The hit-point is defined as the intersection between the run-in curve through lead and the loading curve. Enlarged view is presented at the bottom right hand corner.

II.1.5.2. Data correction

The second step consists in correcting the data for various parameters.

First the displacement is corrected from the Rig stiffness. This value depends on the apparatus used but also on the force exerted. For the Rig 2 in Tromsø it is of 5.04 µm/kN and for the new apparatus in Orléans it depends on the pressure as it is of 13.24 µm/kN at 5 kbar and 15.17 µm/kN at 10 kbars (increases with increasing pressure in a non-linear way). An example of a displacement curve corrected from the Rig Stiffness is presented in Figure II.7.

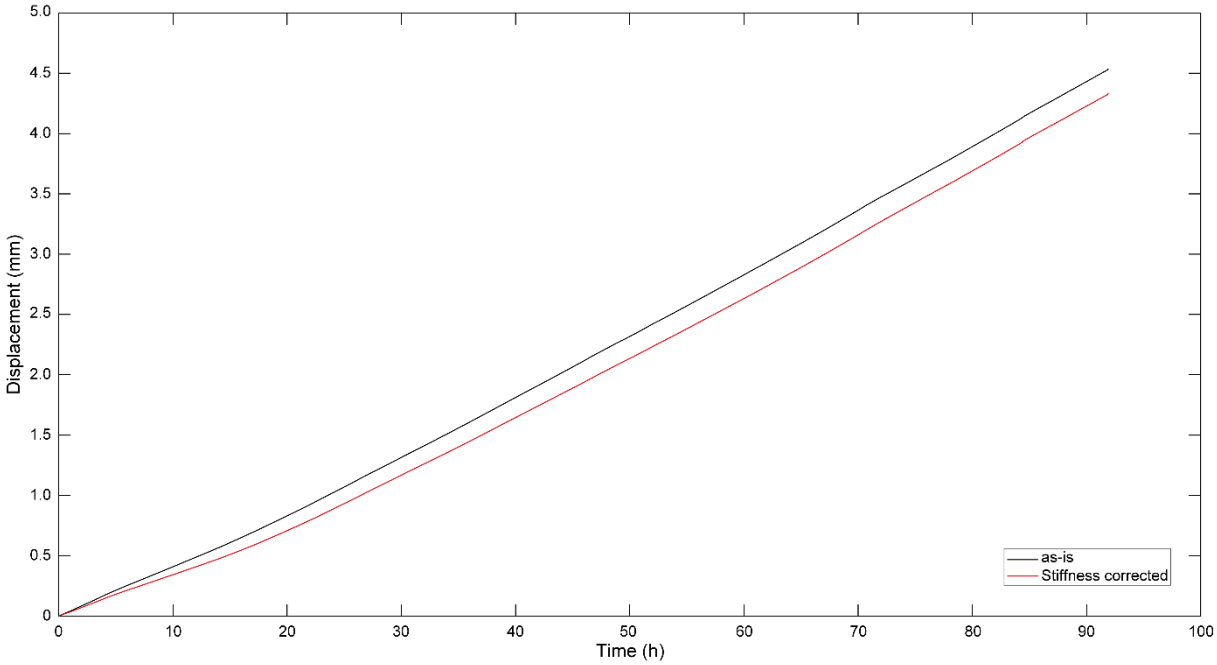

Figure II.7. Example of the displacement of the σ1 piston as-is and corrected from the Rig stiffness for sample OR32 deformed at 1000 MPa.

Then, the data are corrected for the change of the sample cross sectional area during the deformation. Considering that the sample shape (cylinder) stays constant during the coaxial deformation, as it is shortened its diameter increases. This increase of the cross-sectional area has to be taken into account.

For coaxial deformation, the equation used is:

$$d = \left[1 - \nu * \left(\frac{L}{L_0 - 1}\right)\right] * L_0,$$

where d is the sample diameter (mm), ν is the Poisson coefficient (taken at 0.5), L is the sample length (mm) and L_0 the initial sample length (mm).

Other corrections are also possible as pressure correction, friction, and salt corrections. The pressure correction can be applied for samples deformed in Tromsø. As the confining pressure is not regulated by the pump during deformation, it increases slightly. So the variation of the pressure can be taken into account thanks to the equation $\Delta\sigma_{corrected} = \Delta\sigma_{non\ corrected} - \Delta P_{from\ the\ hit\ point}$ with σ the stress (MPa) and P the confining pressure. The elastic compression of the salt during the advancement of the σ1 piston into the assembly can also be taken into account. The friction correction consists in correcting the force for the friction of the apparatus thanks to the equation:

$$F_{corrected} = F_{non\ corrected} - D_{from\ the\ hit\ point} \times f,$$

with F the force (kN), D the displacement (mm) and f the friction (empirically determined as 1.3).

As different corrections can be taken into account, the differential stress values can change considerably (Figure II.8). Here the mechanical curves will only be considered corrected for the Rig stiffness and for the cross sectional area (but not corrected for a friction term).

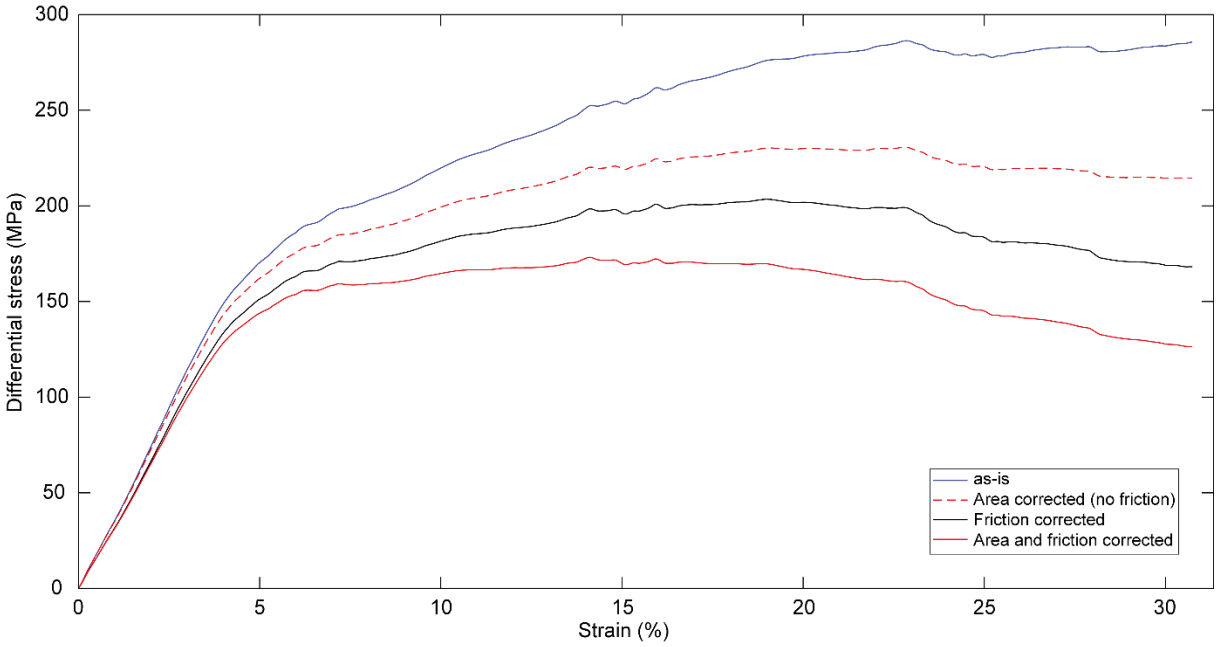

Figure II.8. Effect of the different corrections applicable on the differential stress-strain curve (here for OR32 sample). The most appropriate curve is the red dotted one that is area corrected.

II.1.6. Experiments performed

All deformation experiments performed consisted of coaxial shortening up to approximatively 30 % at temperature of 900°C and constant strain rate of $\sim 10^{-6}$ s^{-1} – corresponding to a constant displacement rate of 1.5×10^{-5} $mm.s^{-1}$. The strain rate of experiments in the rig at Orléans was slightly lower than in the Tromsø rig. However, for a power law solid, this difference in strain rate should lead to only a subtle difference in flow stress. One sample (OR56) was deformed at a higher strain rate of $\sim 10^{-5}$ s^{-1} (1.5×10^{-4} $mm.s^{-1}$).

The confining pressures applied were 600, 700, 800, 1000, 1250, 1500 and 2000 MPa. The lower confining pressure studied corresponds to the lowest possible at 900°C to prevent the confining NaCl medium from melting. The maximum confining pressure was the highest pressure reachable without seriously damaging the new Griggs-type Sanchez apparatus at that time. In the Sanchez Rig, the pressure is regulated by a hydraulic pump to stay constant throughout the experiments' duration whereas in the conventional Griggs apparatus it is not regulated and typically increases toward the end of the experiment (the increase is corrected in the mechanical record).

For all the experiments performed in the coaxial regime, 0.1 wt.% of H_2O was added to the samples except for two that were deformed "as-is" (OR73 and OR76, dried at 110°C overnight).

Three strain rate stepping experiments have been performed to determine the n-exponent of the flow law. During these experiments, the pressure (2000 MPa for OR65 and OR68 and 800 MPa for OR79) and temperature (900°C) conditions were kept constant, but the strain rate was changed. For OR65 experiment, the strain rate sequence was 10^{-6}, 10^{-5}, 10^{-7} and 10^{-6} s^{-1} but the experiment was not successful. For OR68 and OR79 experiments, it was 10^{-5}, 10^{-7}, 10^{-6} and 10^{-5} s^{-1}. The n-exponent was then defined for each experiment as the slope between the log of the strain rates and the log of the differential stresses calculated by linear regression.

In addition to deformation experiments, two hydrostatic “hot-pressing” experiments have been carried out at 1000 and 2000 MPa to distinguish between the contributions of pressure-temperature conditions and coaxial deformation on the microstructures. In these two experiments, samples were kept at temperature (900°C) and pressure conditions for as long as the corresponding deformation experiments (251.7h for OR59 at 1000 MPa and 216.8h for OR66 at 2000 MPa).

Three experiments were performed in Tromsø Norway in a Tullis modified apparatus (Rig 2, samples 542LN, 546LN and 544LN) in November 2017 and all the others were performed in the new generation Griggs apparatus in Orléans (samples OR32 to OR79) from March 2018 to August 2020.

After the experiments, all samples were cut with a diamond saw in the centre (passing through the thermocouples positions) to obtain two longitudinal sections parallel to the σ1 direction. A thin section (30 µm) was prepared from one of the two parts and a thick section (90 and 150 µm) from the other.

Finite strain of the deformed samples was calculated in two different ways: from mechanical records and from measurements of samples lengths before and then after the experiments.

II.2. Study of microstructures

After sample deformation, several analytical techniques have been used in order to study the associated microstructures. The main techniques employed were optical microscopy, cathodoluminescence, image analysis, EBSD and TEM. These techniques were also applied to the starting material.

All the approaches employed have the advantage to allow in-situ study of the microstructures in their original or final arrangement into the samples.

II.2.1. Light microscopy

Light microscopy mainly served for observing and characterising the fabrics and microstructures on thin sections. For that purpose, the cross-polarized light was mostly employed.

Light microscope photographs were also used to construct mosaic images of the whole samples and perform digital fabric analysis (see the description of image analysis, part II.2.3).

II.2.2. Cathodoluminescence

Cathodoluminescence (CL) imaging has been carried out on samples in the light microscope (LM) and in the scanning electron microscope (SEM). The LM-CL has mainly been used for overall study of samples whereas SEM-CL has been used for more detailed analysis of particular areas.

The cathodoluminescence technique allows observing features that are not distinguishable by other means.

II.2.2.1. Principle of cathodoluminescence

The principle of cathodoluminescence lies on the fact that when minerals are bombarded with a high-energy electron beam (whose source is a cathode), they emit photons. The emission of this photons produces a characteristic luminescence in the visible part of the electromagnetic spectrum (400 to 700 nm, but it may also occur in the IR and UV parts).

When the high-energy electron beam interacts with the luminescence activators present in the mineral, the atoms are ionized and go to an excited state (travel of electrons of the external layer from a basic state to an ionized state). To return from their excited to their basic state, the ions emit energy in the form of photons.

Different minerals are able to emit cathodoluminescence: carbonates, zircons, apatite, monazite, feldspar, quartz, etc. The emission of luminescence could originate from different sources. It is principally due to point defects in the crystal lattice such as vacancies or impurities. These impurities can be the presence of trace elements (transition group metals ions or rare earth elements or actinide ions) incorporated during the crystal growth. Other sources of luminescence can be structural defects of the crystal lattice, such as vacancies, substituting elements, interstitial ions, defect centre or broken bonds (e.g., Barbin and Schvoerer, 1997; Pagel et al., 2000; Boggs et al., 2001; Götze et al., 2001).

Because of the diversity of sources that differ from the other analytical techniques, cathodoluminescence is able to reveal microstructures that are not visible by other means. The patterns and colours observed in CL vary from optical visible microstructures and are more or less independent. Cathodoluminescence allows to identify internal fabrics of rocks and minerals such as zonations, fractures, cementation and overgrowths (Ramseyer et al., 1988; Götze et al., 2001, 2013, and references therein).

Two types of devices are commonly used for cathodoluminescence analyses: light and electron microscopes and present several differences. The principle is the same for the two techniques but the information obtained and the resolution differ. Cathodoluminescence images are coloured in the CL light microscope but monochromatic in the SEM. However, the latter provides higher resolution images whereas the first one has a limited resolution.

Both light and SEM cathodoluminescence methods provide qualitative information whereas CL spectroscopy allows a quantitative study and the identification of the emitted luminescence wavelengths.

II.2.2.2. Light Microscopy Cathodoluminescence

LM-CL-images of thin sections have been recorded at ISTO (Orléans, France) with an OPEA cold cathode stage at approximately 10-12 kV and 120-150 µA under low-pressure Argon gas at 6.7 to 7.3 Pa. The image acquisition time was 3 to 4 s.

No coating of the sample was needed (as positive ions generated in the gas phase are sufficient to neutralize charging effects). However, the beam deteriorates the Araldite® glue (that becomes yellow after exposition).

The LM-CL microscope was used on every thin section in order to have a general view of samples. Images with a broad overview were captured to construct mosaic images that were then segmented and studied by image analysis. This technique was also used to locate details and areas of interest before SEM-CL imaging.

Finally, LM-CL allowed to observe luminescence colours of the material and to have a general idea of their wavelength (SEM-CL produces black and white images).

II.2.2.3. Scanning Electron Microscopy Cathodoluminescence

SEM-CL-images have been recorded at BRGM (Orléans, France) with EDAX-Pegasus system equipped with a TESCAN CL-detector (Autrata panchromatic detector with detectable wavelength ranging from 350 to 650 nm, and interchangeable with the Backscatter Electron detector). The conditions of imaging were 5 to 15 kV and 17 to 20 mm working distance. Images were taken with an exposure time between 7 and 15 minutes (depending the desired image quality).

Additional mosaic SEM-CL-images have been recorded at University of Tromsø (Norway) using a Gatan Mono-CL-system on a Zeiss Merlin Compact SEM at 15 kV and 12.5 to 13.7 mm working distance using a blue filter (380 – 515 nm).

Prior to analysis samples were coated with 20 nm of carbon to avoid charging effects.

SEM-CL images have been manually segmented and processed using ImageJ software (see next section for details on the image analysis performed).

Note: the high exposure time needed for SEM-CL imaging deteriorates the thin section surface and samples need to be slightly polished after, especially before EBSD analysis. In addition to that, as the distance of CL emission is few micrometres deeper than the EBSD one, the images do not exactly match.

II.2.3. Image and strain analyses

Image analysis was used in order to characterize the grains from both starting and experimental materials. The analyses performed are based on the book *Image Analysis in Earth Sciences* (Heilbronner and Barrett, 2013) and from the workshop of the same name organized in June 2018 in Basel and animated by Renée Heilbronner and Rüdiger Kilian.

These analyses were all executed thanks to the free open-source software *ImageJ* (available at https://imagej.net/Downloads). In addition, special macro developed by R. Heilbronner and R. Kilian were used (available at https://github.com/kilir/Jazy_macros).

Image analysis was performed on polarized light microscopy and on cathodoluminescence images (lightand SEM). In order to be processed, the images (consisting of reconstituted mosaic images of the samples) were first manually segmented (Figure II.9a&b), i.e., the particles of

interest were drawn on the image (using Adobe Illustrator software). Then, when opened in the ImageJ software, the images were first scaled then converted in 8-bit and the particles of interest were selected (using threshold). The software was then run to calculate the desired parameters.

Grain parameters analysis

The grain parameter analysis consisted in determining and calculating the cross-section area, size, best-fit ellipse, orientation, etc. of the segmented grains.

The grain size is expressed as the area equivalent diameter (D_{eq}) that corresponds to the diameter of the circle with the same area (A) as the measured grain (Figure II.9c). It is calculated as $D_{eq} = 2 * \sqrt{\frac{A}{\pi}}$.

The fit ellipse corresponds to the ellipse which has the same two second-order moments than the analysed particle and whose the axes are scaled in order to have the same area. The ellipse is defined by its two axis: the major axis that is the long diameter ($2a$) and the minor axis that is the short diameter ($2b$). They are scaled so that the area of the best-fit ellipse is equal to the particle area.

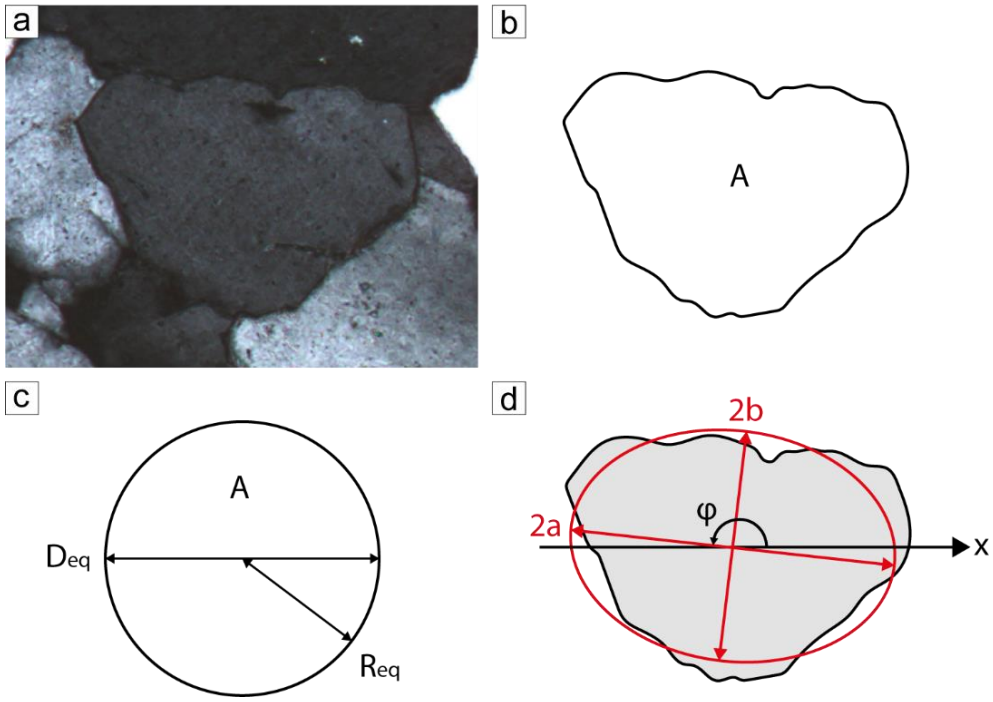

Figure II.9. Principles of grain size and shape analyses. (a) Cross-polarized light microscopy of a quartz grain from Tana quartzite, (b) corresponding outline after manual segmentation with an area A. (c) circle of the same area A than the grain defining the equivalent diameter (D_{eq}) and radius (R_{eq}). (d) Best-fit ellipse calculated with ImageJ software, the major axis is 2a and the minor axis 2b. The angle ϕ is the angle between the horizontal x-axis and the major ellipse axis counterclockwise. Figure modified from Heilbronner and Barrett (2013).

The aspect ratio (AR) is calculated as the ratio between the major and the minor axes of the calculated fit ellipse as $AR = \frac{a}{b}$. It can be used as an indicator for the elongation of the grains as higher the AR is, more elongated is the grain ($AR = 1$ corresponds to a circle).

The angle (ϕ, 0-180°) characterizes the orientation of the major axis of the fit ellipse with respect to the horizontal axis (x-axis) counterclockwise.

Fabric analysis

The same segmented datasets have been run for a fabric analysis, performed thanks to the macros SURFOR add-on for ImageJ software. The method, described by Panozzo (1984), allows obtaining information on 2D sample strain from the preferred orientation of the grains outlines.

The SURFOR analysis is based on the orientation of surface segments. During deformation by homogeneous strain an undeformed material (polycrystalline rock) with random outline orientations, develops a preferred orientation of its outlines that allow to calculate the finite strain ellipse.

The method consists of virtually rotating from 0 to 180° the digitized grain outlines (each considered as a continuity of straight line segments) and calculating the total length of the segments projections on the x-plane. The length of projection changes as a function of the orientation and shape of the grains. This allows defining a projection function (i.e., the projected length as a function of the rotation angle) from which it is possible to calculate the finite strain ellipse of the studied area. The position of the maximum and minimum of the projection function gives the orientation of the short and long axis of the strain ellipse, respectively. The ratio between the minimum and maximum of the projection function values corresponds to the ratio between the strain ellipse short and long axes.

When determining the strain ellipse by this method it is assumed that the initial orientation of the particles outlines is random so that the preferred orientation determined is due to the deformation. That is why the starting material has also been studied with the SURFOR method in order to define the starting fabric anisotropy. Moreover, this method does not take into account where the particles are in the studied area (top, middle or bottom parts) but depends on how the x – y plane is defined (here we took y parallel to the σ1 direction).

Note: to use this technique the boundaries must be regarded as passive markers, i.e., the processes taking place at grain boundaries during deformation (such as grain boundary migration, pressure solution, or recrystallization) are not taking into account. To consider this issue, the SURFOR analysis has been preferentially run on the digitalized contours of the sand grains constituting the quartzite, that are less impacted by these processes than the surrounding cement that defines the quartzite grains boundaries.

II.2.4. Electron Backscattered Diffraction (EBSD)

Crystallographic orientations of grains from starting material and experimental samples have been determined using the Electron BackScatter Diffraction (EBSD) technique. Both, punctual measurements and areas mapping have been performed to characterize local microstructures and sample fabrics.

II.2.4.1. Principle of EBSD analysis

EBSD is a technique that allows to study the orientation of crystal lattice on the surface of samples on a Scanning Electron Microscope (SEM). The crystallographic orientation is obtained thanks to one of the types of emission produced when an incident electron beam interacts with a sample: the backscattered electrons.

These electrons diffract on the different planes of the crystal lattice (with a specific angle respecting the Bragg's condition: $2d \sin\theta = n\lambda$ with d the reticular distance (mm), θ the incidence angle (rad), n an integer and λ wavelength of the incident beam (mm)). The electron diffraction on a family of plans occurs along two cones (Kossel cones). When detected by a phosphorescent screen associated with a CCD (Charge Coupled Device) sensor they produce specific linear patterns: the Kikuchi bands.

The combination of bands resulting from the diffracting family planes of the lattice along with their thickness and intensity are specific to a type of crystal and its orientation. The Kikuchi bands are transformed into points (by Hough transform) and interpreted by the acquisition software (thanks to comparisons with a database) that translates them into crystallographic orientations of the analysed point.

To optimize the occurrence of diffraction pattern (and being in the Bragg's conditions), the sample is titled to 70° with respect to the incident beam.

Two kinds of dataset are possible: punctual measurements or mapping. Mapping consist on recording the data point by point over a delimited area and with a specified step. A diffraction cliché/pattern is produced on each measured point.

To link the crystallographic orientation of the measured areas with the overall deformation of the samples, these ones are spatially oriented into the SEM.

II.2.4.2. Sample preparation

As the backscattered electrons come from very shallow depths, the EBSD analysis is extremely sensitive and require a particularly good surface quality. For this purpose, several polishing steps were made on the thin sections prior to the analysis.

The thin sections were first mechanically polished with diamond paste of decreasing grain size (9 – 3 – 1 – 0.25 µm) during at least 15 minutes for each granulometry. Once the surface conditions were good enough a last polishing step with colloidal silica suspension (0.04 µm) was made for 20 more minutes in order to remove damaged material induced by polishing.

The samples were finally coated with a very thin layer (2-4 nm) of carbon. Copper or carbon adhesive was also used to minimize artefacts due to the accumulation of electrons on the sample surface.

II.2.4.3. Acquisition conditions

Crystal orientations have been determined by electron backscatter diffraction (EBSD) using two apparatus. The first one is a scanning electron microscope TESCAN with EDAX-Pegasus system and equipped with OIM acquisition and data treatment software at BRGM-ISTO (Orléans,

France). The second is a Nordlys detector and an Oxford Aztec system on a Zeiss Merlin Compact FE-SEM at the University of Tromsø (Norway). For the latter the analyses were performed by Amicia Lee (Tromsø University).

Conditions were 70° tilt angle, 20 KV acceleration voltage, and 9 nA probe current. An indexing quote of 75-85% has been achieved on 4 nm carbon coated thin sections.

Thin sections were oriented in the SEM so that the horizontal X axis corresponds to the stretching direction and the Y axis to the shortening direction. The Z axis is in the direction perpendicular to the thin section plane.

Data acquisition on starting material consisted in punctual measurements of grain orientations (1 point per grain on 500 different grains). For deformed samples, the microstructures were mainly studied using area mapping.

Only the quartz phase was considered during the data acquisition, as other phases are present in very small quantities (see the starting material description, part III.1).

II.2.4.4. Data treatment

Recorded data were first corrected and filtered with the acquisition software (OIM or AZTEC, depending on the SEM used) to remove noise and isolated pixels. This correction allowed to re-index some pixels as a function of the orientation of their neighbours.

Maps post-processing was then performed using the MTEX v.5.2.8 program package by Bachmann et al. (2011). Orientation maps were recalculated using the 6/mmm system (hexagonal) in order to avoid displaying Dauphiné twin boundaries.

Grain boundaries were defined with a misorientation angle ≥ 10° and the minimum grain size was set to 5 neighbouring pixels. Subgrains were defined with a misorientation angle comprise between 2 and 10°.

Pole figures were plotted in the lower hemisphere convention, with equal area. Inverse pole figure maps were plotted with respect to the Z axis (axis perpendicular to the thin section plane).

II.2.5. Transmission Electron Microscopy (TEM)

Transmission Electron Microscopy (TEM) allowed us to have a quick look at the starting material. The apparatus used is a JEOL ARM at the electronic microscopy platform of Orléans University. Images were collected under an accelerating voltage of 200 kV.

II.2.5.1. Principle of TEM

Transmission Electron microscopy is an imagery technique where a high-energy electron beam is transmitted through a very thin sample (up to 100 nanometres thick). It allows observing very small details (as dislocations, or fluid inclusions for example) with a high resolution. TEM also allows to obtain diffraction patterns of the sample crystal lattice.

The general principle is the same as for light microscopy, except that electrons are used instead of photons. This allows to highly increase the resolution as the electrons have a much smaller wavelength than photons.

The electrons are generated and accelerated in an electron gun at the top of the apparatus. They are then focussed on the sample thanks to a system of magnetic lenses. The electron beam passes through the sample and interacts with it. The electronic image formed that way is projected on a phosphorescent screen that converts it to a visible image (recorded by a CCD captor). On the image, the bright areas correspond to the parts where more electrons were transmitted and dark areas to parts where less electrons passed. For the diffraction patterns, the diffracted electrons on the lattice are then focused by an electromagnetic lens and recombine in order to obtain the diffraction pattern.

The whole system needs to be maintained under a high vacuum (10^{-7} to 10^{-10} mbar).

II.2.5.2. Sample preparation

As samples have to be thin enough to be crossed by the electrons, the sample preparation is delicate. Moreover, in addition to be very thin, samples have to be very well polished.

The sample prepared for TEM observation is a piece of a thick section of starting material Tana quartzite. It was first manually polished on both sides with water up to a thickness of 100 µm. This polishing was carried out with a series of abrasive sheets of decreasing grain size.

A circular piece of 3 mm diameter was cut inside the sample.

Further polishing steps were then made by Audrey Sauldubois (electronic microscopy department of Orléans University), using diamond paste, colloidal silica solution and then PIPS (Precision Ion Polishing System) tool until the sample reaches 50 µm thickness.

When the required thickness and surface conditions are reached, the centre of the sample was thinned until a hole formed (with a FIB – Focused Ion Beam). The created hole is rectangular shaped and measures about 500 by 200 µm. The studied areas will be located at the border of this hole, on the thinner part of the sample.

Note: all these preparation steps should be as smooth as possible in order to avoid surface effects of hardening that will interfere with crystal defect observations.

In order to prevent sample damaging by the electronic beam, carbon coating was applied.

II.2.5.3. Data treatment

The images recorded during TEM observations have been used to determine the dislocation density of the starting material. For this purpose the number of dislocation observed on each image was counted and the area measured using ImageJ software. The dislocation density was obtained by dividing the number of dislocations by the area of observation.

II.3. Measuring and calculating H_2O contents

II.3.1. Measuring H_2O contents: Fourier Transform Infrared Spectroscopy

Fourier Transform Infrared Spectroscopy (FTIR) was used to measure water in starting and experimental materials. This technique is widely employed to quantify H_2O contents and detect OH defects in nominally anhydrous minerals (e.g., Aines and Rossman, 1984; Rossman, 2006, and references therein), including quartz (e.g., Kronenberg et al., 1986; Kronenberg and Wolf, 1990; Kilian et al., 2016).

II.3.1.1. Principle

Infrared spectroscopy is an analysis technique that provides information on structure and chemical composition of samples. In a qualitative way, it allows to detect and identify functional groups that compose a material and in a quantitative way it can be used to calculate concentrations.

When an infrared beam interacts with a sample, it is absorbed by the constituting molecules as molecular vibrational energy. The quantity of energy absorbed is discrete and corresponds to specific vibrational levels of the molecular interatomic bonds. The frequencies of energy absorbed by a molecule are thus, characteristic of its structure as they depend on the mass of the constitutive atoms and the strength of their bonds. Thus, each molecule possesses a characteristic infrared absorption spectrum for which several modes of vibration exist (the two main types being stretching (symmetric or asymmetric) and bending).

For the Fourier transform infrared (FTIR) spectroscopy an interferometer (Michelson) is used and allows to measure all the infrared frequencies simultaneously. The beam produced by the source passes through the interferometer and is divided into two (by a beam splitter): one part is reflected on a fixed flat mirror while the second is sent to a moving mirror. The recombination of the two beams gives an “interferogram” that consists of an intensity signature (amount of light detected as a function of the mirror position). The infrared spectrum of absorbance as a function of the wavelength (single beam spectrum) is then obtained after being processed with a mathematic operation: the Fourier transform.

In transmission spectroscopy, the sample must be transparent in the wavelength range considered. Among all the wavelengths contained in the infrared beam that passes through the sample, some of them are absorbed by the sample and the others are transmitted through it, to the detector. This latter measures the amount of energy of each frequency after they passed through the sample. By comparison between the initial and final signals, the frequencies of the radiations that have been absorbed and their intensities can be determined. The absorption of infrared specific frequencies leads to the identification of the molecules and concentrations. For this method, it is needed to also measure a “blank” spectrum (or background) without the sample in order eliminate the absorption bands due to the environment (H_2O vapour or atmospheric CO_2, for example).

The resulting spectrum obtained consists of a plot of the intensity absorbed as a function of the frequency. In geosciences, it is usually presented as the absorbance (no unit) as a function of

the wavelength (cm^{-1}). The absorbance (A) is defined as $A = \log(\frac{I_0}{I})$, with I_0 the intensity of the incident light and I the intensity of light transmitted to the detector after been partially absorbed by the sample.

The size of the peaks in the spectrum is a direct indication of the amount of material present (quantitative analysis). For one characteristic wavelength, and thanks to specific calibrations, the concentration of a molecule can be calculated from the intensity of its absorption using the Beer-Lambert law (see latter for details, part II.3.2.5).

II.3.1.2. Sample preparation

The FTIR analysis have been performed on double polished thick sections (80 – 220 µm) prepared from starting material and from experimental samples. For experimental samples, the thick sections have been made from the second halves that were not used to make the thin sections, as close as possible to the centre of the cylinder. After impregnation of the sample with Araldite® and polishing of the first side, that one is glued (with Super Glue®) on a glass. The other side is then cut and progressively polished in order to obtain both the desired thickness and polishing quality (up to 3 µm). These procedures have been made at the thin section laboratory at ISTO (Orléans).

In order to remove the samples thick sections from the glass, they have been immersed into acetone during one day, until the Super Glue® was dissolved. Then, the thick sections have been left in acetone during one more day in order to ensure that all the glue was removed. All these operations were made under an extractor hood and with paraffin films wrapping the container to prevent acetone from evaporating. The samples were then left at ambient conditions to dry.

II.3.1.3. Acquisition procedure

The apparatus used is a Nicolet 6700 spectrometer coupled with a Continµum microscope (Thermo Scientific) at Institut des Sciences de la Terre (ISTO) in Orléans. The software used for measurements acquisition (and spectra pre-processing) is Thermo Scientific OMNIC (version 8).

The spectrometer is equipped with a globar light source and a potassium bromide (KBr) beam splitter. The detector is a Mercury Cadmium Telluride (MCT) that it is cooled with liquid nitrogen. To guarantee a good detection quality for all measurements, the cooling was done twice a day and the room temperature was regulated with an air conditioner. The spectrometer is regularly purged with dry air in order to avoid absorptions by atmospheric H_2O and CO_2.

The infrared objective and condenser used have x32 magnification that allows a small measurement area, the maximum size of the acquisition window being 70 by 70 µm. Thus, the material (grain interiors and grain boundaries) could be measured with precision and good signal quality using a small window aperture.

The measurements were all made at ambient temperature conditions. The settings were determined after several tests on starting material in order to have the best quality with a reasonable time of acquisition. All measurements were made in transmission mode, the

samples being transparent to infrared radiations in the wavelength considered. The incident infrared beam was not polarized.

The standard measurement conditions were 64 scans with a resolution of 4 cm^{-1} for a spectral range lying from 5500 to 1500 cm^{-1}. These range values were chosen to see potential OH overtones at 5200 cm^{-1} and Si-O absorption bands (in the 2000 – 1500 cm^{-1} region) in addition to H_2O vibrations in the 3000 – 3800 cm^{-1} range.

Measured samples were positioned on the top of a CaF_2 pellet (13 mm diameter and 2 mm thickness). Because of the use of this CaF_2 pellet, the condenser needed to be compensated/corrected by a factor of 2. Other consequence of using a CaF_2 pellet is that the infrared signal cannot be recorded for wavenumbers below 1100 cm^{-1}.

The background was recorded on the CaF_2 pellet every hour with the same measurement conditions. It was then directly subtracted from the following quartzite measures by the acquisition software.

For grain interiors, the size of the measuring window aperture was a square of 40 x 40 µm (Figure II.10a) whereas for the grain boundaries, the window was a rectangle of 20 x 50 µm whose the angle is adapted to fit the orientation and shape of the boundary measured (Figure II.10b). The sizes of the windows were chosen as a compromise between having a good signal and precisely measuring the areas of interest.

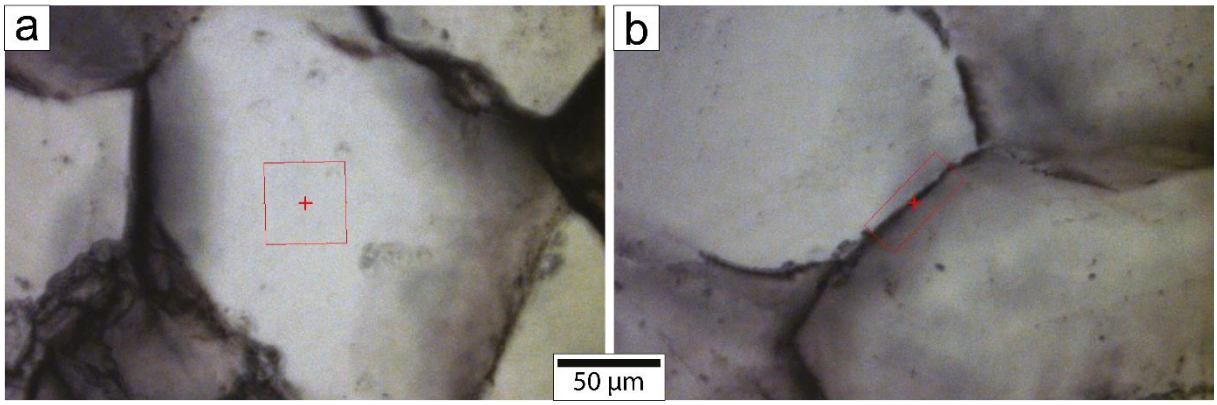

Figure II.10. Examples of the measured windows used for FTIR measurements. (a) 40 x 40 µm square for grain interiors and (b) 20 x 50µm rectangle adapted to the grain boundary orientation.

The gain set was 1 for grain interiors, for which special care was taken to measure areas as clear as possible and with the best signal possible. For grain boundaries, however, the signal was often not strong enough and the gain was increased to 2 (or rarely 4) in order to amplify the detector signal intensity.

II.3.2. Data treatment: calculating H_2O contents

H_2O contents calculations are based on the Beer-Lambert law that establishes a relation between the absorbance of a chemical specie and its concentration.

In order to apply the law, the data treatment usually consist of correcting the spectra for a flat baseline, measuring the absorbance of the H_2O region (3000 – 3800 cm^{-1}) and measuring the samples thicknesses.

Before measuring the area under the curve of the broad H_2O band, the spectra needed to be corrected for a contamination due to the use of Araldite® during the thin section preparation. As this material contains H_2O, some of the spectra recorded showed H_2O absorption signal from both quartzite and Araldite®.

The major part of the infrared spectra data treatment, have been made thanks to MATLAB scripts developed in cooperation with Michael Jollands (Lamont-Doherty Earth Observatory, Columbia University).

II.3.2.1. Correcting the baseline

The first step of the spectra data treatment consisted in correcting them in order to obtain a flat baseline. This was done using the "rubber band" method adapted and patented as a routine by Pirzer and Sawatzki (2008). This baseline correction was written as a MATLAB script by M. Jollands.

This method consists in (i) adding a convex curve (parabolic function) to the spectrum, then (ii) "stretching" a virtual rubber band around the data (convex envelope), (iii) take away the parts of the rubber band function that lie above the spectrum and finally, (iv) subtracting to the spectrum the part of the rubber band lying below it. This operation can be repeated as many times as possible until a straight baseline is obtained. The step (i) is needed in order to obtain a convex spectrum as the rubber band method does not allow to correct the baseline from a concave spectrum.

The baseline correction was made considering the whole spectral range measured (5500 – 1500 cm^{-1}) and only one iteration of the rubber band method was needed. This operation is necessary to correct the infrared spectra and provides better results, especially when comparing the spectra.

II.3.2.2. Correcting from Araldite® contamination

As Araldite® was used for sample impregnation during the thick section preparation, most of the recorded quartzite spectra showed a contribution of H_2O absorption bands coming from the epoxy in the 3000 – 3800 cm^{-1} range. The epoxy is identifiable by the presence of CH bands in the 3100 – 2600 cm^{-1} region (with two principal peaks at ∼2931 and 2869 cm^{-1}) while these bands are normally absent in quartz spectra.

To quantify the H_2O broad band in measured quartz spectra and separate it from the H_2O absorption of the Araldite®, FTIR measurements were conducted on pure Araldite® samples. As these samples have a high absorption in the infrared region, they needed to be as thin as possible to obtain unsaturated spectra. An example of a pure Araldite spectra is showed in Figure II.11. In all, 58 spectra of sufficient quality were obtained using a 20 x 20 µm aperture, 128 scans and an 8 cm^{-1} resolution.

As small differences existed between all the spectra recorded, a mean Araldite® spectrum was calculated in order to obtain a smoothed dataset that will not take into account individual variations inherent to one particular spectrum.

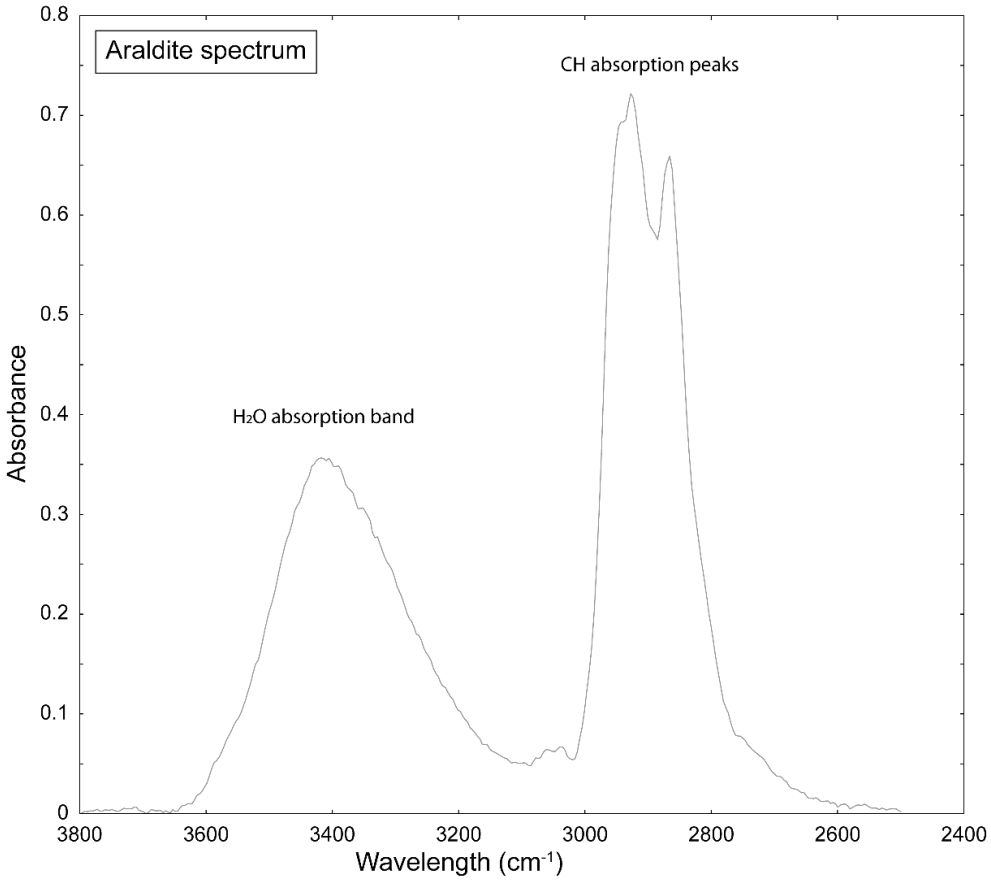

Figure II.11. Example of an IR absorption spectrum of Araldite® in the 3800 - 2400 cm^{-1} range (baseline corrected). The spectrum is composed of a broad H_2O absorption band and of CH absorption peaks.

The data treatment of this mean spectrum first consisted of correcting it for a flat baseline (using the rubber band method, as described above). The H_2O and CH bands of the mean Araldite® spectrum were then deconvoluted in a sum of Gaussian curves. This deconvolution was made with MATLAB scripts (written by Michael Jollands and adapted to the data) and allowed to establish a model of Araldite® IR spectrum (Figure II.12).

A preliminary step consisted in finding the most adapted number of Gaussian curves needed for the deconvolution (for this deconvolution, the physical/chemical signification of the peaks was not taking into account, the deconvolution was only used to fit the spectrum, not to identify the peaks).

Then, the first step of the deconvolution method consisted in obtaining (over 100 iterations) the positions and half-widths of the 8 Gaussian curves describing the Araldite® mean spectrum in the 2500 – 4000 cm^{-1} range (Figure II.12). A second script was then used in order to test the accuracy of the deconvolution on the whole set of Araldite® spectra recorded. This last script uses the positions and half-width previously found and adapts the height of the Gaussian curves to the spectrum considered.

Note: all the parameters used to determine the model of Araldite® spectrum (and fully fit the data) were subjected to several tests. Aside from the number of curves, their positions and half-widths, their bounding values were also subjected to an optimization.

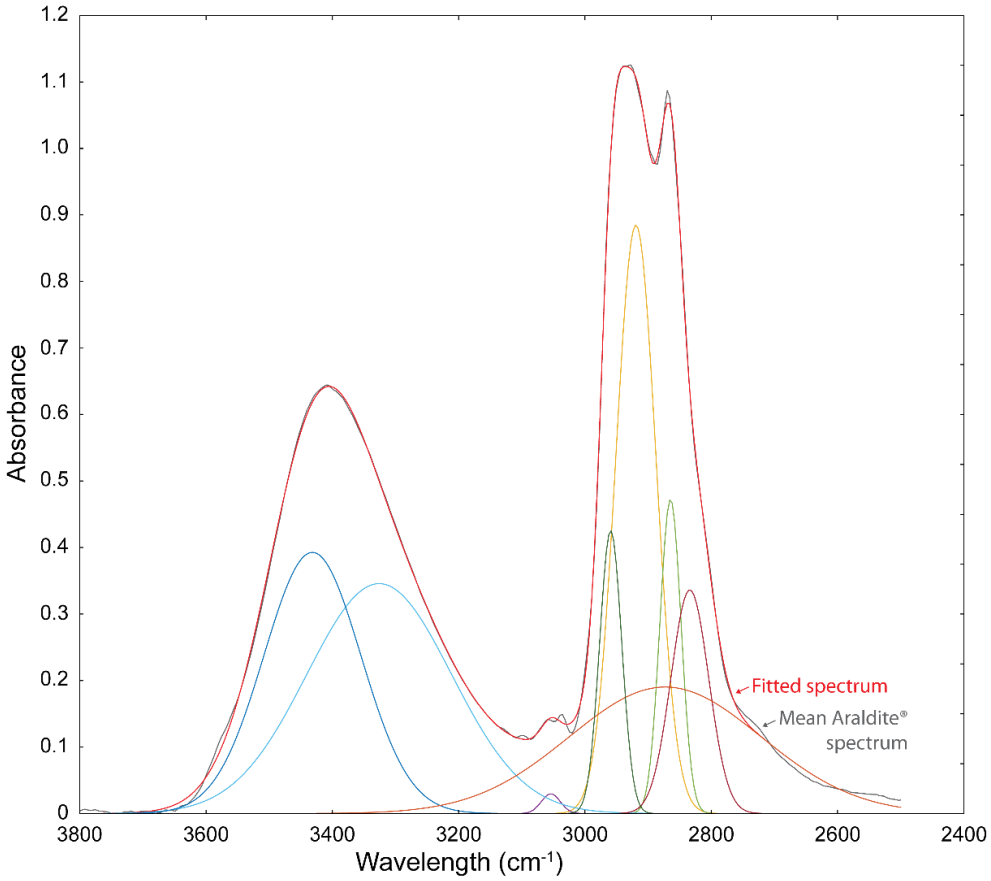

Figure II.12. Mean Araldite spectrum (grey) and resulting fit (red) deconvoluted thanks to 8 Gaussian curves (in colors). The spectrum is baseline corrected.

Once the model of Araldite® spectrum established, a relationship could be determined between the organic part of the spectrum (CH absorptions) and the H_2O part. For that purpose, the half-height between 2860 and 2960 cm^{-1} (between the CH peaks) was calculated and linked to the corresponding area in the H_2O region. This method was chosen because there were variations in the CH parts from one spectrum of quartz to another and the CH Gaussian curves could not be well fitted (variations in positions and shapes in addition to the changes in heights). In fact, in quartzite spectra, the CH peaks were not exactly identic to the ones determined from Araldite®.

Once this procedure was established, the correction was implemented into a script to automatically detect CH peaks in the quartz spectra and correct the H_2O band from the contribution of the absorption due to Araldite®. For that purpose, the assumption was made that the CH peaks present in the quartz spectra were due to Araldite® contamination and that they induce an overestimation of the H_2O area equal to the one determined for the Araldite® samples. As previously done for Araldite spectra, the half-height of the organic band in the 2860 – 2960 cm^{-1} region was calculated for each quartz spectrum and a theoretical Araldite® contaminating spectra established. The corresponding amount of H_2O was then subtracted from the quartz spectra (Figure II.13). The corrected spectrum obtained is considered to correspond to what would be measured without contamination.

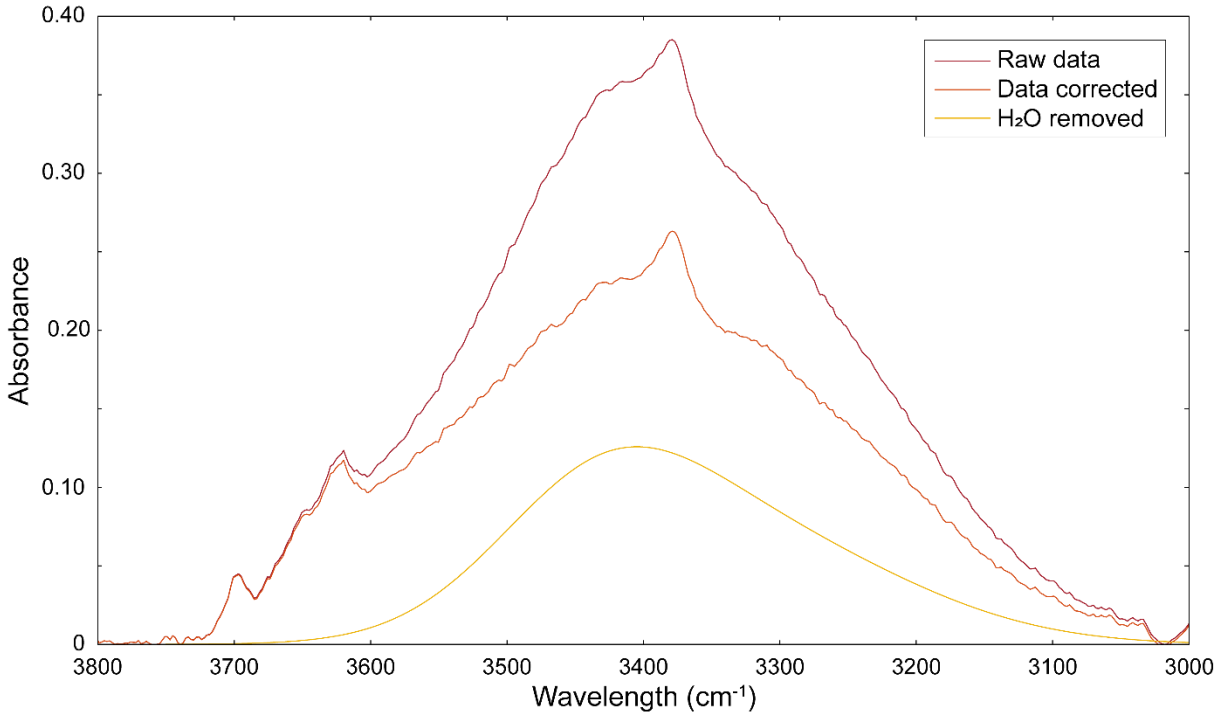

Figure II.13. Example of a quartz spectrum (measured on cement in starting material TQ-2). The raw spectrum (red) contains H_2O due to Araldite® contamination (yellow) that is subtracted to obtain the corrected spectrum (orange). The absorbance values are normalized to 1 mm thickness.

After H_2O contents calculations, the impact of the Araldite® correction on the data was determined by calculating the percentage of H_2O area removed because of the correction compared to the total H_2O area before the correction. This allowed to separate the data into 3 classes: all the spectra, spectra with an H_2O area corrected higher than 30% and to 50% of the total area. The influence of each group on the calculated mean H_2O contents was used to determine the reliability of the corrected data (see part IV.1.1).

Note: before implementing this correction method, it was first tried to calculate a theoretical Araldite® spectrum from the CH peak shape in the contaminated quartzite spectrum and then subtract it. However, this method was not successful as the modelled Araldite® spectrum was deforming the quartzite spectra.

II.3.2.3. Deconvolution of FTIR quartzite spectra

After the baseline and Araldite® corrections, the quartz spectra were deconvoluted in a sum of Gaussian curves to separate the contribution of molecular H_2O from the ones of discrete OH peaks. Two broad Gaussian curves corresponding to the symmetric and asymmetric stretching bands of molecular H_2O (located at 3280 and 3490 cm^{-1}) were used to simulate the H_2O absorption broad band centred around 3400 cm^{-1}. Ten thin Gaussian curves were used to simulate the discrete peaks positioned at 3699, 3653, 3624, 3614, 3596, 3585, 3467, 3429, 3379 and 3319 cm^{-1} were used to simulate OH discrete peaks.

Each of the Gaussian curves used are described by three parameters: the peak position, the peak height and the width at half-height (called half-width). All the spectra were fitted using Gaussian curves whose position and half-width were set (with a certain tolerance) and their height adapted to the shape of each spectrum. The main difference between the thin and broad

peaks is that the half-widths used for the broad ones are more than one order bigger than for the thin ones.

All the peak positions and half-widths have been determined and calibrated using various spectra showing well-defined peaks. The peak positions were chosen as a function of both observed peaks in the starting and experimental material as well as peaks reported in literature (e.g., Aines and Rossman, 1984; Kronenberg et al., 1986; Jollands et al., 2020). Notably, the H_2O broad band Gaussian parameters were calibrated with a spectrum without Araldite® contamination and without thin peaks. The determined values of positions and half-width were then tested on several spectra (randomly chosen) in order to confirm and/or adjust the fitting. Once these two parameters settled up, all the spectra could be processed as the peak heights are adapted to the shape of each spectra as they vary from one spectrum to another.

After all these steps, a deconvoluted spectrum is obtained for each of the spectra measured, giving access for each of the Gaussian curves fitted to their height (as their positions and half-widths were fixed). One example of a deconvoluted spectrum (first baseline and Araldite® corrected) is presented in the Figure II.14. For the curves of interest, the integrated area was also calculated. After this treatment, all the data calculated are exported, they include the Araldite correction parameters, the peak heights and area under the curves.

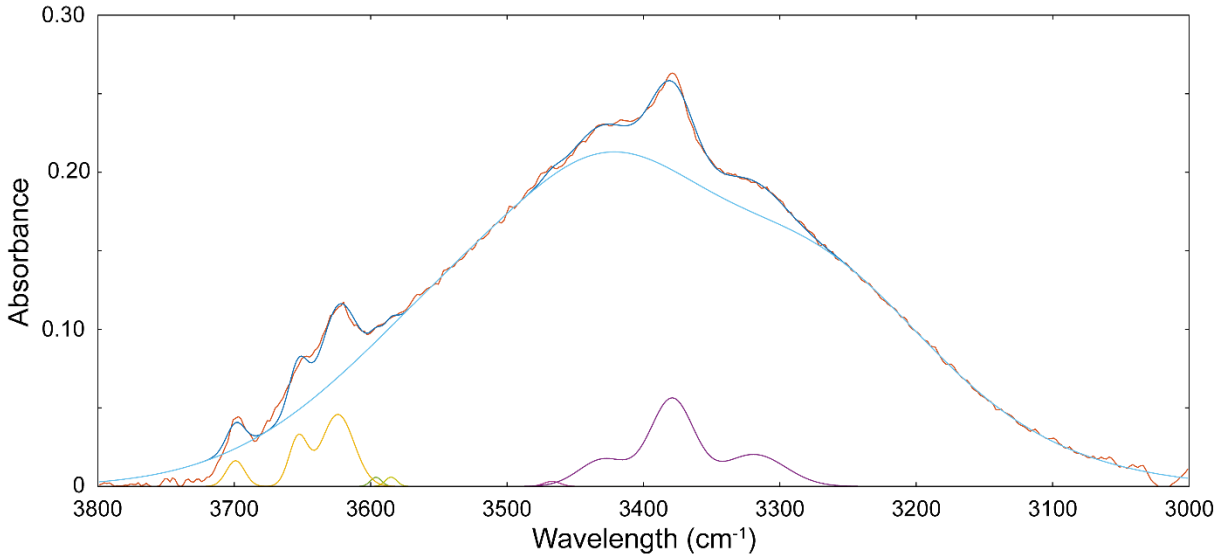

Figure II.14. Example of deconvolution of a quartz spectrum (spectrum corrected in the Figure II.13, measured on cement in starting material TQ-2). The raw spectrum (orange curve) is fitted thanks to Gaussian curves (blue curve) and decomposed into molecular H_2O (the broad blue band, deconvoluted with two Gaussian curves) and OH discrete peaks (smaller Gaussian curves of different colors). The absorbance is normalized to 1 mm thickness.

After the modelling, spectra were subjected to a filtering based on both their quality and the influence of the data treatment. Several spectra showing interferences were eliminated from the dataset and some others because the baseline correction did not work. The effect of the Araldite correction on some spectra involved to eliminate them as they were deformed.

II.3.2.4. Measuring sample thickness

In order to use the Beer-lambert law and calculate the concentration from the infrared absorbance value, thickness of the samples need to be measured. This has been done for every

sample thick section using a Leica (DMRXE Leitz) optical microscope equipped with a motorized precision stage, digitized, and calibrated.

The sample is put on a glass where a mark is already made with a marker. Using reflective light, the focus is first made on the mark and the numerical stage is set to zero. Then, the focus is made on the sample and the difference of height between the two focus points is read. The higher the magnification of the objective used is, the better the thickness estimation is (here the x20 and x50 objectives were used).

This operation was made several times on different places of the sample and the resulting mean value was used for H_2O concentration calculations (Table II.1). Considering that the thickness is the most important source of error, the standard deviations have been used to characterize the error made on H_2O contents calculations.

Table II.1. Thick section thicknesses determined for H_2O content calculations. The error given on the mean corresponds to the standard deviation.

Sample	Number of measurements	Mean thickness (µm)	Extreme values (min – max, µm)
TQ-1	10	193 ± 19	172 – 230
TQ-2	40	80 ± 10	61 – 97
542LN	40	196 ± 17	161 – 231
544LN	40	180 ± 10	156 – 203
546LN	40	227 ± 20	174 – 265
OR32	30	162 ± 6	152 – 173
OR33	50	171 ± 9	150 – 193
OR42	40	161 ± 25	110 – 203
OR48	40	168 ± 8	151 – 187
OR50	40	165 ± 14	136 – 182
OR52	40	175 ± 19	125 – 204
OR54	40	157 ± 6	144 – 167
OR56	50	146 ± 12	122 – 165
OR57	40	187 ± 13	163 – 209
OR59	40	187 ± 7	172 – 198
OR60	40	172 ± 17	143 – 205
OR62	40	148 ± 8	126 – 164
OR63	40	142 ± 15	115 – 168
OR64	40	198 ± 9	178 – 214
OR65	40	181 ± 8	166 – 196
OR66	40	164 ± 18	134 – 204
OR68	40	154 ± 6	146 – 167
OR73	40	138 ± 15	100 – 159

II.3.2.5. Calculating the H_2O concentration

From the infrared spectra, the H_2O contents (hydrous species concentrations) in minerals can be determined thanks to the Beer-Lambert law. This law gives a proportionality relation between the absorbance A (cm^{-1}) and the concentration C ($mol.L^{-1}$) as:

$$A = \varepsilon C t \Leftrightarrow C = \frac{A}{\varepsilon t}$$

with, ε the molar absorption coefficient (mineral-specific calibration, L.mol^{-1}.cm^{-2}) and t the thickness travelled across the sample by the infrared beam (cm). According to that law, higher concentration produces higher absorbance (and vice versa).

Different calibrations exist for the determination of the molar absorption coefficient, either based on the band height at ~3400 cm^{-1} (e.g., mineral-calibrated, Kats, 1962; Thomas et al., 2009) independent of the absorbance variation with the wavenumber, or on the band area under the H_2O region (e.g., Paterson, 1982; Libowitzky and Rossman, 1997; Stipp et al., 2006) that are wavenumber-dependent calibrations.

Here the calibration from Paterson (1982) was used. Thus, the Beer-Lambert law was slightly modified: instead of taking the absorbance at the peak height, the total integrated absorbance of the band area is considered. The absorption coefficient is replaced by the integral molar absorption coefficient (taken at 27000 L.mol^{-1}.cm^{-2}). The concentration is still expressed in mole of H per litre of mineral is obtained. The Paterson calibration uses the band area instead of band height because band heights are reported to present more variations (because of different factors) than the band area.

The integrated absorbance A (cm^{-1}) corresponds to the area under the curve of molecular H_2O broad band between 3000 and 3800 cm^{-1} (region dominated by the stretching vibrations of OH bonds). It was previously calculated as the area comprised between the baseline and the sum of the two broad Gaussian curves (as described in part II.3.2.3). In that way, it is not taking into account the area under the discrete peaks.

The H_2O content can be either expressed as molar proportions (H/10^6 Si) or in weight proportions (ppm). The conversion is made, taking into account that 1 ppm of H_2O per weight of SiO_2 corresponds to 6.67 H/10^6 Si. A density of 2650 g.L^{-1} (corresponding to the one classically used for quartz) was used to convert the concentration from moles per litre (mol.L^{-1}) to weight percent of H_2O (wt.%).

The lower and upper error values on H_2O contents have been determined by calculating the H_2O content using the sample thickness plus or minus its standard deviation, respectively.

II.3.3. H_2O fugacity calculations

Assuming that during the experiments the H_2O pressure approximatively equals the confining pressure, the H_2O fugacity (f_{H2O}) can be calculated using only two parameters: the temperature and the pressure.

The H_2O fugacity has been computed for all experimental conditions from Tony Withers' fugacity calculator (available at: https://www.esci.umn.edu/people/researchers/withe012/fugacity.htm) based on Pitzer and Sterner (1994) equation of state for H_2O.

This JavaScript based program used the analytical solution presented on Pitzer and Sterner(1994) to calculate the fugacity (and the molar volume):

$$\ln(f) = \left[\ln(\rho) + \frac{A^{res}}{RT} + \frac{P}{\rho RT}\right]_{P,T} + \ln(RT) - 1,$$

where f is the fugacity (Pa), ρ is the molar density (mol/m^3), A^{res} is the residual Helmholtz energy (J), P is the pressure (Pa), T is the temperature (K) and R the universal gas constant (8.314 J.K^{-1}.mol^{-1}).

III. Effect of pressure on deformation of quartz natural aggregates in presence of H_2O

This chapter deals with the mechanical and microstructural results obtained from the deformation experiments performed.

First, the natural starting material used is described.

Then, the experiments performed and their mechanical data are presented.

The different analysis used to study the deformed samples are then detailed: microstructural analysis by light microscopy and cathodoluminescence imagery, image analysis and detailed microstructures study by electron backscatter diffraction.

Finally, the results obtained are discussed in the light of previous published studies.

Parts of this chapter have been submitted to Journal of Structural Geology under the name: "Effect of pressure on the deformation of quartz aggregates in the presence of H_2O" by L. Nègre, H. Stünitz, H. Raimbourg, A. Lee, J. Précigout, P. Pongrac and P. Jeřábek. The article has been accepted in April 2021.

III.1. Starting material

III.1.1. General context

The starting material used is a very pure natural quartzite from the ELKEM quarry in Austertana, Northern Norway (N70°28´39.6´´, E28°32´30.1´´). The rocks sampled come from the uppermost part (~40 m) of the Gamasfjell formation. This sequence of late Precambrian age is approximatively 300 m thick and is composed at the top of grey to white quartzite (Pevik, 2015).

The uppermost part of the formation is described as very pure (> 99 % of silica) and is used as raw material by the aluminium, silicon and ferrosilicon industry (Aasly et al., 2007).

The Tana quartzite corresponds to shallow marine deposits that underwent high grade diagenesis to very low grade metamorphic conditions. The formation, presenting a massive bedding, is weakly deformed by a large open antiform (Pevik, 2015). However, no internal deformation in the micro-scale, no schistosity, and no lineation have been identified in the sampled rock. The blocks collected from which the starting material comes from were not oriented.

III.1.2. Chemical analysis

Chemical analysis (from ICP-EOS) have been published in Pevik (2015). The material presents a high chemical purity with Al_2O_3, Fe_2O_3 and TiO_2 as the main contaminating oxides. The mean major oxides values (apart from SiO_2) measured are indicated in the Table III.1 below.

Table III.1. Mean oxide values (ppm) calculated from Pevik (2015). The errors correspond to standard deviation (all calculations have been made from 26 different measurements except for B_2O_3 for which only 6 measurements where available).

Oxide	Mean value (ppm)
Al_2O_3	3547 ± 1083
Fe_2O_3	441 ± 365
TiO_2	207 ± 37
CaO	35 ± 5
Na_2O	42 ± 13
K_2O	654 ± 238
MnO	18 ± 18
P_2O_5	57 ± 18
B_2O_3	13 ± 3

III.1.3. Microstructural analysis

The Tana quartzite is almost completely composed of quartz grains and crystalline authigenic SiO_2 cement (99 %, Figure III.1a) and displays a low porosity. Very few accessory minerals (< 1%) are observed such as sheet silicates (muscovite, sericite, pyrophyllite, kaolinite), iron oxides (hematite), zircons, apatite, xenotime, monazite, rutile, and very rare feldspars.

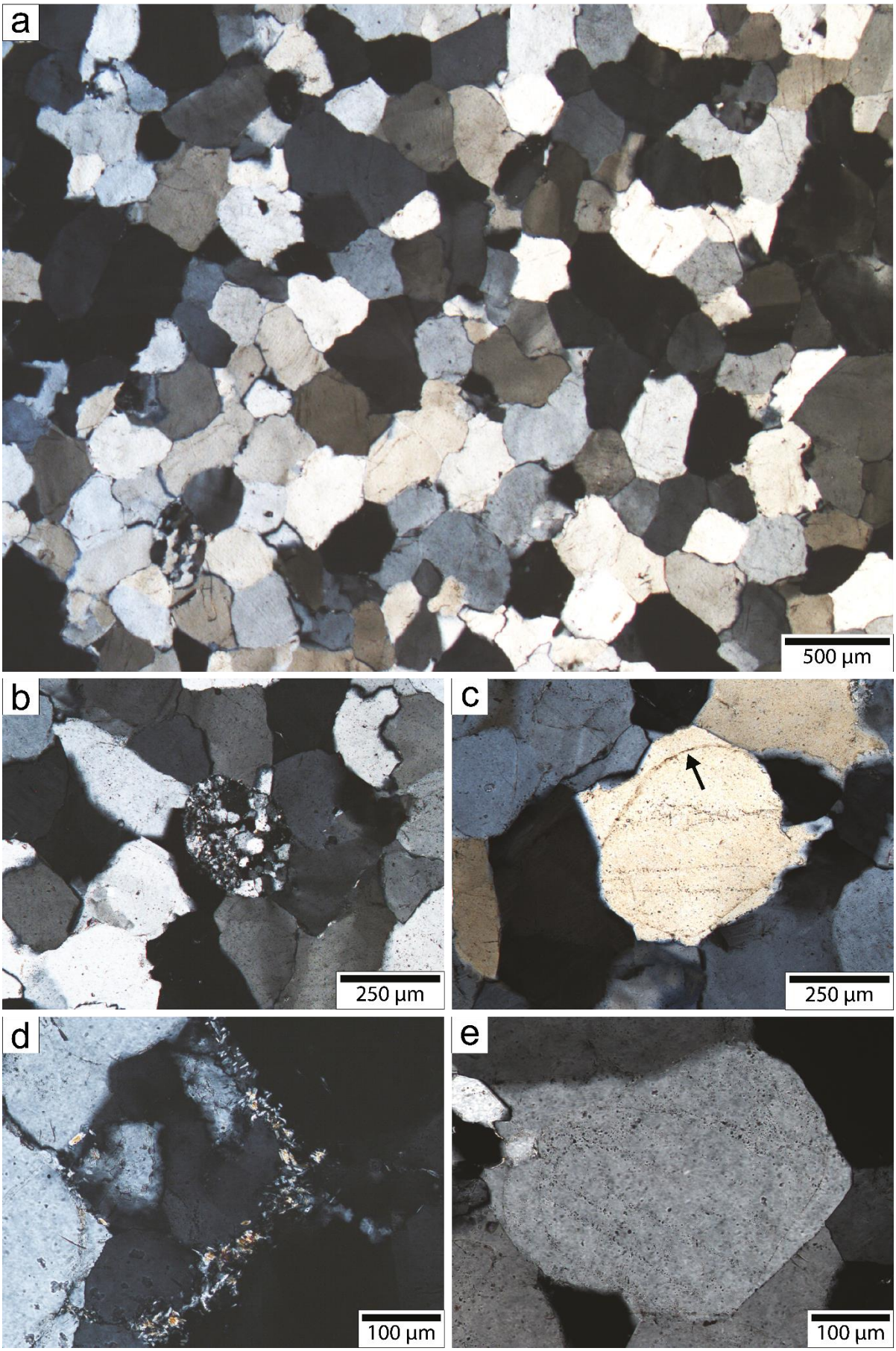

Figure III.1. Optical microscopy cross-polarized images of starting material Tana quartzite. (a) Equant grains showing interlocking texture, (b) polycrystalline grain, (c) dust rim (arrow) revealing initial sand grain shape, (d) white micas at grain boundaries and (e) fluid inclusion trails in a sand grain (also visible in (c)).

On plane-polarized images, grains appear unstrained with mainly uniform straight extinctions. They do not show any undulatory extinction, except for rare sand grains showing inherited, internal recrystallization microstructure (polycrystalline grains, Figure III.1b). Dust rims are sometimes present, witnessing the original shape of detrital sand grains (Figure III.1c). The cement optically appears in crystallographic continuity with sand grains on which it grows epitaxially.

White micas are observed either isolated tablets or as small clusters located at grain boundaries and triple junctions (Figure III.1d). Some grains present abundant fluid inclusions and trails (Figure III.1c&e). These are generally restricted to sand grains and do not continue in the cement neither cross grain boundaries.

Due to filling of the pore space by authigenic SiO_2 cement, no visible porosity was detected in the light microscope or SEM.

Microstructural analysis and cathodoluminescence imaging show that the quartz grains forming the Tana quartzite are composed of a core of equant and rounded detrital quartz sand grains and a non- or dark luminescent cement between (Figure III.2). The sand grains show various cathodoluminescence colours and intensity (from bright blue to dark purple).

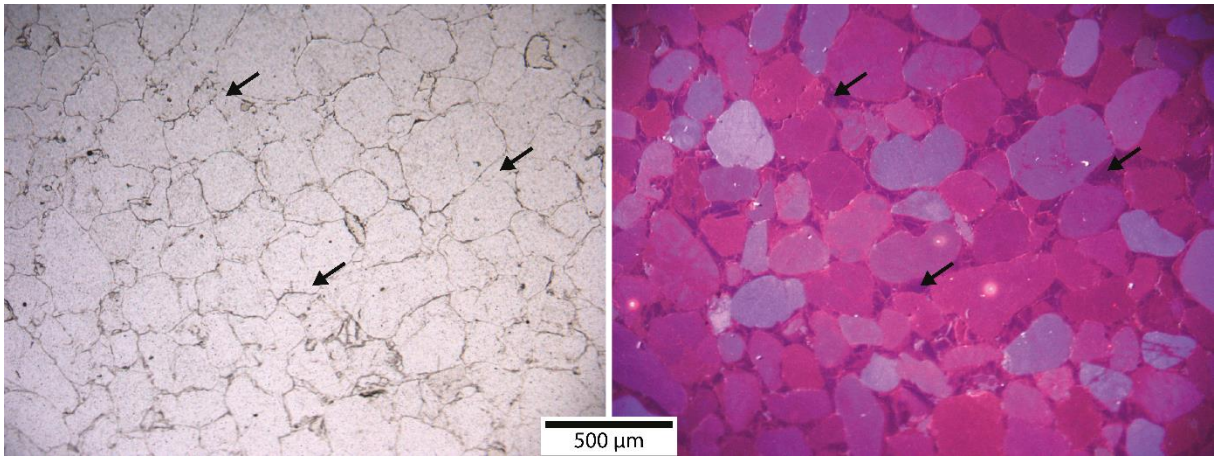

Figure III.2. Natural light and optical cathodoluminescence images from starting material. Equant and rounded sand grains of various luminescence tints are surrounded by a darker cement that grows in crystallographic continuity (arrows).

SEM-cathodoluminescence allowed observing with more details the starting material, particularly some additional sedimentary features. A few pressure-solution contacts (Figure III.3), witnessing the burial of the sediment are present in some places. Micro-fractures healed by authigenic quartz are also observed (dark-luminescing lines cross-cutting the grains). Moreover, details of crystallization appear in the cement that present some luminescence contrasts.

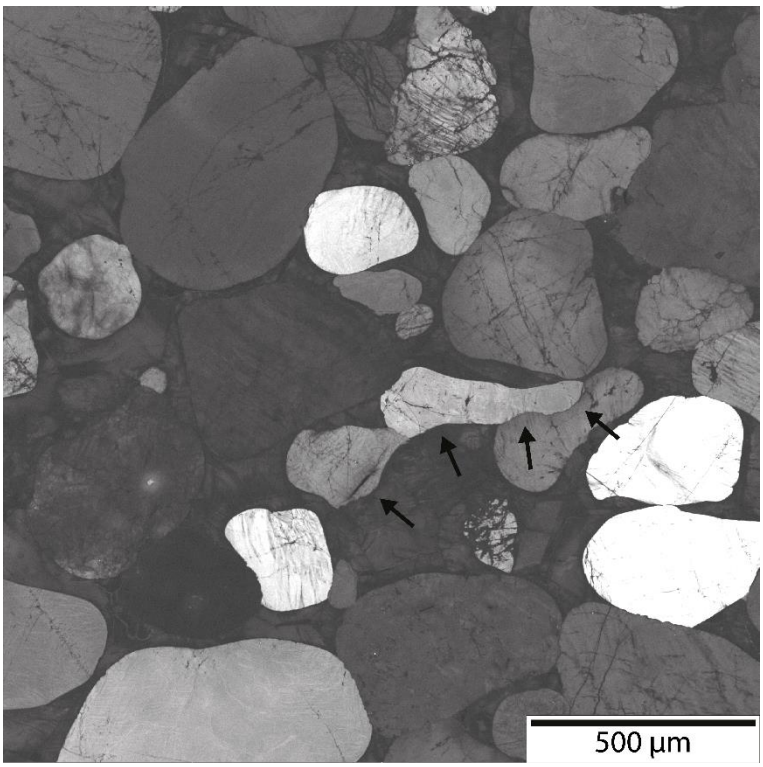

Figure III.3. SEM-CL image of starting material. Pressure solution are observed as a result of burial processes during diagenesis (arrows). Several grains show fractures healed with cement and visible as dark trails.

Electron Backscatter Diffraction (EBSD) measurements of grains orientations from the starting material (one point per grain, on 500 different grains) indicate a random shape fabric (J=1.327 and M=0.027). The c-axis orientations plotted on a pole figure (Figure III.4) are very close to a random/uniform distribution (Bunge, 1982; Skemer et al., 2005).

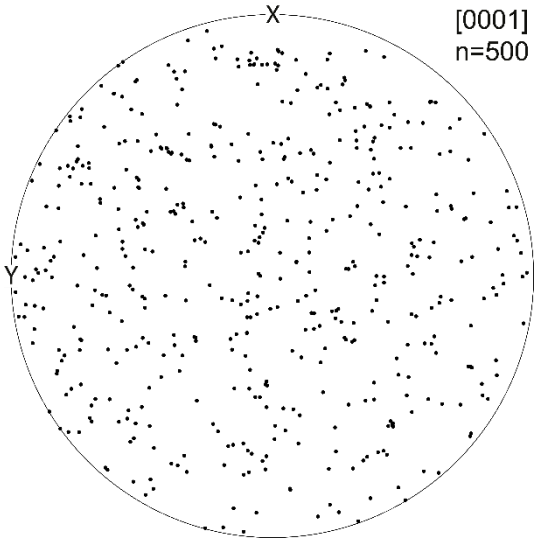

Figure III.4. Pole figure showing a random crystallographic orientation of the c-axis of 500 different grains obtained by Electron Backscatter Diffraction (EBSD) punctual measurements.

III.1.4. TEM observations and dislocation density

The dislocation density of the material was characterized by transmission electron microscopy (TEM) as 6.10^{12} m^{-2}, which is a typical low dislocation density of relatively undeformed natural silicates (McLaren, 2005). This density was calculated from dislocations counting and area measurement on 34 images taken at different places.

Examples of the few observations made on the starting material sample are shown on Figure III.5. On most of the areas free dislocations were observed (Figure III.5a) whereas on some other areas higher dislocations density were present forming walls delimitating grains or subgrains (Figure III.5b). On some rare places micro-aggregates/fluid inclusions were also observed.

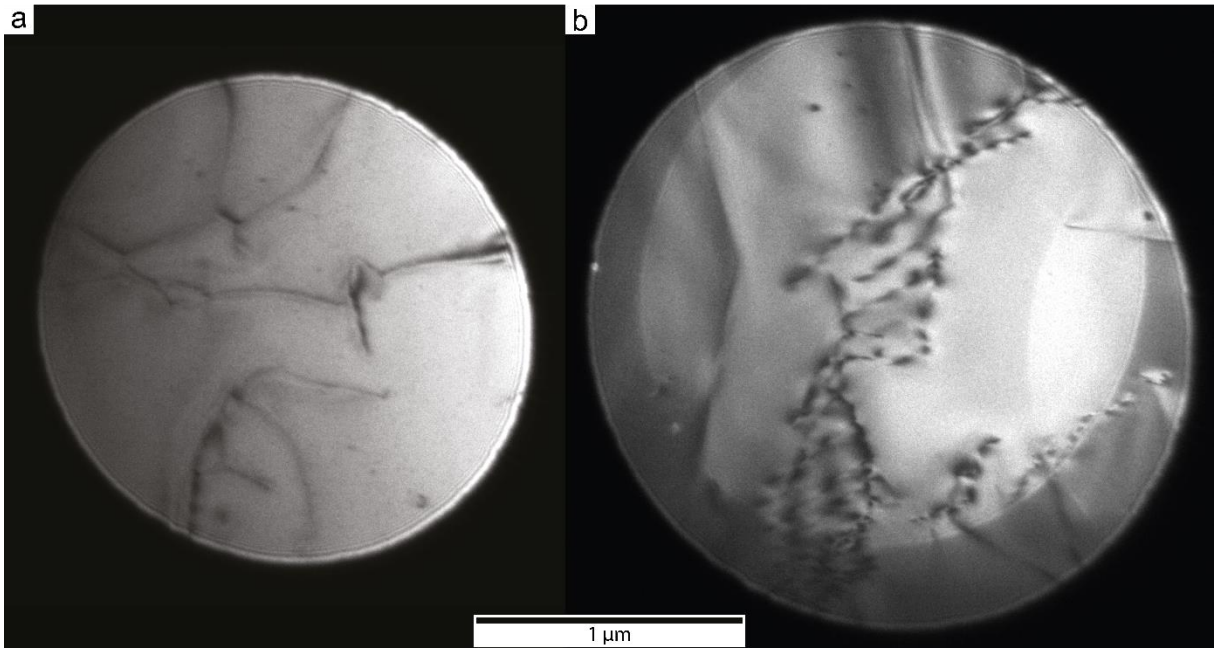

Figure III.5. TEM images in bright field contrast of starting material TQ-2. (a) free dislocations and (b) dislocations walls delimitating subgrains.

III.1.5. Grain size and fabric analysis

The size distribution of quartz grains composing the Tana quartzite was obtained by image analysis using both optical cross-polarized (LM-CP) and light microscopy cathodoluminescence (LM-CL) images. Grains from quartzite (consisting of original sand grains and authigenic quartz overgrowths) and imaged by classic light microscopy will be called “quartzite grains” whereas grains imaged with cathodoluminescence methods, showing original detrital quartz grains will be referred as “sand grains”.

The mean grain size is 204 µm for quartzite grains and 186 µm for sand grains (Table III.2). The grain sizes obtained from classical microscopy optical images (on quartzite grains) are bigger than the ones obtained from LM-CL-images as they include sand grains and the surrounding cement.

The calculated mean aspect ratio (AR) is 1.56 for quartzite grains and 1.55 for sand grains, indicating that grains are somewhat elongated. However, no preferential orientation of the

long axis of the grains appears. The orientations of the fit ellipses long axes are random (see histograms in Figure VII.19 to Figure VII.21 in Appendix part VII.3). For this reason, samples have been cored without reference to any specific orientation.

Table III.2. Grain parameters for starting material Tana quartzite calculated from segmentation of both cross-polarized (CP) and cathodoluminescence (CL) light microscopy images. D_{eq} is the equivalent diameter (diameter of a circle of the same area than the grain) and AR is the Aspect Ratio (ratio of major and minor axes of the fit ellipse).

	D_{eq} (µm)	AR	D_{eq} (µm)	AR
	LM-CP-images analysis		LM-CL-images analysis	
N	1423		2103	
Mean	203.71	1.56	186.18	1.55
Median	198.20	1.47	178.60	1.46
RMS	210.78	-	196.14	-
SD	54.16	0.38	61.72	0.38
Max	451.49	3.54	476.29	4.68
Min	210.78	1.01	57.47	1.01

To better determine grain orientation and eventual strain of starting material the SURFOR method has been run on the same two segmented datasets (LM-CP and LM-CL mosaic images). This program facilitates calculating the sample fabric anisotropy from the particle outlines.

For the starting material, the curves obtained (Figure III.6) indicate a maximum anisotropy of the material is 3.46% for sand grains (segmented from CL images) and 4.54% for quartzite grains (segmented from cross-polarized light microscopy). The anisotropy calculated from the LM-CL segmented images is slightly higher than the one calculated from LM-CL segmented images. The direction of maximum anisotropy for the LM-CL dataset is at 70° (taking as zero reference the horizontal axis of the thin section) and the maximum at 160-165°. For the LM-CP dataset, it is 75° for the minimum and 150 – 160° for the maximum of the projection curve.

However, as the starting material and the corresponding thin sections were not spatially oriented, the slight flattening of the grains calculated does not indicate a starting anisotropy for the experimentally deformed samples. As the cores for were not made in the same orientation, these values only show that starting material has a slight fabric anisotropy and do not correspond to the orientation of the material in the apparatus. Then, the calculated values can be considered as a mean error for strained samples (± 3.46% for sand grains and ± 4.54% for quartzite grains).

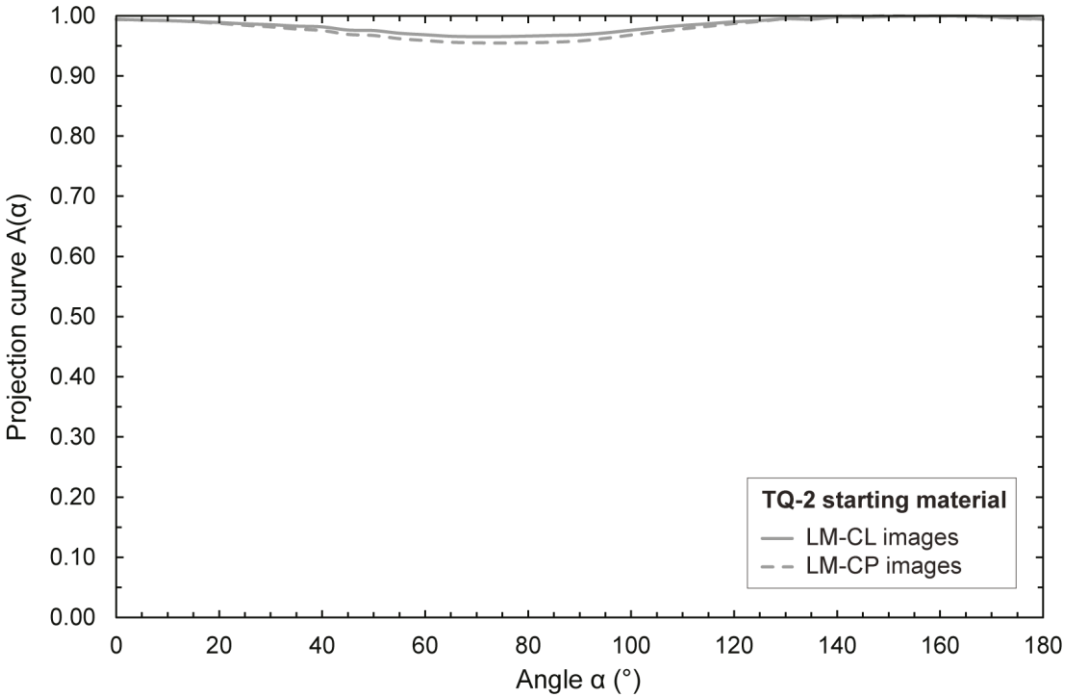

Figure III.6. Projections curves obtained from SURFOR analysis performed on LM-CL and LM-CP segmented images of starting material TQ-2. The two curves indicate a low anisotropy of the starting material fabric.

III.1.6. H_2O contents

The H_2O content of starting material was measured by infrared spectroscopy. The detailed infrared analysis will be presented in the next chapter (part IV.1.2).

Shortly, H_2O contents calculations show that the starting material is heterogeneously hydrated. The mean H_2O content of grain boundaries (2120 H/10^6 Si) is higher than the grain interior one (1659 H/10^6 Si). The H_2O content distributions are highly dispersed (156 – 5488 H/10^6 Si for grain interiors and 501 – 7557 H/10^6 Si for grain boundaries) with a high standard deviation (> 1100 H/10^6 Si in both cases).

III.2. Mechanical data – Experimental deformation

To characterize the effect of confining pressure on deformation of wet quartz aggregates, various experiments have been performed (Table III.3). Three of them were made at the University of Tromsø (Norway) and the others at ISTO Orléans (France).

First, coaxial shortening experiments have been run at 10^{-6} s^{-1} strain rate for confining pressures of 600, 700, 800, 1000, 1250, 1500 and 2000 MPa up to ~30% shortening. For all experiments except two, 0.1 wt.% of H_2O was added. Three experiments with different steps of strain rates (10^{-7} to 10^{-5} s^{-1}) have also been performed at 800 and 2000 MPa confining pressures (named "strain rate stepping" experiments).

Hot-pressing experiments consisting of letting samples at pressure and temperature conditions without deforming have been executed. They are control for P-T conditions for samples deformed at 1000 and 2000 MPa.

For all experiments the temperature was 900°C.

The Table III.3 presents a synthesis of deformation parameters for all the experiments performed.

Table III.3. Experimental conditions for the experiments performed.

Sample name	Griggs apparatus	Temperature (°C)	H_2O added (wt.%)	Confining pressure (MPa)	Strain rate (s^{-1})	Shortening calculated (%)	Shortening measured (%)
542LN	Tromsø	900	0.1	600	1.29E-06	33.46	30.48
544LN				1500	1.37E-06	33.48	30.71
546LN				1000	1.28E-06	31.27	28.01
OR32	Orléans			1000	9.32E-07	30.96	29.39
OR33				800	9.20E-07	24.35	23.30
OR37				1250	*not determined*		36.18
OR42				800	8.12E-07	29.71	30.83
OR45				2000	*not determined*		49.22
OR48				1250	8.80E-07	28.42	27.71
OR50				2000	*not determined*		52.38
OR52				700	8.26E-07	31.98	32.12
OR54				2000	*not determined*		39.75
OR56				2000	*not determined*		74.43
OR57				2000	*not determined*		27.76
OR60				600	7.33E-07	30.92	30.57
OR62				2000	9.29E-07	30.53	29.51
OR63				1500	*not determined*		25.31
OR64				1500	9.40E-07	29.76	26.59
OR59				1000	Hot-pressed (251.7h)		0.53
OR66				2000	Hot-pressed (216.8h)		-
OR65				2000	Strain rate stepping experiment		
OR68				2000	Strain rate stepping experiment		
OR79				800	Strain rate stepping experiment		
OR73			0	800	7.68E-07	31.66	29.02
OR76				700	7.57E-07	31.90	-

The calculated strain rates and shortening from mechanical curves are presented in Table III.3 as well as the shortening measured from thin sections lengths (with an estimated error up to ± 0.8% for a measuring error of 0.1 mm).

Some of the experiments performed failed and the corresponding mechanical curves will not be presented. For some of them, the experiment did not work well (for different reasons): OR33 (800 MPa), OR37 (1250 MPa), OR63 (1500 MPa), OR64 (1500 MPa) and OR65 (2000 MPa). For the others, they are part of the experiments at 2000 MPa for which the hit-point was reach during the pumping stage: OR45, OR50, OR54, OR56 and OR57 (refer to the Methodology chapter part II.1.2.6 for details).

III.2.1. Coaxial deformation experiments

Mechanical data for coaxial experiments have been plotted as strain-stress diagrams (Figure III.7). They can be decomposed into two successive sequences. The initial loading part is characterized by a steep slope in the stress-strain diagram, up to a peak stress (attained around 3 to 5% strain). After the latter, all samples deform for a relatively constant or slightly increasing value of stress.

All samples show a decrease in strength with increasing confining pressure. The maximum final differential stress is nearly 600 MPa for a sample deformed at 600 MPa confining pressure, whereas for sample deformed at 2000 MPa it is ∼100 MPa.

This behaviour is reproducible for the two different apparatuses used (considering a ± 30 MPa accuracy of the solid medium apparatus, Holyoke and Kronenberg, 2010) for a confining pressure of 1000 MPa (samples 546LN and OR32; the strain rate is slightly lower in OR32) whereas for lower pressure at 600 MPa, the sample deformed in Orléans (OR60) is stronger than the deformed in Tromsø (542LN), despite the slightly slower strain rate.

The samples deformed at 1250, 1500 and 2000 MPa have similar strengths at early stages of the experiment (until ∼12% strain). Then, they show lower strength with higher confining pressure.

Concerning the loading parts of the mechanical curves, their variable behaviour is one of the special features attributed to the use of solid medium in the Griggs apparatus. They seem to depend on the sample strengths as the slope is steeper with lower confining pressure, but this behaviour is not systematic. If the sample behaviour was purely elastic, no slope variation would be expected for this part of the mechanical curve (Hooke's law). However this is not the case, as this part of the deformation includes friction and compaction or few strain of the sample and depends on the sample stiffness (see discussion in Précigout et al., 2018).

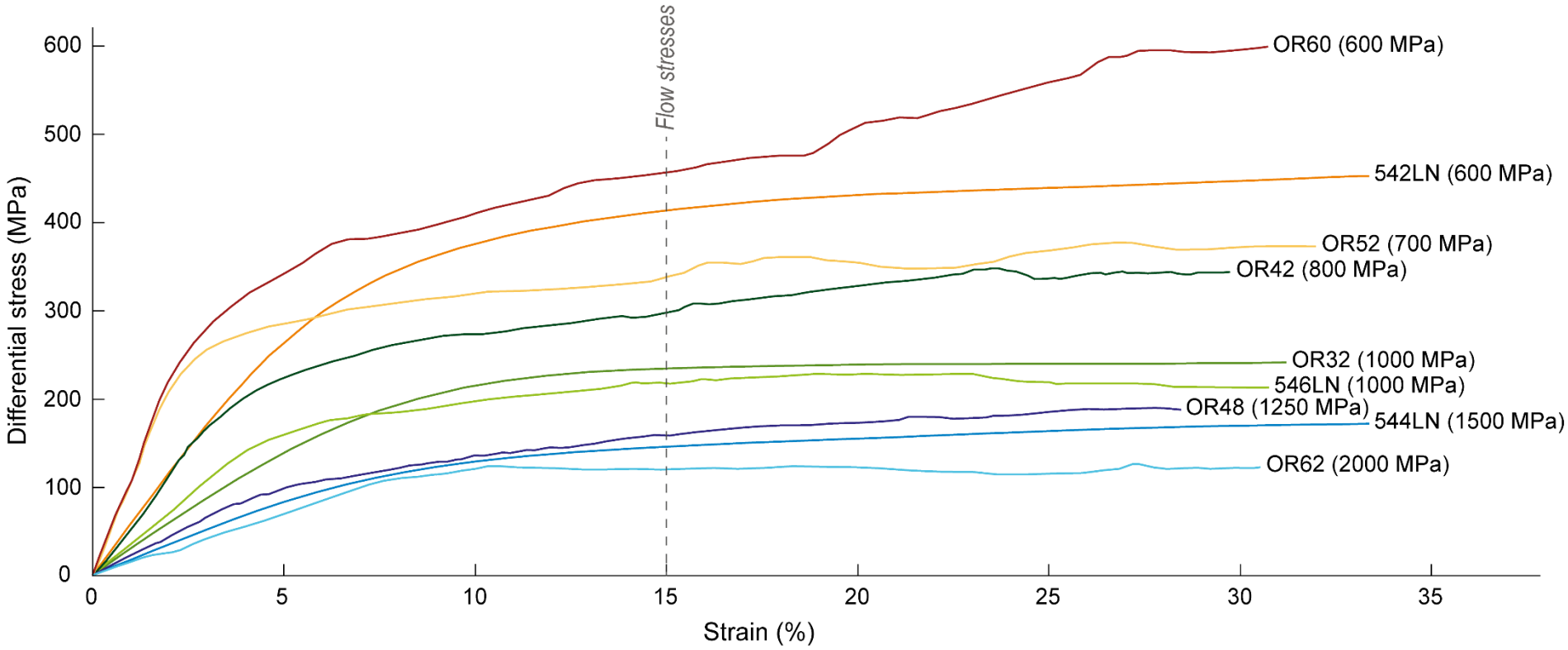

Figure III.7. Mechanical data for samples deformed in wet conditions (0.1 wt.% H_2O added) at 900°C for confining pressures between 600 and 2000 MPa. Samples 54_LN have been deformed in Tromsø (Norway) whereas samples OR_ _ have been deformed in Orléans (France). The sample strengths continuously increase with decreasing confining pressure.

III.2.1.1. Samples deformed without added H_2O

Two samples where deformed “as-is” at 800 and 700 MPa confining pressure, OR73 and OR76 respectively. After 24h of drying at 110°C into the oven, no H_2O was added to the sample into the platinum jacket before sealing. The same experimental settings than for samples deformed in wet conditions were applied.

The stress strain curves of the two “as-is” experiments are both stronger than the corresponding water-added experiments and show a continuous increase in strength (Figure III.8). At 700 MPa the difference in strength between the as-is and the wet samples is more important (final difference of ~200 MPa) than at 800 MPa (final difference of ~110 MPa).

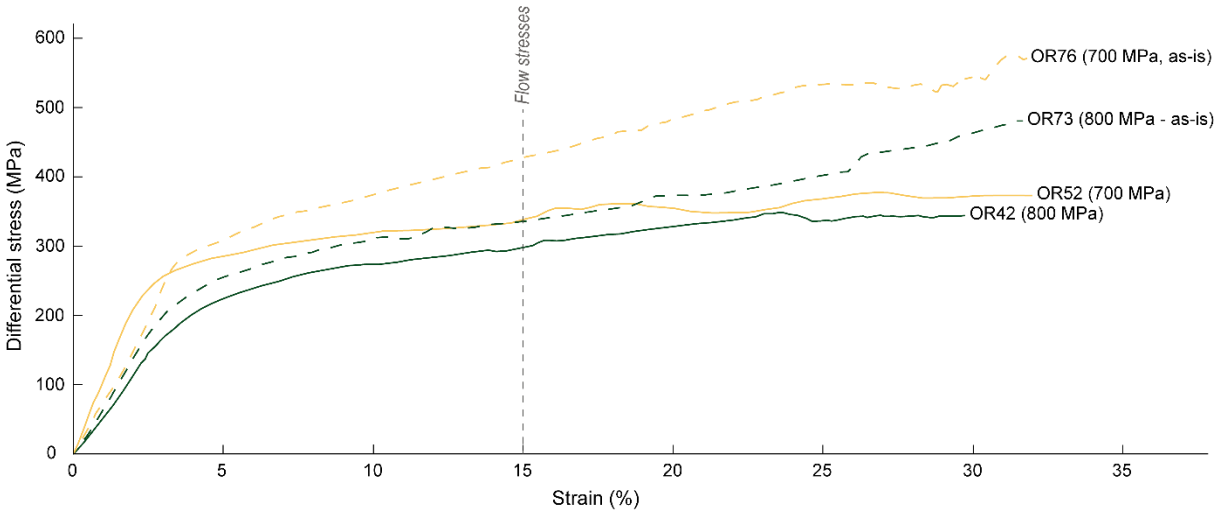

Figure III.8. Strain-stress curves for samples deformed with 0.1 wt.% added H_2O (full lines) and "as-is" (dotted lines) at 900°C and 700 (OR52 and OR76) or 800 (OR42 and OR73) MPa confining pressure.

III.2.2. Strain rate stepping experiments

Two strain rate stepping experiments were performed at high (OR68, 2000 MPa) and low (OR79, 800 MPa) pressures and allowed to determine the stress exponent of the flow law or n-value. Both experiments were conducted at 900°C with 0.1 wt.% H_2O added and with a strain rate sequence of 10^{-5}, 10^{-6}, 10^{-7} then again 10^{-5} s^{-1}. The mechanical strain-stress curves are presented in Figure III.9 and flow stresses for each step are reported in Table III.4.

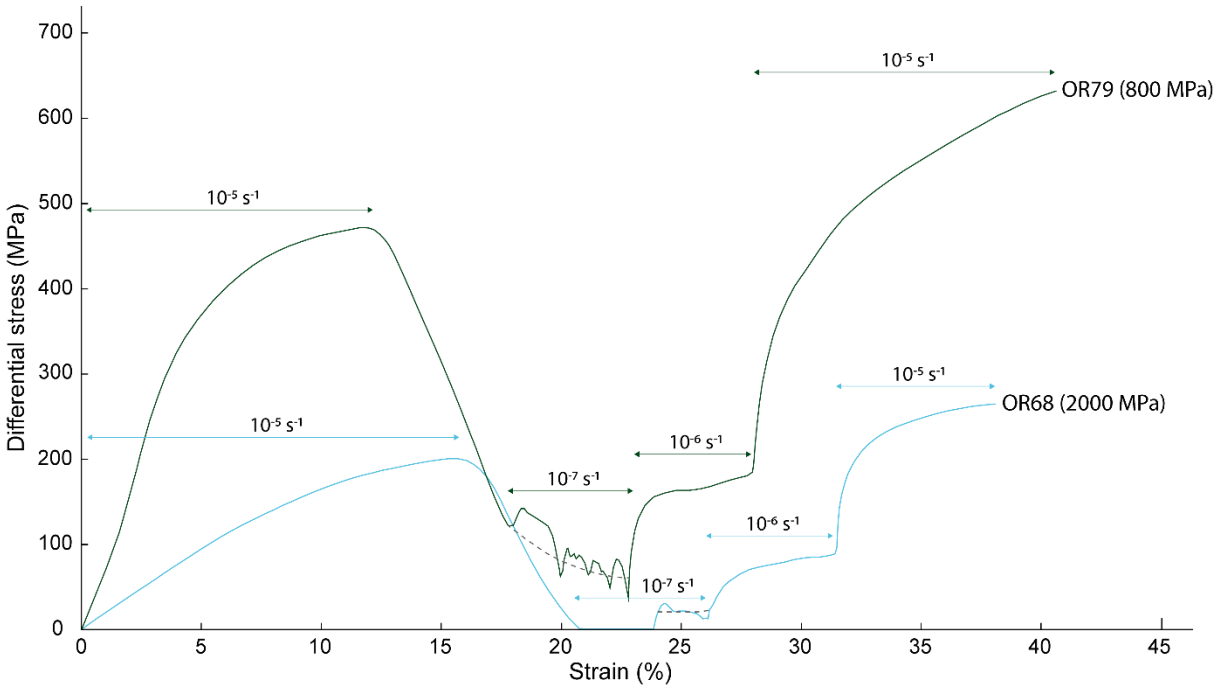

Figure III.9. Stress strain curves obtained for strain rate stepping experiments performed at 800 MPa (OR79) and 2000 MPa (OR68).

The initial step at 10^{-5} s^{-1} has been repeated at the beginning and at the end of the experiments in order to test the reproducibility. The flow stresses associated to that rate are systematically higher during the final step than during the first one, witnessing a strengthening of the samples (shortened up to ~40 %). Moreover, steady state has not really been reached for the lower confining pressure experiment (OR79).

For the steps at 10^{-7} s^{-1}, both samples show an unstable and very variable behaviour, probably due to the low sample strength, so that possibly some friction effects at the pistons start to play a role. In addition, at such low strain rates the initial "friction" of the run-in curve is partially recovered, so that the recorded stresses may be too low (see explanation of this effect in Tarantola et al. (2012), appendix). In the next generation Sanchez apparatus, very low oil flow is injected by the hydraulic pump (0.0007 mL/min) in order to obtain this strain rate, these variations may partially reflect changes in the ambient conditions (daily variations recorded for the force, certainly influenced by room temperature or cooling temperature variations). The strengths values taken for the 10^{-7} s^{-1} steps are indicated by dashed lines on Figure III.9.

Table III.4. Flow stresses obtained and corresponding strain rates for the strain rate stepping experiments performed.

Sample		OR68	OR79
Confining pressure (MPa)		2000	800
Temperature (°C)		900	
Differential Stress (MPa) at	10^{-5} s^{-1}	200.6	471.7
	10^{-7} s^{-1}	85.4	164.3
	10^{-6} s^{-1}	21.2	65.3
	10^{-5} s^{-1}	265.2	633.4

The data of steady state flow stresses from the classical coaxial shortening experiments performed at the same confining pressures have been used to constrain the n-coefficient (open circles Figure III.10). The strengths obtained at 10^{-6} s^{-1} during the two strain rate stepping experiments are lower than the ones obtained for the samples deformed a constant strain rate (285 MPa for OR42 at 800 MPa and 120 MPa for OR62 at 2000 MPa).

The n-exponent is defined as the slope of the linear regression passing in the log-log plot of the flow stresses vs. strain rate values reached at the different steps of the experiment (Figure III.10). For the low pressure experiment (OR79, 800 MPa), n≈1.42 whereas for the high pressure one (OR68, 2000 MPa), n≈1.40. Given the uncertainties of the stress determination in the solid medium apparatus, these n-value are identical. If the slowest strain rate steps are omitted as somewhat less reliable (see above), the resulting n-values are 1.96 for 800 MPa and 2.33 for 2000 MPa confining pressure.

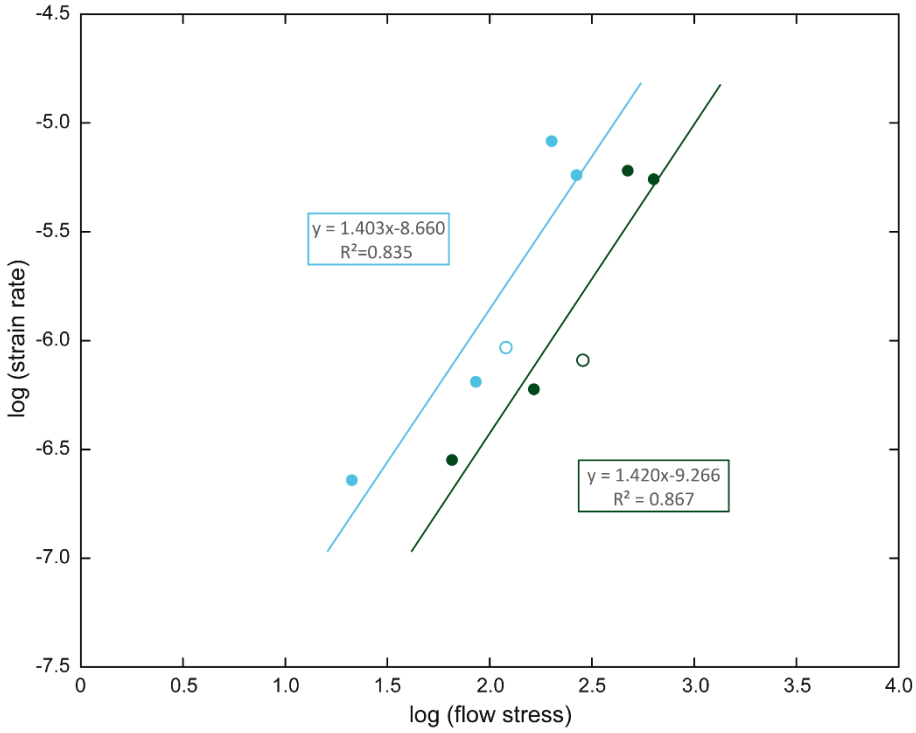

Figure III.10. Plot of the log strain rate vs.log flow stress. Solid circles are data obtained from strain rate stepping experiments whereas open circles are data from samples deformed with 10^{-6} s^{-1} constant strain rate at the same confining pressures.

III.3. Microstructures

III.3.1. Light microscopy

At the global samples scale, microstructural observations show that the local strain distribution in all samples is inhomogeneous. Typically, the centre and/or bottom parts are more strongly deformed.

The strain gradient is slightly more pronounced for samples deformed in the conventional Griggs apparatus in Tromsø (where more of the deformation is located at the lower part of the sample, Figure III.11a) than for those deformed in the new apparatus in Orléans (where more

of the deformation is located in the central part of the sample, Figure III.11b and Figure III.12). This type of strain localisation is common in samples deformed in the solid medium apparatus (e.g., Heilbronner, 2002; Heilbronner and Tullis, 2002; Stünitz et al., 2017) and is related to the temperature gradient in the sample. The thermocouple position indicates the highest temperature of the sample (the temperature difference between sample ends and the hot zone = thermocouple position is < 90%) and this region typically corresponds to the higher strain regions.

For some samples, the global strain partitioning of the sand grains has been characterized with the SURFOR analysis (see part III.3.3.3).

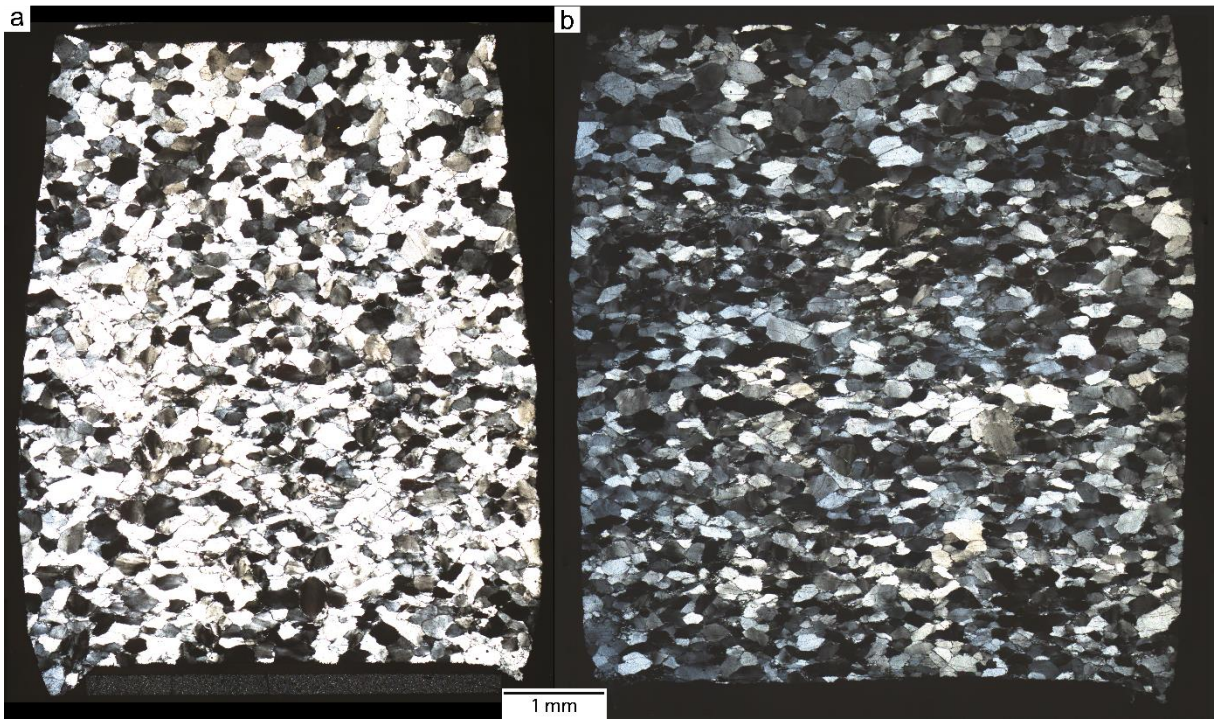

Figure III.11. Mosaic images of samples (a) 546LN and (b) OR32, deformed at the same conditions (1000 MPa confining pressure), both show an inhomogeneous strain partition. The strain gradient is more pronounced for sample 546LN (a) deformed in the conventional Griggs apparatus than for the sample OR32 (b) deformed in the new generation apparatus.

The partitioning of the deformation is typically detected by more elongated grain shapes in the higher strained regions (Figure III.12b) whereas grains are still more or less round shaped in the least deformed part (Figure III.12a). The greater elongation of individual quartz grains is usually accompanied by an increase in the amount of recrystallized material. Original quartz grains in deformed samples show evidence for plastic deformation, such as undulatory extinction, deformation lamellae and, in some places, development of subgrains (Figure III.12c). Some of the progressive subgrain rotation leads to the formation of core-mantle structures (Figure III.12b&c). In addition, much smaller and new grains form during deformation (Figure III.12b), especially in samples deformed at high pressure. The zones where these small grains appear are volumetrically limited and restricted to the boundaries of the plastically deformed grains, in the most deformed part of the samples. The small sized grains appear to be more abundant as the pressure and finite strain increase.

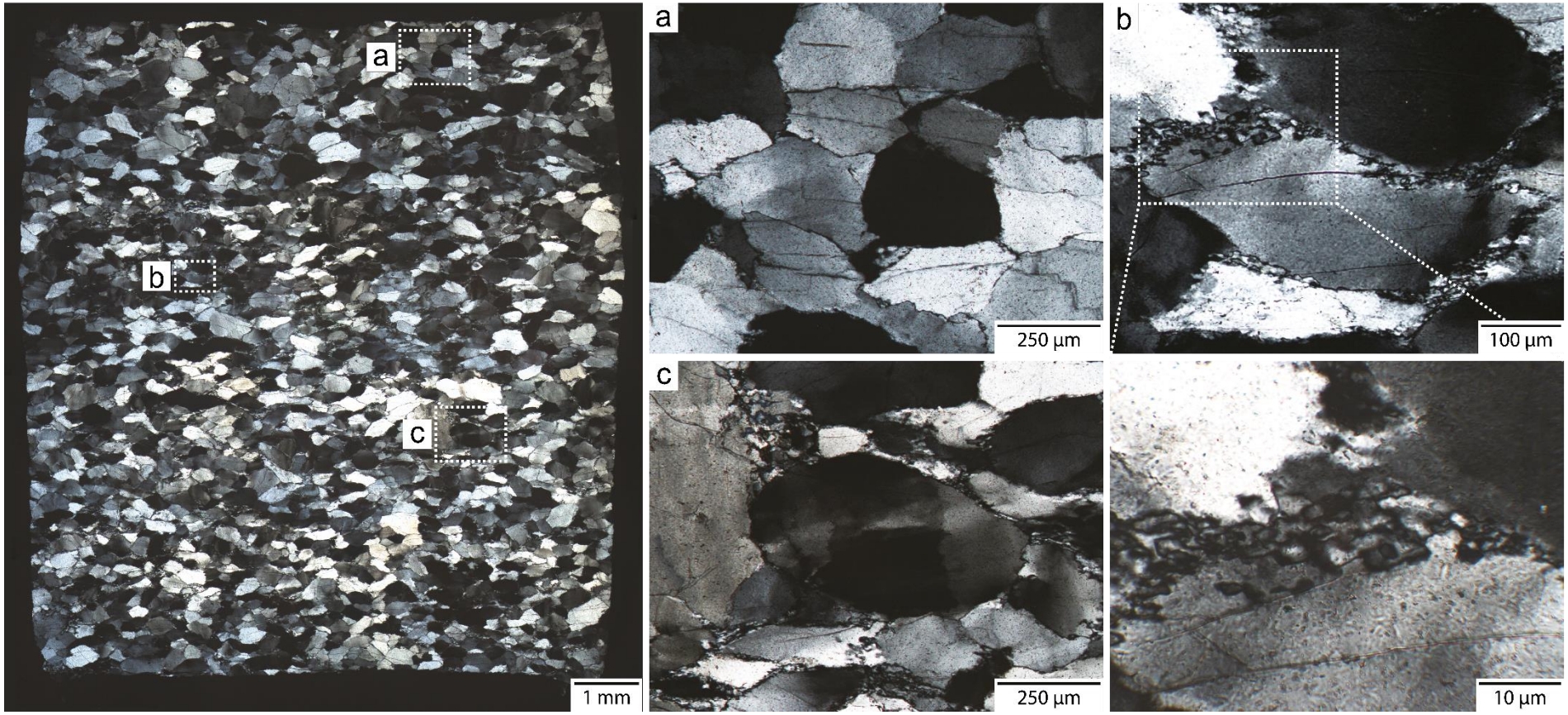

Figure III.12. Cross polarized light images of sample OR32 deformed at 1000 MPa confining pressure. Left: overview of the sample showing higher strain regions near the centre. (a) In the top and least deformed part of the sample, grains are round shaped and display weak undulatory extinction, one small grain is observed. (b,c) In the most strongly deformed part of the sample, clasts are elongated and show undulatory extinction and subgrains. Limited recrystallization is observed at grain boundaries (core and mantle structures). The shortening direction is vertical.

III.3.2. Cathodoluminescence

In cathodoluminescence (light and SEM) images of deformed samples, the original quartzite sand grains and the surrounding cement can still be identified. The same variations of luminescence and tints as in the starting material are observed (Figure III.2 and Figure III.13).

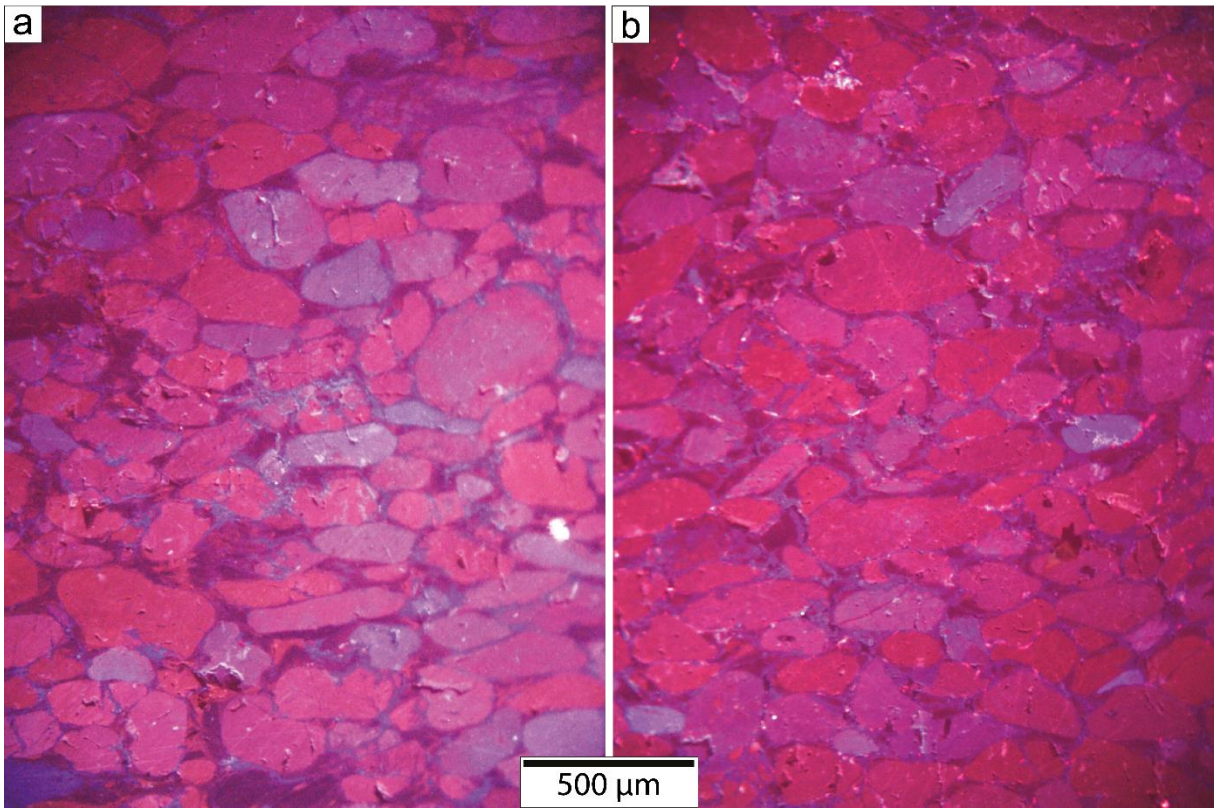

Figure III.13. Light microscopy cathodoluminescence images of samples (a) OR52 and (b) OR64, deformed at 700 and 1500 MPa, respectively. Sand grains (often elongated) present various luminescent tints and are surrounding by a darker cement as in the starting material quartzite (see Figure III.2). In addition, a bright blue luminescence is observed. The shortening direction is vertical.

In the most deformed parts of the samples, the sand grains show a more elongated shape with the long axis at a large angle or normal to the shortening direction. In the cemented area between the sand grains, the darker luminescent cement is clearly observable. However, in the deformed samples, a new material with a bright luminescence appears in CL images (Figure III.13 to Figure III.16). This bright luminescent material invariably has a blue colour and is not short-lived but permanent.

III.3.2.1. Morphology of the bright luminescence

The bright luminescence material in deformed samples is often concentrated in the boundary regions of grains, so that these bright regions appear predominantly in the cement and at the grain boundaries of sand grains (Figure III.14).

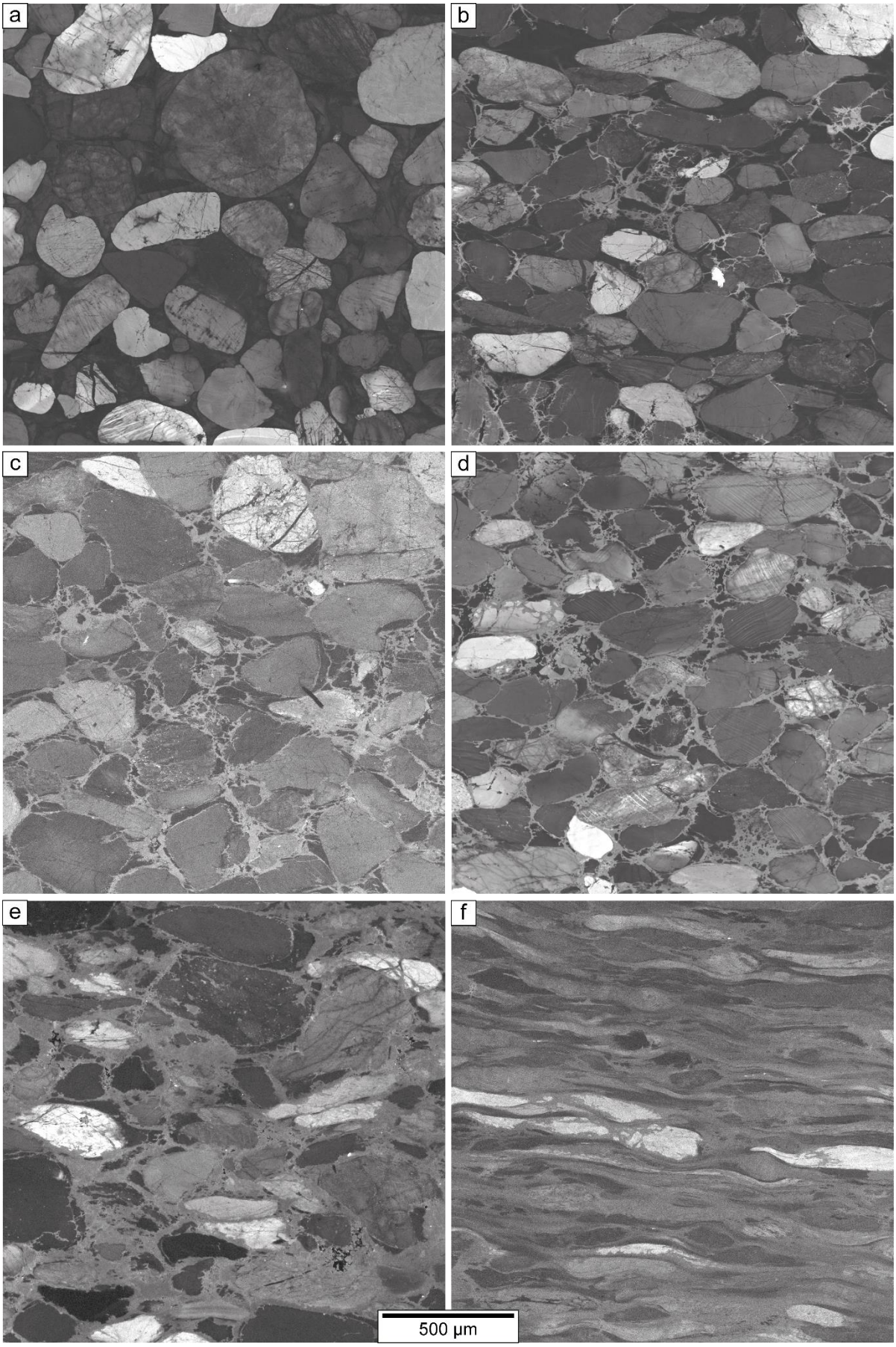

Figure III.14. Cathodoluminescence images of (a) starting material and (b-f) of samples deformed at confining pressure of (b) 700 MPa (OR52), (c) 1000 MPa (546LN), (d) 1500 MPa (OR64), (e) 2000 MPa (OR62) and (f) 2000 MPa high-strained (OR56). The shortening direction is vertical.

With a crack-like geometry, either localized in the cement area, or as transgranular cracks

In some cases, the bright luminescing material cuts across original sand grains (Figure III.15). In the low strain parts of the samples, the brightly luminescing zones follow a clear crack morphology (Figure III.14 and Figure III.15). The bright luminescing material occurs in the cracks cut through both, sand grains and cement. This is observed in samples deformed at low confining pressure (e.g., OR42, deformed at 800 MPa, Figure III.15a) and at higher confining pressure (sample 546LN, deformed at 1000 MPa, Figure III.15b).

In samples deformed at low confining pressure, cracks are subparallel to the loading direction and appear to have been dilatant – mode I cracks – before new quartz material has filled the cracks. The inner part of these cracks can be filled with non-luminescent material (Figure III.15a) – probably epoxy as it deteriorates and becomes yellow under the LM-CL beam. From the boundaries of the healed mode I cracks, very thin cracks extend perpendicular to the mode I cracks, i.e., in an orientation typical for unloading cracks (Figure III.15a). The appearance of such cracks has first been observed in samples deformed in the Griggs-type apparatus by (Fitz Gerald et al., 1991), and these features have been termed "step-ladder cracks". In all deformed samples, many thin cracks with bright luminescence in a direction perpendicular to the shortening direction extend from grain boundaries and cracked regions and have formed as unloading cracks during decompression of the samples (e.g., Figure III.15b).

In samples deformed at higher confining pressure, cracks tend to be thinner, more irregular, and are distributed more pervasively across the samples (Figure III.14e&f). They often (but not necessarily) follow the grain boundaries (intergranular cracks).

For all the cracks in the samples, no or very little displacement has been observed along the cracks.

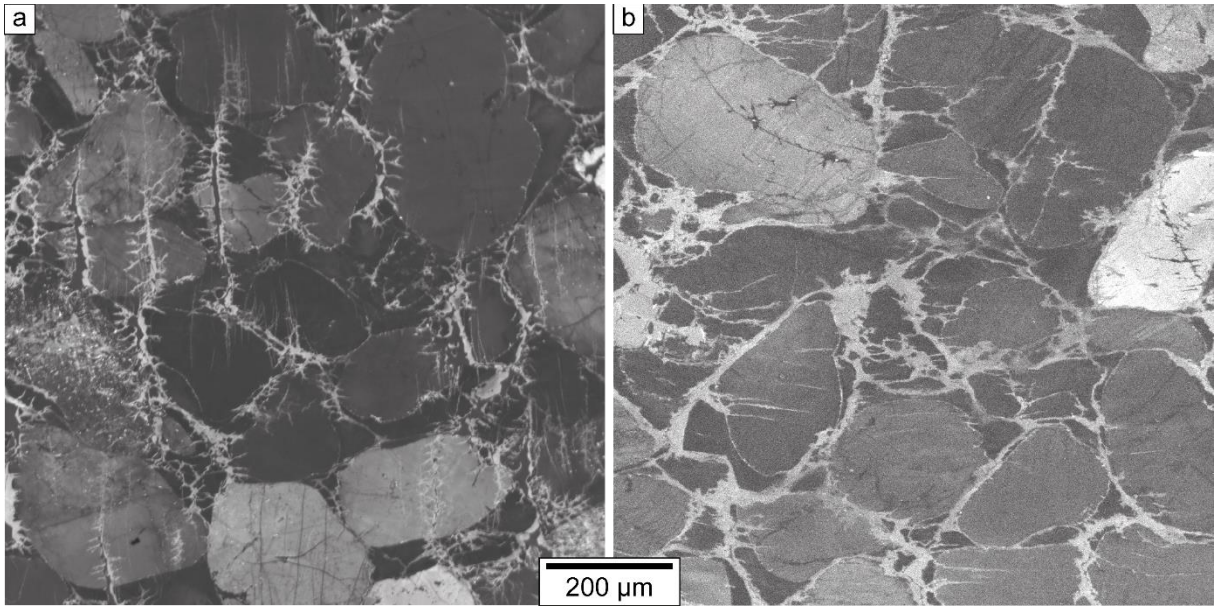

Figure III.15. SEM-CL-images of bright luminescent cracks in both cement and grains in samples deformed at (a) 800 MPa (OR42) and (b) 1000 MPa (546LN) confining pressures. The shortening direction is vertical.

Overgrowths on pre-existing crystals, in intergrain pores

The brightly luminescent material sometimes forms overgrowths with crystal faces on pre-existing large grains or filling intergranular spaces (Figure III.16a). EBSD maps performed on these areas indicate that these faceted overgrowths are in crystallographic continuity with the parent grain (Figure VII.18 in Appendix part VII.2 for 546LN sample). The faceted crystals can be surrounded by non-luminescent material in pore spaces (Figure III.16a).

This non-luminescent material surrounding the crystal faces could either be voids filled with epoxy during the thin section preparation or amorphous material. On EBSD maps, these areas were not indexed (Figure VII.18 in Appendix part VII.2). To determine their nature, a rough approach was used: these areas were put under high voltage electronic beam in the EPMA. Because the beam damages quickly the epoxy (as tested on the border of the sample) and not the glass it could allow to discriminate them. This operation was made on several areas presenting dark luminescent material around crystal faces in sample OR64 (1500 MPa) and no deterioration was observed. This could be an evidence for amorphous silicic material filling the pores and the presence of melt pockets at these places during the experience.

As aggregates of small new grains in the boundary region

Larger regions of bright luminescent material consist of aggregates of many small new grains (Figure III.16b). Many of the small grains are brightly luminescent throughout but others have a darker luminescent core with a bright rim of variable thickness (Figure III.16b). Comparison between bright luminescent zones and the corresponding regions under crossed polarizers indicate that all of these regions consist of small grains, luminescing in blue, but not all luminescent regions consist of small grains.

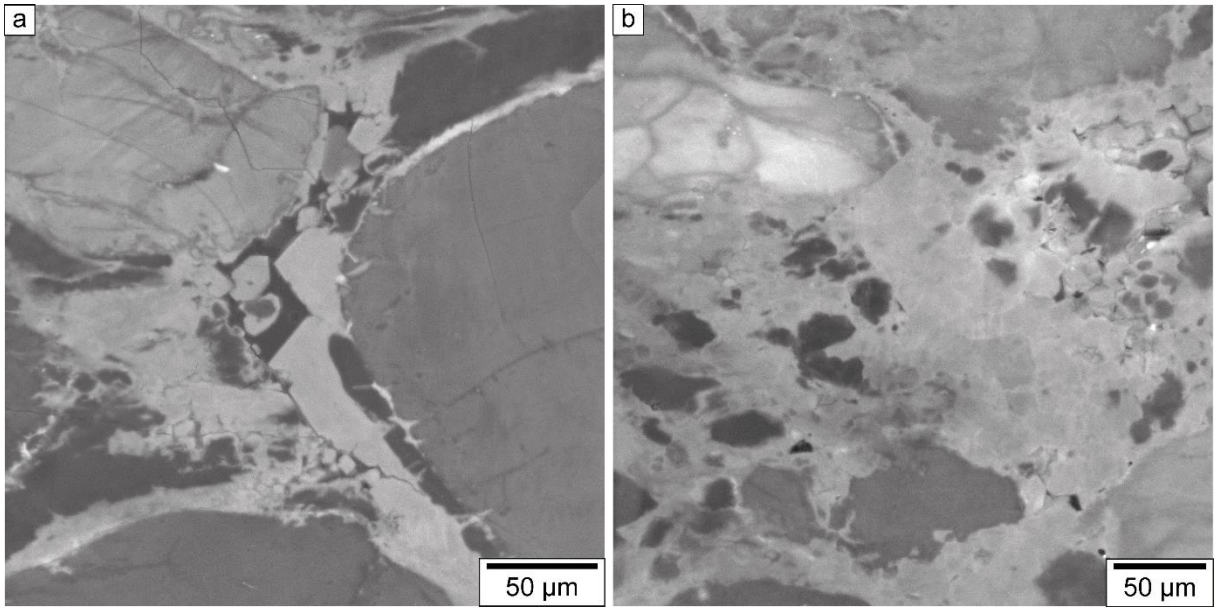

Figure III.16. SEM-CL-images of (a) crystal faces at the border of a grain in sample 546LN (1000 MPa) and (b) small luminescent grains in cement area between grains in sample OR64 (1500 MPa). The shortening direction is vertical.

The amount of brightly luminescent material increases substantially with increasing strain. In a sample deformed to 74% strain (OR56) the original grains are strongly elongated and are embedded in a matrix of 30% luminescent material (Figure III.14f and Figure III.19).

III.3.2.2. Evolution of luminescent regions as a function of pressure and sample strain

For four samples (546LN, OR42, OR57 and OR56), SEM-CL longitudinal transects have been recorded from the top to the bottom (example for OR57 sample on Figure III.17). As the bright luminescent material has a blue colour, so that the blue filter was used in SEM-CL images to enhance its presence. All transects were segmented manually in order to separate the original grains and cement from the bright new luminescent material. The segmented images were then processed with *ImageJ* software to quantify the amount of bright luminescence present in samples.

Domains with higher finite strain show a higher proportion of brightly luminescent areas. This relationship can be observed at the scale of a given sample, between the top – relatively undeformed part – and the bottom part – where deformation is much more intense (Figure III.18). This relationship can also be observed in samples deformed to higher amounts of total strain (e.g., OR56 sample, Figure III.14f and Figure III.18).

There is a relationship between the amount of bright luminescent material and confining pressure demonstrated for the three samples strained up to 30% (OR42, 546LN and OR57). The amount of brightly luminescent material increases in the middle to bottom part of the samples (more deformed regions; Figure III.18): 9.88 % for sample OR42 (800 MPa), 10.72 % for sample 546LN (1000 MPa), 15.08 % for sample OR57 (2000 MPa; Figure III.17). Thus, there is a trend of increasing amount of brightly luminescent material with increasing confining pressure and with strain (Figure III.19).

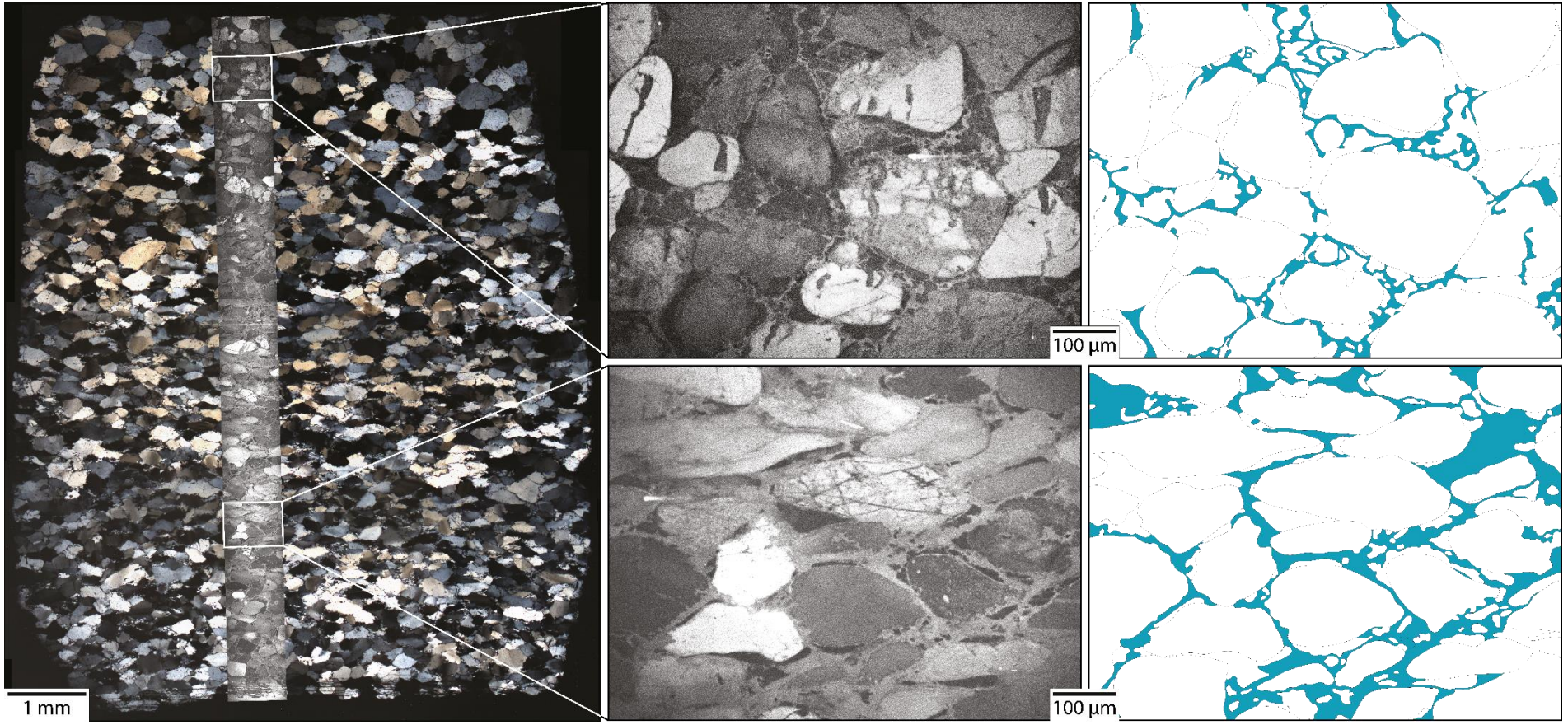

Figure III.17. Left: mosaic of OR57 sample (2000 MPa) in polarized light with associated SEM-CL-images longitudinal transect. Right: examples of segmentation and identification of bright luminescent zones (coloured in blue).

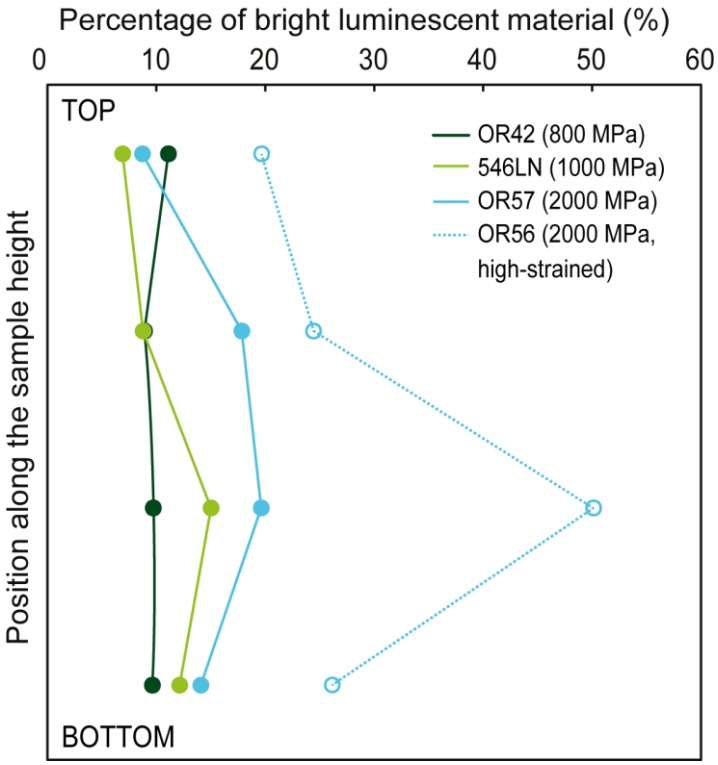

Figure III.18. Percentage of bright luminescence for SEM-CL-images longitudinal transects as a function of the position along the sample. The percentage of bright luminescent material is higher in the higher strained regions (middle and bottom parts) and for samples deformed at higher confining pressure or up to higher finite strain.

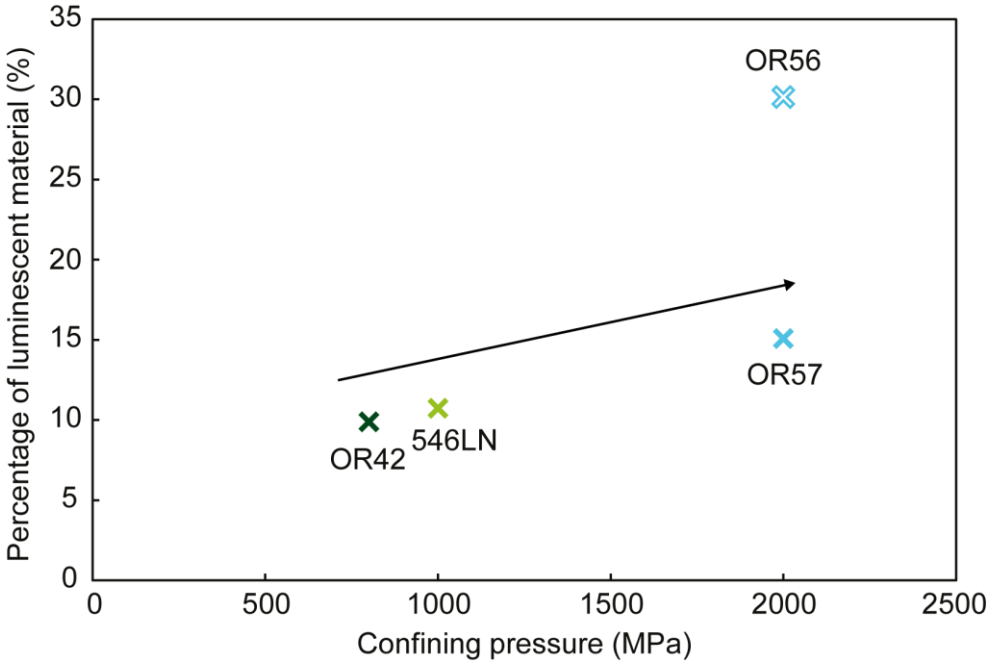

Figure III.19. Percentage of bright luminescence for SEM-CL-images longitudinal transects as a function of the confining pressure. The percentage of luminescent material increases with confining pressure and finite strain.

III.3.3. Strain analysis from fabric and grain shapes

The starting material and experimental samples (samples deformed at 700, 800, 1000, 1500 and 2000 or hot-pressed at 1000 MPa confining pressure) have been studied for their grain shapes and fabric using image analysis. The goal of the analysis was to compare the bulk sample strain determined from the mechanical record and from measuring sample lengths with an analysis based on strain of individual quartz grains. Such an analysis is difficult in normal quartz grain aggregates because the regions of dynamic recrystallization make it difficult to identify original grain shapes as passive markers.

The outlines of original sand grains in the Tana quartzite represent true strain markers for the deformed samples, because dynamic recrystallization typically affects the grain boundary region first (e.g., formation of "core and mantle" structures), i.e., the cement regions. However, the sand grain outlines are located inside the original quartz grains and are only rarely affected by the bright luminescence regions. Furthermore, they present passive markers because the cement overgrowth is in crystallographic continuity with the original sand grains. In addition, the orientation of long axes of the sand grains and their fabric are more or less random in the starting material (Table III.2).

An example of the segmentation of the OR62 sample (2000 MPa) is shown in Figure III.20 (and in Appendix part VII.3 for the other samples). Sand grains are manually separated from surrounding cement in LM-CL-images. In this way, only the original sand grains and their internal plastic deformation are considered for this strain analysis.

III.3.3.1. Grain sizes analyses

Sand grain size and parameters calculated from the analysis of mosaic light microscopy cathodoluminescence images are presented in the Table III.5. The number of analysed grains varies with the grain sizes (and sample size for 546LN that is smaller). The equivalent diameter of sand grains varies with the layers in the starting material and is not a function of deformation. The aspect ratio of individual grains increases for deformed samples (from 1.79 to 2.05) in comparison to the starting material. This latter presents a slight elongation (AR of 1.55) but with no marked preferred orientation (random orientation of grains fit ellipses long axes, see Appendix part VII.3). The same observation is made for the hot-pressed sample OR59 (AR of 1.56). No correlation emerges between confining pressures and equivalent diameters or aspect ratios neither with sample bulk strain (calculated or measured).

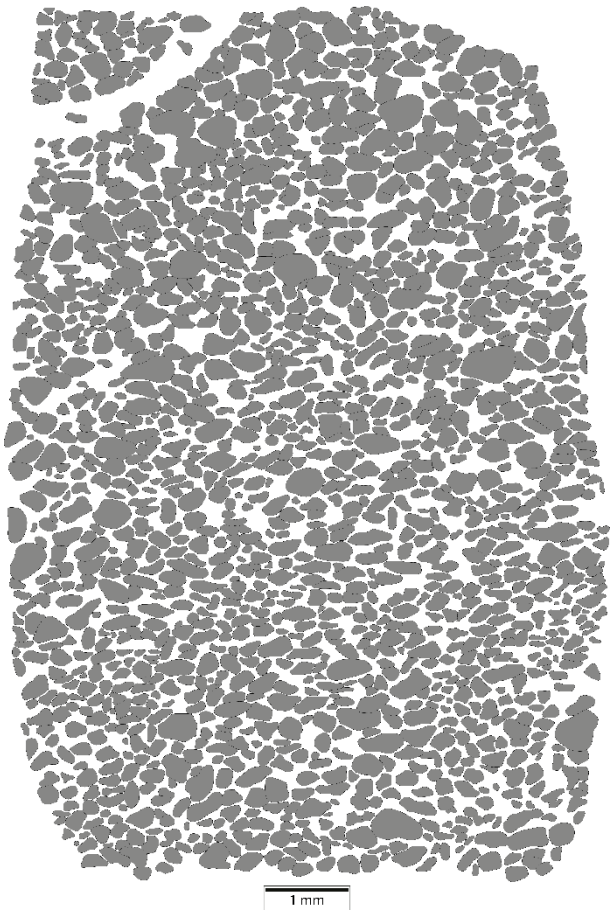

Figure III.20. Example of the manual segmentation made for the OR62 thin section from optical cathodoluminescence images. Interiors of grains are isolated from the surrounding cement based on their luminescence colour contrasts. The shortening direction is vertical.

Table III.5. Results from particle analysis for starting material and experimental samples. The errors correspond to the standard deviation.

Sample	Confining pressure (MPa)	Number of grains analysed	Equivalent diameter (µm)	Aspect Ratio
TQ2	Starting material	2103	186 ± 62	1.55 ± 0.38
OR52	700	2203	174 ± 62	1.95 ± 0.64
OR42	800	1849	194 ± 70	1.94 ± 0.68
546LN	1000	1135	228 ± 69	1.79 ± 0.56
OR32	1000	1835	204 ± 69	2.05 ± 0.73
OR59 (HP)	1000	2343	202 ± 68	1.56 ± 0.38
OR64	1500	2603	172 ± 54	1.81 ± 0.55
OR62	2000	3072	181 ± 66	1.85 ± 0.57

III.3.3.2. Strain analysis

The SURFOR program facilitates the calculation of the sample strain/fabric anisotropy from the particle outlines of the starting material and deformed samples. The results are shown in Figure III.21 and the corresponding data presented in Table III.6. The difference between the minimum and maximum of the projection curves corresponds to the global strain value (from 0 to 1). The angular difference between the maximal and minimal position of the projection curve should

be 90° (corresponds to the angle between shortening and extension direction), and the value of the minimum corresponds to the shortening direction.

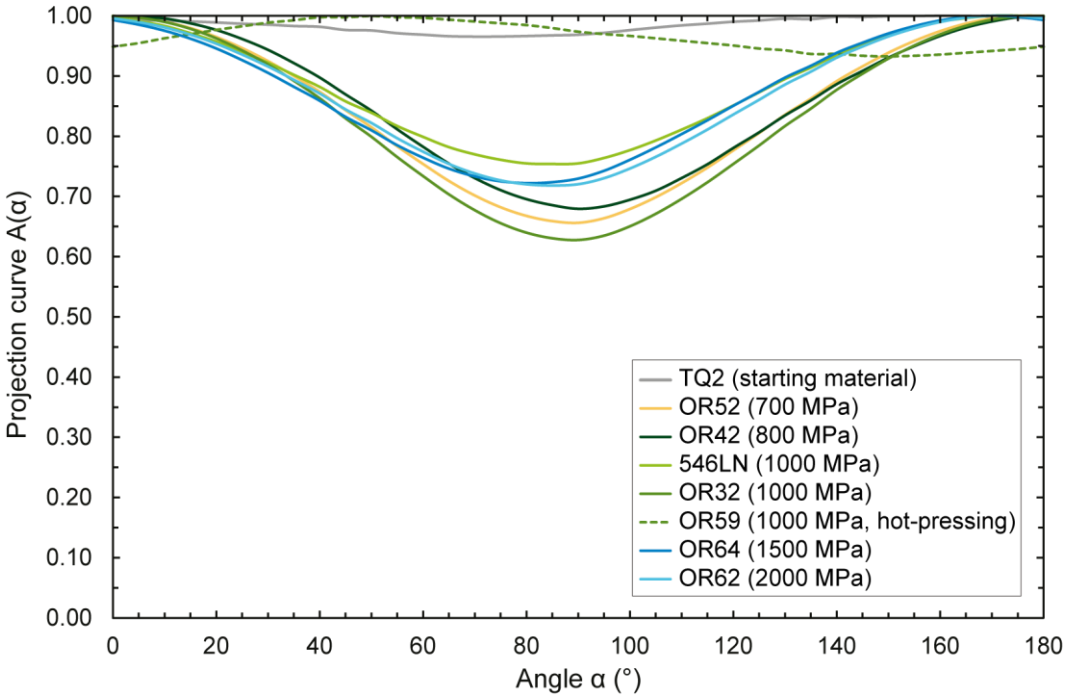

Figure III.21. SURFOR projections curves showing that the starting material TQ2 has a slight strain of 3.5% whereas deformed samples at various confining pressures have an orientation comprise between 80 and 90° for a strain comprise between 24.6% (546LN) and 34.4% (OR52). The global shortening direction for deformed samples is theoretically 90°.

Table III.6. Results from SURFOR analysis. For the finite sample strain, the first column corresponds to the calculated strain and the second column to the measured strain.

Sample	Confining pressure (MPa)	Min. of the projection curve	Angle of min. (°)	Angle(s) of max. (°)	Fabric anisotropy (%)	Finite sample strain (%) Calc.	Meas.
TQ2	Starting material	0.965	70	160-165	3.5	-	
OR52	700	0.656	90	0-175	34.4	31.98	32.12
OR42	800	0.680	90	0-175	32.0	29.71	30.83
546LN	1000	0.754	85	170-175	24.6	31.27	28.01
OR32	1000	0.628	90	0-180	37.2	30.96	29.39
OR59 (HP)	1000	0.933	150	50	6.7	-	0.53
OR64	1500	0.722	80	170	27.8	29.76	26.59
OR62	2000	0.718	85	170-175	28.2	30.53	29.51

For the starting material (TQ) the minimum of the curve is 0.965 for α=70°, indicating a very slight flattening of the grains. However, as the studied thin section was not oriented in a particular way and the cores for experimental samples were not made in the same direction, this value indicates the general fabric anisotropy of the starting material but does not correspond to the orientation of this material in the apparatus. Yet, the ± 3.5% anisotropy should be considered as a mean error for strained samples.

For deformed samples, the bulk shortening for the grain fabric calculated by the SURFOR analysis is between 22.9 and 37.2%. For the samples OR52, OR42, OR64 and OR62 the values are very close to the ones calculated from mechanical data and measured on thin sections and are within the error range (± 3.5%). However, for 546LN sample, the shortening value is underestimated and overestimated for OR32 (difference up to > 8 %).

For the hot-pressed sample OR59, the SURFOR analysis indicates a slight anisotropy (6.70%) of the sand grains (but the direction does not correspond to the shortening direction) whereas the finite strain measured is close to zero (0.53%).

III.3.3.3. Additional analyses

The strain partition was characterized along some samples by calculating the anisotropy of four equal parts longitudinally divided (from bottom to top) on LM-CL segmented images. As these analyses are not part of the discussion, their results are presented in Appendix part VII.3.13.

Grain size characterisation as well as anisotropy calculations (SURFOR analysis) were also performed on segmented light microscopy mosaic images. Contrary to the sand grain limits, the quartzite grains boundaries cannot be truly considered as passive markers because processes occurring during deformation may modify them (e.g., core and mantle structures, cracks, recrystallization …). The results from these analyses were then not taken into account in this chapter but are presented in Appendix part VII.3.

III.3.4. EBSD maps and misorientation calculations

Two regions were selected for detailed EBSD analysis: (1) a low strain region with limited recrystallization and formation of discrete luminescence in response to cracking (546LN), and (2) a high strain region affected by more extensive recrystallization/luminescent material (OR56).

In region (1) the cracks are visible in the SEM-CL image, cutting through original quartz sand grains as well as cement (Figure III.22a). The corresponding EBSD map of this region shows small new grains (clasts) that make high angle boundaries with the larger quartz grains in the traces of the cracks. In addition, some low angle boundaries also separate the small clasts from the host quartz grains (Figure III.22b). The size of the clasts (new grains) can be as small as 1-2 µm and as large as ∼10 µm (Figure III.24). Low angle new grains (in Figure III.24 marked as “subgrains”) and the high angle new grains (in Figure III.24 marked as “recrystallized grains”) do not show different size distributions, only high angle new grains are more frequent (Figure III.24). On the scale of the EBSD maps, the smaller and larger clasts all have more or less rounded shape (Figure III.16). This is the case in light microscope images, too (Figure III.12). The clasts typically have a bright blue luminescence colour. The clasts with low angle boundaries (<10°) only show a weakly preferred misorientation axis in [0001], whereas the larger angle boundaries are misoriented with axes in [0001] and [-12-10].

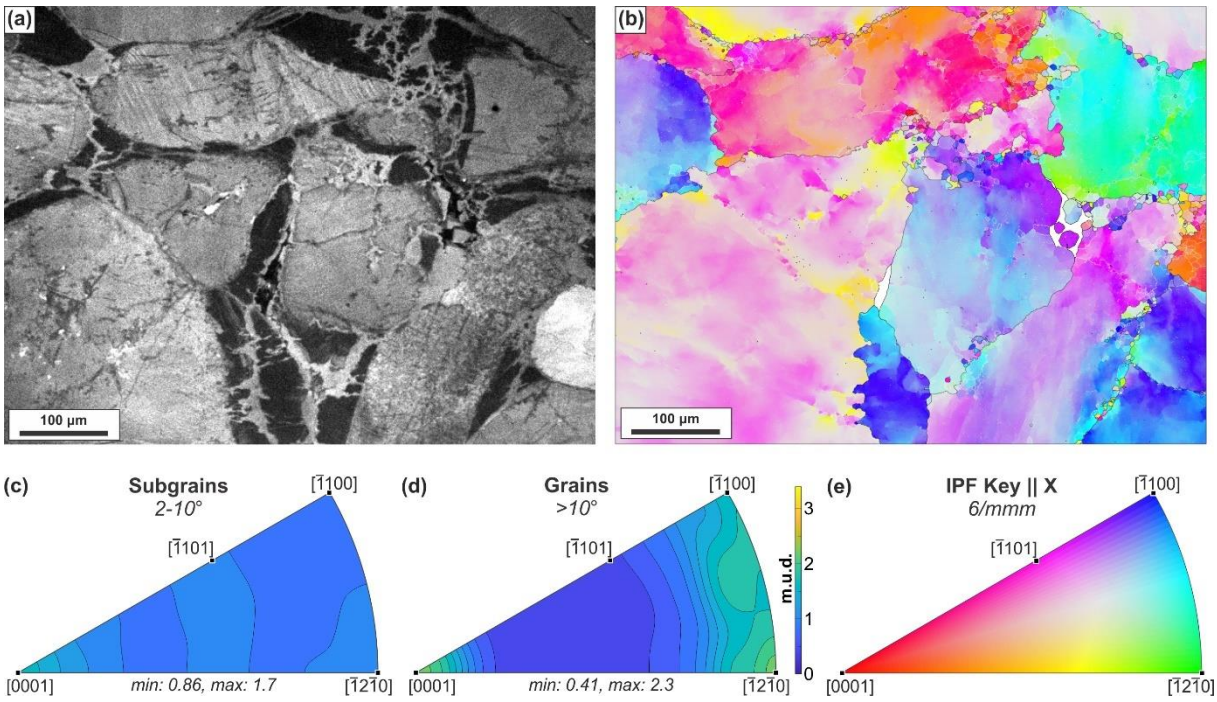

Figure III.22. (a & b) Cathodoluminescence (CL) image, EBSD orientation map and inverse pole figures (IPF) for sample 546LN. (a) CL image with blue (380-515 nm) optical filter to highlight recrystallized areas; (b) EBSD map of quartz orientations coloured parallel to the X direction, sample is plotted with hexagonal symmetry (6/mmm) to account for the effect of Dauphiné twins. Grain boundaries are identified by black bounding lines and subgrains are identified by white boundaries. (c) IPF's for subgrain (defined by a misorientation between 2 and 10°) boundaries and (d) grain (defined by a misorientation greater than 10°) boundaries. All IPF's are plotted in hexagonal 6/mmm symmetry with the same scale for multiples of uniform (m.u.d.) for each plot. (e) Colour key for IPF || X map.

In the high strain region (2) the original quartz grains appear bright in the SEM-CL image, and the recrystallized matrix in medium grey (blue luminescence, Figure III.23). Some relict parts of original quartz grains are present as porphyroclasts with bright luminescence surrounded by a matrix of recrystallized grains (separated mostly with high angle boundaries). The corresponding EBSD map shows a large number of recrystallized grains of 1-2 µm size with high angle boundaries (Figure III.24) in the matrix. The two large relict quartz grains (labelled as 1744 and 3542 in Figure III.23) show a number of subgrains with low angle boundaries (<10° misorientation from the large quartz porphyroclast) forming regions of subgrains between the porphyroclast and the recrystallized matrix. The subgrains do not show different luminescence from their host grains. The two large grains show different distributions of misorientation axes for their subgrains: [0001] (in 1744) and no preferred axis (in 3542). The high angle grain boundary misorientations (Figure III.23c & d) have rotation axes of [1-100] (in 3542) and axes between [1-100] and [-12-10] (in 1744). The subgrain sizes are in the same range as the sizes of small recrystallized grains (Figure III.24).

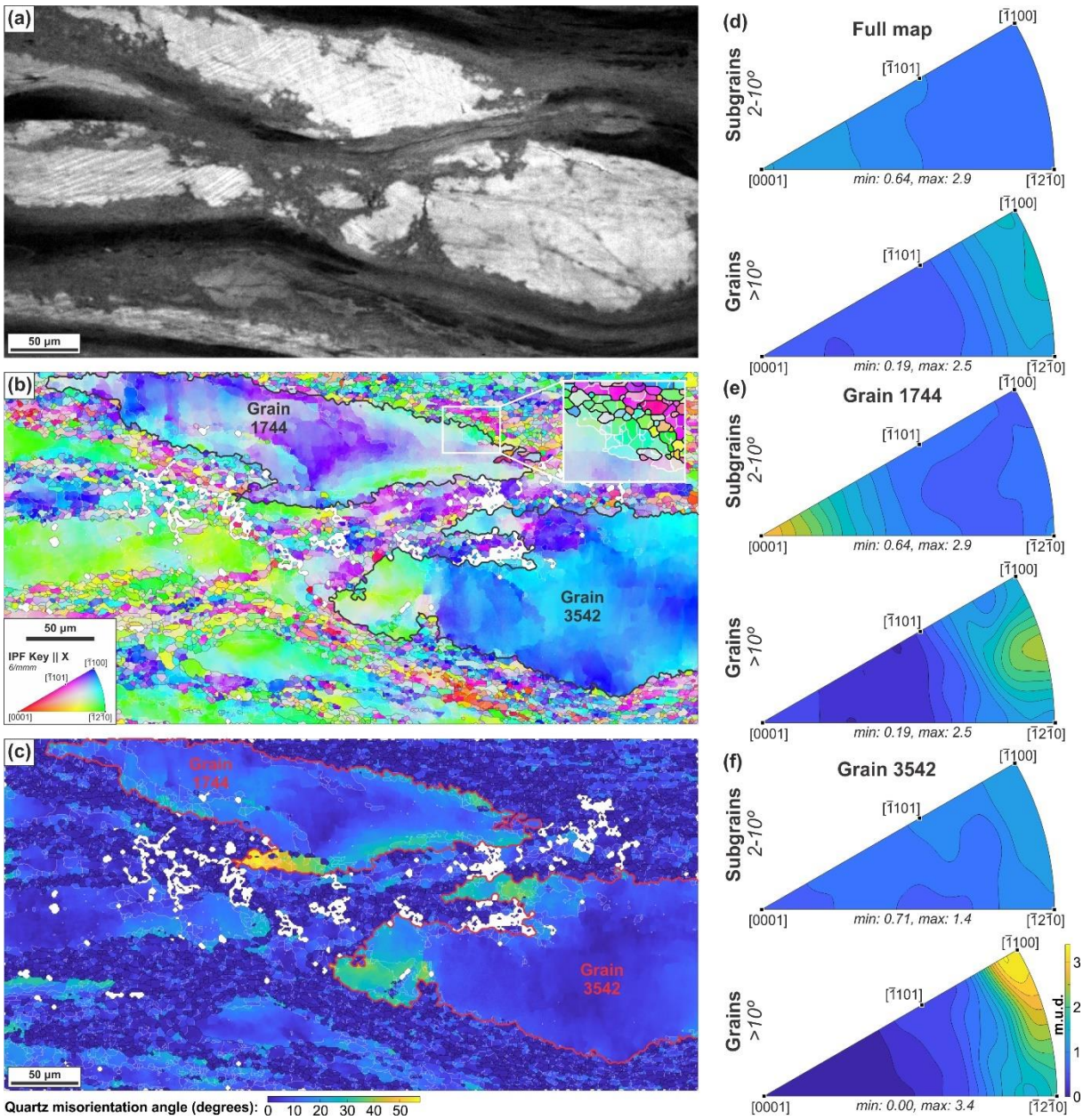

Figure III.23. Cathodoluminescence (CL) image, EBSD orientation map, misorientation map and inverse pole figures (IPF) for high strain sample OR56. (a) CL image with blue (380-515 nm) filter to highlight recrystallized areas. (b) EBSD map of quartz orientations coloured parallel to the X direction, sample is plotted with hexagonal symmetry (6/mmm) to account for the effects of Dauphiné twins. Grain boundaries are identified by black bounding lines and subgrains are identified by white boundaries (see detailed insert at the top right hand corner). (c) Misorientation map where blue shows low misorientation and yellow shows high misorientation relative to the mean grain orientation. Grains 1744 and 3542 are highlighted on the IPF (bold black) and misorientation (red) maps. (d-f) IPF's for subgrain (defined by a misorientation between 2 and 10°) and grain (defined by a misorientation greater than 10°) boundaries with the d) full map, (e) grain 1744 and (f) grain 3542. All IPF's are plotted in hexagonal 6/mmm symmetry with the same scale for multiples of uniform distribution (m.u.d.) for each plot.

The sizes of relict grains do not differ between the two microstructures (Figure III.24 and Table III.7). Relict grains are those grains that are located in a matrix of recrystallized grains. The original large porphyroclasts of the starting material typically are too large to be included completely in the EBSD maps. They are cut off at the margins of the map and therefore are not counted. The proportion of subgrains and recrystallized grains is much higher in the high strain sample OR56 than in the lower strain sample 546LN (Figure III.24).

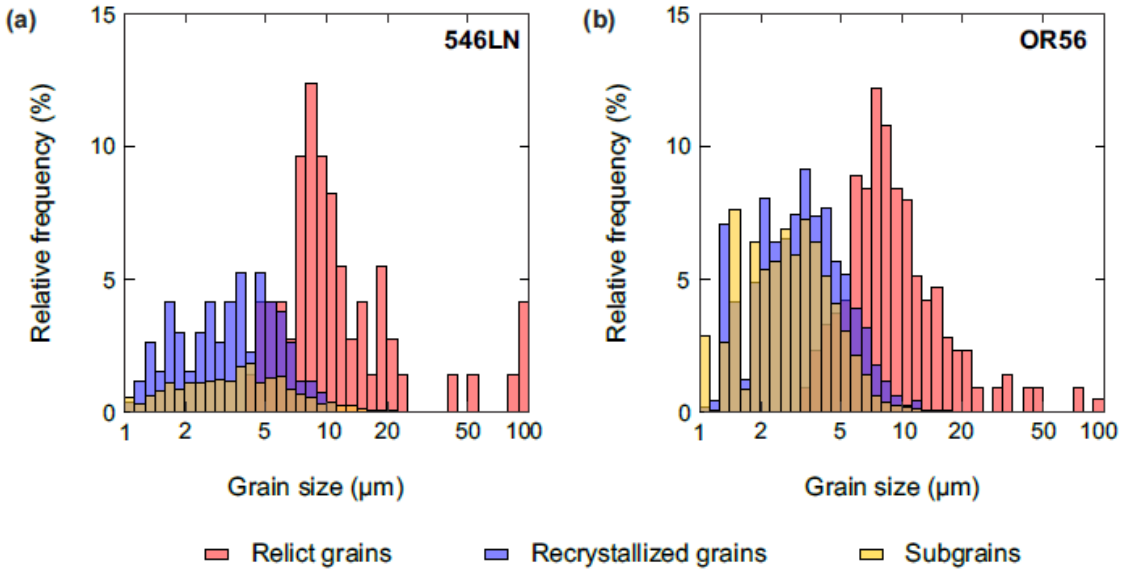

Figure III.24. Log_{10} grain size distributions for samples (a) 546LN and (b) OR56. Grain size distributions are separated into relict, recrystallized and subgrain populations.

Table III.7. Grain sizes obtained from EBSD analysis on 546LN (1000 MPa) and OR56 (2000 MPa, high-strained) samples (corresponding maps in Figure III.22 and Figure III.23).

Sample	546LN			OR32		
Grain sizes	Relict grains	Recryst. grains	Subgrains	Relict grains	Recryst. grains	Subgrains
Arith. Mean	7.967	3.789	3.854	9.030	3.323	2.683
Geom. Mean	7.595	3.291	2.884	8.314	2.825	2.121
RMS	8.613	4.282	4.879	9.853	3.824	3.871
Median	7.930	3.450	3.230	8.091	2.968	2.252
Mode	7 – 8	3.5 – 4 4.5 – 5	4 – 4.5	7 – 9	3.2 – 3.6	1.5 – 1.7
Std. Dev	2.603	2.003	2.993	3.955	1.894	2.790

III.4. Discussion

III.4.1. Deformation processes

Two deformation processes operating in all deformed samples are observed: cracking and crystal plastic deformation. Crystal plastic deformation is visually dominant in the microstructures, and the fact that the bulk sample strain can be calculated from the particle strain of original sand grains within a few percent error (Figure III.21, Table III.3 and Table III.6) documents that most of the bulk shortening of the samples is produced by crystal plastic deformation of individual original quartz grains. The undulatory extinction, deformation lamellae, and progressive subgrain rotation (Figure III.12 and Figure III.23) observed in the quartz grains are consistent with this observation. Thus, the dominant process of deformation in all samples is crystal plastic deformation, i.e., dislocation creep, as it has been documented previously for quartz under these pressure, temperature, strain rate conditions (e.g., Griggs, 1967; Jaoul et al., 1984; Kronenberg and Tullis, 1984; Hirth and Tullis, 1992).

Despite the dominance of plasticity, cracking takes place in all samples (Figure III.14, Figure III.15 and Figure III.16). Even though the crack morphology changes with confining pressure, there is one feature that is common to all observed cracking: the cracks accommodate or very little displacement, so that the cracks do not contribute significantly to the finite strain. Furthermore, the highest stresses attained in these experiments are all (except sample OR60) below the Goetze criterion ($\Delta\sigma \leq P_{conf}$). This criterion defines the upper differential stress limit of plastic or viscous deformation (brittle-plastic transition, Kohlstedt et al. (1995). In the presence of a pore fluid, this criterion has to be considered with some care (Hirth and Beeler, 2015; Beeler et al., 2016). The effect of pore pressure at high pressure and temperature conditions and small amounts of pore fluid is poorly investigated, but recent results by (Okazaki et al., 2021) indicate that at the porosity of our experiments (0.12 vol% using the density of H_2O from Larrieu and Ayers, 1997), the potentially expected reduction of differential stress by pore pressure effects should be in the range of experimental error (± 30 MPa, Holyoke and Kronenberg, 2010). Thus, the effective pressure coefficient α in $\sigma_{eff} = \sigma_n - \alpha P$ (see (Beeler et al., 2016) should be close to zero, so that dominant viscous deformation can be concluded from the mechanical data for all of the samples, consistent with the dominant deformation mechanism in the microstructures.

The observed mode-1-cracking (Figure III.15a) have geometries typical of those formed at low confining pressures (P_{conf}), (e.g., Paterson and Wong, 2005) and their occurrence in samples deformed at the lowest P_{conf} is not surprising. We expect that such cracks in the higher pressure samples have formed during early stages of the experiments by processes described previously in quartz experiments in the solid medium apparatus (Fitz Gerald et al., 1991; Chernak et al., 2009; Tarantola et al., 2010; Stünitz et al., 2017). These stepladder cracks (Figure III.15a&b) form as the result of a sequence of initial cracking and subsequent crack healing, during which dislocations are produced, followed by the glide of some of these dislocations. As a consequence, there is a zone of plastically shortened material that forms immediately adjacent to the crack. During unloading of the sample at the end of the experiment this zone expands and develops unloading cracks (Fitz Gerald et al., 1991; Stünitz et al., 2003, 2017). In this way the stepladder cracks document the initiation of crystal plastic deformation in which local brittle processes and healing of cracks play an important role.

The CL observations document that cracking is a ubiquitous feature during the dominant plastic deformation of quartz at high temperatures of 900°C. At higher confining pressures cracks tend to have a different geometry, but the interaction of cracking, crack healing, and plastic deformation is not expected to change. The microstructures also document that cracking without major displacement and thus without major kinematic contribution to strain accommodation may be common at high temperatures when the sample strain is dominantly accommodated by plastic mechanisms and flow stresses are low, especially at high confining pressure (Figure III.7).

III.4.2. Recrystallization processes

Recrystallized material in all samples is marked by blue luminescence. The blue luminescence colour is caused by a re-working (recrystallization) of quartz involving an interaction with the aqueous fluid facilitating an exchange of trace elements or producing defects during crystal

growth (e.g., Ramseyer et al., 1988; Götze et al., 2001). The blue luminescence has been attributed to Ti-incorporation into quartz (Spear and Wark, 2009; Bestmann and Pennacchioni, 2015). It is unclear how Ti-incorporation could have been achieved in the deformed samples in our experiments, because aa major Ti-source is lacking (although minute amounts of Ti-phases (rutile) are present in the starting material) and Ti-incorporation during recrystallization has been demonstrated to be slow and not producing homogeneous equilibrium compositions easily (Negrini et al., 2014).

A detailed analysis of the trace element exchange that causes the luminescence was not attempted here because it is beyond the scope of this study. However, a potential origin of luminescence by deformation-induced defects is very unlikely, these defects in quartz typically show red luminescence colours (Hamers et al., 2016, 2017), and this type of luminescence disappears after some electron beam irradiation (Bestmann, pers. comm.) – it is inferred that luminescence is caused by an interaction of the quartz with an aqueous fluid during the reconstitution of the material. Therefore, it is concluded that the luminescence observed in our samples is the result of exchange of trace elements with a fluid during recrystallization of quartz (facilitated by boundary migration). This makes luminescence a useful tool to trace recrystallized material in the deformed samples.

Some of the recrystallization takes place by progressive subgrain rotation as documented by EBSD maps (Figure III.22 and Figure III.23). Subgrains with misorientation angles of < 10° are dominantly rotated around the [c] axis. Such rotations can be produced by tilt walls made up of edge dislocations in the prism planes with <a> Burgers vectors or by twist boundaries in the basal plane made up of screw dislocations with <a> Burgers vectors (e.g., Trépied et al., 1980; Kilian and Heilbronner, 2017). Thus, this constitutes evidence for prism <a> or basal <a> slip. For misorientations >10°, rotation axes are parallel to [-1100] or between [-1100] and [-12-10], consistent with basal <a> or combined basal <a> and prism <c> slip. However, it is difficult to infer slip systems accurately for larger misorientation angles, because misorientations may partially be produced by grain boundary sliding processes once high angle boundaries are established.

The microstructures of subgrain boundaries within original quartz porphyroclasts and the immediately adjacent grains with high angle boundaries exhibit core-mantle structures (Figure III.23) and indicate progressive subgrain rotation as the dominant recrystallization mechanism for such grains. Subgrains with low angle boundaries and recrystallized grains with high angle boundaries do not differ systematically in size (Figure III.24).

The pressure, temperature, strain rate conditions of deformation of the samples are those of regime 2 creep according to Hirth and Tullis (1992), where rotation recrystallization is dominant. In these microstructures, the luminescence of the porphyroclasts and their subgrains does not change, so that non-recrystallized parts of porphyroclasts with subgrains still maintain the original luminescence of the porphyroclasts (Figure III.23a). This observation is consistent with the process of fluid exchange discussed by Negrini et al. (2014): formation of subgrain boundaries is a climb process, which does not a priori involve any grain boundary mobility and thus no interaction or exchange with a fluid phase. Once high angle boundaries are established, grain boundary mobility may lead to exchange with a fluid, producing different luminescence colours of these recrystallized grains.

A completely different process can form new grains in the deformed samples, too. Local cracking produces small new grains, especially at grain boundaries and in local cracks cutting through original quartz grains (Figure III.14, Figure III.15, Figure III.16 and Figure III.22). Some new grains show high angle misorientation relationships, whereas others show low angle relationships along the same zones of cracks (Figure III.22). The CL images indicate that in some cases, inner parts of clasts can still show the original luminescence of old grains, whereas rims and small grains nearby show the blue luminescence typical of reconstituted material (Figure III.22 Figure III.16b and Figure III.27). From these microstructures it is inferred that the small clasts in cracks have mobile boundaries that migrate and can produce a reconstitution (recrystallization) of the quartz and exchange trace elements to produce the different luminescence.

Local grain boundary migration processes have been inferred in previous studies (Stipp et al., 2002a, 2002b), where the migration process is inferred to be the first step. A second type of process is subsequently required to produce isolated new grains, because the local migration itself cannot isolate small new grains. This second step can be subgrain formation and/or local cracking (Stipp et al., 2002a, 2002b). In this study, we can observe the dominance of cracking in certain locations of the sample, where new grains form (Figure III.12 and Figure III.14). The sequence in this study is reversed: the cracking occurs first, followed by boundary migration to exchange with the fluid. It is proposed here that cracking and local boundary migration operate to produce microstructures that are consistent with what is termed “bulging recrystallization” in the literature (e.g., Bailey et al., 1962; Stipp et al., 2002a, 2002b; Stipp and Kunze, 2008). Local bulging may occur in these samples, too, so that probably not all the bulging recrystallization microstructures are induced by cracking.

The brittle origin of new grains in quartz and other silicates during plastic deformation has been described by van Daalen et al. (1999) in natural rocks, and by Stünitz et al. (2003, 2017) and Vernooij et al. (2006) in experiments. The CL-microstructures of these deformed samples indicate that the original clasts become modified by grain boundary migration processes after their initial formation by cracking. The misorientation of the small clasts with low angle boundaries shows a weak preference of c-axis rotation, whereas higher angle boundaries can be misoriented by c-, a-, or m-axis rotation (Figure III.22).

Grains with blue luminescence and faceted crystal shapes in open pore spaces tend to show oriented overgrowth in crystallographic continuity with original porphyroclasts (Figure III.16 and Figure III.22b) and have been described by Palazzin et al. (2018) for dilatant sites that act as small local reservoirs of fluids. These microstructures testify to the fast precipitation in dilatant sites and to the fact that there is excess H_2O in these samples (so that $a_{H2O} = 1$).

Thus, the samples deformed at different confining pressures show two types of recrystallization that takes place during deformation: (1) progressive subgrain rotation, and (2) crack-related local grain boundary migration that appears to be a type of bulging recrystallization. Both operate at the same time in samples, although the geometry of some cracks indicates an early origin of these.

III.4.3. Dislocation creep and stress exponent

From the conclusion of crystal plasticity, the operation of climb and dislocation glide are dominant deformation mechanisms, an n-value for the stress exponent of n = 3 to 5 would be expected for climb controlled creep (e.g., Paterson, 2012). Our strain rate stepping experiments have yielded n-values of ≈1.4 or ≈2, depending on whether the slowest strain rate steps are considered or not (Figure III.10). The variance of these values and the uncertainty of the slowest strain rate steps require more detailed investigation and a better data base to determine the stress exponent more accurately. However, the present determination of n≈2 suggests values of n < 3 and is consistent with observations of Fukuda et al. (2018) and Richter et al. (2018) in quartz aggregates. Both research groups have concluded a contribution of diffusion creep (including dissolution precipitation creep) to the viscous deformation of quartz. Richter et al. (2018) have observed weaker preferred orientation of quartz in fine grained aggregates, and the n≈2 values are explained by a combination of dislocation and diffusion creep deformation in their samples. The values obtained here are lower than n = 3 to 5, too, and therefore inconsistent with typical n-values for pure dislocation creep (Figure III.10).

The starting material in the samples of this study is coarse grained, so that diffusion creep in the starting material is very unlikely. However, some of the recrystallized material (in particular the cracked material in bulging-type microstructures) is fine grained, and some diffusion creep in the recrystallized material is conceivable. In addition, extensive exchange with aqueous fluid in the recrystallized material is observed in our samples, so that diffusive mass transfer processes are evident. Thus, it is inferred that the low n-values of n≈2 in our samples may also be explained by a combination of dislocation and diffusion creep processes. A potential explanation of dislocation accommodated grain boundary sliding (disGBS), as it is inferred in olivine (e.g., Hansen et al., 2012) is unlikely, because it would require the whole material to consist of fine grain sizes.

As diffusion creep is grain size dependent, its contribution to the deformation process is expected to increase with an increase of fine grained material or decrease with grain growth. In most of our samples, steady state deformation is observed (Figure III.7), as it is typical for the dislocation creep regime 2 as defined by Hirth and Tullis (1992). This observation suggests that an increase of recrystallized material does not increase the contribution of diffusion creep. The reason for this may be that grain growth (= migration processes) of very small grains produced by cracking takes these grains out of the diffusion creep field (producing an equilibrium recrystallized grain size). Continued microcracking may produce new very small grains, which in turn may grow. These processes appear to be in a steady state to produce steady state deformation. However, it is premature to speculate further on this aspect, and more research is required to investigate the relationship between cracking and recrystallization processes in more detail.

III.4.4. Effect of H_2O and pressure

The progressive lowering of the flow stress with increasing confining pressure in our samples is consistent with the initial observations by Kronenberg and Tullis (1984) and Mainprice and Paterson (1984). When the stresses (taken at 15% shortening, where all samples reach more

or less steady state flow stress, Figure III.7) are plotted as a function of the confining pressures, a power law relationship between the flow stress and the confining pressure of the form $\sigma_{diff} = 505522 P_c^{-1.113}\ MPa$ is found (Figure III.25), similar to that of Kronenberg and Tullis (1984). However, in this study, a coarse grained quartzite instead of fine grained novaculite was used (as in Kronenberg and Tullis, 1984), confirming that the process of pressure-dependent weakening in quartz is not dependent on grain size of the starting material.

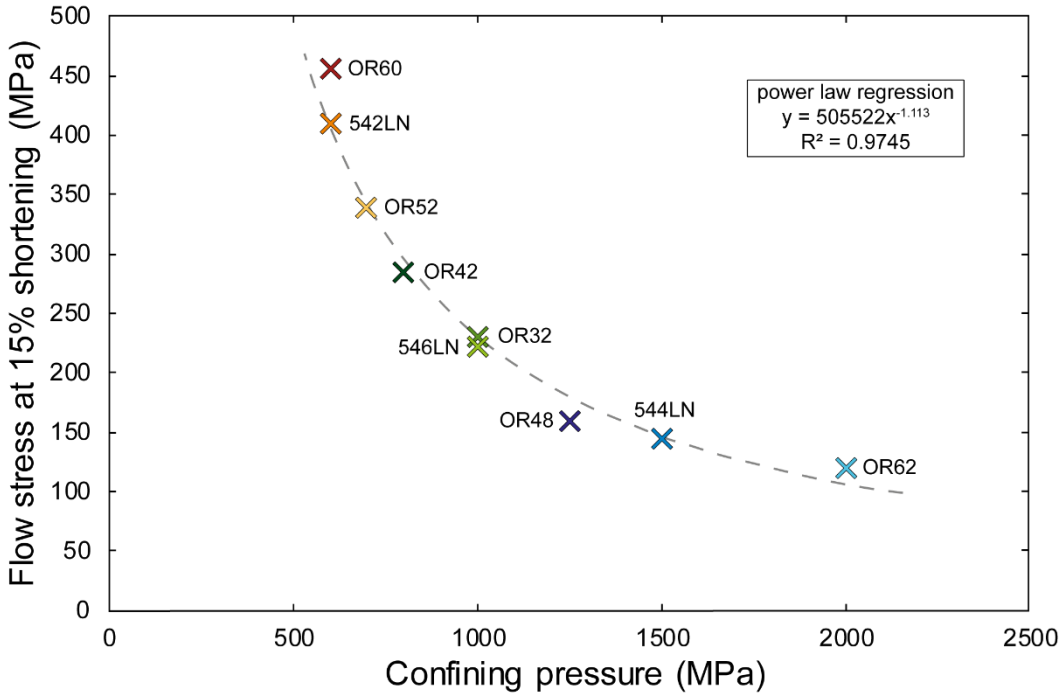

Figure III.25. A power law relationship connects the flow stresses (taken at 15% strain) and the confining pressures.

Kohlstedt et al. (1995) proposed that the pressure dependence of the rheology should be expressed as a fugacity term with exponent m in the quartz flow law. The log-log plot of flow stresses vs fugacity (Figure III.26) allows a fit of the m/n value, which is -0.46 for our samples. The plot in Figure III.26 shows other data from the literature together with our data, but the curve fit is only shown for data of this study. The r = m/n value is similar to that of Post et al. (1996) (-0.47), Kronenberg and Tullis (1984) (-0.5, as fitted by Post et al., 1996), Chernak et al. (2009)(-0.40), and of Holyoke and Kronenberg (2013) (-0.63, for their quartzite). It should be noted that experiments by Kronenberg and Tullis (1984) and Holyoke and Kronenberg (2013) were performed at 800°C, those of Post et al. (1996) and Chernak et al. (2009) at 900°C and 1500 MPa. A linear regression to all existing data yields almost the same slope as our data (0.458 vs. 0.460), but with a much lower correlation coefficient (0.71 vs. 0.93). This situation confirms the validity and applicability of our new data set.

The exponent m for the fugacity depends on the n-value of the stress exponent. In this study, a stress exponent of n≈2 is inferred (Figure III.10), which would result in an m-value of 0.92, or m≈1. An m-value of m=1 has been determined by Fukuda et al. (2018) for their n-value of 1.7, quite consistent with our results. If n-values closer to n=4 are chosen, as determined by Paterson and Luan (1990) and Gleason and Tullis (1995) and used in Hirth et al. (2001) and others, or n=2.7 (or n≈3, Rutter and Brodie, 2004a), as proposed by Tokle et al. (2019), the m-value would be m=1.84 or 1.24. However, the original m-value of 1 proposed by Kohlstedt et

al. (1995) is consistent with our results and those of Fukuda et al. (2018) for their m/n and n-values.

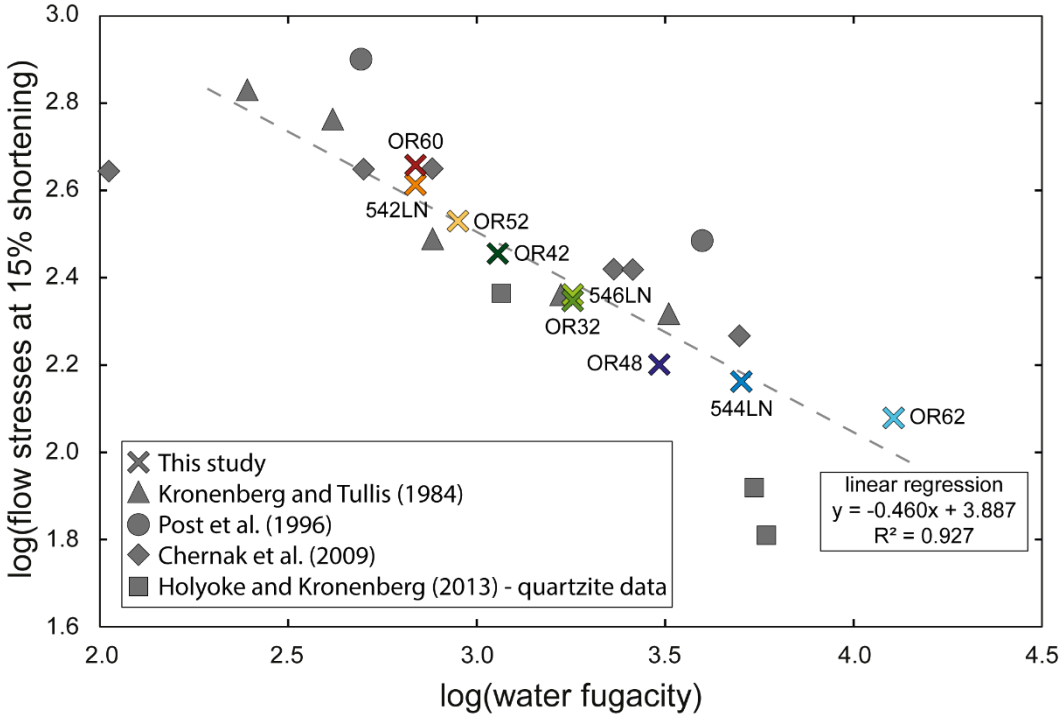

Figure III.26. Relationship between H_2O fugacity and flow stresses. The slope indicates a m/n coefficient of 0.46.

Lu and Jiang (2019) have proposed to correct the quartz flow law for pressure by using an activation volume term. This correction would have the opposite effect as the fugacity correction, and it is only meaningful to employ such a term once the activation energy is precisely determined. The presently existing data base of Q-values shows a large scatter (see compilation in, e.g., Richter et al. (2018), so that it appears to be necessary to determine Q accurately as a first step, before an activation volume term needs to be considered. We therefore do not consider the activation volume here.

III.4.5. What is the cause of sample weakening with increasing pressure?

In previous studies of quartz deformation with the presence of H_2O the weakening effect has been inferred as due to enhanced recrystallization or recovery (Tullis et al., 1979; Tullis and Yund, 1989). Subgrain boundary formation is enhanced in quartzites deformed with H_2O and grain boundary migration forms dislocation-free grains during dynamic recrystallization. Both processes are faster at higher confining pressures. The results presented here are consistent with this interpretation. The amount of recrystallized material increases with increasing confining pressure (Figure III.19), and this is the most obvious difference in the microstructures with increasing confining pressure, apart from a different crack geometry. The recrystallization in our samples involves grain boundary migration, which, in the presence of an aqueous fluid, can be described as a process of solution and precipitation with a very short transport distance of dissolved species across the boundary region. The solubility of SiO_2 increases non-linearly with increasing pressure (e.g., Manning, 1994, 2018), so that enhanced boundary migration rates are likely with increasing pressure because of enhanced solubility of quartz, provided that an efficient precipitation process can be identified. The precipitation may be favoured at local

dilatant sites which may form by grain boundary sliding and in which precipitation has been observed or inferred (Fusseis et al., 2009; Menegon et al., 2015; Okudaira et al., 2015; Précigout and Stünitz, 2016; Précigout et al., 2017, 2019). In fine grained material, grain boundary sliding is an important mechanism to accommodate shape changes of grains induced by plastic deformation of grains (glide of dislocations) and to adjust for the plastic strain incompatibilities as a consequence of an insufficient number of slip systems in silicates (compared to metals). The low n-values (Figure III.10) in strain rate stepping experiments are consistent with grain boundary sliding and diffusion creep components of deformation. Grain boundary sliding and local dilatancy in the form of cavitation is likely to occur in these aggregates and may cause immediate oversaturation of the fluid and precipitation of quartz. Overgrowth of quartz seams on quartz grains is observed in larger dilatant sites (Figure III.16a). Replacement of quartz material during grain boundary migration is evident from the change of CL colours in the recrystallized material, indicating boundary migration, by dissolution, precipitation, and exchange of elements with a fluid.

It has been pointed out above that once high angle boundaries are established, the distinction of grains formed by progressive subgrain rotation and those produced from initial cracking is possible (Pongrac et al., in prep.), but it is not easy, because their size is similar, and they all show bright luminescence. It is inferred that in this material the weakening effect takes place as a consequence of increased confining pressure. The inference that the pressure-dependent H_2O weakening is caused by grain boundary processes is supported by the observation by Holyoke and Kronenberg (2013) that the pressure dependence of the flow stress in polycrystalline aggregates is greater than in single crystals. Consequently, these authors have attributed the weakening effect to recrystallization/recovery processes (Tullis and Yund, 1989) at grain boundaries, too.

The plot in Figure III.26 suggests that the pressure effect of H_2O weakening could be greater at low pressure than at high pressures. A potential greater m-value may be caused by a change in n- or r- values in m = r/n. The determination of the stress exponent is not precise enough at this stage to decide whether a constant n-value would require an intrinsic effect of the H_2O fugacity or whether the potentially changing pressure dependence of flow stress could be caused by a change in the stress exponent n.

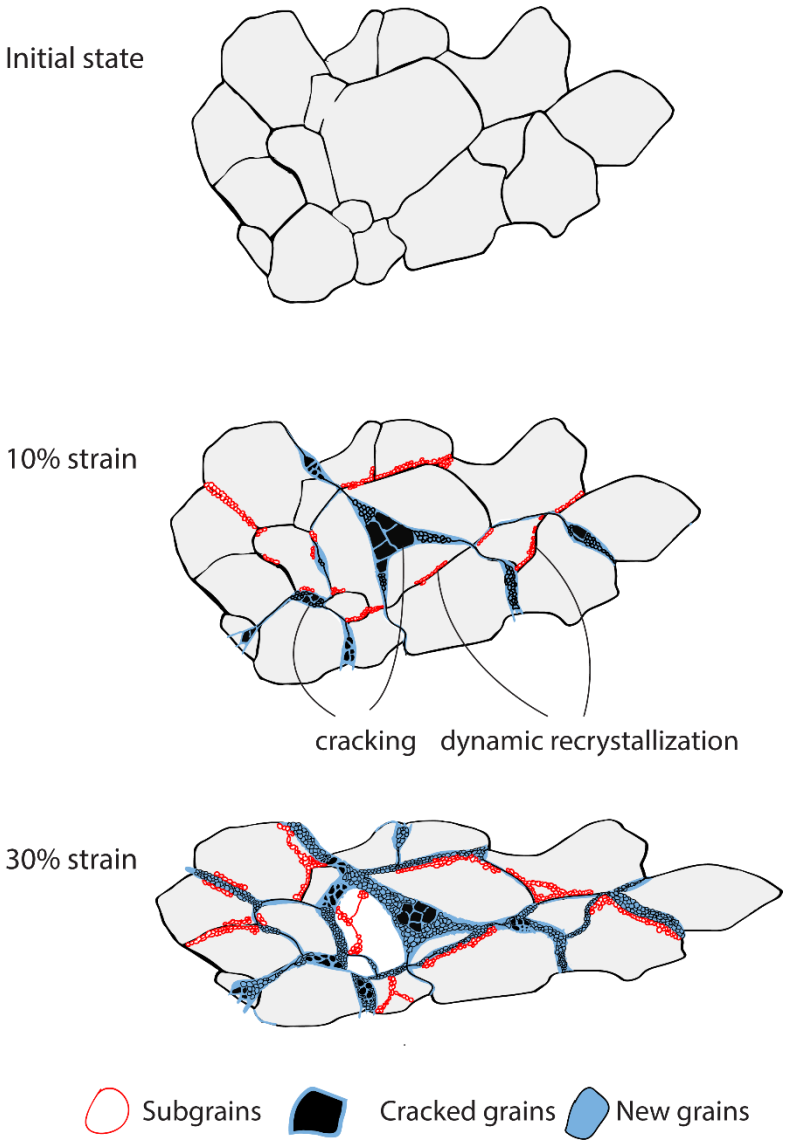

Figure III.27. Sketch of the grain assemblage evolution during deformation.

III.4.6. Geological application

The lowering of quartz flow stresses with increasing confining pressures that has been documented since the study by Kronenberg and Tullis (1984) - also documented in this study - suggests that in subduction channels at high pressure the strength of quartz dominated lithologies is expected to be very low. Low stresses for deformation in subduction zones have been inferred by Stöckhert et al. (1997, 1999), Stöckhert and Renner (1998), Stöckhert (2002) and Wassmann and Stöckhert (2013), partly based on different deformation mechanisms. This study confirms that even for dislocation creep, where stresses tend to be higher than for diffusion creep, flow is expected to take place at very low stresses at high confining pressures of 2 GPa and higher.

The recrystallization mechanism of bulging recrystallization in quartz is usually observed at low temperature conditions or the onset of crystal plastic deformation (e.g., Stipp et al., 2002a, 2002b). The interaction of cracking and local grain boundary migration indicates that some new grains in this recrystallization process can be generated by cracking. One consequence of this process is that the host control in new grain nucleation will be more difficult to determine,

because small rotation of new grains is likely, (e.g., van Daalen et al., 1999) but the rotation sense and misorientation relationship is not necessarily clear and is not dependent on slip systems.

Cracks are abundant in high pressure samples deformed by plastic mechanisms at high temperature, in spite of the low deviatoric stress (~ 100 MPa) and the high normal stress acting on any potential fracture plane ($P_c \approx 2$ GPa) – there is no or very little displacement on these cracks. The interaction of cracking, crack healing, and plasticity has been shown by Fitz Gerald et al. (1991) and Stünitz et al. (2017). These observations suggest that in natural rocks, microcracks may play an important role in the initiation of plastic deformation and during dynamic recrystallization, even for the deep levels of the crust where high temperatures enable viscous deformation at low deviatoric stresses.

III.5. Conclusions

The deformation of quartzites in the presence of 0.1 wt.% of added H_2O shows decreasing flow stresses with increasing confining pressure. A r-value of 0.46 can be fitted to the fugacity data, resulting in a m-value of ≈1 for the fugacity coefficient and a n-value of ≈2. In addition, the following observations have been made:

1. The dominant deformation process is crystal plasticity in original quartz grains, so that the strain analysis of quartz grains matches the bulk sample strain with an error of a few percent. Dynamic recrystallization and recovery processes are observed, too, so that the dominant deformation mechanism is dislocation creep. Some cracking occurs during plastic deformation, but as the cracks do not display significant offset, their contribution to the bulk strain is negligible.

2. Dynamic recrystallization of the deforming quartz grains takes place by progressive subgrain rotation and by local grain boundary migration. The grain boundary migration affects small clasts produced by cracking as well as former subgrains once high angle boundaries have been established. The recrystallized material acquires a different luminescence colour (blue), which can be used to track the recrystallized material in the microstructures. The processes indicate that nucleation of new grains may take place by cracking (in addition to other processes) and appears to be an important part of a process that is termed “bulging recrystallization”.

3. The stress exponent n is approximatively equal to 2, when some diffusive mass transfer is important during dislocation creep. This contribution is likely to be fluid-dependent or fluid enhanced.

4. The amount of recrystallized material increases with increasing confining pressure. It is inferred that the increasing confining pressure has an enhancing effect on the grain boundary migration rate and thus recrystallization rate.

IV. Evolution of H_2O contents and speciation in natural quartz aggregates deformed in presence of H_2O

This chapter focuses on the H_2O concentrations, OH species and H_2O transfers linked to the experimental deformations performed on the studied material. For this purpose, Fourier Transform Infrared Spectroscopy (FTIR) was used to measure grain interiors and boundaries both on starting and experimental materials.

The results obtained from infrared spectroscopy measurements will be presented after a correction for overlapping epoxy (Araldite®) absorption. The Araldite® correction made on the spectra and its consequences will be presented and discussed in order to select the reliability of the infrared data that will next be described.

Two different aspects obtained from FTIR spectra will be treated: the H_2O contents and then the H_2O speciation. The H_2O contents have been calculated from the broad H_2O band centred at 3400 cm^{-1} in the infrared spectra due to stretching of molecular H_2O. The OH speciation is established from the presence of discrete absorption bands in the 3000 – 3800 cm^{-1} range that are assigned to different hydrogen defects (e.g., substituting or compensating ions).

The obtained results will finally be discussed and compared with previous publications on both experimental and natural systems.

IV.1. H_2O contents

FTIR spectra have been recorded on starting material and on samples deformed at different confining pressures. The application of increasing confining pressures resulted in a decrease in mechanical strength of the samples (see details in the previous chapter, part III.2.1)

The measurements have been made on grain interiors (centre of grains) and on grains boundaries (at the junction between two grains). For some samples deformed at 2000 MPa, measurements were also made on regions showing small grains (recrystallized/cracked material).

The spectra were corrected for a flat baseline and for eventual presence of H_2O due to Araldite®. H_2O contents have been calculated from Beer-Lambert law, using the Paterson (1982) calibration (see the Methodology chapter part II.3.2.5 for details).

In the following, the H_2O contents will be presented in molar proportions as the number of H atoms per million of Si atoms ($H/10^6$ Si). The data converted in weight proportions (ppm H_2O) are available in Table VII.2 to Table VII.4 (Appendix part VII.4.2).

Unfortunately, some epoxy impregnation had been used for the samples to assure their integrity after deformation. This epoxy (Araldite) produces some absorption spectra overlapping some regions of interest in quartz. In order to correct the spectra from the influence of the Araldite® (especially in the broad H_2O region) a correction method was developed. This method uses the deconvolution of measured pure epoxy spectra that shows both CH and H_2O signals.

IV.1.1. Araldite® correction

As Araldite® epoxy was used during the thick section preparation, most of the infrared spectra recorded on the quartzite samples contained signals coming from the epoxy (for more details, refer to the Methodology chapter, part II.3.2.2).

Taking into account the fact that quartzite spectra do not show CH bands, contaminated spectra have been identified. The quartzite spectra could then be corrected by subtracting a modelled epoxy spectrum.

To characterize the influence of the epoxy correction on the H_2O concentration calculation, the percentage of the area corrected in the 3000 – 3800 cm^{-1} range was determined. Three classes were established: (i) all the spectra, (ii) spectra for which the area of H_2O related to epoxy corrected represents more than 50% of the total H_2O area and (iii) spectra for which the H_2O area corrected represents more than 30% of the total H_2O area. “Area” here refers to the area between the absorption spectrum curve and the fitted baseline.

The influence of the Araldite® correction varies according to the samples and to the areas measured. Table IV.1 indicates the number and percentage of spectra for which the area corrected represents more than 30% or more than 50% of the total H_2O area compared to the total number of spectra for grain interiors and grain boundaries.

Table IV.1. Number of spectra impacted by the Araldite® correction for each sample. The number of spectrum affected is indicated between brackets.

Sample name	Number of data		Area corrected > 30%		Area corrected > 50%	
	Grain interiors	Grain boundaries	Grain interiors	Grain boundaries	Grain interiors	Grain boundaries
TQ-1	71	150	0	(10) 6.7%	0	0
TQ-2	67	66	(21) 31.3%	(27) 40.9%	(2) 3%	(3) 4.6%
542LN	73	61	0	0	0	0
OR60	101	80	(80) 79.2%	(75) 93.8%	(41) 40.6%	(49) 61.3%
OR52	119	115	(51) 42.9%	(79) 68.7%	(27) 22.7%	(37) 32.2%
OR33	112	137	(62) 55.4%	(105) 76.6%	(31) 27.7%	(59) 43.1%
OR42	116	120	(54) 46.6%	(79) 65.8%	(30) 25.9%	(46) 38.3%
OR73	77	79	(52) 67.5%	(61) 77.2%	(28) 36.4%	(44) 55.7%
546LN	140	141	(2) 1.4%	(124) 87.9%	0	0
OR32	134	166	(75) 56.0%	(143) 86.1%	(41) 30.6%	(92) 55.4%
OR59	70	70	(18) 25.7%	(30) 42.9%	(3) 4.3%	(3) 4.3%
OR48	106	129	(29) 27.4%	(82) 63.6%	(9) 8.5%	(38) 29.5%
544LN	130	129	(2) 1.4%	(2) 1.6%	0	0
OR63	81	81	(4) 4.9%	(11) 13.6%	(1) 1.2%	(3) 3.7%
OR64	108	115	(17) 15.7%	(30) 26.1%	(6) 5.6%	(10) 8.7%
OR57	96	126	0	(1) 0.8%	0	0
OR62	105	120	(2) 1.9%	(6) 5%	(1) 1%	(4) 3.3%
OR54	124	61	(4) 3.2%	(12) 19.7%	(1) 0.8%	(4) 6.6%
OR50	106	50	0	(3) 6%	0	0
OR56	71	41	(4) 5.6%	(9) 22%	(1) 1.4%	(4) 9.8%
OR66	53	58	(2) 3.8%	(1) 1.72%	(1) 1.9%	0

Regardless of the amount of area corrected, for almost all samples, the percentage of spectra corrected is higher in the grain boundary region than in the grain interiors. When considering one sample, if the number of contaminated spectra for grain boundaries is high, the number of contamination for the grain interiors is, most of the time, high too (positive trend in Figure VII.46 in Appendix part VII.4.1). This indicates that the amount of epoxy present is relative to the sample itself. The number of spectra corrected highly increase with the percentage of area corrected taken into account.

Considering significant contamination of a spectrum when the area correction is superior to 50% (taking into account the highest percentage for grain interiors or grain boundaries), 6 samples show no contamination (TQ-1, 542LN, 546LN, 544LN,OR57 and OR50), 8 show between 0 and 10% of spectra contaminated (TQ-2, OR59, OR63, OR64, OR62, OR54, OR56 and OR66), 1 between 20 and 30% (OR48), 2 between 30 and 40% (OR52 and OR42), 1 between 40 and 50% (OR33), 2 between 50 and 60% (OR73 and OR32) and 1 more than 60% (OR60).

Considering significant contamination of a spectrum when the area correction is superior to 30% (for grain interiors or grain boundaries), only 1 sample shows no contamination (542LN), 6 show between 0 and 10% of spectra contaminated (TQ-1, 544LN, OR57, OR62, OR50, and OR66), 2 between 10 and 20% (OR63 and OR54), 2 between 20 and 30% (OR52 and OR42), 2 between 40 and 50% (TQ-2 and OR59), 3 between 60 and 70% (OR52, OR42 and OR48), 2 between 70 and 80% (OR33 and OR73), 2 between 80 and 90% (546LN and OR32) and 1 more than 90% (OR60).

The variable number of spectra contaminated depending on the samples suggests that the influence of the Araldite® correction on the mean H_2O contents calculations is variable depending on the samples and areas measured.

The percentage of spectra with a H_2O area corrected more than 30% due to Araldite® correction has a decreasing trend with confining pressure (Figure IV.1). Samples deformed at low confining pressure (600 – 1000 MPa) present more spectra corrected than samples deformed at high confining pressures (1500 – 2000 MPa). As samples show more cracks with lower confining pressure, the Araldite® is certainly more ubiquitously incorporated.

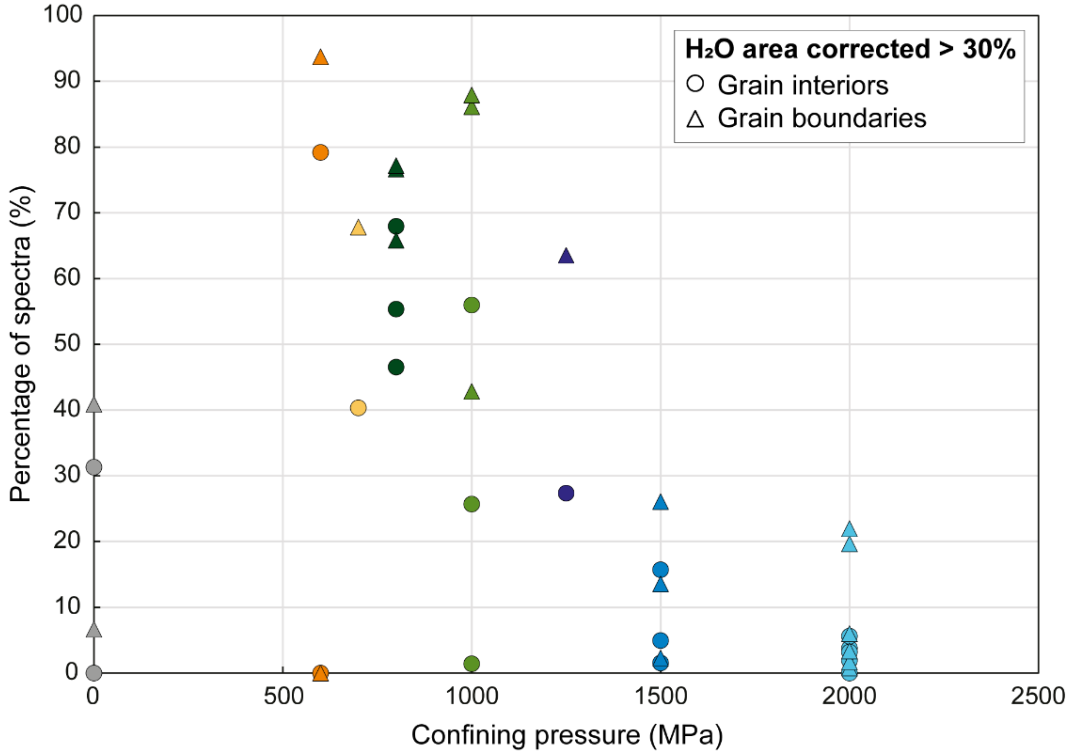

Figure IV.1. Percentage of spectra with a correction of the H_2O area due to Araldite® superior to 30% of the total H_2O area as a function of the confining pressure. The percentage of spectra affected for the deformed samples decreases with increasing pressure.

The mean H_2O contents have been calculated for the three classes considered. For each sample, the mean H_2O contents calculated for (i) all the data, for data restricted to spectra where area correction is lower than 30% (ii) or lower to 50% (iii) are shown in Figure IV.2 . As previously supposed, it appears that – independently of the number of spectra affected by the correction – the influence is variable according to the samples.

For the great majority of samples, the influence of the percentage of H_2O area corrected is very low, but for some of them it is not negligible. The calculated mean H_2O contents as a function of the area corrected are presented in the Table VII.1 in Appendix part VII.4.1.

The removal of spectra with more than 50% or 30% of the total area corrected has either no effect or leads to an increase of the mean. This indicates that the spectra with a high percentage of area corrected have a lower mean than the one taking into account all the data.

Moreover, removing the spectra for which the H_2O area of Araldite was superior to 30% of the total H_2O area has a larger effect on the mean than removing the ones with a percentage of

area corrected superior to 50%. This is partly explained by an upper number of spectra taken into account in the former class than in the latter.

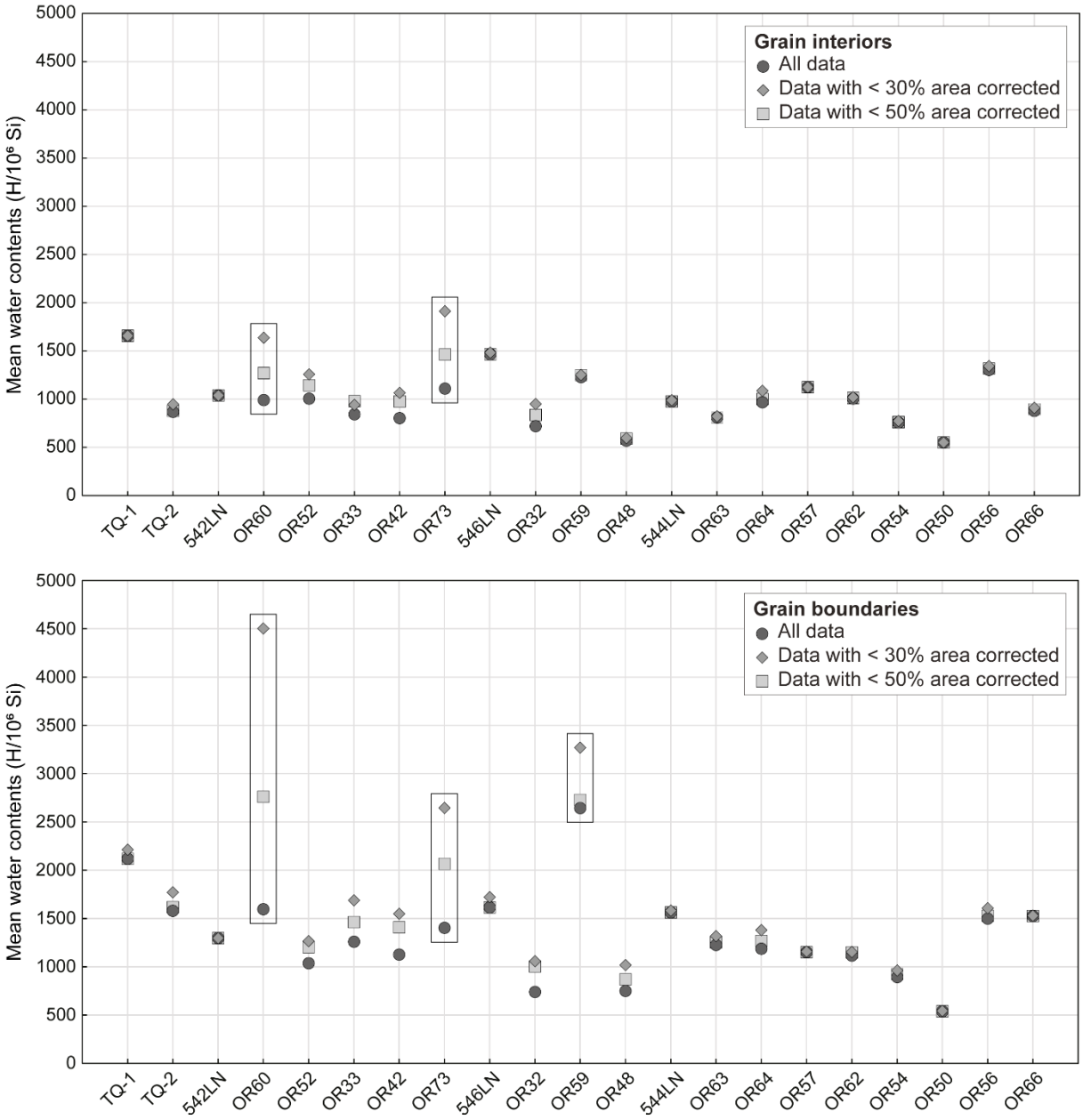

Figure IV.2. Mean H_2O contents ($H/10^6$ Si) for grain interiors and grain boundaries as a function of the percentage of H_2O area corrected. The data showing too much difference and excluded from the study are indicated by a rectangle.

In order to determine the reliability of the data both the absolute and percentage difference between the three calculated means have been considered.

For 11 of the samples, the influence of the area correction (< 50 or < 30%) on the mean H_2O content calculated is inferior to 10% (and to 110 $H/10^6$ Si) both for grain interiors and grain boundaries (TQ-1, 542LN, 546LN, 544LN, OR63, OR57, OR62, OR54, OR50, OR56 and OR66).

For TQ-2 sample, the influence on the mean is also below 10% but only for grain interiors, for grain boundaries it is between 0 and 15% (but below 200 $H/10^6$ Si).

For OR64 sample, the influence on the mean is below 10% when removing samples with an area corrected > 50% and between 10 and 20% (and below 200 H/10^6 Si) when removing samples with an area corrected > 30%.

For all the samples cited before, the influence of the correction is considered as low. Thus, the mean H_2O contents calculated from the whole set of data will be considered in the rest of the chapter.

For the other samples, the mean variation is below 32.5% (and 270 H/10^6 Si) for the grain interiors except for the samples OR60 (65.3%) and OR73 (72.1%) and for the grain boundaries, the mean variation is below 37.5% (and/or 430 H/10^6 Si) except for the two same samples OR60 (181.9%) and OR73 (88.5%) and the sample OR59 (626 H/10^6 Si).

As the errors presented by these last three samples are significant, it has been chosen to remove them from the studied dataset.

IV.1.2. Starting material

Two samples from two different blocks of starting material have been measured: TQ-1 (starting material for samples OR32 to OR62) and TQ-2. For both samples, grain interiors and grain boundaries have been measured and for TQ-2 additional measurements have been made on cement and at triple junctions.

Starting material TQ-1

The calculated statistics for H_2O contents of grain interiors and grain boundaries for starting material TQ-1 are presented in the Table IV.2.

Table IV.2. Molar proportion (H/10^6 Si) of H_2O content in grain interiors and grain boundaries for starting material sample TQ-1.

Molar proportion (H/10^6Si)	Grain interiors	Grain boundaries
Number of data	71	150
Mean	1659	2120
Median	1404	1965
Standard deviation	1139	1137
Min value	156	501
Max value	5488	7567

The mean H_2O content is higher in the grain boundary region than in the grain interiors (difference of 461 H/10^6 Si). The related histogram (Figure IV.3) indicates a broad dispersion of the measurements, ranging from 156 to 5488 H/10^6 Si for the grain interiors and from 501 to 7567 H/10^6 Si for the grain boundaries.

For grain interiors, the mode is in the 250 – 500 H/10^6 Si range (at 15.5%) whereas for grain boundaries it is in the 1000 – 1250 H/10^6 Si range (at 12%).

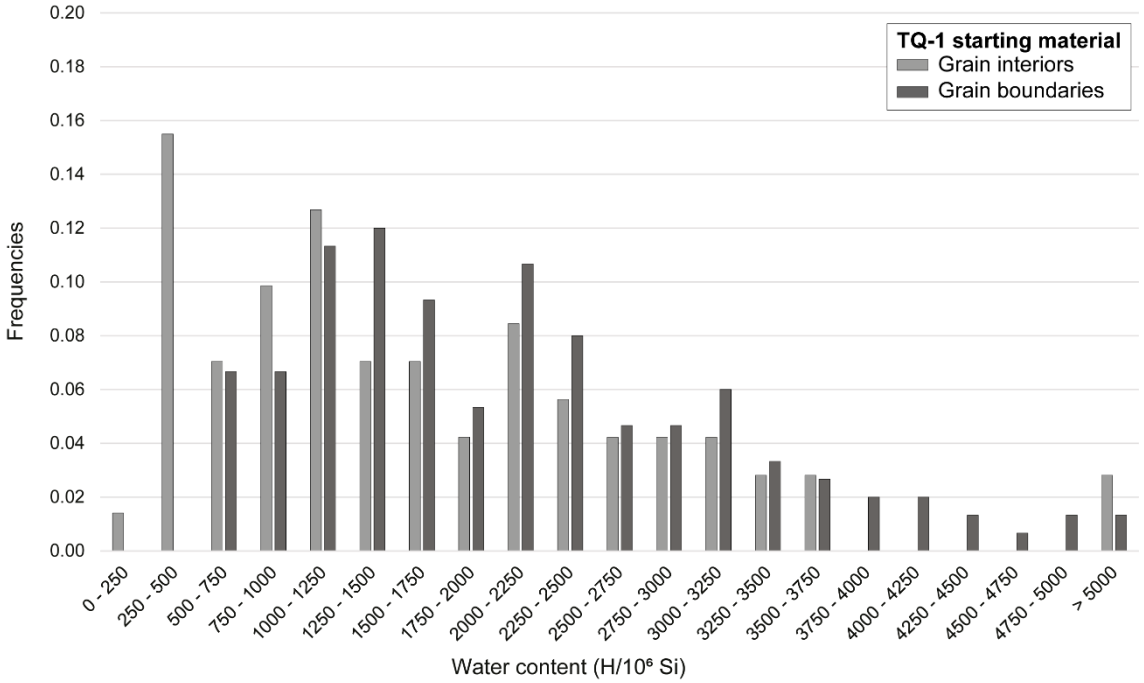

Figure IV.3. Histogram showing the dispersion of H_2O contents ($H/10^6$ Si) for grain interiors and grain boundaries of starting material TQ-1. The maximum frequency is in the 250 – 500 $H/10^6$ Si range for the grain interiors and in the 1250 – 1500 $H/10^6$ Si range for the grain boundaries.

Starting material TQ-2

For this second sample of starting material, cement and triple junctions have been measured in addition to the grain interiors and grain boundaries, the data are presented in the Table IV.3.

Table IV.3. Molar proportion ($H/10^6$ Si) of H_2O content in grain interiors, grain boundaries, cement and triple junctions for starting material sample TQ-2.

Molar proportion ($H/10^6$Si)	Grain interiors	Grain boundaries	Cement	Triple junctions
Number of data	67	66	69	69
Mean	869	1579	1727	1815
Median	1424	1424	1593	1733
Standard deviation	653	705	561	774
Min value	72	461	608	430
Max value	3470	3870	3427	5323

The mean H_2O content of grain interiors (869 $H/10^6$ Si) is almost twice times lower than that of grain boundaries, cement and triple junctions (1579, 1727 and 1815 $H/10^6$ Si, respectively), but the median is similar to the one of grain boundaries. The dispersion of the data ranges from tens or hundreds to thousands of H per 1 million of Si.

The mean H_2O content of the triple junctions (intersection of 3 grains) is higher than the grain boundaries (intersection of 2 grains).

The histogram associated to H_2O contents distribution of TQ-2 sample is presented in Figure IV.4. For the grain interiors, the mode is in the 250 – 500 $H/10^6$ Si range (at 22.4%), for grain boundaries it is in the 1000 – 1500 $H/10^6$ Si range (at 16.7%) and for both cement and triple junctions it is in the 1250 – 1500 $H/10^6$ Si range (at 21.7% and 14.5% respectively).

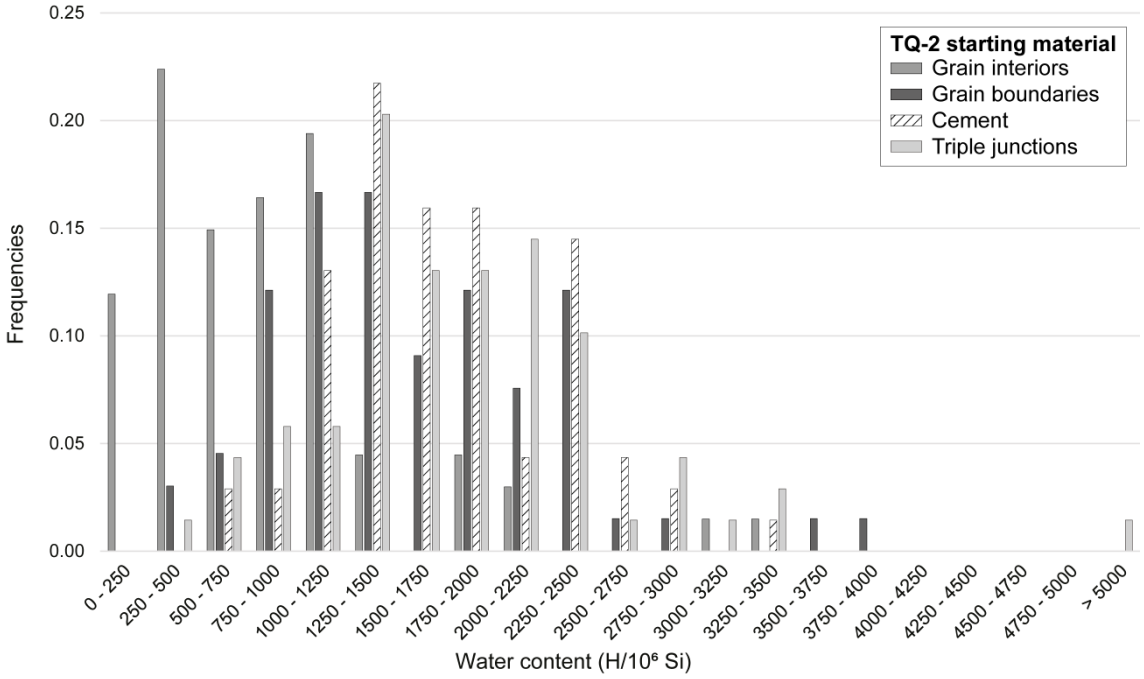

Figure IV.4. Histogram showing the dispersion of H_2O contents ($H/10^6$ Si) for grain interiors, grain boundaries, cement and triple junctions of starting material sample TQ-2. The maximum frequency is in the 250 – 500 $H/10^6$ Si range for grain interiors, 1000 – 1500 $H/10^6$ Si range for grain boundaries, and in the 1250 – 1500 range for both cement and triple junctions.

Comparison between the two starting material samples

When comparing the two starting material samples, the mean H_2O content is lower for TQ-2 sample for both grain interiors and grain boundaries (Figure IV.5). For grain interiors, the difference between the mean H_2O contents is 790 $H/10^6$ Si and for grain boundaries, it is 540 $H/10^6$ Si.

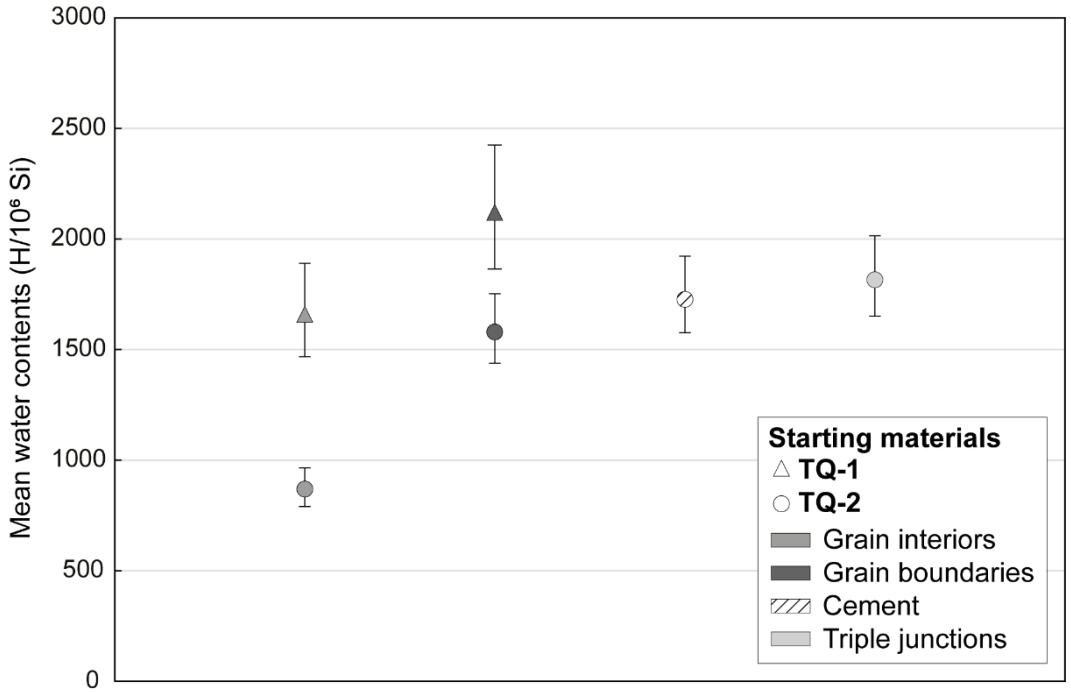

Figure IV.5. Plot of the mean H_2O contents ($H/10^6$ Si) for the two samples of starting material studied: TQ-1 and TQ-2. The mean H_2O contents of sample TQ-1 for grain interiors and grain boundaries are higher than H_2O contents of sample TQ-2.

For the H_2O content distributions (Figure IV.6), even if the mean H_2O contents are different for the two starting materials, the ranges of maximum frequency are comparable. For grain interiors, the maximum frequency range is 250 – 500 $H/10^6$ Si for both starting materials. For grain boundaries, the maximum frequency range is (1000) 1250 – 1500 $H/10^6$ Si.

The global shapes of the histograms are quite similar, especially when considering the low H_2O contents regions. For grain interiors, the same second mode at 1000 – 1250 $H/10^6$ Si is observed in the two samples.

The dispersion of TQ-1 H_2O contents is higher than for TQ-2 sample for which the data are less spread around the mean. These results are also shown by the standard deviation values that are higher for TQ-1 sample than for TQ-2.

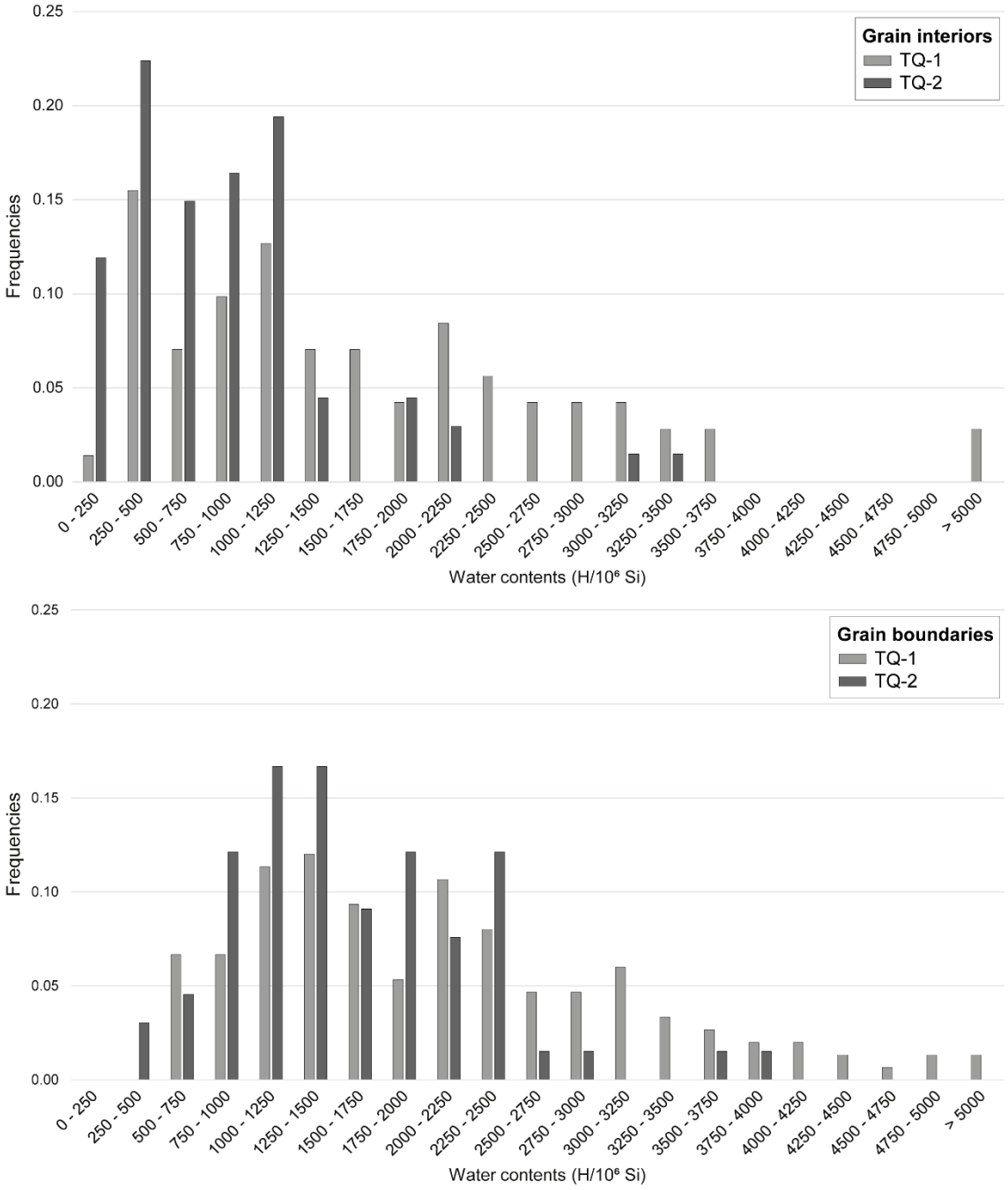

Figure IV.6. H_2O contents distributions for grain interiors and grain boundaries of starting material samples TQ-1 and TQ-2. Although that for both grain interiors and grain boundaries, the mean H_2O contents of TQ-1 sample are higher than for TQ-2, the two samples present the same ranges of maximum frequencies (250 – 500 H/10^6 Si for grain interiors and 1250 – 1500 H/10^6 Si for grain boundaries).

IV.1.3. Deformed samples

For deformed samples, measurements have been made on the top of the sample (low strain part, where the deformation is less pronounced) and in the middle part of the sample (high strain part, where the deformation is more visible and witnessed by elongated grains). For hot-pressed samples (not deformed), measurements of grain interiors and grain boundaries have been made in the central part.

Image analysis performed on some deformed samples show no systematic strain difference between the top and the middle part of the samples (refer to the previous chapter part III.3.3.2 and to the Appendix Figure VII.45 part VII.3.13). Thus, for those samples where the strain difference was not significant, only two categories of measurements are presented: grain interiors and grains boundaries without taking into account their relative position into the sample.

For four samples a significant difference in strain across the sample has been established. For these samples, two zones are considered: a low strain part (at the top) and a high strain part (~at the middle). These four samples are: OR42, 546LN, 544LN and OR62, deformed respectively at 800, 1000, 1500 and 2000 MPa confining pressure.

IV.1.3.1. Grain interiors and grain boundary mean H_2O contents

The H_2O contents of the samples either shortened to ~30% at 10^{-6} s^{-1} or hot-pressed for which only two categories are made (grain interiors and grain boundaries), are presented in the Table IV.4.

Table IV.4. Molar proportion ($H/10^6$ Si) of H_2O content in grain interiors and grain boundaries of samples for which no apparent strain partitioning between top and middle part is observed.

Sample	Molar proportion ($H/10^6Si$)	Grain interiors	Grain boundaries
542LN 600 MPa	Number of data	73	61
	Mean	1040	1297
	Median	760	1063
	Standard deviation	875	860
	Min value	84	196
	Max value	4072	5251
OR52 700 MPa	Number of data	119	115
	Mean	1006	1037
	Median	793	960
	Standard deviation	765	535
	Min value	79	167
	Max value	4584	3097
OR33 800 MPa	Number of data	112	137
	Mean	845	1260
	Median	673	1068
	Standard deviation	574	845
	Min value	139	253
	Max value	3370	6950
OR32 1000 MPa	Number of data	134	166
	Mean	722	739
	Median	550	528
	Standard deviation	586	600
	Min value	59	66
	Max value	3213	4505

OR59 1000 MPa Hot-pressing	Number of data	70	
	Mean	1228	
	Median	1132	
	Standard deviation	863	
	Min value	78	
	Max value	3551	
OR48 1250 MPa	Number of data	106	129
	Mean	570	750
	Median	475	638
	Standard deviation	400	593
	Min value	120	100
	Max value	2216	4966
OR63 1500 MPa	Number of data	81	81
	Mean	813	1227
	Median	610	944
	Standard deviation	718	1009
	Min value	80	201
	Max value	4183	4717
OR64 1500 MPa	Number of data	108	115
	Mean	969	1187
	Median	770	1068
	Standard deviation	844	834
	Min value	90	75
	Max value	5412	4652
OR57 2000 MPa	Number of data	96	126
	Mean	1125	1151
	Median	946	908
	Standard deviation	792	1037
	Min value	149	233
	Max value	4211	8421
OR66 2000 MPa Hot-pressing	Number of data	53	58
	Mean	880	1525
	Median	631	1214
	Standard deviation	825	1010
	Min value	86	172
	Max value	4330	4504

For all samples, the mean H_2O content calculated for grain boundaries is always higher than the grain interior one. This is best observed on Figure IV.7 where the mean H_2O content of grain interiors is plotted against grain boundaries ones, all the data lies above the 1:1 line. However no clear trend appears between grain interiors and grains boundaries mean H_2O contents as all the data are more or less grouped in the same range.

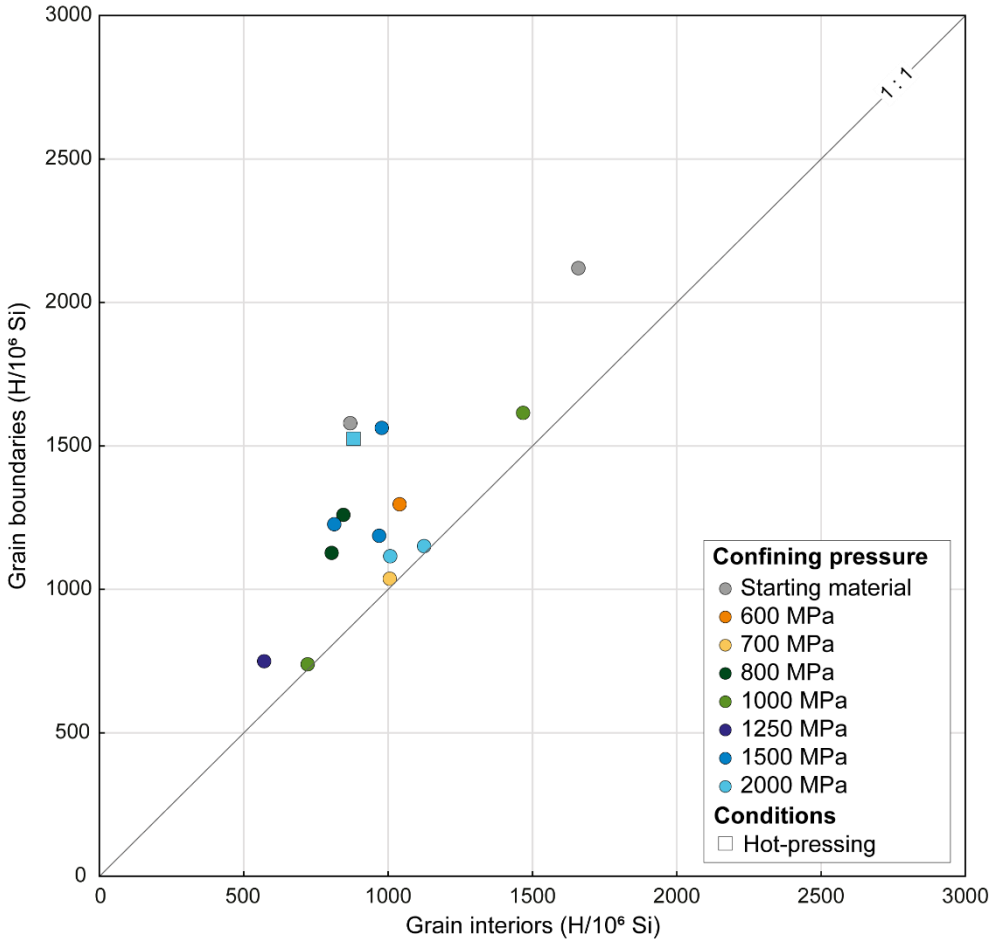

Figure IV.7. Relationship between mean grain interior and grain boundaries H_2O contents ($H/10^6$ Si). The mean H_2O content of grain boundaries is always superior to the grain interior one.

IV.1.3.2. Influence of confining pressure on H_2O contents

In order to determine whether there is an influence of the confining pressure on the H_2O content, the H_2O content data of grain interiors and grain boundaries are plotted as a function of the confining pressure (Figure IV.8). No influence of pressure is visible as the data are quite close. The mean H_2O contents of deformed and hot-pressed samples stay, more or less, in the same range (~570 – 1470 $H/10^6$ Si for grain interiors and ~740 – 1620 $H/10^6$ Si for grain boundaries).

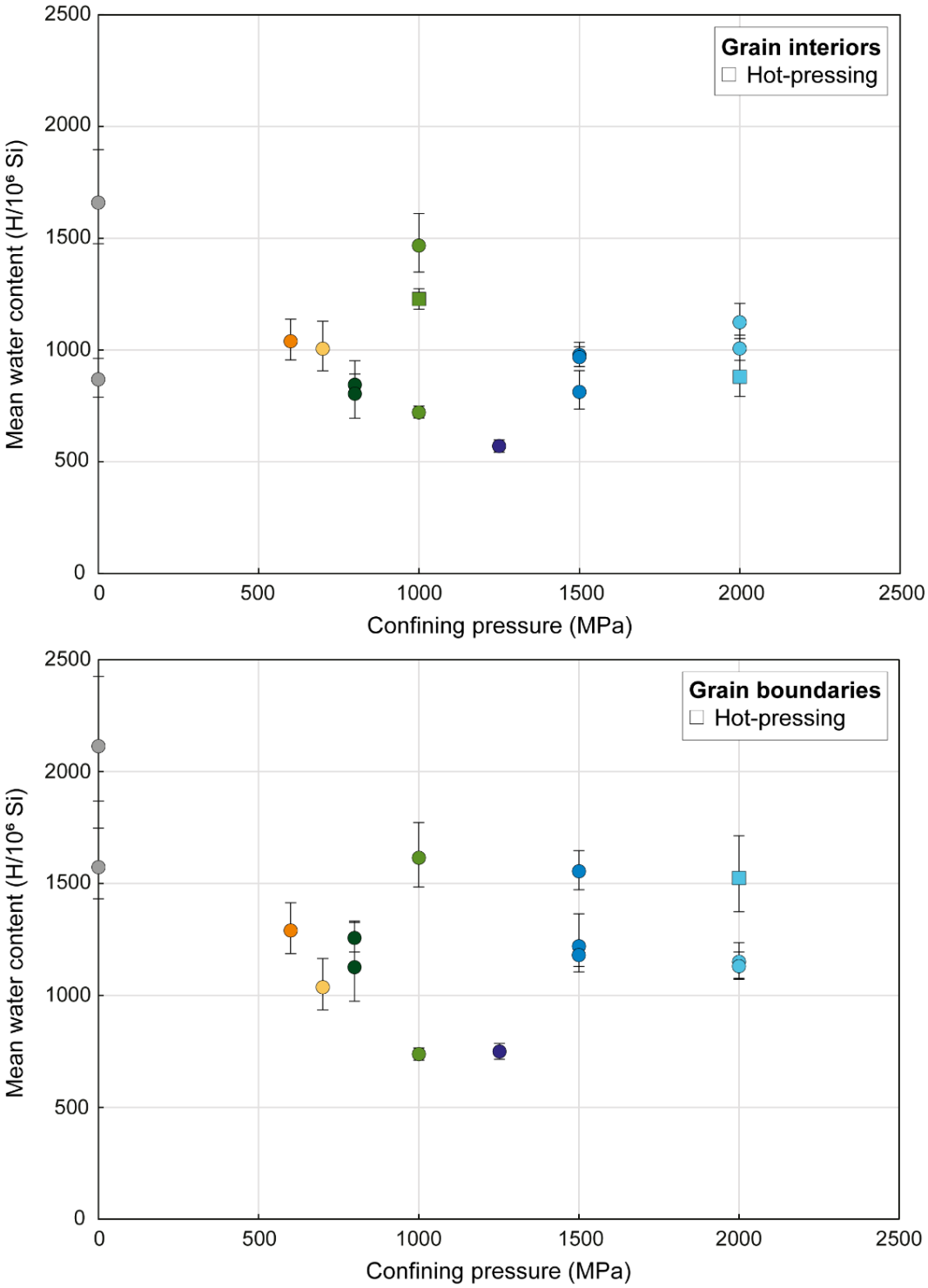

Figure IV.8. Mean H_2O contents ($H/10^6$ Si) for grain interiors (top) and grain boundaries (bottom) as a function of the confining pressure.

Comparison with starting material

As several blocks of starting material were used for the experiments and as the two starting materials measured show some discrepancies (see the starting material description, part IV.1.2) all measured samples and starting material cannot be directly compared.

Figure IV.9 shows the mean H_2O contents of the experiments for which starting material TQ-1 was used (OR32 to OR62). For both grain interiors and grain boundaries, the mean H_2O content

of deformed samples is lower than in the starting material. The same observation is made for grain interiors of the hot-pressed sample (OR59).

For samples deformed from 700 to 1250 MPa a negative trend is observed but not confirmed by the sample deformed at 2000 MPa for which the mean H_2O contents are similar to the sample deformed at 700 MPa.

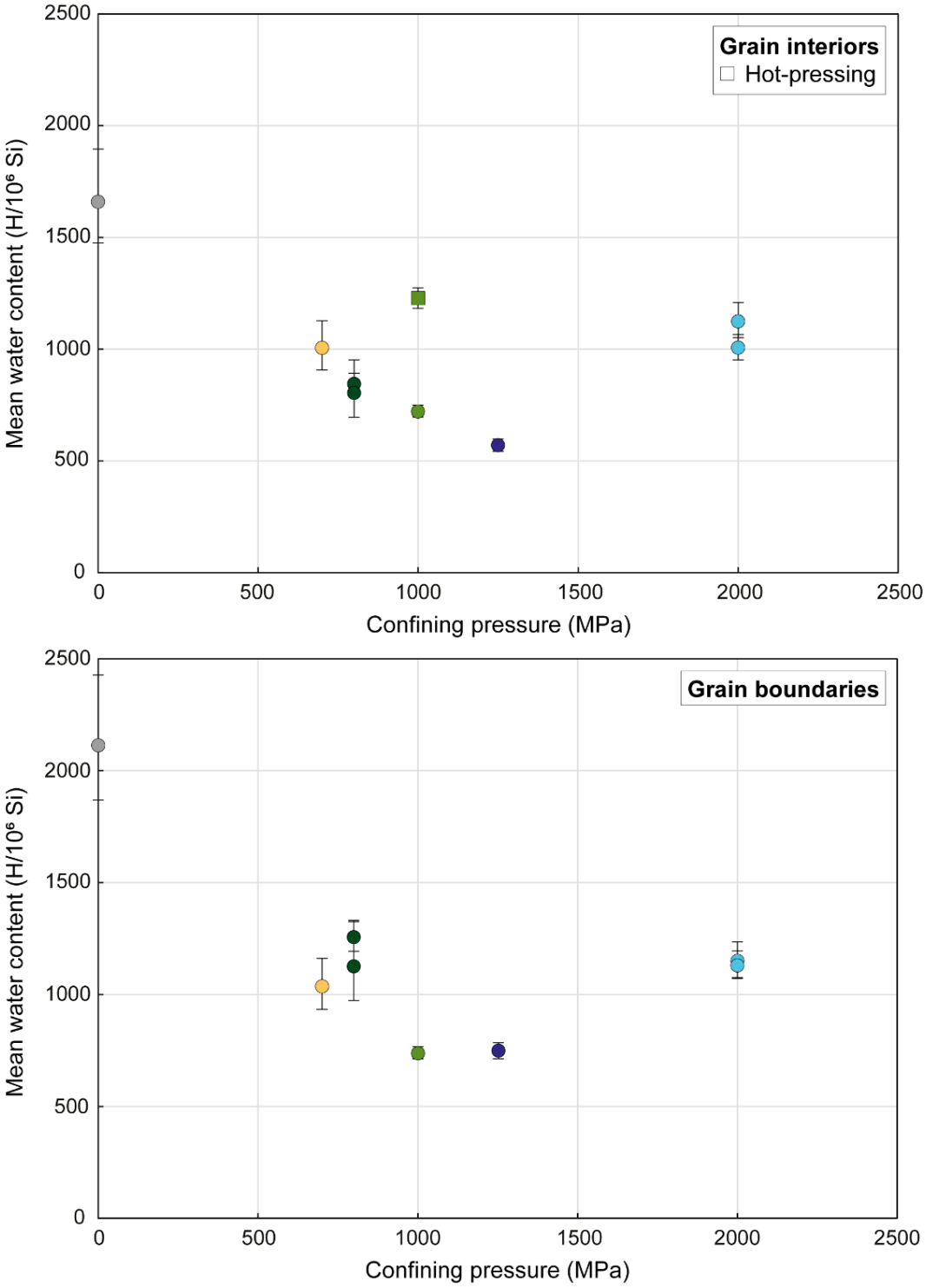

Figure IV.9. Mean H_2O contents ($H/10^6$ Si) for grain interiors (top) and grain boundaries (bottom) as a function of the confining pressure. The mean H_2O content of deformed samples is lower than the starting material.

Then, when comparing the starting material and corresponding deformed or hot-pressed samples the H_2O content distribution can also be considered (Figure IV.10 to Figure IV.13).

For the sample OR52 deformed at 700 MPa confining pressure (Figure IV.10), the H_2O content mode (21%) is located at 500 – 750 H/10^6 Si for grain interiors and at 1000 – 1250 H/10^6 Si for grain boundaries (22.7%).

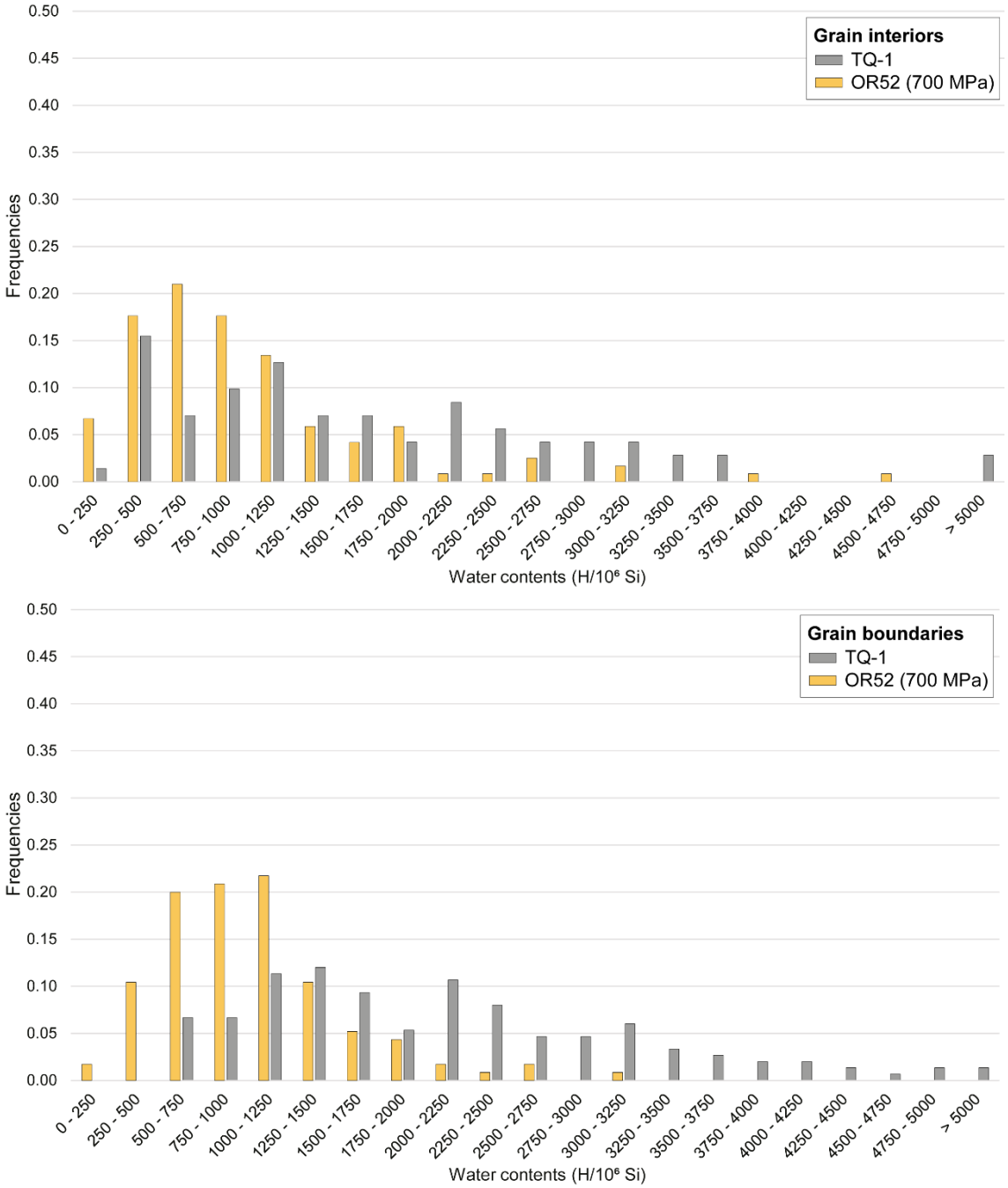

Figure IV.10. H_2O contents distributions for grain interiors and grain boundaries (H/10^6 Si) in deformed sample OR52 (700 MPa) and starting material sample TQ-1. The H_2O content distribution is less dispersed and has higher frequencies in the deformed sample than in the starting material.

Compared to the starting material TQ-1, both grain interiors and grain boundaries show less dispersed H_2O contents. For grain interiors, H_2O contents of sample OR52 are concentrated between in the 0 – 2000 H/10^6 Si range compared to 250 – 3750 H/10^6 Si range for starting material. For the grain boundaries, the H_2O contents of sample OR52 are located between 250 and 2000 H/10^6 Si while for the starting material they extend up to 4500 H/10^6 Si.

The H_2O content distributions of grain interiors for samples OR32 (deformed) and OR59 (hot-pressed) at 1000 MPa are presented in Figure IV.11. For grain boundaries only the sample OR32 is taken into account as data from OR59 were excluded (see part IV.1 on Araldite® contamination).

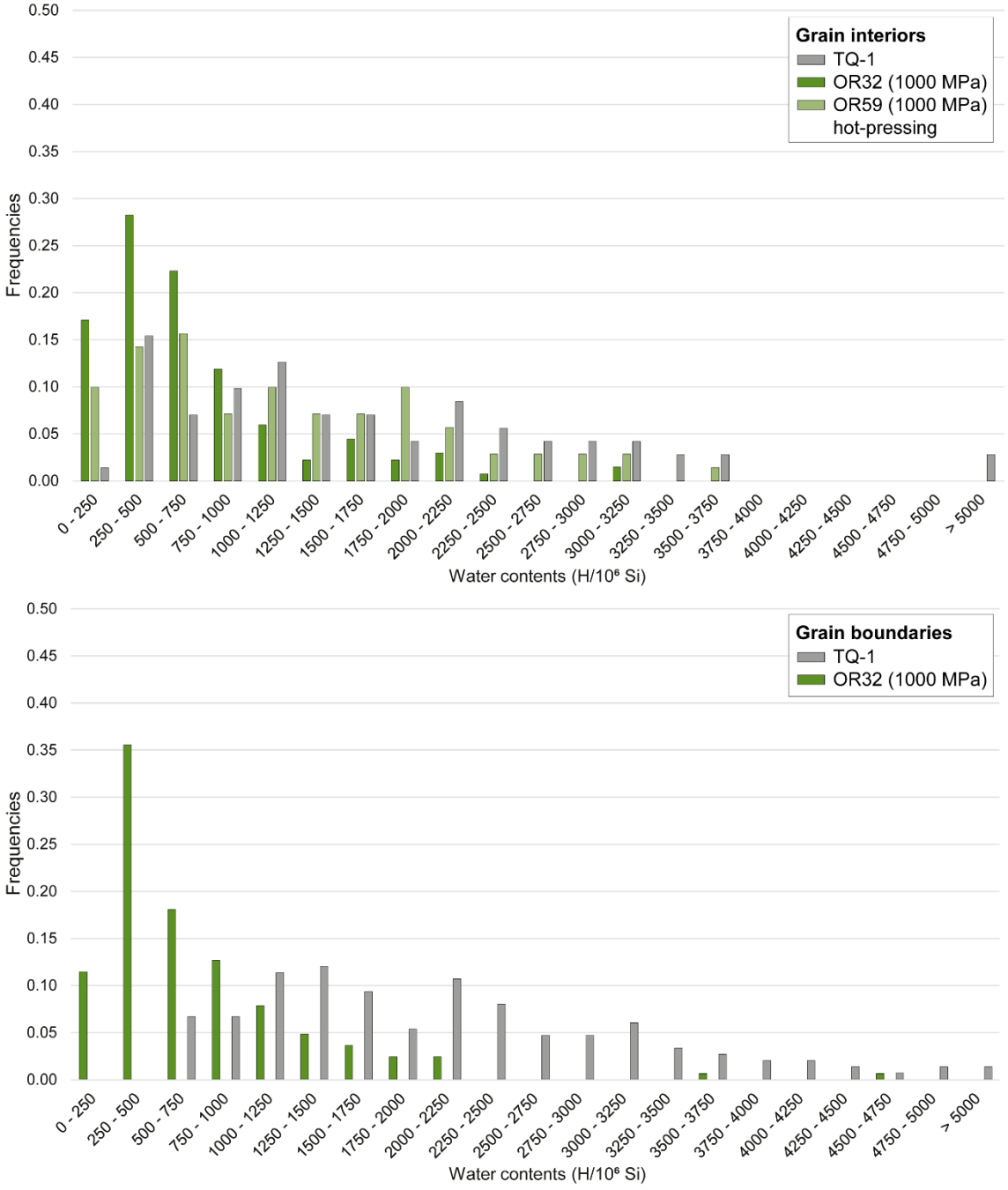

Figure IV.11. H_2O contents distributions for grain interiors and grain boundaries (H/10^6 Si) in samples OR32 deformed at 1000 MPa and for grain boundaries for sample OR59 hot-pressed at 1000 MPa compared to the starting material TQ-1. The H_2O content distribution of deformed sample OR32 is less dispersed than the hot-pressed and starting material ones.

For the grain interiors, the H_2O content mode of the sample OR32 (28.4%) is located at 250 – 500 H/10^6 Si with a distribution concentrated in the 0 – 1750 H/10^6 Si range. For the hot-pressed OR59 sample, the mode (15.7%) is at 500 – 750 H/10^6 Si with a broader distribution from 0 to 3250 H/10^6 Si. For grain boundaries, the mode is at 250 – 500 H/10^6 Si and very pronounced (35.5%) with a distribution concentrated in the 0 – 2250 H/10^6 Si range.

Compared to starting material TQ-1, the deformed sample OR32 has a more concentrated distribution for both grain interiors and grain boundaries. The hot-pressed sample OR59 presents a similar broad distribution for grain interiors than the starting material.

For the sample OR48 which was deformed at 1250 MPa confining pressure (Figure IV.12), the grain interior H_2O contents are concentrated in the 0 – 1500 H/10^6 Si range with a very pronounced mode (40.6%) at 250 – 500 H/10^6 Si. The grain boundaries H_2O contents are in the 0 – 1750 H/10^6 Si range with a mode (31.8%) at 250 – 500 H/10^6 Si.

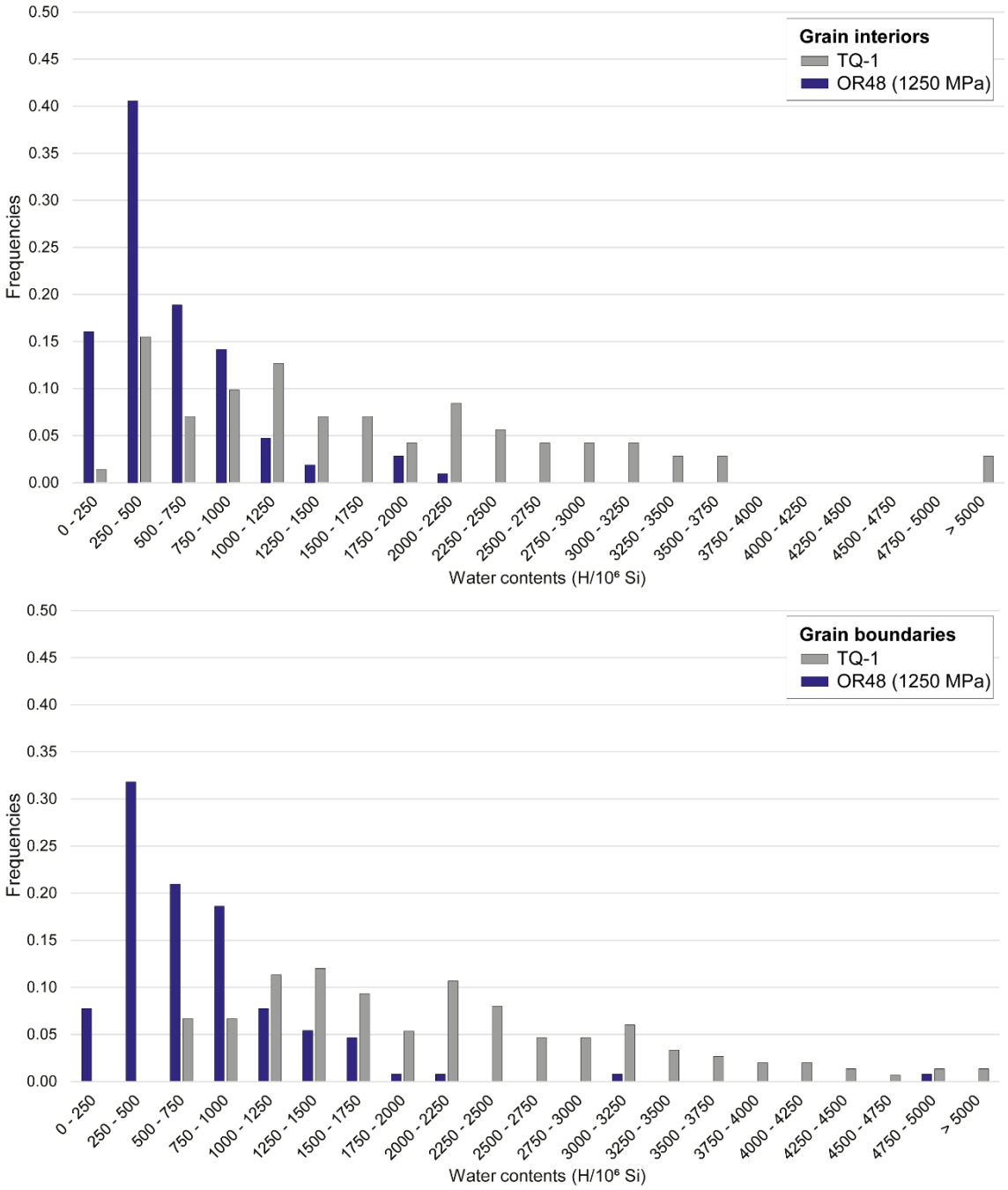

Figure IV.12. H_2O contents distributions for grain interiors and grain boundaries (H/10^6 Si) in deformed sample OR48 (1250 MPa) compared to the starting material TQ-1. The H_2O contents distributions of the deformed sample are concentrated at lower values and show less dispersion than the starting material.

The H_2O contents of OR48 sample show a very low dispersion compared to the starting material TQ-1 (and to the other samples).

Distribution of grain interior and grain boundaries H_2O contents of samples OR57 and OR62 deformed at 2000 MPa confining pressure are presented in Figure IV.13.

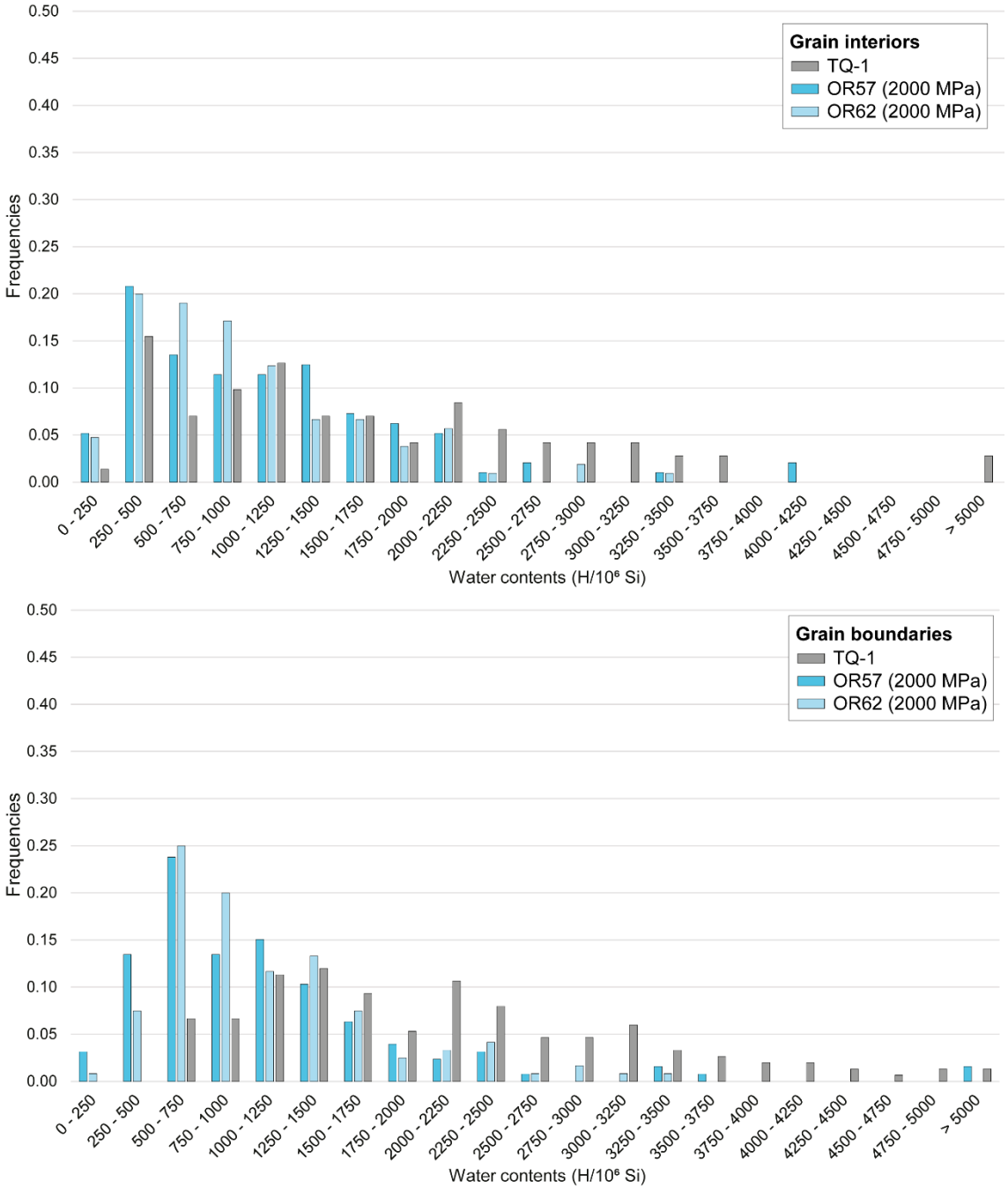

Figure IV.13. H_2O contents distributions for grain interiors and grain boundaries (H/10^6 Si) for samples OR57 and OR62 deformed at 2000 MPa confining pressure and starting material sample TQ-1. The deformed samples show lower dispersion and higher grouping in the low H_2O content values.

For the grain interiors, the distribution of the deformed samples OR57 and OR62 is quite similar with a mode at 250 – 500 H/10^6 Si (at 20.8% for OR57 and 20% for OR62) and a dispersion of H_2O contents in the 0 -2250 H/10^6 Si range. For the grain boundaries, the H_2O content distribution of the two deformed samples is also quite similar with a mode higher than the grain interiors at 500 – 750 H/10^6 Si (at 23.8% for OR57 and 25% for OR62) and a dispersion between 0 and 2500 H/10^6 Si.

Compared to the starting material TQ-1, the histograms of deformed samples OR57 and OR62 are more grouped to lower H_2O content values.

The H_2O content distributions of deformed samples are always less dispersed than starting material one. Their frequencies are closer and always higher than the starting material frequencies. They are all more grouped on smaller H_2O contents and rarely excess 2000 to 2500 $H/10^6$ Si for grain interiors and grain boundaries, respectively.

IV.1.3.3. Influence of the amount of deformation on H_2O contents

The first comparison that can be made is between deformed samples and the samples that were subjected to the same pressure and temperature conditions during the same time without any deformation (hot-pressing). Two experiments of this type have been carried out: OR59 (1000 MPa) and OR66 (2000 MPa).

For both grain interiors and grain boundaries, given the data variability, no significant difference appears between the mean H_2O contents of hot-pressed samples and the samples deformed at the same conditions (Figure IV.8). But, as described for OR59 sample (Figure IV.11) the data dispersion is closer to the starting material rather than to the corresponding deformation experiment, for which the dispersion is narrower.

Influence of local strain variations

Then, the effect of deformation can be examined by considering variations of mean H_2O contents with strain inside a sample. For this, the four samples that present strain variations between top and middle part are used (OR42, 546LN, 544LN, OR62). Their related H_2O contents are presented in the Table IV.5.

Both for the least and the most deformed parts, the mean H_2O contents of the grain interiors are lower than the grain boundaries (except for the least deformed part of 546LN sample for which they are equivalent).

Table IV.5. Molar proportion ($H/10^6$ Si) of H_2O content in grain interiors and grain boundaries in both less deformed and most deformed parts of samples which present a strain gradient between top and middle part.

Sample	Molar proportion ($H/10^6Si$)	Grain interiors		Grain boundaries	
		Least deformed	Most deformed	Least deformed	Most deformed
OR42 800 MPa	Number of data	62	54	65	55
	Mean	1165	391	1296	927
	Median	811	341	1056	678
	Standard deviation	952	265	854	816
	Min value	181	55	358	200
	Max value	5236	1136	4642	5017
546LN 1000 MPa	Number of data	70	70	73	68
	Mean	1854	1081	1841	1373
	Median	1775	934	1802	1178
	Standard deviation	1139	847	767	984
	Min value	191	130	239	281
	Max value	5765	4620	3970	5687

544LN 1500 MPa	Number of data	70	60	62	67
	Mean	1116	817	1812	1326
	Median	761	578	1655	1075
	Standard deviation	1232	676	960	875
	Min value	88	159	183	136
	Max value	5900	3372	5880	4266
OR62 2000 MPa	Number of data	56	49	67	53
	Mean	1104	899	1195	1054
	Median	854	723	1148	746
	Standard deviation	675	596	548	744
	Min value	317	135	228	290
	Max value	3379	2968	2909	3401

For the four samples considered, the mean H_2O content of the grain interiors and grain boundaries measured in the most deformed part is lower than the corresponding mean H_2O content measured in the least deformed part (Figure IV.14).

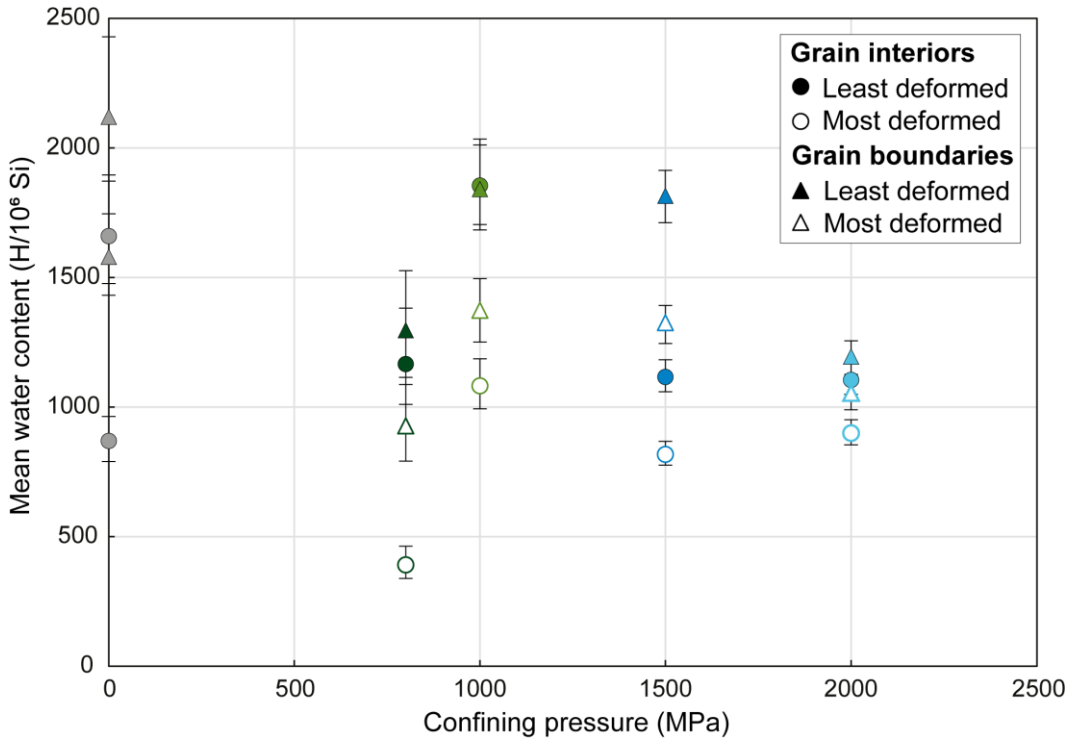

Figure IV.14. Mean H_2O contents ($H/10^6$ Si) as a function of pressure and of the level of strain. No link between mean H_2O contents and confining pressure is shown. Mean H_2O contents decrease with increasing strain.

When considering the evolution of the mean H_2O content with deformation, it decreases with increasing strain in every microstructure (grain interiors or grain boundaries): for grain interiors and grain boundaries, the mean H_2O content is always higher in the least deformed part than in the most deformed part.

When plotting for grain interiors and grain boundaries the mean H_2O content of least deformed part versus most deformed part, (Figure IV.15), the most deformed parts always contain less H_2O than the least deformed parts.

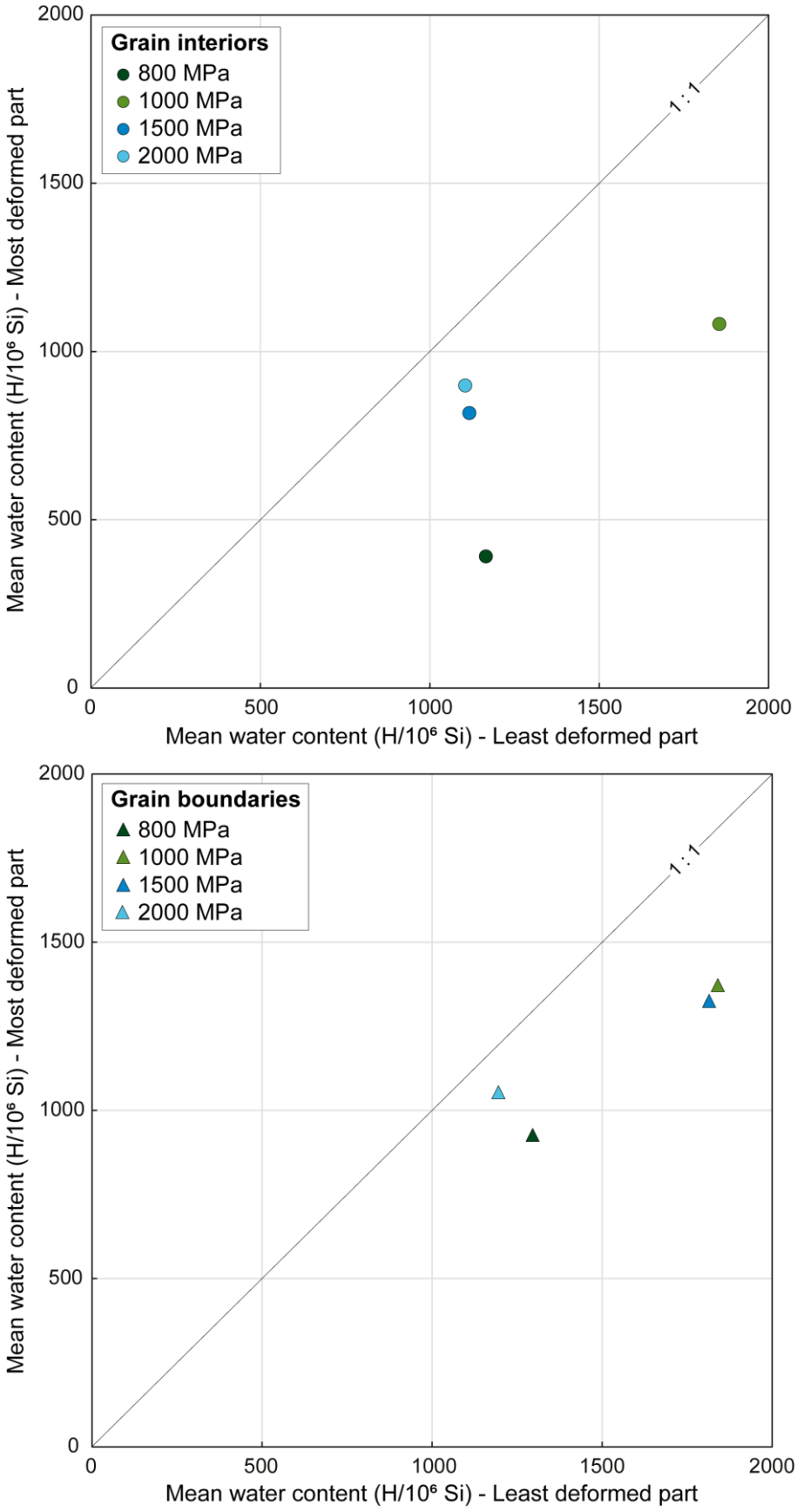

Figure IV.15. Mean H_2O contents ($H/10^6$ Si) of the least deformed parts against most deformed parts in samples showing a strain partitioning.

Influence of global strain

The effect of deformation on H_2O content can also be characterized by comparing the mean H_2O contents calculated for samples with different global strain achieved. This is the case for the samples deformed at 2000 MPa confining pressure: OR57, OR62, OR54, OR50 and OR56 whose global strains are 27.76%, 29.51%, 39.75%, 52.38% and 74.43%, respectively (Table IV.6).

One can note that the OR56 sample has been deformed faster than the other samples (10^{-5} instead of 10^{-6} s^{-1}) and thus for a shorter period of time (32h instead of 112-217h).

Table IV.6. Molar proportion ($H/10^6$ Si) of H_2O content in grain interiors, grain boundaries and recrystallized grains for samples deformed at 2000 MPa confining pressure presenting different global strains. The duration of experiment (hot-pressing + deformation stages) are indicated.

Sample	Molar proportion ($H/10^6Si$)	Grain interiors	Grain boundaries	Recrystallized grains
OR57 27.76% ~112h	Number of data	96	126	35
	Mean	1125	1151	1604
	Median	946	908	1442
	Standard deviation	792	1037	748
	Min value	149	233	438
	Max value	4211	8421	3319
OR62 29.51% ~217h	Number of data	105	118	*not measured*
	Mean	1007	1116	
	Median	844	907	
	Standard deviation	574	649	
	Min value	135	228	
	Max value	2968	3401	
OR54 39.75% ~138h	Number of data	124	61	69
	Mean	759	894	705
	Median	637	700	484
	Standard deviation	560	531	694
	Min value	140	155	83
	Max value	4244	2482	3782
OR50 52.38% ~182h	Number of data	106	50	66
	Mean	552	540	1016
	Median	396	503	803
	Standard deviation	480	290	706
	Min value	118	126	198
	Max value	3127	1175	3800
OR56 74.43% ~32h	Number of data	71	41	52
	Mean	1304	1500	926
	Median	1265	1232	958
	Standard deviation	533	832	491
	Min value	216	278	90
	Max value	2682	3423	2640

In Figure IV.16 the different mean H_2O contents measured (grain interiors, grain boundaries and recrystallized grains) are plotted as a function of the global strain achieved by samples. For samples deformed at 10^{-6} s^{-1}, the mean H_2O contents of grain interiors and grain boundaries decrease from the lowest to the highest strain (27.76% to 52.38%). For the sample that achieved 74.43% strain at 10^{-5} s^{-1} the H_2O content is much higher. For recrystallized material, the mean H_2O content also decreases with the global strain.

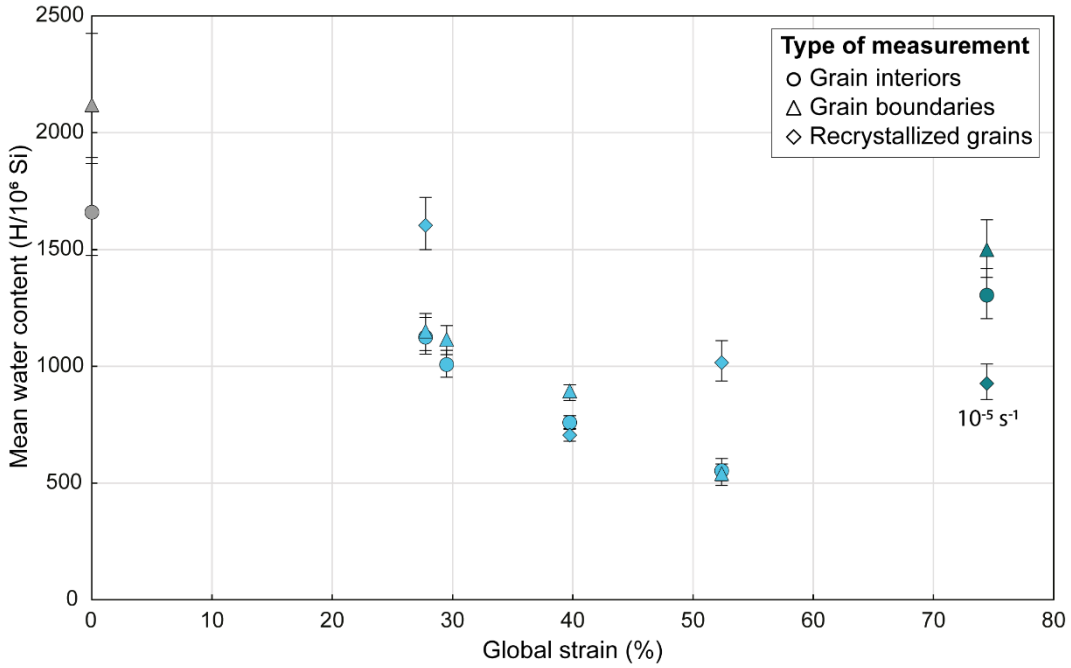

Figure IV.16. Mean H_2O contents ($H/10^6$ Si) for samples deformed at 2000 MPa (and starting material for comparison) as a function of the global strain achieved. Samples with 27.76 to 52.38% strain were deformed at 10^{-6} s^{-1} strain rate whereas sample with 74.43% strain was deformed at 10^{-5} s^{-1}.

The mean H_2O contents of samples deformed at 2000 MPa confining pressure and different global strains can also be plotted as a function of the experiment duration (Figure IV.17). The experiment duration considered takes into account the hot-pressing phase, when the sample was let during ~one night at pressure and temperature conditions (2000 MPa and 900°C) and the deformation phase (that lasted different amount of time depending on the samples).

The mean H_2O contents seem to be higher for lower experiment duration (sample OR56) but no clear trend appears as a function of time.

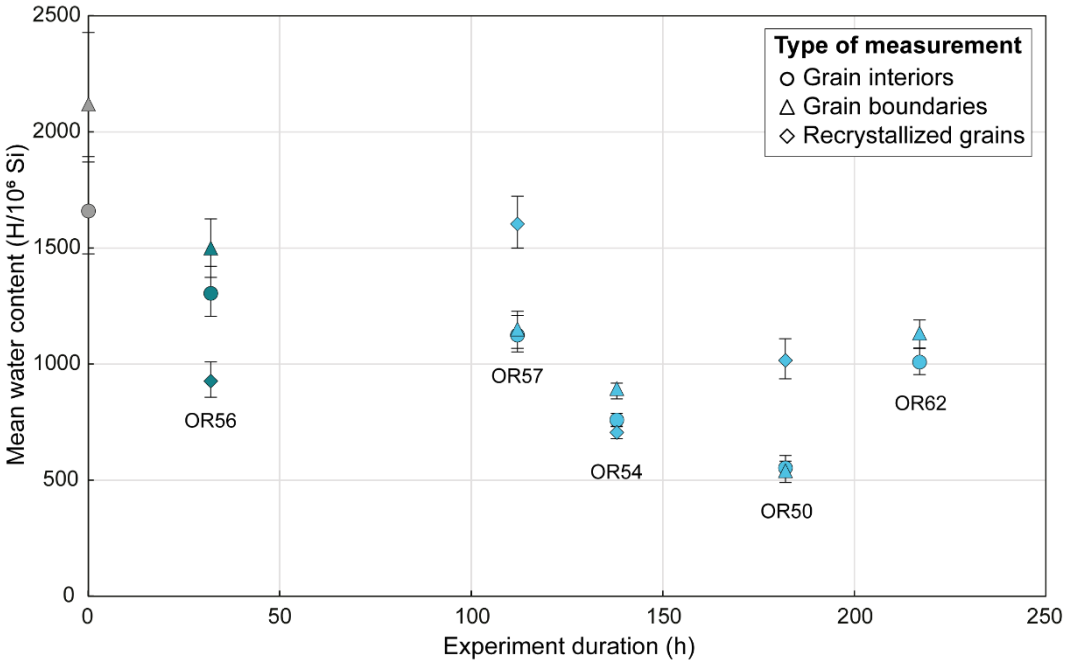

Figure IV.17. Mean H_2O contents ($H/10^6$ Si) for samples deformed at 2000 MPa (and starting material for comparison) as a function of the experiment duration (hot-pressing and deformation phases, in hours).

IV.1.1. Microstructures associated to H_2O content measurements

The starting material Tana quartzite (Figure IV.18a) has a sedimentary and polygenic origin (see detailed description in the previous chapter, part III.1). The equigranular quartz grains that compose it are round shaped and do not show internal strain (no undulatory extinction). The heterogeneity of the starting material is reflected by the large differences of H_2O content measured (Table IV.2, Table IV.3, Figure IV.5) and the broad data dispersion (Figure IV.3, Figure IV.4, Figure IV.6). In light microscopy, no difference can be made between the grains, except for the presence of fluid inclusions trails, visible in some of them. The grain boundaries are clearly identifiable, and the presence of sheet silicates is sometimes observed (but avoided during measurements).

For the deformed samples (Figure IV.18b-f), quartzite grains present elongated shapes (that increase in the higher strained regions) and display features characteristic of plastic deformation such as undulatory extinction, deformation lamellae and in some places, development of subgrains. In the grain boundary region, small new grains are observed as the result of progressive subgrain rotation but also cracking (as detailed in the discussion of the previous chapter, part III.4.2). For the samples deformed at 2000 MPa, the areas presenting enough small grains were measured ("recrystallized grains", Figure IV.16 and Figure IV.17). During the FTIR measurements, the areas labelled as "grain boundaries" correspond to places where two quartzite grains were adjacent (recrystallized areas were avoided).

For the samples deformed at the same strain rate (10^{-6} s^{-1}) and to the same global strain (~30%), the microstructures observed do not change much, but the plasticity is enhanced by the confining pressure (Figure IV.18b&c, and precisions in the previous chapter). The formation of small grains is also more important at higher pressure and larger sized.

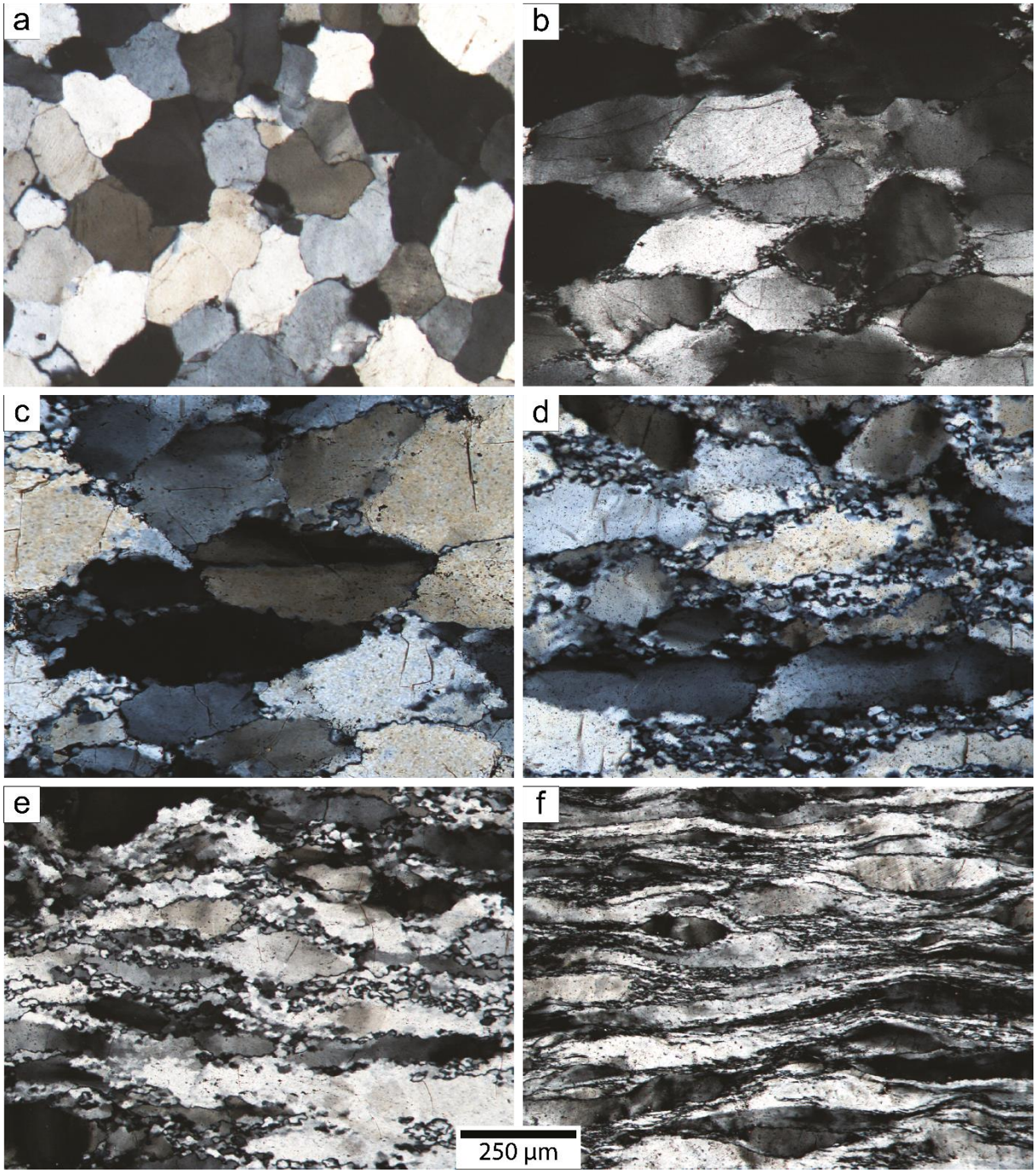

Figure IV.18. Cross polarized light microscopy images of (a) starting material and (b - f) deformed samples at (b) 1000 MPa, ~30% strain and 10^{-6} s^{-1} (OR32), (c) 2000 MPa, ~30% strain and 10^{-6} s^{-1} (OR62), (d) 2000 MPa, high-strained to ~40% at 10^{-6} s^{-1} (OR54), (e) 2000 MPa, high-strained to ~52% at 10^{-6} s^{-1} (OR50) and (f) 2000 MPa, high strained to ~74% at 10^{-5} s^{-1}. The shortening direction is vertical.

However, for samples deformed at the same confining pressure (2000 MPa) and same strain rate (10^{-6} s^{-1}) but that achieved different finite strains (Figure IV.18c-e), some differences in the microstructures are observable. As the sample shortening increases, the development of subgrains increases, and chess-board features as well as sutured grain boundaries are observed for samples which strain is up to ~40 or ~52 % (OR54 and OR50, respectively) which is not the case for samples deformed to ~30% (OR57 and OR62). The quartz grains are also more elongated and the amount of recrystallized material by cracking, subgrain rotation and grain boundary migration increases as well. The grain boundaries between the original quartzite grains become less frequent.

The sample OR56 (2000 MPa) was deformed faster (10^{-5} s^{-1}) and with an achieved strain of ~74% (Figure IV.18f). The quartzite grains are extremely elongated and in most cases displays well pronounced deformation lamellae. A very finely recrystallized material occurs in almost continuous bands between the grains.

IV.2. OH speciation

In addition to measuring the broad H_2O area in order to calculate H_2O contents, the identification of some discrete narrow absorption bands in the 3000 – 3800 cm^{-1} region has been performed on spectra. These discrete bands (previously selected from literature and from starting material pre-processing analysis) were automatically fitted during the data treatment with the MATLAB script but an additional manual data treatment was also needed. Representative spectra for samples and measurements categories have been selected and will be presented in the following section. For each sample and measured category (grain interiors, grain boundaries, cement, triple junctions and recrystallized grains) a mean spectrum has been calculated and submitted to the same data treatment as the individual spectrum.

All spectra measured consist of an association of a broad H_2O band and of discrete OH bands. The broad band is almost symmetric and centred around 3400 cm^{-1}. The discrete bands identified in the 3000 – 3800 cm^{-1} region are located at 3699, 3653, 3624, 3596, 3585, 3467, 3429, 3379 and 3319 cm^{-1}. The bands at 3699, 3653 and 3624 cm^{-1} are associated with OH adsorbed to sheet silicates (muscovite and kaolinite notably, Farmer and Russell, 1964). The bands at 3429, 3379 and 3319 cm^{-1} commonly appear together and are related to the presence of Al^{3+} substituting for Si^{4+} and the corresponding H^+ or Li^+ compensating charges (e.g., Kats, 1962). The band at 3467 cm^{-1} may also be related to the presence of Li^+ (3470 – 3480 cm^{-1}, (Aines and Rossman, 1984). Absorption at 3596 cm^{-1} is described to be due to protons charge balanced by B^{3+} (Müller and Koch-Müller, 2009; Baron et al., 2015; Jollands et al., 2020) or to H^+ compensating for Al^{3+} substitution (Niimi et al., 1999; Gleason and DeSisto, 2008). Finally, the band at 3585 cm^{-1} is either described as silicon vacancy charge balanced by protons (hydrogarnet substitution for which $Si^{4+} = 4H^+$, e.g., Stalder and Konzett, 2012) or as isolated OH^- groups bridging two Si atoms (Jollands et al., 2020) and OH defects related to dislocations (Stünitz et al., 2017).

IV.2.1. Starting material

IV.2.1.1. Starting material TQ-1

Starting material infrared spectra show a wide diversity of band associations. For measurements made on the grain interiors, most of the spectra present a broad H_2O band without pronounced discrete OH bands (Figure IV.19 and Table IV.7). Several other spectra display an Al-H/Li triplet (bands at 3429, 3379 and 3319 cm^{-1}, the band at 3379 cm^{-1} being the most important one) in addition to the broad H_2O band. Few spectra indicate the presence of sheet silicates with related OH bands at 3699, 3653 or 3624 cm^{-1}. The bands at 3596, 3585 and 3467 cm^{-1} are rarely present (respectively only in 12, 9 or 16 spectra over the 72). The height of each discrete band is variable from one spectrum to another.

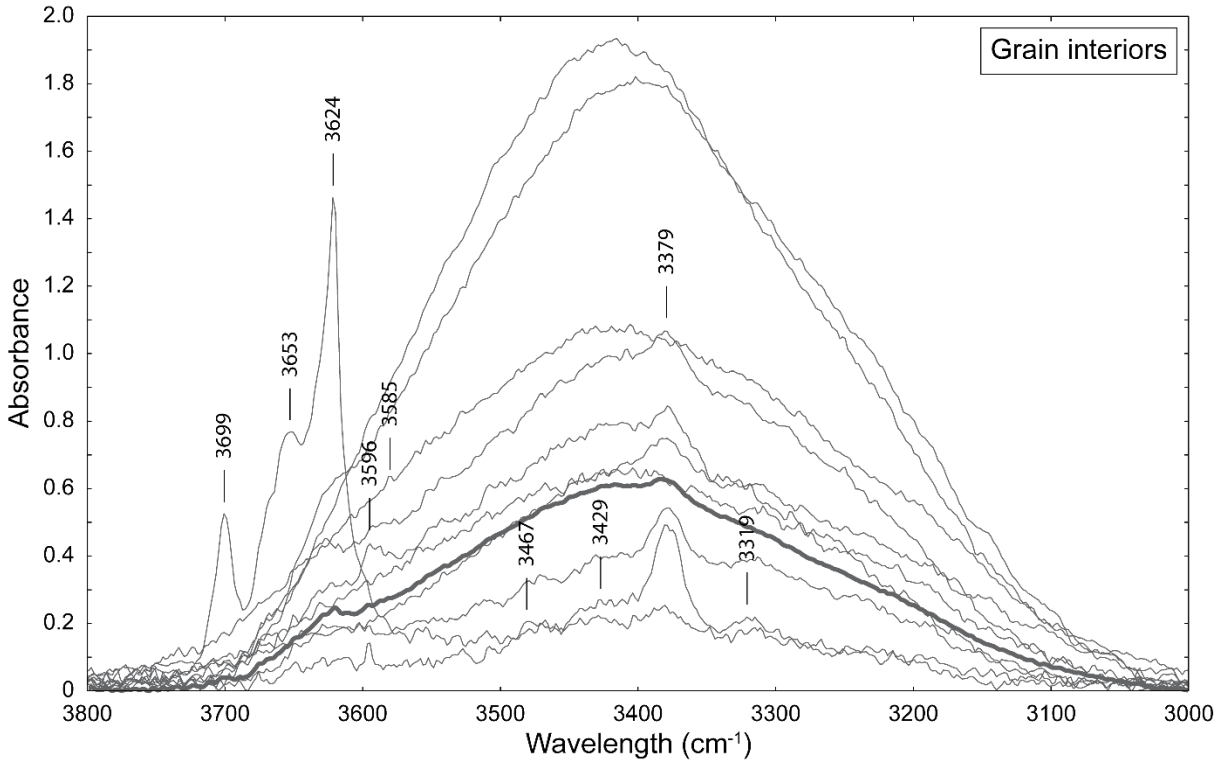

Figure IV.19. Examples of some spectra characteristic from starting material TQ-1 grain interiors. Some spectra show only a broad H2O band whereas some others show different combinations and intensities of bands. The bold spectrum corresponds to the average of all the spectra. Spectra are normalized to 1 mm thickness.

For measurements made on the grain boundary region, OH bands related to the presence of sheet silicates (bands in the 3700 – 3650 cm^{-1} region) are present in almost all the spectra (and well-marked in more than 70 of them). The same two categories of spectra are present: the ones with a predominant H_2O broad band and the others with discrete bands from the compensating Al-H/Li triplet (Figure IV.20 and Table IV.7). Contrary to the grain interiors, for grain boundaries the former type is the most represented (in 96 spectra over 150). Concerning the other discrete bands, they are more present in the grain boundary region than in the grain interior but still have a low percentage of occurrence. The band at 3467 cm^{-1} (Li-OH defect) is observed in 30% of the spectra, mostly in the ones presented an Al-H/Li triplet. The bands at 3596 and 3585 cm^{-1} are present in 25 and 16% of the spectra, respectively.

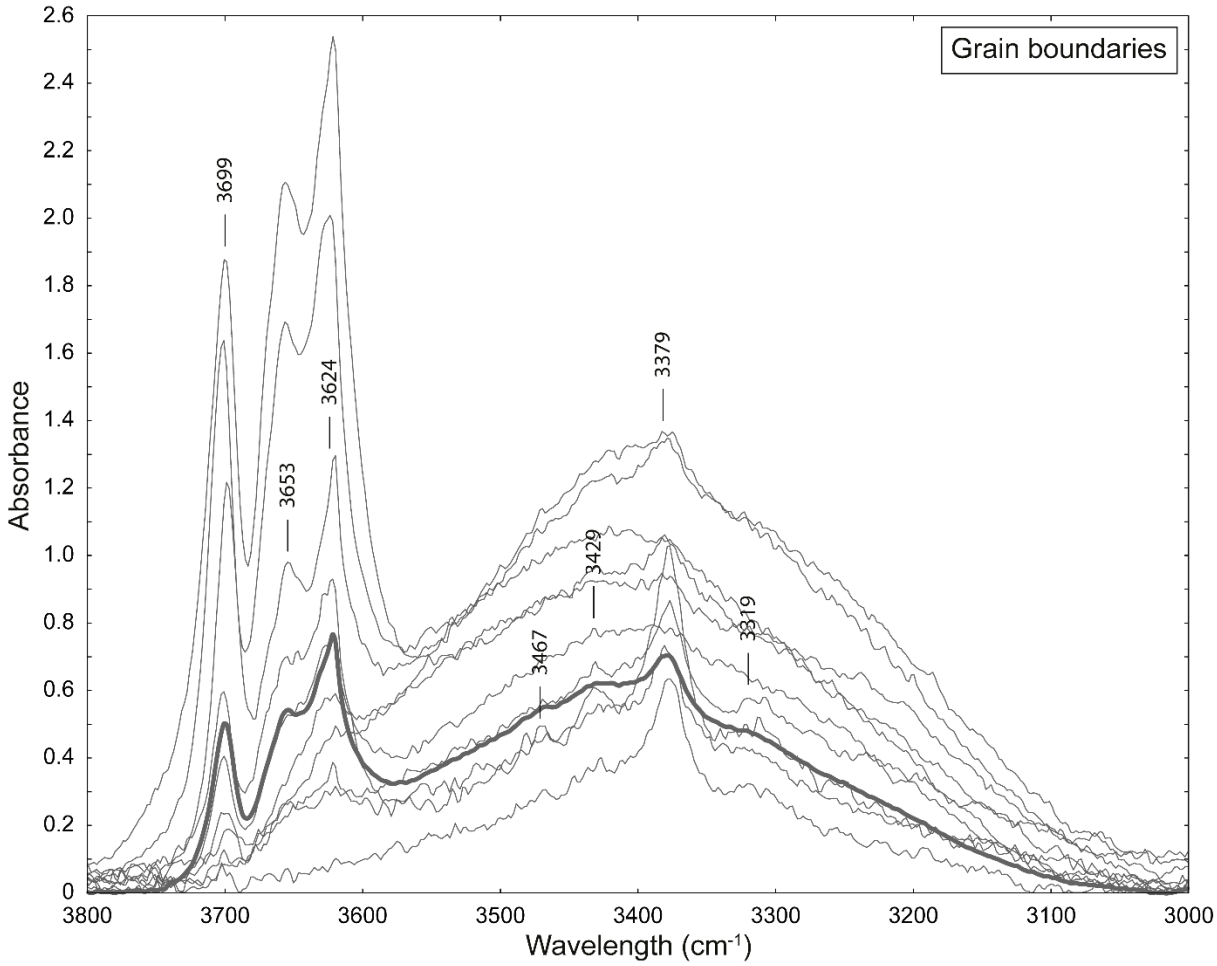

Figure IV.20. Examples of some spectra characteristic from grain boundaries of starting material TQ-1. Spectra show different combination and intensities of bands but the presence of sheet silicates is almost ubiquitous. The bold spectrum corresponds to the average of all the spectra. Spectra are normalized to 1 mm thickness.

IV.2.1.2. Starting material TQ-2

For starting material TQ-2 grain interiors, the same types of spectra are observed with ~50% of the spectra showing a broad H_2O band only and in the other ~50% the triplet Al-H/Li is visible (Figure IV.21 and Table IV.7). Even in the grain interiors, the presence of sheet silicates is visible with 50 spectra over 67 presenting OH bands in the 3700 – 3650 cm^{-1} region. The presence of the other discrete bands is less current with only 23 spectra with the 3596 cm^{-1} band, 13 with the 3585 cm^{-1} and 16 with the 3467 cm^{-1} one.

Note: all the spectra from the TQ-2 starting material sample display smaller absorbance values than the TQ-1 starting material. This is reflected by the lower H_2O contents calculated for the former compared to the latter (Figure IV.5).

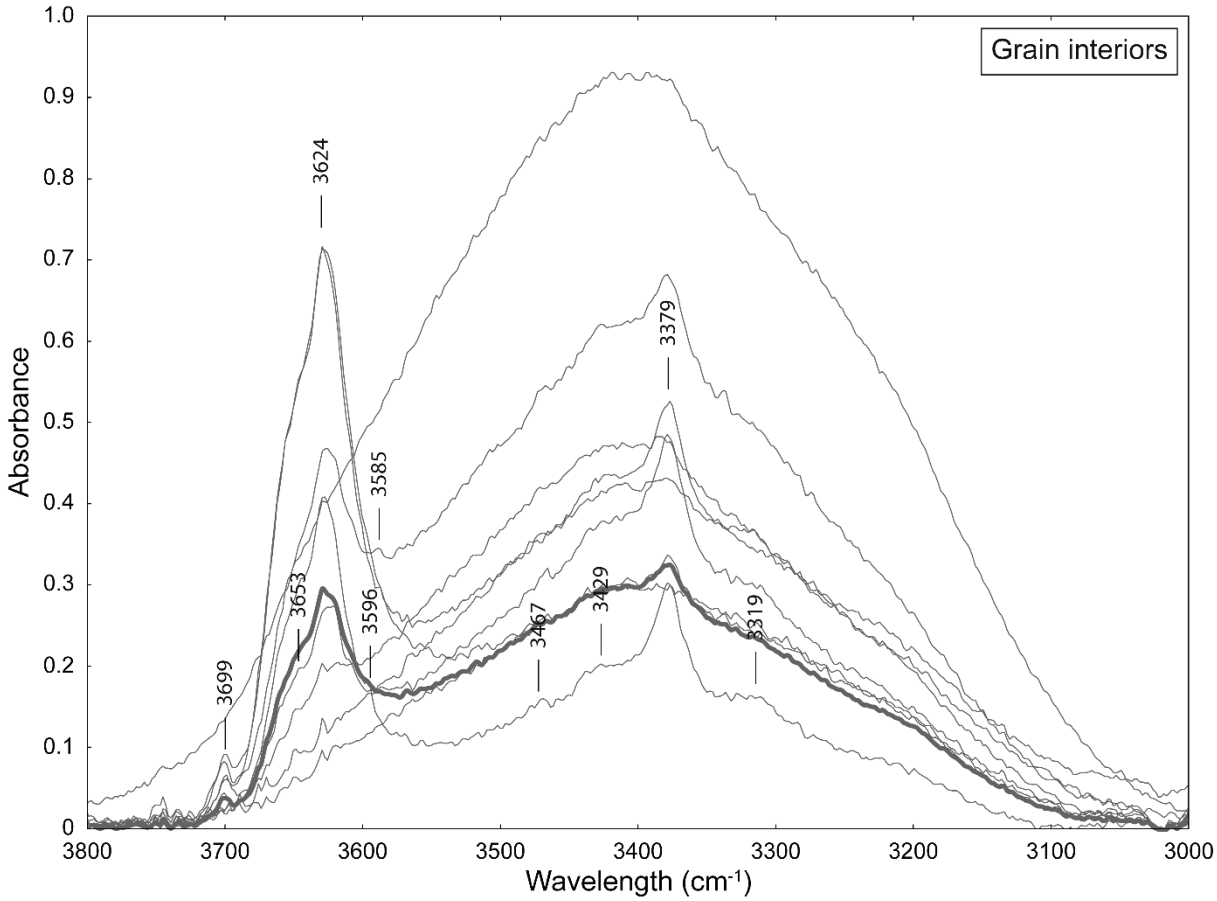

Figure IV.21. Examples of some spectra from starting material TQ-2 grain interiors. The bold spectrum corresponds to the average spectrum calculated from the mean of all the spectra recorded. The average spectrum is shown as a bold line. Spectra are normalized to 1 mm.

For the grain boundaries of the starting material TQ-2 (Figure IV.22 and Table IV.7), only 23 spectra over the 66 analysed show no bands associated with the Al^{3+} for Si^{4+} substitution which are thus present in 43 of the spectra. The presence of sheet silicates is also very important with 58 spectra presenting bands in the 3700 – 3650 cm^{-1} region. The presence of the other thin OH bands is more pronounced than for the grain interiors notably with 34 spectra displaying the 3596 cm^{-1} band, 19 the 3585 cm^{-1} and 35 the 3467 cm^{-1} band. Most of the spectra showing these 3 bands also show the Al-H/Li triplet.

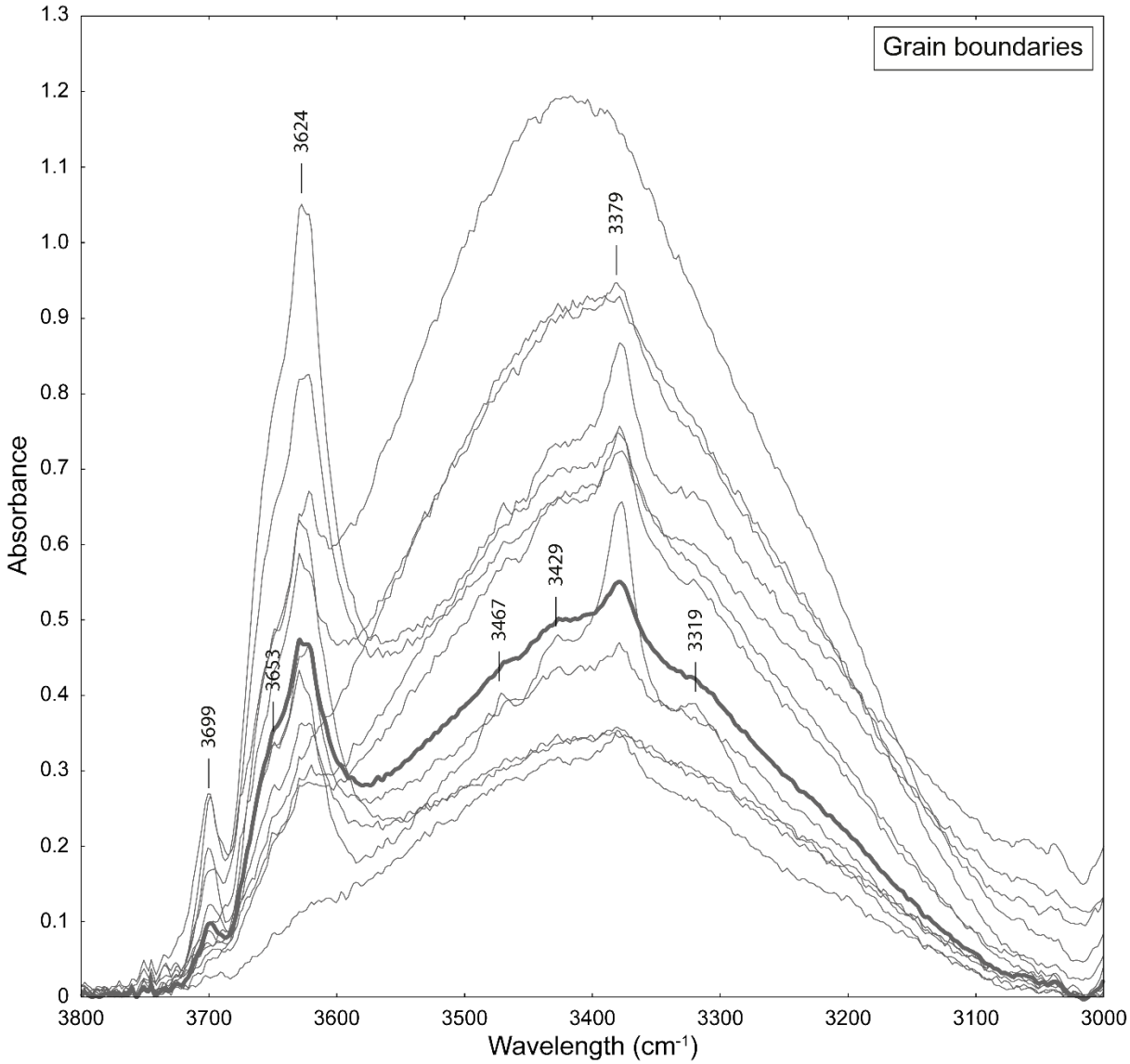

Figure IV.22. Examples of some spectra from starting material TQ-2 grain boundaries. The average spectrum is shown is bold. Spectra are normalized to 1 mm thickness.

For the cement (Figure IV.23 and Table IV.7), the great majority of the spectra (59 over 69) displays the three Al-H/Li bands. Sheet silicate bands are also frequently present (48 spectra over the 69). Compared to the grain boundaries, the bands at 3596 and 3585 cm^{-1} are most rarely present (on 11 and 4 spectra, respectively) but the band at 3467 cm^{-1} associated to Li^{+} is observed in almost half of the spectra (35).

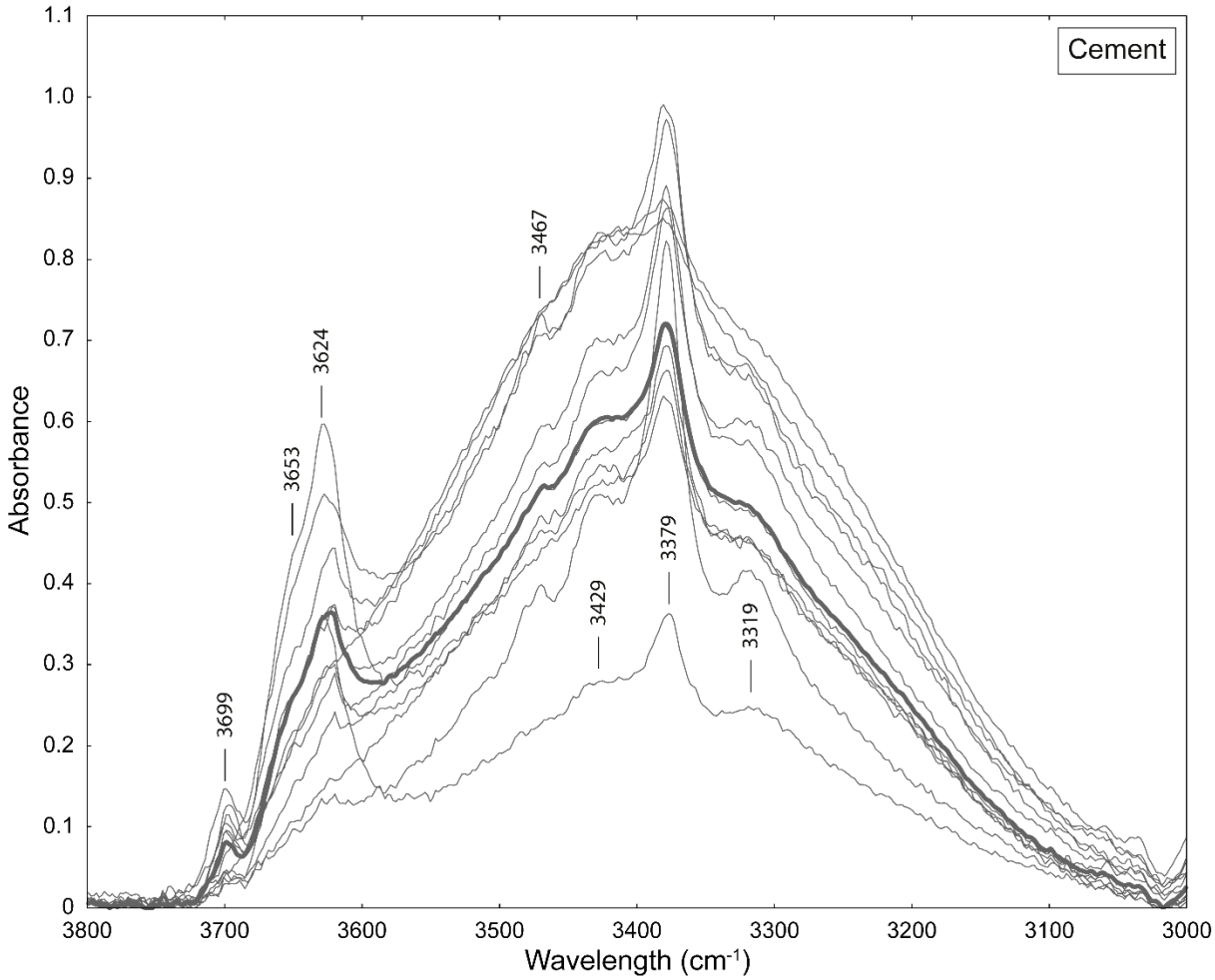

Figure IV.23. Examples of some spectra from starting material TQ-2 cement. The average spectrum is shown in bold. Spectra are normalized to 1 mm thickness.

Finally, for the triple junctions (Figure IV.24 and Table IV.7), as for the cement, almost all of the spectra show the triplet at 3429, 3379 and 3319 cm^{-1} (61 spectra over 69) and the presence of sheet silicates in the 3700 – 3650 cm^{-1} region (60 spectra over 69). The band at 3467 cm^{-1} is also frequently present (in 43 spectra) and the other bands are less frequently observed (28 spectra for the 3596 cm^{-1} bands and 18 spectra for the 3585 cm^{-1} one).

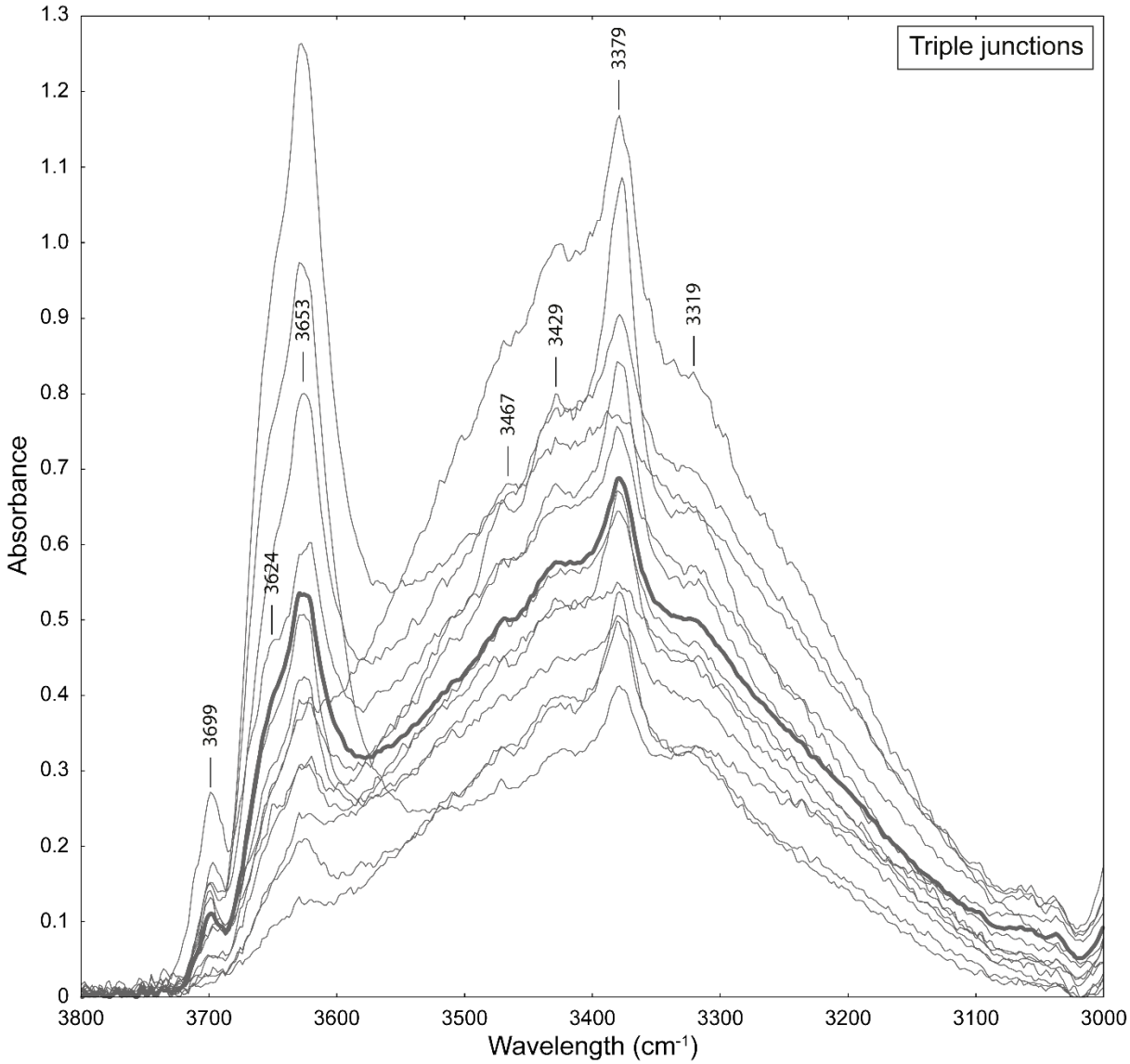

Figure IV.24. Examples of some spectra from starting material TQ-2 cement. The average spectrum is shown in bold. Spectra are normalized to 1 mm thickness.

IV.2.2. Deformed samples

Deformed samples also show a wide diversity of spectra. The first comparison is made thanks to the average spectrum calculated for each sample on grain interiors and grain boundaries. Then, given the large number of spectra recorded, only few deformed samples were considered for the detailed analysis of spectra: three samples deformed at 10^{-6} s^{-1} up to ~30% strain (OR52, OR32 and OR62, respectively deformed at 700, 1000 and 2000 MPa confining pressure) and one high-strained sample deformed at 10^{-5} s^{-1} (OR56, strained up to ~74% at 2000 MPa confining pressure).

IV.2.2.1. Average spectra

For grain interiors (Figure IV.25), the average spectra of deformed samples for grain interiors display fewer bands related to the presence of sheet silicates than the starting material TQ-2 (except for deformed sample OR64). Secondly, deformed samples show more markedly the Al-H/Li triplet but no correlation can be made between the pressure and the height of the 3379

cm^{-1} band, the band heights lying in the same absorbance range. However, the mean spectrum shows that the Al-H/Li triplet is more frequently present in deformed and hot-pressed samples than in the starting materials. Finally, the most remarkable change with pressure is the occurrence of the band at 3585 cm^{-1} (related to isolated OH^- groups) that is not present in the mean spectrum of starting material and samples deformed at 600 MPa, and then appears at 700 MPa and increases in height with the pressure.

For the grain boundaries (Figure IV.26), the Al-H/Li triplet is more frequently present for all samples (starting material, deformed and hot-pressed) compared to the grain interiors. The intensities of the three bands in the grain boundary region are superior to the ones in the grain interiors and the intensity of the band at 3379 cm^{-1} is more pronounced for grain boundaries than for grain interiors (Figure IV.27). The presence of sheet silicates is also more visible with bands in the 3700 – 3650 cm^{-1} region for some spectra from starting material (TQ-1 and TQ-2) and deformed samples (OR64 especially). The band at 3585 cm^{-1} is observed for samples which underwent more than 600 MPa pressure and then increases as the pressure increases. For the lower confining pressures (600 – 800 MPa) it rather appears as a shoulder and then become thinner and higher with the pressure.

For none of the bands considered a correlation could been established between the amount of finite strain and the absorbance values.

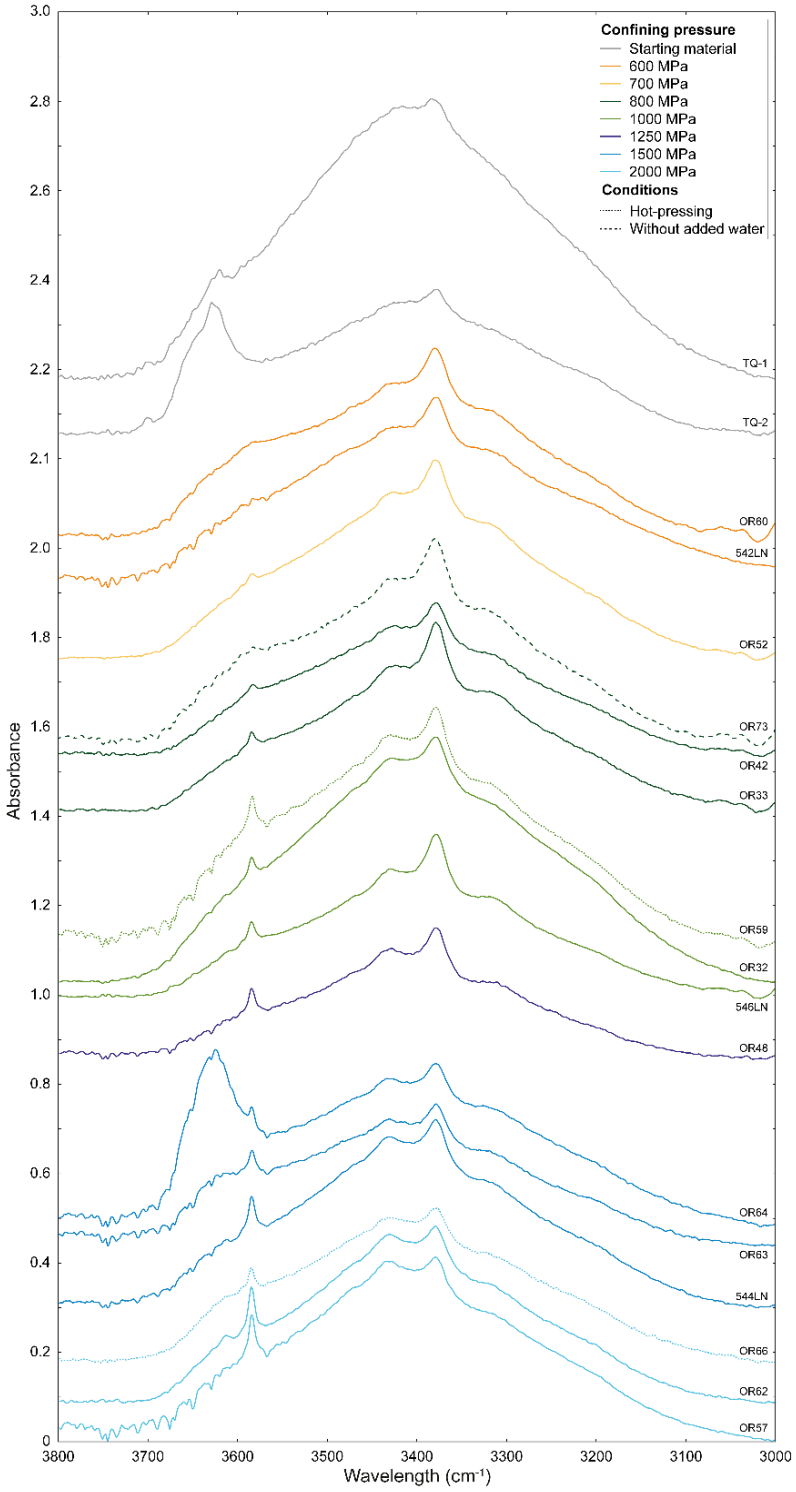

Figure IV.25. Average spectra for grain interiors of starting material and samples deformed at 10^{-6} s^{-1} or hot-pressed at pressure from 600 to 2000 MPa. Spectra are normalized to 1 mm thickness and shifted.

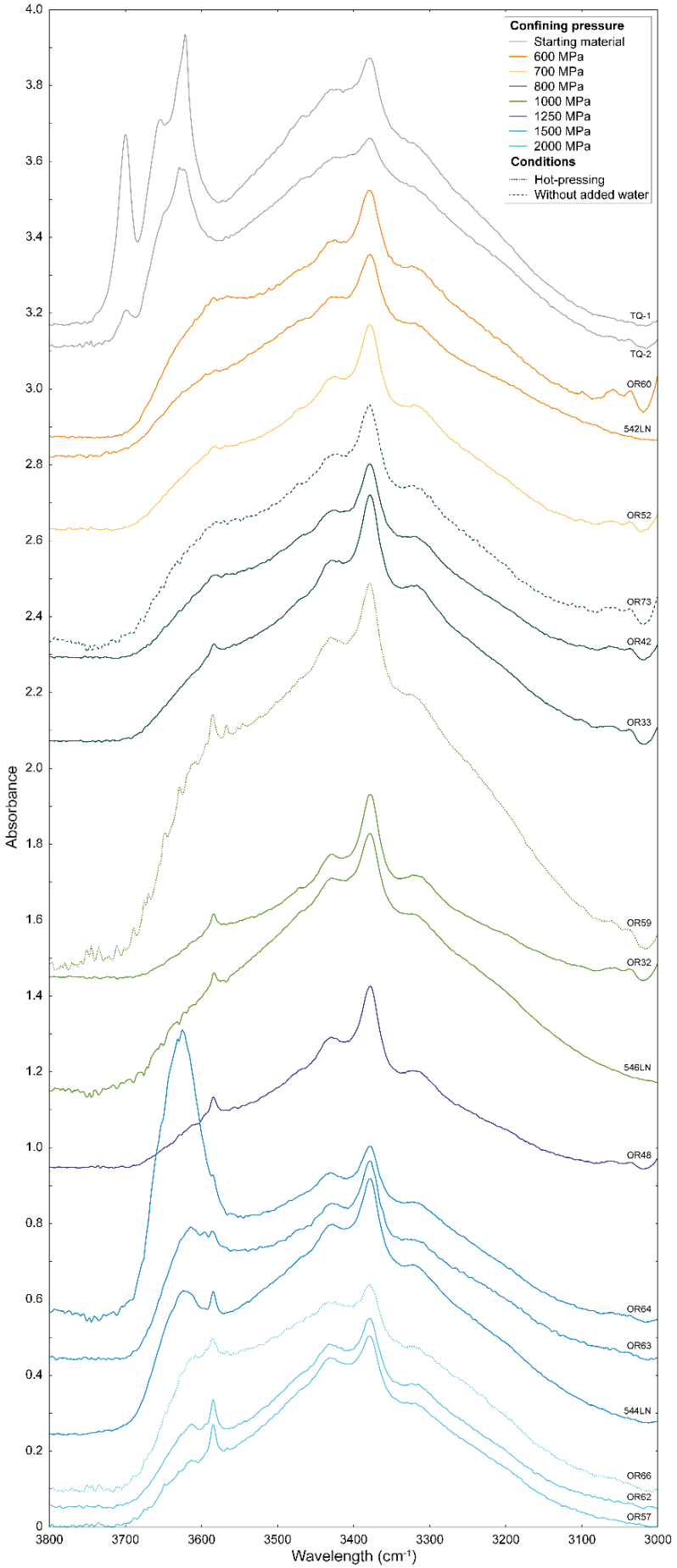

Figure IV.26. Average spectra for grain boundaries of starting material and samples deformed at 10^{-6} s^{-1} or hot-pressed at pressure from 600 to 2000 MPa. Spectra are normalized to 1 mm thickness and shifted.

The intensities of the Al-H/Li triplet in the mean spectra can be correlated with the type of microstructures measured (grain interiors or grain boundaries, Figure IV.27). For all the samples considered, the triplet is more present in the mean spectra calculated for the grain boundaries than for the grain interiors. The 3379 cm^{-1} band shows the highest absorbance values then the 3429 cm^{-1} band and then the 3319 cm^{-1} one. The behaviour of the three bands is similar inside one sample and from one sample to another.

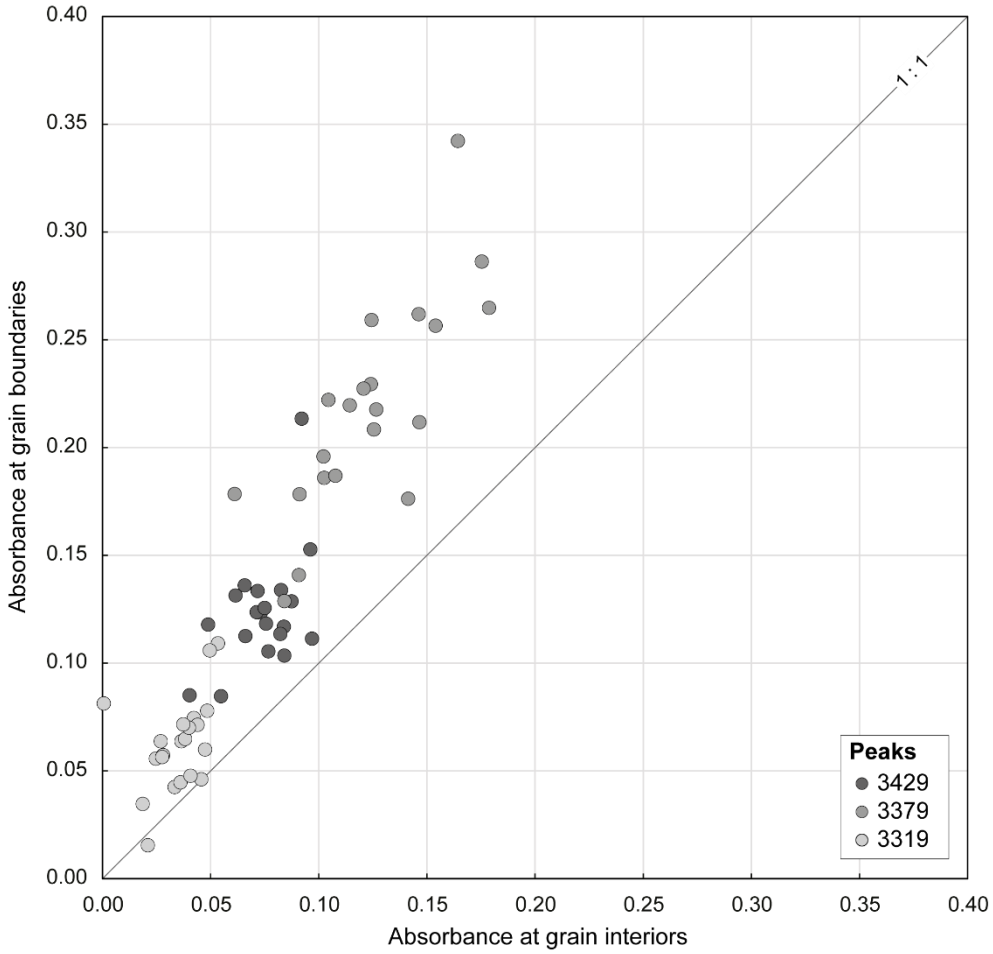

Figure IV.27. Absorbance values of the bands composing the Al-H/Li triplet (3429, 3379 and 3319 cm^{-1}) at grain interiors vs. grain boundaries. The absorbance is greater at grain boundaries with band at 3379 cm^{-1} higher than the one at 3429 cm^{-1} and band at 3319 cm^{-1} with lower height. The absorbance values have been normalized to 1 mm thickness.

No dependence of the Al-H/Li triplet absorbance values with pressure could be established. But the band heights of deformed samples are higher than starting material ones, both for grain interiors and grain boundaries. For samples deformed at 2000 MPa, the mean spectra calculated for the recrystallized area display higher triplet absorbance values than in the grain boundaries and grain interiors.

When considering the intensity of the 3585 cm^{-1} band from the mean spectra as a function of the pressure (Figure IV.28), a positive trend is observed. The band height increases with pressure and is higher in the grain boundary region than in the grain interior. However, the data show an important scattering.

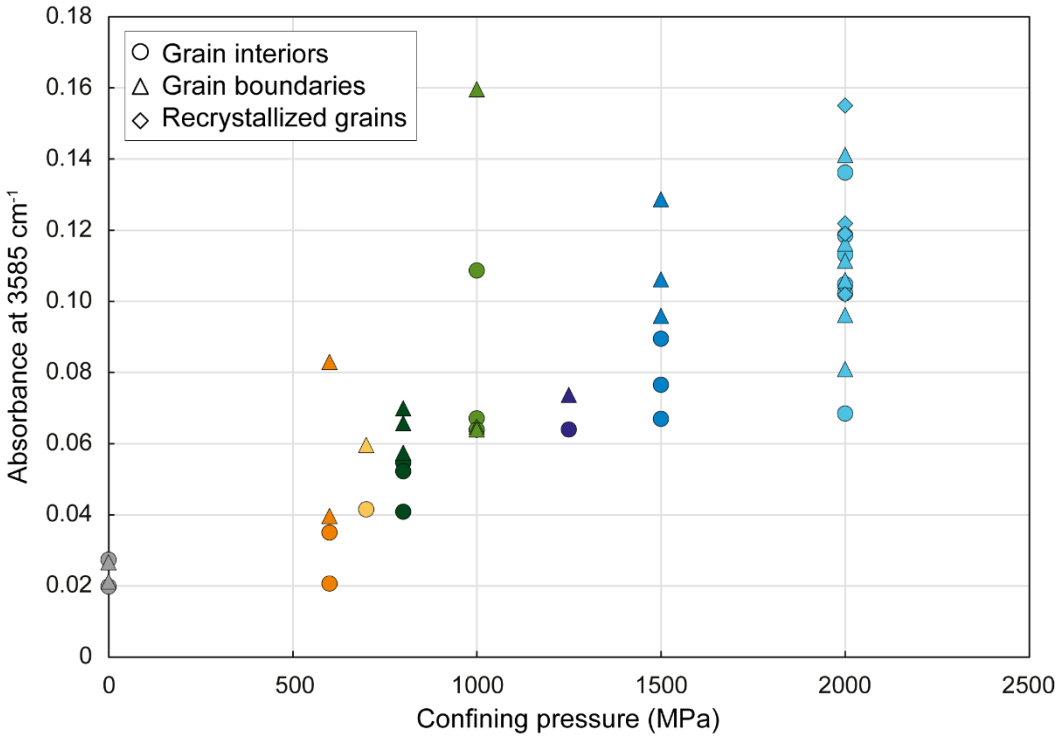

Figure IV.28. Absorbance at 3585 cm^{-1} as a function of the confining pressure. The intensity of the band increases with the pressure. Absorbance values are normalized for sample of 1 mm thickness.

For the samples deformed at 2000 MPa which achieved different finite strain, the intensities of the 3585 cm^{-1} band shows a trend of decreasing intensity with increasing finite strain (Figure IV.29) comparable to the one observed for the mean H_2O contents (Figure IV.16) indicating a probable influence of the deformation mechanisms on this band.

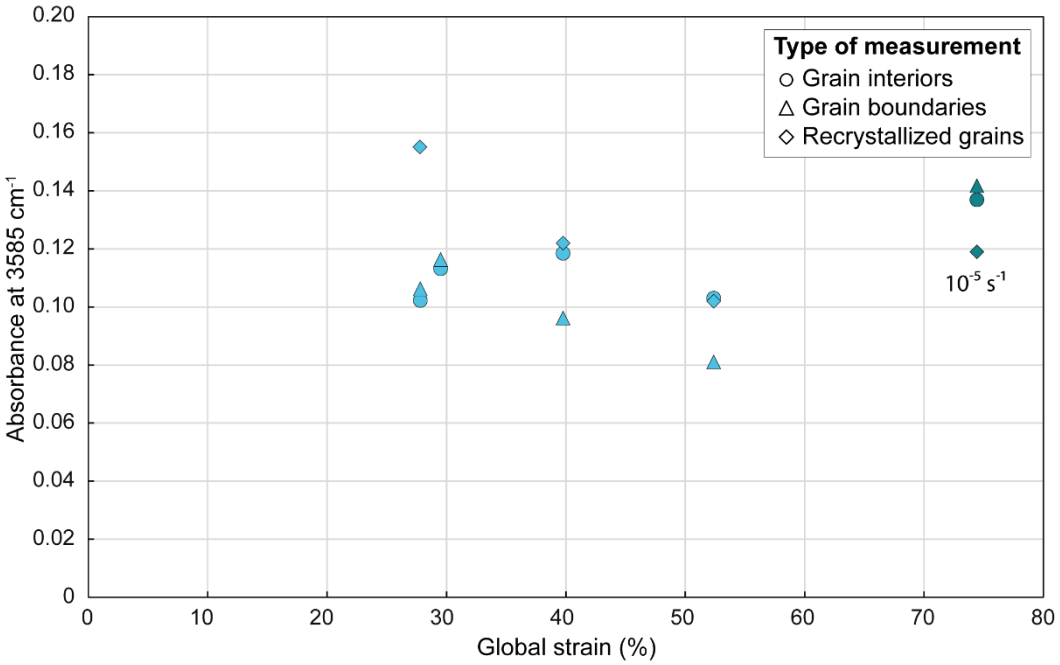

Figure IV.29. Intensities of the absorbance of the 3585 cm^{-1} band from average spectra of samples deformed at 2000 MPa as a function of the global strain achieved. Samples with 27.76 to 52.38% strain were deformed at 10^{-6} s^{-1} strain rate whereas sample deformed with 74.43% strain was deformed at 10^{-5} s^{-1}. The absorbance values have been normalized to 1 mm thickness.

IV.2.2.2. Band frequency for some of the deformed samples

For samples deformed at comparable finite strain ~30% and different confining pressure (OR52, OR32 and OR62, respectively at 700, 1000 and 2000 MPa) or strain rate and finite strain (OR56 at 2000 MPa, ~74% and 10^{-5} s^{-1}), the percentage of spectra displaying some of the interest bands have been listed (Table IV.7). For each spectrum, it has been considered whether it was rather displaying only a broad absorption band or an Al-H/Li triplet and if the absorption bands at 3596, 3585 and 3467 cm^{-1} or related to sheet silicates (3700 – 3650 cm^{-1}) were present or not. This was done for both grain interiors and grain boundaries, as well as cement and triple junctions for sample TQ-2 and recrystallized areas for sample OR56. Spectra measured on the OR62 sample (2000 MPa), show no significant difference between the least and most deformed part, yet, they have then been grouped for this section.

The description and presentation of the spectra related to the starting material samples are detailed in the part IV.2.1 and in Figure IV.19 to Figure IV.24.

Only the starting material samples show a majority of spectra displaying a broad absorption band whereas deformed samples present a majority of spectra where the Al-H/Li triplet is present. For all the samples, the number of spectra with the triplet increases in the grain boundary region compared to the grain interiors.

The bands related to the presence of sheet silicates are less present and with lower intensities in deformed samples than in the starting material (except for sample OR62 grain boundaries). They are in majority observed in the grain boundary region than in the grain interiors.

For the thin absorption band at 3596 cm^{-1}, its occurrence in deformed samples decreases with pressure (with a slightly higher presence in the grain interiors than in the grain boundaries).

As previously shown for the mean spectra (Figure IV.25, Figure IV.26 and Figure IV.28), the deformed samples significantly display the absorption band positioned at 3585 cm^{-1}. While starting material samples (grain interiors, grain boundaries, cement, and triple junction) show few spectra with this band, its presence strongly increases in deformed samples and with pressure. It is present in all the spectra (either in grain boundaries or grain interiors) of samples deformed at 1000 and 2000 MPa (OR32, OR62 and OR56).

Finally, the presence of the 3467 cm^{-1} band is quite similar in deformed samples and frequently associated to spectra also displaying the Al-H/Li triplet.

Table IV.7. Percentage of spectra displaying the absorption bands considered for starting material and samples deformed at different conditions.

Grain interiors (%)						
Sample	TQ-1	TQ-2	OR52	OR32	OR62	OR56
Broad band	65.28	52.24	21.85	19.40	10.48	19.72
Al-H/Li triplet	34.72	47.76	78.15	80.60	89.52	80.28
Sheet silicates	22.22	74.63	23.53	17.16	33.33	7.04
3596 cm^{-1}	16.67	34.33	34.45	17.16	10.48	11.27
3585 cm^{-1}	12.50	19.40	76.47	98.51	100	100
3467 cm^{-1}	22.22	23.88	43.70	56.72	37.14	30.99
Grain boundaries (%)						
Sample	TQ-1	TQ-2	OR52	OR32	OR62	OR56
Broad band	37.33	34.85	10.43	3.01	5.83	19.51
Al-H/Li triplet	62.67	65.15	89.57	96.99	92.50	80.49
Sheet silicates	69.33	87.88	32.17	5.42	78.33	4.88
3596 cm^{-1}	25.33	51.52	29.57	11.45	17.50	9.76
3585 cm^{-1}	16.00	28.79	57.39	98.80	98.33	100
3467 cm^{-1}	30.67	53.03	55.65	50.60	41.67	41.46
Other categories (%)						
Sample	TQ-2				OR56	
category	Cement		Triple junctions		Recrystallized grains	
Broad band	14.49		11.59		3.85	
Al-H/Li triplet	85.51		88.41		96.15	
Sheet silicates	69.57		86.96		9.62	
3596 cm^{-1}	15.94		40.58		17.31	
3585 cm^{-1}	5.80		26.09		100	
3467 cm^{-1}	50.72		62.32		36.54	

Compared to the samples deformed at lower strain rate and lower finite strain, the sample OR56 does not show significant differences, either in the band occurrences or absorbance intensities.

IV.3. Discussion

IV.3.1. Araldite® contamination and correction estimation

Araldite® contamination represents a problem for FTIR measurements of H_2O contents in minerals because it also contains H_2O, and total H_2O concentrations are increased. This issue was previously reported by few authors (e.g., Mainprice, 1981; Mainprice and Paterson, 2005; Gumez, 2010).

As epoxy was used to ensure the coherence of the material during the thick sections preparation and because it was not possible to remove it without compromising the sample coherence, a correction procedure was developed in order to address the issue.

As seen at the beginning of this chapter (part IV.1.1), this method of correction has a non-negligible influence on the H_2O contents. When quantifying the effect of the correction on the calculated mean H_2O contents, it appears that the spectra contaminated with araldite generally show lower H_2O contents than the rest of the data (Figure IV.2). Indeed, when removing the contaminated spectra (with an area superior to 30 or 50% of the total absorption area), the mean H_2O content is generally increased. This probably also indicates that with an increasing amount of H_2O the error becomes larger.

In addition to that, the influence of the Araldite® depends on the sample microstructure. As shown Figure IV.1, samples with more cracks (or porosity) seem to more incorporate the epoxy into their structure and then show more contaminated spectra. Thus, the correction may affect cracked samples to a greater extent. The comparison between samples presenting different amounts of cracks can become more difficult as the error induced by the correction is not equal.

Moreover, during the data pre-treatment some spectra were removed from the data set because the Araldite® correction induced a negative absorbance for some wavelengths. As a general form was taken for the corrected broad H_2O region, it sometimes led to a deformation of the spectra and to an overestimation of the area to be corrected. Some improvements should be made here.

The best solution remains not to use Araldite® or epoxy showing infrared absorption bands in the OH region for sample preparation in order to obtain reliable data that do not need a correction. Moreover, if the consistency of the material is not important, the epoxy can also be removed chemically. However, if these solutions are not conceivable, a correction procedure is now available to overcome this issue, but it cannot be used automatically and still requires careful examination of the data.

IV.3.2. H_2O content variations with pressure and deformation

Note concerning the incertitude of the areas measured

Before going further, a precision has to be made concerning the different microstructures measured. The thick sections studied (except TQ-1) have a thickness of the same order of magnitude as the grain diameters. This implies that the infrared beam may have crossed

different microstructures during its path through the sample. The probability is lower for the grain interiors for which special care was taken to measure clear areas but for the grain boundaries, that are thinner and complex microstructures, the probability is greater.

This issue was previously reported by others, for example Mainprice and Paterson (1984) indicated that the comparable size of grains and section thickness leads to an underestimation of the amount of hydroxyl concentrated near the grain boundaries. In this study, as the H_2O contents for grain interiors were measured on clear areas, the perturbation induced by grain boundaries (and recrystallized area) on the beam path is low, and this is supported by generally lower contents found for grain interiors than for the grain boundaries (Figure IV.7). However, for the grain boundaries, the probability for the infrared beam to cross grain interiors in addition to only grain boundaries is high and certainly has induced certainly an underestimation of the H_2O content for these regions, i.e., the measured H_2O content is not only that of the grain boundary region itself (in agreement with Mainprice and Paterson, 1984).

In addition to that, it could be added that as the thick sections were cut parallel to the shortening direction, the grains (considered as round shaped in the starting material) should be elongated in the same way in all the directions perpendicular to the shortening one, including the direction along which the infrared measurements were carried out. Thus, the measurements made on grain interiors should be quite reliable.

These considerations have to be kept in mind as a source of errors for the rest of the interpretation and discussion.

Starting material

The H_2O contents of the grain interiors of the starting material show a wide diversity reflecting the sedimentary nature of the material. This is highlighted by elevated standard deviations and broad data dispersions (Table IV.2 and Table IV.3 and Figure IV.3 and Figure IV.4), grains displaying H_2O contents of 100 H/10^6 Si up to 5500 H/10^6 Si. The grain boundary regions the of starting material contain more H_2O than the grain interiors and show an even wider dispersion ranging from 500 to more than 7500 H/10^6 Si. The highest concentration in the grain boundary region is confirmed by the elevated mean H_2O content also found at triple junctions. Despite the absence of fluid inclusions, the authigenic cement, presents a higher mean H_2O content than the grain interiors (1727 H/10^6 Si) which sometimes contain visible fluid inclusions (see Figure III.1 in the previous chapter).

The two samples of starting material measured have different mean H_2O content values (Figure IV.5), but similar distributions (Figure IV.6). These differences confirm the heterogeneity of the starting material and will presumably influence the dispersion of H_2O contents measured in the experimental samples.

As quartzite samples consisted of polycrystalline aggregates, different behaviour may be expected to occur within the grain and at the grain boundaries. Microstructural differences have been highlighted in the deformed sample in the previous chapter (Figure III.12 and part III.3).

IV.3.2.1. Grain interiors

As evidenced by the lower H_2O contents measured for both hot-pressed and deformed samples, the H_2O content decreases as a result of applied pressure and temperature conditions (Figure IV.9). The deformation of samples induces, in addition to the decrease of H_2O content, a narrowing of the range of H_2O content distribution towards the lower values (Figure IV.10 to Figure IV.13). Therefore, the highest H_2O content values (> 2500 H/10^6 Si) become rarer in the deformed samples. This is also shown by the similar broad H_2O content distribution displayed by the hot-pressed samples and starting materials (Figure IV.11).

Within the samples presenting a strain partitioning, the higher strain parts contain less H_2O (both in grain interiors and grain boundaries) than the lower strain parts (Figure IV.14 & Figure IV.15), indicating that the mechanisms responsible for the decrease of H_2O content with strain are effective at a local scale. As presented in the previous chapter, differences in strain are reflected in microstructural features. Grains in the least deformed part show little evidence of plastic deformation and keep their original rounded shapes, whereas grains in the most deformed parts display elongated shapes, undulatory extinction and development of subgrains with, sometimes, the formation of core-and-mantle structures.

For the same conditions of deformation (2000 MPa confining pressure, 900°C temperature and 10^{-6} s^{-1} strain rate), when the finite strain of samples increases, the mean H_2O content decreases in grain interiors and grain boundaries (Figure IV.16).

The samples deformed at the same conditions also spend different amount of time at pressure and temperature conditions (Table IV.6). This duration is not necessarily linked with the amount of finite strain achieved as the sample OR62 shortened to ∼30% spent more time than the other samples at pressure and temperature conditions in the apparatus. For this sample, the assembly was modified compared to the others in order to increase the time before the hit-point (theoretical point at which the sample starts deforming, see details in the Methodology chapter, part II.1.5.1). So, the OR62 sample spent, in fact, more time in “hot-pressing” stage (during the run-in curve, i.e., when the σ1 piston is pushing through the lead) than in the deformation stage compared to the other samples (especially OR57 deformed at the same finite strain which displays the same H_2O contents, Figure IV.16). Moreover, it must be noted that for the samples OR50, OR54, OR56 and OR57, no run-in curve could be observed (the hot-pressing stage last only one night and then the recorded time directly corresponds to the deformation stage, as the hit-point was certainly attained during the pumping stage, see details in the Methodology chapter, part II.1.2.6).

So, it appears that the duration for which samples underwent the pressure – temperature conditions has a positive influence on the decrease of H_2O content when the duration is directly related to the deformation (samples OR57, OR54 and OR50 and OR56, Figure IV.17). However, the duration cannot necessarily be connected to the application of pressure and temperature conditions (sample OR62, Figure IV.17). This implies that the mechanisms acting during the deformation are more effective to reduce the H_2O content than the processes acting with the pressure and temperature conditions (such as diffusion).

At the same pressure – temperature – strain rate conditions, the global amount of strain seems to have a higher influence on the H_2O content evolution than the experiment duration. This

observation is a first evidence indicating a stronger influence of the plastic mechanisms on H_2O mobilisation than diffusion processes. This evolution of H_2O contents with finite strain can be linked to the evolution of the microstructures observed as a function of the same parameters (Figure IV.18).

The OR56 sample was deformed at higher strain rate (10^{-5} s^{-1}) and to a higher amount of finite strain (∼74%) and small amount of time (32h). It contains more H_2O than the samples deformed at the same pressure-temperature conditions but at lower strain rate and to lower finite strains (Figure IV.16). The microstructures developed by this sample also differ from the ones observed in the other samples (Figure IV.18) with deformation lamellae in the highly elongated grains and small recrystallized material. For this sample, the influence of the global strain is lower than the influence of the faster strain rate (with ∼74% shortening a very low H_2O content would be expected if the sample was deformed at 10^{-6} s^{-1}). The change in the microstructures and the deformation processes at their origin thus has a high influence on the H_2O content. The higher H_2O content measured in the OR56 sample is in agreement with the fact that lower time of deformation leads to higher H_2O content (Figure IV.17).

Several hypotheses can be examined to explain the loss of H_2O during the experiments but before considering the processes occurring during the deformation, some external influences have to be discussed.

First, the loss of H_2O during the preparation of the thick sections cannot be excluded. However, as starting and experimental materials were prepared and measured the same way, even if H_2O was lost, the measurements should still be comparable. Moreover, this H_2O loss should concern more the H_2O stored at grain boundaries than in the grain interiors.

A H_2O loss by a jacket leak during the experiment is unlikely because it would have been seen on the mechanical curves and then with presence of salt inside the jacket. That was not the case, for none of the samples.

Then, the causes responsible for the diminution of H_2O contents in the grain interiors with deformation that can be envisaged are (i) volume diffusion of H_2O out of the grains, (ii) microcracking favouring the H_2O loss or (iii) plastic deformation processes redistributing H_2O (dislocation motion, recrystallization).

Diffusion

For clear areas, where no cracks are observed, very low values of both diffusivity and solubility of H_2O into quartz are reported. Gerretsen et al. (1989) calculated low values of solubility of H_2O into quartz less than 100 H/10^6 Si that correspond to a diffusion coefficient of H_2O limited to 10^{-12} m^2/s. These values are in agreement with the previous studies of Kronenberg et al., (1986) (10^{-10} to 10^{-11} m^2/s) and Rovetta et al. (1986) (10^{-7} to 10^{-6} cm^2/s) performed at 900°C and 1500 MPa.

Considering these diffusion coefficients, the amount of H_2O that could diffuse into (or out of) the quartz grains during the experiments is thus far below the variations observed in our samples (Figure IV.9) and to the sensibility of infrared measurements. The diffusion of H_2O is too slow to be effective during the experimental times and thus certainly not responsible of the H_2O loss at the grain interior scale. The diffusion process cannot be considered to explain the

H_2O content variations of several hundreds of $H/10^6$ Si in deformed samples compared to the starting material.

Diffusion phenomenon of H_2O is too slow to attain the equilibrium during the experiment duration. However, diffusion of hydrogen is possible and rapid enough for equilibration within the experimental times (Kronenberg et al., 1986) but, the hydrogen has no apparent mechanical effect on the quartz strength (Kronenberg et al., 1986), as this is the broad absorption band that is correlated with the H_2O weakening (Kekulawala et al., 1978).

Thus, the diffusion of H_2O is not enough effective to explain the amount of H_2O content that is lost inside the grains during the deformation. This is in adequacy with the observation that the duration of pressure and temperature conditions seems to have a lower influence in the H_2O contents variations than the deformation (Figure IV.17).

Microcraking

The presence of cracks is of concern because their presence has been shown to be an effective process for the penetration and diffusion of molecular H_2O into (or out of) quartz (e.g., Kronenberg et al., 1986; Rovetta et al., 1986).

Microscopic observations indicate that microcracks occur in the studied samples (confirmed by the presence of epoxy for some grain interiors measurements). Several types of cracks can be distinguished in the samples as some certainly formed during the different stages of deformation whereas some others formed during the thick section preparation (and filled with the Araldite® epoxy glue). The latter are not thought to cause a change in the H_2O contents measured, as they were avoided during the grain interior infrared measurements.

Cracks formed during the depressurization of the samples (unloading cracks, perpendicular to the shortening direction) are commonly observed and could have affected the grain interiors but in a minor way. Moreover, during the infrared data acquisition, special care was made so that the areas measured for the grain interiors were clear (in particular, without visible cracks or fluid inclusions) and with a good signal.

As detailed in the previous chapter, grain plastic deformation was accompanied by the formation of a dense network of fluid assisted microcracks, sealed by the precipitation of a quartz displaying a bright blue luminescence. Most of these cracks revealed by cathodoluminescence formed during deformation, are located in the grain boundary region and affect the cement rather than grain interiors (Figure III.14 and Figure III.15, part III.3.2.1, previous chapter). Therefore, these microcracks visible in cathodoluminescence, are unlikely to account for the decrease in fluid concentration in the grain interiors.

As fluid inclusions were present in the starting material (Figure III.1 in the previous chapter, part III.1.3) but less observed into the deformed samples, it is probable that cracks formed during the early stages of the experiments and then subsequently healed, redistributing the fluid inclusions into smaller fluid aggregates, which cannot be observed with optical microscopy (Tarantola et al., 2010). The dispersion of the fluid inclusions to a more homogeneous distribution would not be characterized by an increase of the broad absorption band as it is just supposed to redistribute it. This is not the case for the samples considered here, where the broad band intensity decreases with grains deformation. The crack healing could occur rapidly in the early stages of the experiments and participate to redistribute the H_2O into the quartz

grains (Fitz Gerald et al., 1991; Tarantola et al., 2010). The presence of the healed cracks could then promotes the plastic deformation by allowing the generation and multiplication of dislocations (Tarantola et al., 2010; Stünitz et al., 2017).

Even if the fluid inclusions decrepitate at the early stages of deformation, and that healed cracks form, the expulsion of H_2O by such a cracks network is not observed in the samples, especially in cathodoluminescence images where the cracks are not affecting the grains.

All of this implies that other processes are required to induce a reduction of H_2O contents in the deformed samples. So, early cracks certainly redistribute H_2O in the sample, as it is observed that they are associated with visible small fluid inclusions, but do not explain the decrease in H_2O content at final stages of deformation. Cracking and crack healing can contribute to the crystal plastic deformation of samples (Tarantola et al., 2010; Stünitz et al., 2017).

Plasticity

The last hypothesis that could be envisaged to explain the loss of H_2O during the deformation is the action of plastic deformation processes.

The H_2O contents measured on the grain interiors for samples deformed up to 30% shortening at 10^{-6} s^{-1} reveal a decrease compared to starting material (Figure IV.9). This decrease is observed for all the confining pressures applied and with deformation. Compared to the starting material where the grains are not deformed, the grain interiors of deformed samples display different features associated to plastic deformation (elongated shapes, undulatory extinction, formation of subgrains, presence of deformation lamellae and recrystallization by subgrain rotation) characteristic of dislocation creep mechanisms (regime 2 of Hirth and Tullis, 1992). In the previous chapter, it was deduced that the strain achieved by the samples is accommodated by the plastic deformation of individual grains (which centre is measured by FTIR). This suggests the evolution in the H_2O content during deformation could be facilitated by the movement of dislocations.

The evolution of H_2O contents with finite strain can be linked with the different microstructures displayed in the samples (Figure IV.18). The regime of deformation undergone by the samples apparently plays a role on the H_2O contents. Indeed, the H_2O contents decrease when finite strain increase and samples display microstructures characteristics of regime 2 to regime 3 (Hirth and Tullis, 1992).

This is highlighted by the higher H_2O contents measured for the sample OR56 deformed at higher strain rate and displaying microstructures different from the other samples (Figure IV.16 and Figure IV.18f). The grain interiors present abundant deformation lamellae and a great amount of small-sized recrystallized grains but less undulatory extinctions and subgrains.

As discussed earlier, the H_2O present as fluid inclusions in the starting material is certainly rearranged and more homogeneously distributed into the grains during the early stages of deformation (pressurization) by decrepitation, cracking, and crack healing (Fitz Gerald et al., 1991; Tarantola et al., 2010; Stünitz et al., 2017). But these processes do not induce a significant change in the H_2O content repartition, as shown by the hot-pressed sample (Figure IV.11). However, the associated formation and multiplication of dislocations with the redistribution of small fluid inclusions may facilitate the subsequent deformation processes (Vityk et al., 2000).

With deformation by dislocation creep, the diffusion of H_2O may be facilitated by the movement of dislocations under the action of differential stress. The migration of the dislocation is an efficient way to transport H_2O, in the form of the small H_2O aggregates associated with dislocations. In addition, the rearrangement of dislocations to form subgrains boundaries and then new grains by consecutive subgrain rotation could also contribute to expulse the H_2O out of the original grains, as diffusion of H_2O along the subgrains and grains boundaries is enhanced compared to volume diffusion into the quartz crystal.

During dislocation creep deformation, H_2O could then be transported from the grain interiors to the edges and then to the grain boundaries. As the amount of subgrains and recrystallized grains formed increase, the H_2O content decrease in the original quartz grains (Figure IV.16 and Figure IV.18). The formation of subgrains and recrystallization accommodates the plastic deformation of samples and increase with the finite strain. The H_2O concentration of the samples depends, then, on their deformation (notably on the formation of subgrains and on recrystallization) that controls the diffusion of H_2O.

The formation and mobility of (sub)grains boundaries as already been proposed as efficient processes to increase (Gleason and DeSisto, 2008) or decrease (Palazzin et al., 2018) the H_2O content.

Based on the measurements carried out, no clear relationship could be established between the grain interior H_2O contents and the mechanical weakening observed with increasing confining pressure. Indeed, except for a reduction in H_2O contents compared to the starting material, no clear link appears between the confining pressure and the H_2O contents measured (Figure IV.8 and Figure IV.9) whereas there is a relationship between the confining pressure and the flow stress (Figure III.25 part III.4.4 in the previous chapter). From infrared measurements, it is observed that the plastic deformation of samples enhances the reduction of the grain interiors H_2O contents, but even if the pressure was not the same, all the samples shortened to 30% were deformed by similar deformation mechanisms. There is not a strong influence of pressure on the microstructures associated to plastic deformation of the samples even if the amount of subgrains and recrystallized material increases slightly with increasing pressure. Thus, it is not surprising that no pressure dependence on mean H_2O content is observed.

One important question that emerges with the general decrease in H_2O content with deformation is why the samples do not exhibit hardening with increasing strain? Indeed, the mechanical curves (except for OR60 sample deformed at 600 MPa) show a continuous flow stress (or even slight weakening) up to 30% shortening (Figure III.7 in the previous chapter, part III.2.1). As the strain is principally accommodated by plastic deformation processes, a sufficient amount of H_2O is needed to promote the plastic deformation all along the experiment. Even if the H_2O content decreases, grains do not become dry and there may still be sufficient H_2O available for the weakening process to take place.

IV.3.2.2. Grain boundaries

For all the samples considered (starting material, hot-pressed and deformed samples), the H_2O content is always higher in the grain boundary region than in the grain interiors (Figure IV.7). This observation is still valid, regardless of the pressure, strain rate or the strain amount (local

– Figure IV.14 – or global – Figure IV.16). This supposes that the H_2O content is rather concentrated into the grain boundaries of the polycrystalline aggregate.

The comparison between deformed samples and the starting material from which they come from indicates that the H_2O contents of grain boundaries are lower for deformed samples (Figure IV.9). In addition, the H_2O content distributions are less dispersed for deformed samples than for the starting material (Figure IV.10 to Figure IV.13). The grain boundaries in the most deformed parts always contain less H_2O than in the least deformed parts (difference of 860 $H/10^6$ Si, Figure IV.15). The elevated H_2O content values are then less present with deformation, indicating a probable redistribution.

When considering the samples deformed at the same conditions but with different amount of finite strain achieved, the mean H_2O content in the grain boundaries decreases with increasing finite strain (Figure IV.16) for samples deformed at the same strain rate. For higher amount of strain but faster strain rate (OR56 sample), the mean H_2O content is more elevated than the samples deformed at the same pressure-temperature conditions, as observed for the grain interiors.

The same tendencies of mean H_2O content evolution with deformation than for the grain interiors are observed for the grain boundaries.

It must be mentioned again that the measured areas for grain boundaries were made on microstructural sites where two original grains were adjacent. Moreover, there is a significant uncertainty concerning what it is measured as the grain boundaries represent small objects compared to the thickness crossed by the infrared beam (as discussed earlier). In addition to that, grain boundaries are complex places where several processes can occur (see in the following).

As H_2O contents are calculated from the broad infrared absorption band related to molecular stretching of H_2O (3000 – 3800 cm^{-1}), the higher mean H_2O contents indicate that more molecular H_2O is contained in the grain boundaries than in the grain interiors. This difference is explained by the very limited solubility of H_2O into the crystal lattice (Gerretsen et al., 1989) compared to the grain boundary region where defects are more likely incorporated.

Several models are proposed to describe how the H_2O may be distributed on grain surfaces, along the grain boundaries as: thin film, channel and islands or as more or less interconnected networks (e.g., Farver and Yund, 1992; Nakashima, 1995; den Brok, 1998). In the first one, a thin film of confined fluid (few nanometres) is present around (and so between) the grains surfaces whereas for the two others, the fluid is present in some places (channels or networks, larger sized than the thin films) which are isolated by solid grain contacts (islands).

In this study, it is difficult to consider one special model for the intergranular H_2O, but it can be supposed that in one way or another molecular H_2O has been able to move and diffuse along the grain boundaries during the deformation.

Different processes could take place in the grain boundary region during the experiments. First, the processes of fluid inclusion decrepitation, cracking and crack healing as previously described for the grain interiors could also happen near the grain boundaries (but should not constitute a major process as very few fluid inclusions were observed into the cement). In the thin section, optical and cathodoluminescence images show (stepladder) cracks affecting the

grain boundary region (Figure III.15 in the previous chapter, part III.3.2.1). The healed cracks observed present for some of them associated fluid inclusions. Decrepitation of fluid inclusions and cracking and crack healing occurring during the pressurization of the samples could have induced H_2O to be transported from the grain interiors to the grain boundary region and increase their H_2O content.

Then, several processes occurring at the grain boundaries during deformation have been identified (cf. previous chapter), such as formation of new grains by recrystallization and cracking processes. Light blue luminescence revealed by cathodoluminescence images show that these processes imply an interaction with a fluid phase (the luminescence certainly highlight the material precipitated during the deformation).

It has been described previously how dislocation creep certainly allowed H_2O to be transported (via dislocation motion and preferential diffusion of H_2O along grain boundaries) from the grain interiors to the grain boundary region. These processes would cause an increase in the amount of the fluid phase along the grain boundaries.

The processes described above imply that the H_2O loss from the grain interiors goes to the grain boundaries and thus, an increase in the H_2O content in the grain boundary region is expected. However, the formation of new and small grains (by recrystallization or cracking) lead to an increase of the grain boundaries surface in the sample. The capacity of storage of H_2O into the sample is then increased by the formation of new grains and with the action of a fast diffusion, the H_2O could be redistributed all along them.

The grain boundary diffusion is described as several order faster than the volume diffusion into the grains and along dislocations cores (Nakashima, 1995) and could be effective at the experimental time scale. Evidence of diffusion during deformation are given by the bright blue luminescence observable in the grain boundary region in cathodoluminescence images.

Distribution of H_2O along the grain boundaries certainly includes several processes, and it is difficult to quantify the contribution of each one. The processes of H_2O redistribution are certainly complex and involve different mechanisms such as cracking, recrystallization, solution-precipitation, dislocation movement and diffusion. The diffusion at grain boundaries does not seem to play an important mechanical role as the main deformation mechanism of the samples was mainly accommodated by dislocation creep but it could be important process for H_2O redistribution.

Lastly, as H_2O (0.1 wt.%) was added to the samples prior to the experiment, it also would be expected to find this H_2O in the grain boundary region but it is apparently not the case. An overall decrease in the total amount of H_2O contained in the sample, with respect to the starting material, irrespective of the H_2O added to the experimental assemblage. There are two possibilities to explain this apparent H_2O loss: (i) the system has not been closed, and H_2O has been transferred to the confining medium or (ii) H_2O has been expelled to the boundary between the sample and the jacket, next to the weak confining medium. In this region the H_2O would be lost during sample sectioning and preparation and would therefore not be measured. The latter is the preferred explanation.

Recrystallized areas

Measurements made on the recrystallized areas of samples deformed at 2000 MPa indicate either lower or higher H_2O contents than in the grain interiors and grain boundaries (Figure IV.16). As the aperture (40 x 40 µm) used for measuring these areas was larger compared to the size of the recrystallized grains (< 10 µm) the mean H_2O content values include both the small grains and the surrounding boundaries. In addition to that, the volume of these recrystallized areas is certainly not constant through the thickness of the measured section. The measured values, thus, do not indicate that these grains are more or less hydrated than the coarser grains because too many parameters can influence on these values. Moreover, the measured areas do not contain the same number of recrystallized grains as they show different sizes from one sample to another.

In addition to that, these areas certainly did not form in the same way as two mechanism of small grains formation are possible. The origin of small grains could occur by either recrystallization by subgrain rotation or by cracking (cf. previous chapter). Moreover, for the samples deformed to high finite strain other mechanism for recrystallization could be possible such as grain boundary migration. These areas would then require a more detailed study.

Note: certain parts were too complex after deformation and then not measured, this is the case for all the cement regions. Whereas it was observed (in cathodoluminescence images notably), that processes take place in these regions. A detailed study by, for example, area mapping could be interesting to implement.

IV.3.3. H_2O storage in the microcrystalline aggregate

IV.3.3.1. OH speciation

Large band vs. discrete bands

Infrared measurements on quartz are commonly described as composed of an association of a broad isotropic absorption band and to thinner discrete bands (Kats, 1962). The broad absorbance is centred at 3400 cm^{-1} and related to molecular H_2O (Aines and Rossman, 1984) whereas small bands correspond to the stretching absorption of OH bonded to different defects in the 3000 – 3800 cm^{-1} range.

Aines and Rossman (1984) attributed the broad band to the stretching of OH bounds in molecular H_2O within the quartz grains. It corresponds to molecular H_2O contained in small inclusions, clusters or aggregates (Aines and Rossman, 1984; Kronenberg and Tullis, 1984; Kronenberg and Wolf, 1990; Kronenberg, 1994). The broad absorption band is thus a marker of different things as it can show the presence of sub-micron scale H_2O clusters (non-freezable H_2O) to micron-scale fluid inclusions (freezable).

The characterisation of this band is of interest since the hydrolytic weakening of quartz has been correlated with the broad absorption centred at 3400 cm^{-1} (e.g., Kekulawala et al., 1978, 1981; Kronenberg et al., 1986) and not related to the discrete absorption bands. The mechanical properties of quartz depend on the presence of molecular H_2O related to the broad absorption band, with a decrease in strength when the band increases.

The measurement of the broad absorption band area (taking into account the discrete thin bands) allows the quantification of the H_2O content contained in the quartz grains (e.g., Paterson, 1982; Libowitzky and Rossman, 1997; Stipp et al., 2006). The H_2O contents calculated earlier, are thus good indicators for the evolution of the area of the band with the experimental conditions. But no distinction between fluid inclusions or the size of H_2O defects (freezable/unfreezable) was made as measurements were recorded at ambient conditions.

Most of the spectra recorded on the starting material grain interiors present a broad H_2O band to structurally bonded molecular H_2O without discrete OH bands (Figure IV.19 and Figure IV.21). In grain boundaries, discrete bands are frequently superimposed to it (parts IV.2.1 and IV.2.2.2). The occurrence of broad spectra is characteristic of undeformed starting material and of grain interiors, correlating with the observation of fluid inclusions.

In the deformed samples, the presence of the thin discrete bands increases relative to the broad band whose intensity is reduced, both for grain interiors and grain boundaries (Figure IV.25 and Figure IV.26). The presence of a broad absorption band for undeformed material with a growth of discrete bands with deformation has already been reported in experimental studies on single quartz crystals and quartz aggregates (Kronenberg et al., 1986; Stipp et al., 2006; Stünitz et al., 2017).

The characterization of the discrete bands that compose the infrared spectra of quartz is also of interest because with deformation, either appearance or amplification (growth) of several discrete bands has been widely observed (Kronenberg et al., 1986; Rovetta et al., 1986). These bands present in the 3000 – 3800 cm^{-1} range are sometimes polarized (in one or several directions of the crystal lattice) and are attributed to the stretching of bonds established between interstitial H and O in the quartz structure (Kats, 1962). The presence of the thin bands allows to identify some of the defect-related H_2O species but, the attribution of these bands to precise defects is – for some of them – still a matter of discussion (details below).

As the H_2O content (and so the broad H_2O band amplitude) evolves with deformation, changes in the discrete absorption bands have been identified in the infrared spectra of studied samples. With the application of pressure, temperature, and deformation there is a general growth of several absorption bands (3429, 3379, 3319 and 3585 cm^{-1} notably) while others reduce (in particular bands related to sheet silicates), both in grain interiors and grain boundaries. This suggests that specific H_2O related defects appears because during the deformation while they are absent in the starting material.

The contribution of some discrete bands has been taken into account during the deconvolution procedure and separated from the broad absorption band. However, it must be pointed out that the absorbance of some of the H defect related to the absorption bands studied are anisotropic. For this study, the infrared beam used was not polarized, and the orientations of the grains measured were not known, so the intensities of the bands reported cannot be considered as exact absorption values.

Moreover, the band growth observed in spectra could be either related to the decrease of the large band or to a real growth of the band. It can be supposed that bands whose presence is increase with deformation were maybe already there but with lower intensities and thus overlapped by the large broad band whose intensity was reduced with deformation.

The presence and evolution with deformation of the some of the discrete bands in grain interiors and grains boundaries in the samples is detailed below.

Absorption bands related to the presence of sheet silicates

The absorption bands positioned at 3700, 3654 and 3624 cm^{-1} are described as OH linked to kaolinite or muscovite (Farmer and Russell, 1964).

Starting material samples display a large number of spectra where bands related to sheet silicates are present. They are more often observed for measurements made on grain boundaries (and cement and triple junction, Figure IV.19 to Figure IV.24) than in the grain interiors. The appearance of these bands in the infrared spectra of starting material is in agreement with the observation of sheet silicates in thin sections (Figure III.1 in the previous chapter, part III.1.3). Before the acquisition, the presence of sheet silicates in the area measured was not detected (not observed in the FTIR microscope). The recorded spectra indicate that sheet silicates are common and heterogeneously distributed inside the starting material (mainly in the grain boundaries).

The bands related to sheet silicates are less common in most of the deformed samples (especially the band at 3699 cm^{-1} which is no longer observed, Figure IV.25 and Figure IV.26). Due to the experimental pressure and temperature conditions (900°C and 600 to 2000 MPa), they probably have melted resulting in a disappearance or reduction of the characteristic absorption bands.

The presence of sheet silicates in the infrared spectra was often problematic as the intensity and width of the band at 3424 cm^{-1} was masking the presence of the absorption bands at 3596 and 3585 cm^{-1}. For the same reasons, the band a 3614 cm^{-1} could not be detected.

Absorption bands related to the presence of sheet silicates are quite common in infrared measurement of natural quartzite (e.g., Kronenberg et al., 2020) and are often described in experimental studies when the starting material is a natural quartzite (Mainprice, 1981; Mainprice and Paterson, 1984).

Bands at 3429, 3379 and 3319 cm^{-1}

These three bands mostly appear associated and are observed on all the types of samples and areas measured (Figure IV.19 to Figure IV.26). The band at 3379 cm^{-1} is the most pronounced one and is often more clearly present than the two other ones which often appear as shoulders. The spectra recorded on the starting material grain interiors are the category where the triplet is the least present while grain boundaries, cement and triple junction show a majority of spectra with the three bands. Then, the number of spectra displaying the bands at 3429, 3379 and 3319 cm^{-1} increase in deformed samples and especially in the grain boundary region where they are present in majority (Table IV.7).

The occurrence of these three bands has been first described by Kats (1962) which attributed them to OH groups associated to Al^{3+} ions substituting for Si^{4+}. Aluminium is the most frequent ion that substitutes for Si (similar ionic radius) but the difference of charge needs compensating cations (such as H^+, Li^+, Na^+). The bands at 3380 and 3432 cm^{-1} correspond to stretching vibrations of the hydrogen defect compensating for Al substitution for Si (with the band at 3432 corresponding to Fermi resonance) and the band at 3319 cm^{-1} is the smallest one of the triplet.

The attribution of the 3379 cm^{-1} band has been confirmed with theoretical simulations (Jollands et al., 2020).

While their exact positions slightly vary, these three bands are very often observed in quartz infrared spectra (e.g., Kronenberg et al., 1986; Rovetta et al., 1986; Stipp et al., 2006; Gleason and DeSisto, 2008; Baron et al., 2015).

The fact that these defects are more present in the grain boundary region (and cement and triple junctions) than in the grain interiors for starting material (and consequently for deformed samples), could indicate the occurrence of Al substitution in the material. Indeed, sources of aluminium were certainly present during the diagenesis because (presence of rare feldspars then altered to kaolinite).

However, the increase of the triplet into the grain interiors is difficult to explain as Al (and Si) presents a low mobility in quartz and also because of the lack of an Al source during the experiments. The Al defect growth cannot either be correlated to most favourable orientation of the grains in deformed samples as no strong CPO were displayed by the original grains, even after deformation. The hypothesis that these discrete bands growth relatively to the decrease of the broad band is a possible explanation.

Stünitz et al. (2017) made the same observation of growth of the bands associated to Al substitution with deformation of a single milky quartz crystal (without any source of Al). They proposed that the discrete bands at 3433, 3400 (not observed here) and 3378 cm^{-1} were caused by structurally bound OH defects incorporated by dislocations.

The negative correlation between the incorporation of these (Al-OH specific) defects and the pressure related by Baron et al. (2015) has not been observed here. Indeed, no real correlation between the triplet intensities and the pressure or finite strain could be established, maybe in part because of the use of non-polarized light.

Band at 3596 cm^{-1}

The Band at 3596 cm^{-1} is observed both in individual spectrum of starting material and deformed samples but does not appear in the averaged spectra (Figure IV.19 to Figure IV.26). Its occurrence is variable and difficult to count as it is partially overlapped by the large sheet silicates bands (at 3624 cm^{-1}). This band seems to be more present in the starting material and in the low pressure sample than in deformed samples and slightly more in the grain interiors than in the grain boundaries but its intensity is higher in the latter than in the former (Table IV.7).

This band (at 3595 or 3596 cm^{-1}) is accounted for by different explanations in previous studies. One of the hypothesis is the presence of OH defects compensating for the substitution of Si^{4+} by B^{3+} (e.g., Müller and Koch-Müller, 2009; Baron et al., 2015; Jollands et al., 2020). One another attribution of the 3596 cm^{-1} band is related to compensating OH defect for Al-Si substitution (Niimi et al., 1999) occupying a structural position in the quartz structure. Then, for Palazzin et al. (2018) the band at 3595 cm^{-1} consists on OH defects adsorbed on silanol present at the surface of quartz with higher occurrence in spectra recorded on subgrains and grain boundaries (correlation between the presence of this discrete band and the increase of surface area).

Concerning the attribution of the 3595 cm^{-1} band related to the presence of B^{3+} ion substituting for Si^{4+} with OH compensating charge, the presence of boron has effectively been detected in the starting material chemical analyses (Table III.1 in previous chapter, part III.1.2). As the chemical analyses have been made on crushed material and that the presence of accessory minerals where B could be incorporated have been observed, it is difficult to know if the presence of B is due to substitution of Si or not. Moreover, the 3596 cm^{-1} absorption band is described in naturally deformed quartz as strongly polarized (Niimi et al., 1999). This also could constitute an explanation for the fact that it is not always observed in our samples (as they were not oriented and that no polarized light was used).

Further work on this band is needed to attribute it to one specific OH defect and to determine if there is a correlation between its presence and intensity and the deformation (and notably recrystallization).

Band at 3585 cm^{-1}

The sharp absorption band at 3585 cm^{-1} only appears in deformed samples but not (or very rarely) in the starting material and is observed both in grain interiors and grain boundaries (Figure IV.25 and Figure IV.26). This band appeared better developed in samples deformed at higher pressure, there is a positive correlation between confining pressure and intensity of the 3585 cm^{-1} band, both for grain interiors and grain boundaries (Figure IV.28).

The correlation between the occurrence of this band and deformed quartz samples has already been shown and its intensity related to the increase of the degree of local deformation (Stünitz et al., 2017).

Different explanation can be found in the literature, the first one is that the 3585 cm^{-1} band is due to the absorption caused by the hydrogarnet substitution (silicon vacancy charge balanced by protons, $Si^{4+} = 4H^{+}$, e.g., Stalder and Konzett, 2012). The second and more recent one is that this band is due to OH defects bound to dislocations (Stünitz et al., 2017), this explanation is based on the fact that the 3585 cm^{-1} band is strongly polarized which is in favour of structurally bound OH defects and is supported by theoretical simulations in which the stable configuration of the hydrogarnet defect do not produce stretching band at 3585 cm^{-1} (Jollands et al., 2020). These authors attributed the 3585 cm^{-1} band potentially corresponds to isolated OH^{-} groups bridging Si atoms where the charge compensation is ensured by a nonlocal mechanism.

The increase of the absorption band at 3585 cm^{-1} with increasing confining pressure (Figure IV.28) has also been described by Stalder and Konzett (2012) who linked its intensity to a proportional relation with the H_2O fugacity. The same relation with confining pressure is observed but the data show a large scattering, maybe because of the use of non-polarized light. It is however possible to roughly estimate the absorbances of polarized bands by multiplying by a factor 3 the values obtained from unpolarised spectra (Müller and Koch-Müller, 2009). When applying this factor on the 3585 cm^{-1} band intensity, comparable values to the ones obtained by Stalder and Konzett (2012) with polarized measurements are found.

If the apparition and growth of the 3585 cm^{-1} band is correlated with OH defects associated with dislocations (as proposed by Stünitz et al., 2017), in addition this defect appears to be pressure dependent, suggesting easier and greater dislocation density or/and glide with pressure.

Band at 3467 cm^{-1}

The band present at 3467 cm^{-1} commonly show small absorption intensities and is frequently found as a shoulder. This band is quite minor and large and was hardly resolved during the spectra deconvolution (the value of 3467 cm^{-1} has been taken, but large variations in position were observed). This band is almost present in half of the spectra recorded on starting material and deformed samples, both on grain interiors and grain boundaries and its occurrence seems to be associated with the Al-triplet. The exact position of the 3467 cm^{-1} absorption band is not found as is in the literature, so several hypothesis can be made with reported bands at close wavenumbers.

The band at 3467 cm^{-1} could be associated with Li related OH defect as described by (Kats, 1962) for bands present in the 3470 – 3480 cm^{-1} range specified to consist on Li-OH interstitials located in the structural channel by Aines and Rossman (1984) which are positioned between 3475 and 3485 cm^{-1} following the authors.

It could also be related to the band at 3363 cm^{-1} that is assigned to surface Si-OH groups (Yamagishi et al., 1997). Further work would be needed to determine both the importance and the signification of this band.

Other bands

Over the years, a great number of bands have been identified in spectra from several varieties of quartz (e.g., Kronenberg and Tullis, 1984 and review by Kronenberg, 1994).

During the treatment of the infrared spectra, only a reduced number of them has been considered and even fewer in the final data treatment. The choices were made as a function of their frequency occurrence and of description in other studies. Few other bands than the ones previously discussed were observed in some spectra but their presence was not systematic, and so they were not included into the data treatment.

The band at 3613 cm^{-1} that is described as occurring associated with the 3585 cm^{-1} one (Jollands et al., 2020) was not clearly observed, certainly in part because it was hidden by the sheet silicate bands or shoulders. Its presence was not systematic and only observed in few spectra. This band is described as related to the presence of K^+ (Aines and Rossman, 1984; Stalder and Konzett, 2012).

IV.3.3.2. H_2O storage

Estimating the quantity of H_2O stored into the samples before and after the experiment from the spot measurements made is a complex procedure. From the results previously described, a general H_2O loss is expected (in the microstructures measured) as the mean H_2O content decreases in grain interiors and grain boundaries, and even if H_2O was added to the samples. At this stage, one can wonder where does the H_2O go?

As previously discussed, a leak of the jacket is unlikely as no evidence was recorded on mechanical curves or even seen when the samples were removed. It is however possible that small quantities of hydrogen passed through the nickel foil and platinum jacket, but it cannot explain the missing quantities. The existence of a fluid phase (in excess) into the jacket is difficult to determine as the loss of fluid phase was not measured after the experiments (by

measuring weight loss after making a small hole into the jacket and let the sample in an oven at 110°C during few hours). If that phase existed, it was certainly lost during sample cutting and the thick section preparation.

One additional question is about the H_2O that was added to the samples before the experiment (0.1 wt.%). This H_2O was expected to – at least – increase the content in the grain boundary region. The porosity of the samples is quite low (estimated to be ~1.25 vol.% from the sample weight) but it could have contained a part of the added H_2O.

The loss of H_2O concerns the measured areas, that is clear grain interiors (mostly in the middle part of the grains) and straight grain boundaries between original quartzite grains. The most probable hypothesis is that H_2O should have been redistributed (and maybe more homogeneously) into the sample as several mechanisms occurring during the deformation have been highlighted, especially at the grain edges and boundaries.

The measurements made on all the samples show that the H_2O is preferentially contained in the grain boundaries with higher H_2O contents. During the deformation, the movement of dislocations (after decrepitation) and the formation of subgrains may have caused the redistribution of the intragranular H_2O toward the grain boundary regions, causing an increase of the intergranular H_2O (as discussed earlier). In addition to that, several mechanisms took place in that region, as evidenced by optical, EBSD and cathodoluminescence images (cf. previous chapter): formation of new and small grains (by recrystallization or cracking), precipitation (formation of crystal faces) and small patches of melt (amorphous material). All these elements should have increased the H_2O storage volume in the intergranular region within the samples. As the diffusion of H_2O at the grain boundaries and inside cracks is reported as effective at experimental times (e.g., Farver and Yund, 1991a), the H_2O could have been distributed more homogeneously on the newly available surfaces/volumes. In addition, as mentioned above, H_2O probably has been moved to the region between the mechanically stronger sample and the weak confining medium, i.e., to the boundary between the sample and the jacket. In this location, the H_2O is lost during sample sectioning.

All these hypotheses go in a direction of a global redistribution of H_2O into the sample with a preferential storage in the grain boundary regions (as already suggested by Palazzin et al., 2018) rather than global loss of H_2O indicating a negative balance with deformation (and only based on punctual measurements). To further study how the H_2O is redistributed into the samples, high-precision infrared mapping could better define the H_2O content at a larger scale, especially at the grain edges (where there is a transition between the subgrains and the recrystallized grains formed by subgrains rotation) and in the grain boundary region, where evidence of cracking and reworked material have been observed with cathodoluminescence images. Thus, this mapping should be coupled with other analytical methods such as cathodoluminescence or EBSD mapping (Muto et al., 2005; Kronenberg et al., 2017).

Associated with the change in broad band area (from which H_2O content were measured), several changes in the OH speciation are observed in deformed samples. The increase of the discrete absorption bands is consistent with the diffusion rates of hydrogen under the experimental conditions (e.g., Farver and Yund, 1991b). However, the H content displayed by the associated defects is not expected to be high (few H/10^6 Si).

IV.3.4. Comparison with experimental and natural studies

The decreasing behaviour of intragranular H_2O contents with deformation observed in this study is in contrast with the theoretical concept of hydrolytic weakening which requires available amounts of H_2O to operate (e.g., Griggs and Blacic, 1965). Based on it, H_2O is needed for the quartz to plastically deform (all along the deformation process) and a positive correlation between strength and H_2O content is expected for H_2O weakening of quartz deformed by dislocation creep (Kekulawala et al., 1978, 1981). A decrease in H_2O content is thus expected to produce an increase of strength of the sample by hardening because of limited hydrolytic weakening.

Previous studies supported the idea of plastic deformation promoting the increase of H_2O contents into the grain interiors in experimentally and naturally deformed quartzites in the dislocation creep regime. The following idea was that high H_2O contents caused hydrolytic weakening and induced strain localisation.

Kronenberg et al. (1990) reported increased amounts of intragranular H_2O in quartz (measured in optically clear regions, without visible cracks) related to increase of strain in a ductile shear zone within granitic rocks (Sierra Nevada). The increase in H_2O content toward the centre of the shear zone correlated with the presence of fine fluid inclusions along healed microcracks and dislocations. These observations lead the authors suppose that hydrolytic weakening played an important role in the localisation of the ductile shear zone by reduction of the rock strength after formation of water-related defects due to the infiltration of H_2O by diffusion along microcracks and mobile dislocations.

Post and Tullis (1998) measured a decrease in bulk H_2O content when vacuum drying Heavitree quartzite samples. The vacuum-dried samples were then deformed – at 800°C and 1500 MPa – as-is or with small amounts of H_2O added (0.1, 0.2 or 0.3 wt.% of H_2O added) and an increase in the intragranular H_2O content was observed related to the addition of H_2O. When compared with hydrostatically annealing experiments they deduced that H_2O penetrated the grains during the preheating time before deformation, but they did not exclude the fact that a part of this H_2O could be incorporated by cracking and crack-healing. As the strength of samples deformed with added H_2O was significantly lower than the vacuum-dried sample deformed as-is, they postulated that the defect enhancing dislocation climb penetrated the grains (by diffusion).

Gleason and DeSisto (2008) described higher H_2O contents in quartz grains deformed (at mid-greenschist facies conditions) by dislocation creep compared to the starting material. Measurements were performed on clear areas, avoiding grain boundaries and in grains without any evidence of microcracking. They related the H_2O uptake to several possible mechanisms but that the incorporation of H_2O into the quartz was promoted by the deformation with the action of subgrains boundaries and dislocations. The system is then supposed to be self-sustainable: deformation enhancing the rate of incorporation of H_2O which in turn enhances the hydrolytic weakening.

Nakashima et al. (1995) showed a systematic decrease in quartz H_2O contents with increasing metamorphic grade and an increase of H_2O content with increasing degree of deformation (dynamic recrystallization). The increase in H_2O content is related to an increase of plastic

deformation showed by a decrease of the mean grain size of quartz grains in the dynamically recrystallized aggregates. They linked the higher H_2O contents to higher grain boundary volumes and thus to larger H_2O storage capacity (H_2O trapped in the grain boundary region), the grain size reduction being correlated with a drastic increase in quartz H_2O content.

den Brok et al. (1994) deformed a natural quartzite (Dongelberg) as-is or with 0.4 wt.% H_2O added at 800°C, 1200 MPa and 10^{-7} s^{-1}. Despite the weakening induced by the added H_2O, intragranular H_2O content determinations by infrared spectroscopy showed no measurable difference between as-is and H_2O -added samples and a great diversity of H_2O contents from grain to grain. They deduced that the H_2O weakening occurred without change in grain interiors H_2O concentration and proposed that the weakening effect is caused by the H_2O that did not enter the grains.

On the other hand, the decrease of intragranular H_2O content with deformation of initially hydrated quartz grains was also reported in several studies (described below).

Ito and Nakashima (2002) observed a decrease in H_2O content with increasing metamorphic grade associated with increasing recrystallization. They postulated that the H_2O content decrease as a result of recrystallization and established a relationship between the H_2O content and the grain size allowing to estimate the H_2O volume that can be stored into the aggregate (inverse relationship with grain size). As they displayed large evidence of deformation, the dry recrystallized porphyroclast were certainly wet before deformation.

Muto et al. (2005) observed that dynamic recrystallization of deformed natural quartz (Hatakawa shear zone) reduced the H_2O content within the small grains by decreasing the defects density (recovery process).

In experiments conducted on Black Hills quartzite, Stipp et al. (2006) related lower H_2O contents in samples deformed either vacuum-dried, as-is or with added H_2O than in the starting material. In that samples a decrease in H_2O content also occurred with decreasing H_2O available (also measured by Chernak et al. (2009) for the same material). The areas measured were including both grain interiors and grain boundaries. They postulated that during deformation the H_2O from the grains (inclusions) went into the grain boundaries where it controlled the fugacity and was the lost during the thick section preparation.

Finch et al. (2016) observed a lower H_2O content in ultramylonites compared to the corresponding mylonites and weakly deformed rocks within a natural shear zone (El Pichao). The decrease in H_2O content is correlated with deformation (increase in strain) and recrystallization which caused the release of the intracrystalline H_2O to the grain boundaries.

Kilian et al. (2016) reported low H_2O contents for deformed quartz within a shear zone compared to their magmatic precursor (Truzzo metagranite) which display high H_2O contents due to the presence of fluid inclusions. The quartz within the shear zone deformed by dislocation creep and dynamically recrystallized by grain boundary migration (and minor subgrain rotation) without microstructures witnessing hardening. They suggested that the loss of intragranular H_2O occurred during the grain boundary migration recrystallization but that enough H_2O was available to ensure the recovery.

Palazzin et al. (2018) deformed samples constituted of wet or dry quartz porphyroclasts and reported either loss or gain of H_2O content during deformation. The two populations showed

different microstructures: extensive recrystallization for initially wet porphyroclasts whose H_2O content decreases and limited recrystallization at the borders and weakly deformation for initially dry porphyroclasts whose H_2O content increases.

Fukuda and Shimizu (2019) suggested that the progressive decrease on quartz H_2O content with increasing metamorphic grade they observed in schists belonging to the Sanbagawa metamorphic belt (Japan) was related to the progressive decrease in grain boundary volume when the grain size increases and suggested that the H_2O is mainly contained into the grain boundary region.

Recently, Kronenberg et al. (2020) presented a natural case of quartz mylonites (from the Moine thrust) for which the H_2O content decreases with increasing recrystallization. They proposed that the decrease was due to the loss of H_2O from fluid inclusions and hydrous defects within the grains during the recovery processes (mobile grain boundary sweeping and grain boundary diffusion).

To briefly resume the observations reported by the previous studies, the hydrolytic weakening is usually associated with an increase of the intragranular H_2O content. However, for some other studies – especially when deformation implies recrystallization processes – it appears that a decrease in H_2O contents can also be observed contrary to what is expected. The measured decrease is often related to an increase of H_2O within the grain boundaries. It could also be noted that despite the precautions taken, the presence of grain boundaries and/or cracks cannot be excluded.

H_2O speciation and weakening

Despite several hypothesis (and a very large number of different studies), the exact mechanism which acts in correlation with the presence of H_2O to reduce the strength of quartz and leading to hydrolytic weakening is not precisely known yet.

Since the hydrolytic weakening mechanism has been brought to light by Griggs and Blacic (1965), it has been correlated with the presence of H_2O in the quartz crystal enhance the rate of dislocation glide, but not the form in which H_2O was present. Kekulawala et al. (1978, 1981) and Kronenberg et al. (1986) showed that hydrogen interstitials (indicated by the presence of discrete absorption bands in the infrared spectrum) have no measurable influence on the strength of quartz compared to molecular H_2O (broad band absorption). The effect of hydrolytic weakening was then correlated with the presence (and/or amount) of intragranular molecular H_2O (and not hydrogen).

The elevated H_2O contents (> 1000 H/10^6 Si) commonly measured in natural quartz have been related to the presence of defects in the quartz crystal such as fluid inclusions (variably sized, e.g., Kronenberg and Wolf 1990) and H_2O along the dislocation cores (e.g., Post and Tullis, 1998). These defects occupy the major part of the broad infrared absorption band and constitute excess H_2O compared to its low solubility into quartz (100 to 200 H/10^6 Si (Kekulawala et al., 1981; Gerretsen et al., 1989). The hydrolytic weakening has been then reported as a non-equilibrium process (e.g., Post and Tullis, 1998; Stünitz et al., 2017).

Fluid inclusion decrepitation

The presence of fluid inclusions in the quartzite grains of starting material constitutes a source of H_2O available during deformation. The increase in pressure (and temperature) of samples leads to decrepitation of the fluid inclusions, and redistribution of H_2O into the grain interiors via cracking and crack healing processes (Fitz Gerald et al., 1991; Tarantola et al., 2010). In that way, small clusters of H_2O are created from the fluid inclusions, facilitating the nucleation and multiplication of dislocations (Fitz Gerald et al., 1991; Tarantola et al., 2010; Stünitz et al., 2017). This is correlated by fewer and smaller fluid inclusions observed into the grains after deformation.

Volume diffusion

For all the studies previously described (except Post and Tullis, 1998), what makes a general consensus is that volume diffusion into the quartz crystals cannot account for the observed H_2O content variations. Indeed, since Kronenberg et al. (1986) and Gerretsen et al. (1989) reported extremely low diffusion coefficients for H_2O into quartz, it is widely accepted that the diffusion of H_2O cannot be considered as an effective mechanism for intragranular H_2O gain or loss at experimental times. Then, the increase of H_2O content (broad band infrared absorption) in several previous studies has been attributed to cracking processes inducing formation of small fluid inclusions along the healed cracks (e.g., Kronenberg et al., 1986; Rovetta et al., 1986). Microcracking and subsequent healing are thus considered as effective processes for the penetration of H_2O into quartz. Afterwards, most of studies paid attention to perform measurements in clear areas in order to remove this bias from the H_2O contents calculated.

Note: while the diffusion of H_2O is not effective at experimental times, the diffusion of hydrogen is possible (Kronenberg et al., 1986), and efficient as evidenced by the growth of sharp absorption bands.

Considering that the equilibrium solubility of H_2O in quartz has been estimated to 100 to 200 $H/10^6$ Si (Kekulawala et al., 1981; Gerretsen et al., 1989) and that the experiment duration does not allow to reach an equilibrium in H_2O distribution by diffusion (which is exceedingly too slow), there was a necessity to explain the high H_2O contents measured in natural quartz. The volume diffusion having been ruled out, other mechanisms have been envisaged to explain the variations of H_2O content measured due to deformation, such as microfracturation (Kronenberg et al., 1986, 1990; Gerretsen et al., 1989; Fitz Gerald et al., 1991; Stünitz et al., 2017), diffusion along subgrain and grain boundaries (Post and Tullis, 1998; Gleason and DeSisto, 2008), diffusion along or with moving dislocations (Post and Tullis, 1998).

Deformation processes

Whatever the direction of the H_2O content variation (grain or loss), the deformation plays a major role in controlling the essential of H_2O transfers and it is largely accepted that weakening process of quartz necessitates the presence of intracrystalline H_2O.

The movement of mobile dislocations (hydrolysed) with deformation by dislocation creep could be considered as effective paths for fluid transfers into (or out to) the quartz grains (e.g., Kronenberg et al., 1990). The diffusion rates of H_2O related defects along the dislocation cores may be a rapid process, increased by high dislocation densities (Tullis and Yund, 1985; Paterson and Luan, 1990; Fitz Gerald et al., 1991). The amount of structurally bound OH and then of

potentially movable H_2O is thus a function of the dislocation density. In grains where inclusions have been decrepitated, the H_2O should be more homogeneously redistributed in smaller clusters and then presumably more easily movable by dislocations which, in addition to that, preferentially nucleate and multiply in these regions.

Several studies related the H_2O content variations with recrystallization processes (e.g., Nakashima et al., 1995; Ito and Nakashima, 2002; Kilian et al., 2016; Palazzin et al., 2018; Kronenberg et al., 2020). The effect of recrystallization is dual as it could both participate in fluid transfer and to increase of the grain boundaries storage surface. Depending on the conditions, different mechanisms could be implicated for the recrystallization of the material during the deformation and potentially not promoting the same paths and rates for H_2O transfer. The recrystallization by subgrains rotation may involve the transport of H_2O by dislocations, with an accumulation at the subgrains boundaries and then to the newly formed grain boundaries after rotation. The recrystallization by grain boundary migration could act more efficiency and rapidly to expel and redistribute H_2O from the grain interiors (fluid inclusions or clusters) to the grain boundaries. In addition to that, dynamic recrystallization is expected to reduce the dislocation density in grain interiors deformed in the dislocation creep regime (Hirth and Tullis, 1992).

One another mechanism which could operate in a non-negligible way is the formation of small grains due to cracking. The cracking can also contribute to the nucleation of new grains, leading also to an increase of the grain boundaries surface (den Brok and Spiers, 1991; Trepmann and Stöckhert, 2003).

In the current study, a decrease of grain interiors H_2O content is observed and (as suggested by (Finch et al., 2016) there could have been a release of intracrystalline H_2O to the grain boundaries. However, no hardening is observed instead there is an almost continuous flow stress (Figure III.7, part III.2.1). One hypothesis that could be advanced is that the deformation conditions (finite strain and duration) have certainly not been high enough to dry all the H_2O out of the grains, and thus did not cause the expected strain hardening. As grains still contained H_2O and that intergranular H_2O is still present, the weakening process was still active at the end of the experiment.

It could be specified that even if large variations in H_2O contents were observed for individual grains (due to the sedimentary origin of the starting material), the H_2O content distribution tends to gather to the lower values and the grains all displayed similar deformation features. As already suggested by (Post and Tullis, 1998), this could indicate that not all the H_2O contained into the grains participates to the deformation and contributes to the dislocation creep strength.

Nevertheless, it seems from the previous studies that recrystallization plays a major role in diminishing intragranular H_2O content, which is not the case here for most of the samples (shortened to 30%) where the recrystallization is limited except for high-strained samples. For those, the extensive recrystallization and transition between subgrain rotation to grain boundary migration recrystallization mechanisms could have been important factors for the decrease in H_2O content. However, as evidenced by the bright blue luminescence in cathodoluminescence images, for most of the sample recrystallization and grain boundary processes involved the action of an aqueous fluid.

H_2O available (± added)

A number of studies on experimental deformation of quartzite with different amounts of added H_2O (usually samples were deformed vacuum-dried, as-is or with different quantities of H_2O added, e.g., Jaoul et al., 1984; Stipp et al., 2006; Chernak et al., 2009) showed that the H_2O content added (in addition to pressure and temperature conditions) has a strong effect on the strength of quartz as the increase of available H_2O correlated with an increase in weakening (decrease of strength). The presence of trace defects of H_2O has also an effect on the development of microstructures of the dislocation creep regimes (Hirth and Tullis, 1992) with mainly regime 1 microstructures for vacuum dried samples, regime 2 for samples deformed as-is and regime 3 for H_2O-added samples (deformed at 900°C, 1500 MPa and 10^{-6} s^{-1} by Jaoul et al. (1984).

In the study of Chernak et al. (2009) the effect on deforming Black Hills quartzite with different amounts of H_2O (as-is, pre-heated, and with 0.05, 0.2 or 0.5 wt.% H_2O added) lead to a decrease of strength with increasing amount of H_2O available. However, no difference by infrared spectroscopy could be made between the samples which all presented similar spectra with a lower H_2O content than the starting material. The H_2O added does not seem to increase the grain interiors H_2O contents and is yet probably restricted to the grain boundary region.

The results of Post and Tullis (1998) – described above – also showed that samples with added H_2O present lower stresses (even if the starting material was vacuum-dried quartzite) and that deforming sample as-is or a vacuum-dried sample with added H_2O produces similar strengths, indicating that they have something in common that plays a role on the weakening. One question raised by the authors is why does the quartzite deformed with H_2O -added show a decrease in strength while it should already contain enough H_2O as-is to deform. Post et al. (1996) suggested that the intergranular H_2O may also play a role in the weakening process and proposed that the external H_2O provides a fluid phase which increases the H_2O fugacity and by this way reduces the strength.

In most of the studies, the H_2O is added into the jacket before welding it. Considering the intergranular and intragranular rates of diffusion, at the beginning of the experiment (after pressure and temperature conditions were attained and sometimes after a more or less long annealing time), the added H_2O certainly occupies the grain boundaries and pores but does not have the time to enter the grains. However, as all the previously cited studies showed the externally added H_2O has anyway an effect on the samples strength by reducing dislocation creep flow stresses with increasing amounts of H_2O. These studies suggest that intergranular H_2O should also play a role into the weakening process of the samples.

As underlined by Kronenberg and Wolf (1990) the samples deformed without added H_2O (anhydrous conditions) should lost a part of their initial intragranular H_2O content what should imply higher strengths than H_2O-added samples. However, it is not the case as samples with additional H_2O either show no increase or a decrease in H_2O content without showing higher strain strength (Post et al., 1996; Stipp et al., 2006). To explain that, Holyoke and Kronenberg (2013) proposed that the decrease of strength due to H_2O added should be controlled by the H_2O into or near the grain boundaries which may enhance the rates of recovery by recrystallization processes such as grain boundary migration.

Grain boundaries

As the current study, higher H_2O contents in the grain boundaries of quartz aggregates compared to the grain interiors are currently reported (e.g., Kronenberg et al., 1990; Post and Tullis, 1998; Ito and Nakashima, 2002; Palazzin et al., 2018). This leads notably to an increase in H_2O content for bulk measurements or when the area measured comprises both grain interiors and grain boundaries (e.g., Nakashima et al., 1995; Ito and Nakashima, 2002; Kilian et al., 2016).

As highlighted by Post and Tullis (1998), the dislocation creep strength of natural quartzite appears to be related to the amount of intragranular H_2O as well as to the presence of externally available H_2O. H_2O present as a free fluid phase along the grain boundaries could regulate the equilibrium intragranular H_2O content (buffer) and thus control the dislocation creep strength (Kronenberg and Wolf, 1990). The fact that the H_2O contained at the grain boundaries is important for the H_2O weakening mechanism is also highlighted by the higher stresses displayed by deformed vacuum-dried samples than as-is or H_2O added samples (e.g., Jaoul et al., 1984; Stipp et al., 2006), as discussed above). The interpretation of grain boundary mediated process supporting the H_2O weakening has been emitted by (e.g., Kronenberg and Tullis, 1984; Holyoke and Kronenberg, 2013).

The H_2O present at the grain boundaries could come from the liberation of fluids by the quartz during recrystallization, from added H_2O for experimental studies or from hydrous phases in natural rocks. Intergranular H_2O should diffuse several orders faster than intragranular volume diffusion (Nakashima, 1995) allowing its repartition (at least at the sample scale).

Several authors reported that the free fluid phase along the grain boundaries could have an effect on the recovery rates by increasing the grain boundary mobility but could also play a role on the control of the H_2O fugacity and consequently the flow stress (e.g., Stipp et al., 2006; Holyoke and Kronenberg, 2013).

Concerning the recovery processes, intergranular H_2O could facilitate grain boundary migration and grain boundary sliding (Kronenberg, 1994; Finch et al., 2016; Kilian et al., 2016). The H_2O present at grain boundaries could also reduce the strength between the grains and facilitate dissolution precipitation processes (den Brok and Spiers, 1991; den Brok et al., 1994). However, as already indicated by Stipp et al. (2006), as the main microstructures observed correlate with the dislocation creep regimes described by Hirth and Tullis (1992), solution-precipitation creep is not expected to play a significant role in the deformation of the samples. However, solution precipitation processes (evidenced by cathodoluminescence images) could participate to the fluid transfers during the deformation.

The H_2O present as a free fluid (film) along the grain boundaries is expected to equilibrate (buffer) the H_2O activity (Mainprice and Paterson, 1984) and yet the H_2O presents as a free fluid phase along the grain boundaries could regulate the H_2O fugacity (Post and Tullis, 1998). If there is enough H_2O at the grain boundaries to attain saturation, then the fugacity can be calculated from the confining pressure which equals the H_2O pressure. The weakening of quartz with pressure is could be due to H_2O present in the grain boundaries (in addition to H_2O into the grain interiors).

Porosity in the recrystallized domains

In addition to H_2O present at the grain boundaries, some could be contained into the porosity that is certainly present within the material. In some of the samples studied, cathodoluminescence images (Figure III.16 in the previous chapter part III.3.2.1) showed newly formed crystal overgrowths of quartz into small intergranular pore spaces (certainly melted at the pressure and temperature conditions during the experiment). Similarly, Palazzin et al. (2018) described the presence of porosity located into shear band and which fluids contents allowed the precipitation of euhedral quartz crystals. These porosity sites could participate to the storage of some of the intercrystalline H_2O content (fluid reservoirs) and provide a free fluid phase acting on H_2O activity and fugacity (Post and Tullis, 1998).

In their "granular fluid pump" model Fusseis et al. (2009) postulated that fluid migration in shear zones is permitted during the deformation accommodated by diffusion creep process. They described pores surfaces with crystallites (but at a much smaller scale than observed here) communicating through the grain boundaries. Grain boundary sliding in addition to dissolution or precipitation at grain boundaries are proposed to operate synkinematically during diffusion creep and allowing the fluid migration in the shear zone at the grain scale. A feedback between fluid migration and ductile deformation is proposed.

Pressure and fugacity dependence

The inverse relation between pressure and strain – as observed for the samples studied here – has already been described many years before (e.g., Tullis et al., 1979; Kronenberg and Tullis, 1984; Mainprice and Paterson, 1984; Post et al., 1996; Holyoke and Kronenberg, 2013). The weakening effect due to increasing confining pressure has been attributed to enhanced rates of recrystallization or recovery (dislocation climb and grain boundary migration) when H_2O is available (Tullis et al., 1979; Tullis and Yund, 1989) and thus directly related to an effect of fugacity. The dependence of strength on confining pressure has been, by the way, integrated into the quartz flow law via the H_2O fugacity (f_{H2O}) and its exponent m (Kohlstedt et al., 1995).

In the samples deformed during this study at various confining pressures, an increase of recrystallized (bright luminescent) material has been observed with increasing confining pressure (Figure III.18 and Figure III.19 part III.3.2.2). The processes involved (recrystallization, subgrain boundary formation and grain boundary migration) are enhanced in the presence of fluid and when the fugacity increases. Then, they may at their turn enhance the H_2O transfers.

H_2O decrease and hardening?

As the H_2O weakening effect is positively related to the presence of H_2O, a decrease in H_2O contents is commonly correlated to strength hardening. Several deformation experiments showed that high intragranular H_2O contents (> 1000 H/10^6 Si) are required for samples to deform plastically by dislocation creep (e.g., Kronenberg and Tullis, 1984; Post and Tullis, 1998) dry quartz being too strong and deforms in a brittle manner.

In the samples considered here, no hardening has been observed in the mechanical curves neither in the microstructures even if the mean H_2O content showed a decreasing behaviour during deformation for all the deformed samples compared to the starting material. However, the grains deformed were still hydrated at the end of the experiment and H_2O content

measured. This indicates that not all the H_2O was lost during the experiment and the weakening effect was still effective at the quenching time. In addition, as previously discussed, H_2O was certainly available within the grain boundaries. Deformation strengthening is not observed at that time of experiment but could be expected to occur whether the deformation is increased until the grains become totally dry.

In recent studies, Finch et al. (2016), Kilian et al. (2016) and Kronenberg et al. (2020) indicate that plastic deformation of quartz under natural conditions is possible either with a decrease of H_2O content with strain and recrystallization or when grains display very low H_2O quantities (Kilian et al., 2016). While Finch et al. (2016) reported hardening of the studied shear zone, Kronenberg et al. (2020) and Kilian et al. (2016) both reported quartz weakening and discussed the participation of H_2O contained at grain boundaries to the process.

Kilian et al. (2016) observed natural quartz samples with very low H_2O contents (< 100 H/10^6 Si) deforming by dislocation creep and dynamically recrystallizing (by grain boundary migration). The loss of intragranular H_2O did not produce any visible microstructure witnessing strain hardening. Following them, the conditions of natural deformation (and especially the slow strain rates) could then allow quartz with extremely low intragranular H_2O content to deform by dislocation creep when intergranular H_2O is available to promote the recovery.

Kronenberg et al. (2020) reported a decrease in H_2O content with increasing recrystallization for naturally deformed quartzites (from Moine thrust). They postulated that the H_2O weakening was certainly controlled by the presence of H_2O at grain boundaries and within fluid inclusions (which regulate the fugacity) and not directly by the grain interiors H_2O concentration.

Our experiments demonstrate that low H_2O contents of a couple of hundred H/10^6 Si as intragranular H_2O are sufficient to facilitate dislocation creep in quartz. The excess H_2O can be stored in the grain boundary region, where it may enhance recrystallization processes.

Shear localization

The localisation of deformation within a shear zone is commonly linked to the weakening of the rock and related with a continuous presence of a fluid phase (Kronenberg et al., 1990; Nakashima et al., 1995; Gleason and DeSisto, 2008). Conversely, the loss of H_2O is usually supposed as leading to widening the shear zone due to hardening of the rocks composing it.

From the study of a ductile shear zone (in Sierra Nevada), Kronenberg et al. (1990) postulated that an increase in H_2O facilitates the shear localization in a natural shear zone by promoting H_2O weakening which reduces the strength. The penetration of H_2O was permitted by cracking and participated to the localization thanks to hydrolytic weakening which reduced the strength. In that case, but at a smaller scale, the H_2O exsolved from the grain interiors could help the localisation of deformation within the grain boundaries.

Finch et al. (2016) measured lower H_2O contents in ultramylonites compared to the surrounding mylonites, that is, less H_2O in the most deformed part of the shear zone. They proposed that the H_2O was extracted from the ultramylonite (from hydrous phases but also from recrystallized quartz and feldspar) and transported into the surrounding rock via the grain boundaries. In that way, the shear zone centre hardened while the H_2O weakened the surrounding proto-mylonites which cause (little by little) a widening of the shear zone. By this

process the centre of the shear zone displays lower H_2O contents than parts where the deformation is less pronounced.

Kronenberg et al. (2020) described loss of H_2O in quartz mylonites during recrystallization which did not induce strain hardening but conversely an intense strain localisation. They postulated that even if a decrease of H_2O content took place with deformation, enough H_2O was still available to promote weakening by maintaining the H_2O fugacity elevated. The weakening was apparently not at the origin of the strain localisation.

The loss of intragranular H_2O during deformation is thus not necessarily a synonym of hardening and strain localization but can act as a source of fluids that can help the localisation. The widening of the shear zone by transfer of H_2O from the most deformed part to the surrounding part causing is possible. Either increase or decrease in H_2O contents are related to localization of the deformation.

Natural structures

From the studies previously considered, it is evident that the H_2O concentrations and transfers in naturally and experimentally deformed quartz is not straightforward as a great diversity of results are reported.

The first discrepancy concerns the H_2O contents described for plastically deformed quartz in dislocation creep regime. Usually lower H_2O contents are observed for natural cases than for experimentally deformed samples (e.g., data compiled by Kilian et al., 2016). This suggests that possibly a higher amount of intragranular H_2O is needed under experimental conditions than in nature for the hydrolytic weakening to be effective. In addition to that, most of the studies performed highlighted the importance of the intergranular H_2O both for H_2O transfers through the rock and shear zone but also for the weakening promotion. Care must be taken when measuring H_2O contents in the identification and precision of the measured structures. For that point, recent studies have shown the usefulness of FTIR mapping (Kronenberg et al., 2017; Fukuda and Shimizu, 2019) which combine a great resolution and a direct comparison between deformation microstructures and H_2O contents or speciation.

Compared to the natural samples for which the starting material is inferred from undeformed neighbouring outcrops the experimental samples possess the advantage of a known and characterized starting material. Even if the material presents a great variability the conditions of deformation (pressure, temperature, strain rate, time, etc.) are known. In addition to that, in nature, a close system is not expected (contrary to the experiments) and the fluid sources are multiple. H_2O in the grain boundaries can come from local sources of fluids such as hydrous minerals or from loss due to recrystallization or decrepitation of fluid inclusions (as discussed above) but can also come from external sources located further away.

One issue about the extrapolation of the laboratory results to geological conditions concerns the equilibrium question. Indeed, during experiment (particularly due to short times and rapid strain rates) none of the structures observed and measured attained an equilibrium state. The weakening effect can occur at experimental times because it is a non-equilibrium process which takes place in grains in which the H_2O content is higher than the equilibrium solubility of H_2O into quartz.

Kronenberg et al. (2020) reported a decrease in H_20 content with increasing recrystallization for naturally deformed quartzites (from Moine thrust). They postulated that the H_20 weakening was certainly controlled by the presence of H_20 at grain boundaries and within fluid inclusions (which regulate the fugacity) and not the H_2O concentration. Moreover, even if H_20 is lost, what is important is that the fugacity stays elevated, i.e., that it does not decrease and as H_20 is found in the grain boundaries, so it is still enough H_20 for sample to deform plastically

IV.4. Conclusion

It has been shown that there is a diminution in the H_20 contents in all the microstructures measured (grain interiors and grain boundaries) with the application of pressure, temperature and strain rate conditions. It is inferred that the H_20 is transferred from the grain interiors to the grain boundary region.

The H_20 contents measured on the grain interiors reveal a decrease compared to starting material. This decrease is observed with pressure-temperature conditions, deformation and amount of strain achieved. Even if grains are plastically deformed, they keep their original heterogeneity as in starting material, but the decrease in H_20 content occurs together with a less extended data dispersion. The grain interiors are plastically deformed, compared to the starting material, they display features characteristics for plastic deformation by dislocation creep mechanisms. This suggests the contribution of dislocations to the evolution in the H_20 content during deformation. H_20 contents of a couple of hundred $H/10^6$ Si are sufficient as an intragranular H_20 content to facilitate dislocation creep deformation in quartz.

It appears that time and deformation act differently as with a greater influence of the deformation on the H_20 remobilisation compared to diffusion under high pressure and temperature conditions.

H_20 and deformation appear to play mutual roles, with intracrystalline H_20 content enhancing the deformation (rate of dislocation creep) and deformation accompanying the transport of H_20. Grains rarely become totally dry, because it is a self-sufficient system as H_20 accelerates the rates of recovery and recrystallization, and microcracks may allow H_20 to re-enter the interior of grains from the grain boundary region, which acts as a storage site.

V. Discussion, summary, and some general conclusions

In this chapter, the objectives of the study, the principal results and their interpretations will be summarized and will be put into some context.

Then, some short perspectives for further work will be presented.

V.1. Summary of the objectives

The study of rheological behaviour of quartz and quartz aggregates in presence of H_2O and their dependence on pressure is of great interest in order to constrain geodynamic processes at many continental crust levels. Even if some pressure effect has been recognized since the late 70's (Paterson and Kekulawala, 1979; Tullis et al., 1979; Blacic, 1981; Mainprice and Paterson, 1984), the processes causing the pressure dependence are still not well understood. Particularly, the dominant deformation processes (whether they are dominated by dislocation or diffusion creep) have been still unclear, because fine grained quartz aggregates (novaculite, < 5 µm) have been used in the seminal study by Kronenberg and Tullis (1984) that has documented and quantified the pressure dependence for the first time. Novaculite had also been used in experiments where diffusion creep has been concluded to contribute to the deformation mechanism, demonstrated by n-values < 2 for the stress exponent (Fukuda et al., 2018). Therefore, it was decided to repeat the experiments of Kronenberg and Tullis (1984) with coarse grained material in order to reduce the potential contribution of diffusion creep.

In addition to the effect of pressure, it has been demonstrated that the amount of H_2O available in the quartz aggregate samples during deformation has an effect on their strength (Jaoul et al., 1984; Post and Tullis, 1998; Stipp et al., 2006; Chernak et al., 2009). However, the role of H_2O in dislocation creep deformation has been challenged recently (Kilian et al., 2016; Stünitz et al., 2017), so that the necessary amount of intragranular H_2O content for plastic deformation is uncertain. A second PhD project has been launched in close collaboration with this project at the Charles University, Prague (PhD student: Petar Pongrac, PI: Petr Jerabek) to study the effect of the amount of H_2O on quartz deformation.

Based on the state of knowledge, the issues that were investigated in this study were:

(i) Is the weakening effect of H_2O with pressure the same in coarse grained aggregates deformed by dislocation creep as in fine grained aggregates?

(ii) What causes the pressure effect?

(iii) How does the H_2O redistribute in the polycrystalline aggregate of quartz during deformation?

V.2. Summary of the main results

Experimental deformation: H_2O weakening with pressure

The first chapter describes the mechanical behaviour of wet natural quartz aggregates and their microstructures. A new starting material (Tana quartzite) was used to perform the deformation experiments in this study as well as in the collaborative project in Prague. The Tana quartzite has been characterized carefully and has been found to be a good starting material to explore the deformation of coarse-grained quartz aggregates because of its high purity, grain size of ~200 µm, and more or less random shape and crystallographic fabric.

The coaxial shortening experiments were performed at confining pressures from 600 to 2000 MPa on H_2O-added samples and show a systematic decrease of strength with increasing confining pressure, consistent with the results obtained by Kronenberg and Tullis (1984) for

novaculite material. Therefore, it is concluded that the process of pressure-dependent weakening in quartz is not directly dependent on the grain size of the starting material.

Similar low stress exponents (n≈1.4) have been obtained from strain rate stepping experiments performed for samples deformed at 800 and 2000 MPa. Due to uncertainties and difficult stress resolution at the lower strain rates, n-values of 1.96 (at 800 MPa) and 2.33 (at 2000 MPa) can also be determined, if low strain rate data are omitted. Despite the uncertainties, the stress exponents determined are closer to 2 than to 3 or 4 and are in agreement with determinations by Fukuda et al. (2018) and Richter et al. (2018). However, the Tana quartzite has a rather uniform and much larger grain size than the materials used in these two studies. The similar n-values should be interpreted in a similar way as in those two studies (the study by Richter et al., 2018 contained some coarser material in addition to fine grained material, so that it may represent a combination of the Fukuda et al., 2018 study and this one), so that some component of diffusion creep mechanism could be considered to be involved in the deformation process.

The deformed samples display clear features of intracrystalline plastic deformation (elongated grains, undulatory extinction, deformation lamellae, development of subgrains, core-mantle structures). At the boundary of the plastically deformed large grains, small-sized grains are formed in quantities that are volumetrically limited to ∼10%. The grain shape anisotropies have been calculated by image analysis and yield strain values using the original sand grains (performed on segmented light microscopy cathodoluminescence images) that correspond closely to the bulk strains of the mechanical record for the samples and the measured post-mortem sample shortening. Thus, the shortening of the samples is mainly accommodated by crystal plastic deformation of individual grains, so that a dominant dislocation creep mechanism can be inferred for all samples.

Light and scanning electron microscopy cathodoluminescence of deformed samples reveal a new bright (blue and long-living) luminescence appearing predominantly at the boundaries of the quartz grains. The areas displaying the bright luminescence are more frequent in the most deformed part of the samples and their volume increases with increasing confining pressure and local strain. The bright luminescence is caused by an exchange of the quartz material with an aqueous fluid (exchange of trace elements), so that the luminescent material traces a reconstituted material. This material occurs in different features in the samples, such as cracks, overgrowths and small grain aggregates.

EBSD analysis allowed to identify two mechanisms of new grain formation (with respect to the old grains), often present in the luminescent regions: subgrain rotation and cracking. The results show that two processes may cause the luminescence and both are operating in deformed samples: cracking and crystal plastic deformation, inducing dynamic recrystallization. The latter is the mechanism that accommodates the bulk shortening of the samples (crystal plastic deformation of individual grains by dislocation creep). Cracking does not contribute to sample shortening (cracks do not show offsets) but helps to reconstitute the material during plastic deformation (by developing dislocations during healing in larger grains and by forming new small grains). Thus, small new sized grains that appear during the deformation have two types of origin: some may have formed by cracking (small fragments) and the change in luminescence demonstrates that local grain boundaries are mobile, reconstituting this material by local grain boundary migration. Other small new grains have formed by progressive subgrain

rotation (dominant recrystallization mechanism of regime 2 from Hirth and Tullis (1992). Subgrains (low angle) and adjacent recrystallized grains display similar sizes. Local grain boundary migration processes affect all small sized grains, regardless of their origin of formation.

The dominant deformation processes are dislocation glide and climb, for which stress exponents of 3-5 are expected. However, the n-values obtained are close to 2, inconsistent with pure dislocation creep deformation. Diffusion creep always is a grain size sensitive process, so that if diffusion creep were to operate in parallel with dislocation creep (and causing the low stress exponent), a strong grain size dependence should be observed, which is not the case. However, there is plenty of evidence for grain boundary processes being active. The von Mise's criterion requires 5 independent slip systems for homogeneous deformation by dislocation glide. This condition is almost never realized in silicates, and there is evidence for only one or two slip systems from EBSD misorientation analysis in these quartzites. The grain boundary processes (boundary migration, solution-precipitation) are interpreted to form an important accommodation mechanism for grain boundary sliding to achieve bulk sample deformation by intracrystalline plasticity. Without grain boundary sliding the local strain incompatibilities could not be accommodated. Therefore, one explanation for the low n-values may be a contribution of local diffusion creep process to accommodate the dominant dislocation creep deformation in grain boundary regions.

The coarse-grained starting material certainly is not subjected to diffusion creep, but the recrystallized material is fine grained and local accommodation by diffusion creep may be possible in these places. Moreover, evidence of exchange with a fluid in the small grains is documented by cathodoluminescence (diffusive mass transfer and dissolution precipitation processes).

If the grain boundary processes involve solution and precipitation (as demonstrated by cathodoluminescence), the pressure dependence may be explained by the strong and non-linear increase of silica solubility by pressure (Manning, 1994). The inferred strain accommodation processes in the grain boundary regions represent recovery or recrystallization processes. The importance of enhanced recrystallization or recovery for H_2O weakening has already been proposed by Tullis et al. (1979) and Tullis and Yund (1989). Our samples show an increased amount of recrystallized material produced by local grain boundary migration with higher confining pressure. The pressure dependence of the H_2O weakening may thus be an effect of increased solubility of silica during the recrystallization in the grain boundary regions.

From mechanical data and H_2O fugacity calculations, a H_2O fugacity exponent (as integrated into the flow law by Kohlstedt et al. (1995) of $m \approx 1$ is determined, consistent with previous studies (Kohlstedt et al., 1995; Post et al., 1996; Holyoke and Kronenberg, 2013). Its value ($r=m/n$) is dependent on the n value. Holyoke and Kronenberg (2013) have determined a similar m-value for polycrystalline quartz samples, whereas their values for single crystal quartz are substantially lower. The different m-values are consistent with and support the idea that grain boundary processes are important for the pressure dependence.

H_2O in quartz: distribution with deformation

In the second part of the work, H_2O content and structure-related OH defects of the starting material and deformed samples were qualitatively and quantitatively analysed by Fourier

transform infrared (FTIR) spectroscopy. Because of the coarse grain size of the starting material, individual grain measurements with FTIR were possible, allowing the distinction of the contribution of the grain boundaries and grain interiors to the total H_2O content.

For the starting material as well as for deformed samples the H_2O contents calculated for the grain interiors are lower than those of the grain boundary regions. No systematic dependence of H_2O content on pressure was found but a systematic decrease in the mean H_2O content was observed for the deformed samples compared to starting material, both for grain interiors and grain boundaries. The H_2O distribution in the deformed samples also becomes narrower and closer to the lowest values (both grain interiors and grain boundaries).

The mean H_2O content depends on local strain because, within the same sample, lower H_2O content values have been determined in the most deformed parts compared to the least deformed parts (both for grain interiors and grain boundaries). This dependence is also observed for samples deformed to a higher bulk strain. These samples contain (on average) less H_2O than samples deformed to a lower strain (at the same pressure, temperature and strain rate conditions). These two observations highlight the influence of deformation on the H_2O redistribution inside individual grains.

No dependence of H_2O content on duration of the experiment has been observed, consistent with the demonstrated effect that diffusion of H_2O should be negligible at an experimental time scale (Kronenberg et al., 1986; Gerretsen et al., 1989). These authors have shown that H_2O is transported through cracks or grain boundaries to enhance weakening and to produce measurable variations in H_2O content.

The OH speciation has been qualitatively analysed by FTIR and shows changes in discrete absorption bands in grain interiors and grain boundaries with deformation. Several structural OH defects are present in the spectra measured.

In the starting material, spectra of grain interiors display fewer discrete OH defects than the grain boundary regions. This observation suggests that in the grain interiors, the principal form of H_2O occurs in fluid inclusions. With deformation, it appears that the broad molecular H_2O band becomes less prominent and more discrete OH absorption defects appear in the spectra.

FTIR measurements also demonstrate that some sheet silicates are present in the starting material, especially in the grain boundary regions. With increasing pressure and temperature conditions, these bands tend to disappear, caused by the melting of sheet silicates at the high experimental temperature (900°C).

The discrete absorption band triplet indicating Al/Li-OH exchange is more pronounced in FTIR spectra recorded in grain boundaries than in grain interiors, and it is frequent everywhere in the studied material. The bands of the triplet occur more frequently in the grain boundaries than in the grain interiors and in the deformed samples compared to the starting material.

With sample deformation, a discrete absorption band appears at 3585 cm^{-1}. This band growths with confining pressure and has previously been attributed to OH associated with dislocations (Stünitz et al., 2017; Jollands et al., 2020).

As pointed out above, diffusion of H_2O cannot explain the H_2O loss of grain interiors towards the grain boundary regions. Instead, microcracking and plastic deformation processes have

certainly participated in the redistribution of H_2O during deformation. The former process has helped H_2O redistribution during fluid inclusion decrepitation, whereas both microcracking and plastic deformation have allowed H_2O to be transported from grain interiors to the grain boundaries.

In addition to these processes, the formation of small grains during deformation (either by recrystallization by grain boundary migration and subgrain rotation or by cracking) has created new boundaries that increase the H_2O storage capacity of the aggregate (Palazzin et al., 2018).

General model: H_2O weakening with pressure and H_2O content

The two parts of the study allow to understand the important role of H_2O in the deformation of "wet" natural quartz aggregates better.

The clear pressure dependence of weakening displayed by the mechanical data is not found in the distribution of H_2O contents, suggesting that the presence of H_2O has a stronger effect than its total amount, i.e., as long as there is a minimum amount of H_2O present, deformation proceeds.

It is shown here that processes occurring at the grain boundaries of the aggregates are particularly important for the deformation and for H_2O redistribution. Grain boundaries play a dual role of accommodation of strain incompatibility and as a storage site of H_2O. in addition, the recrystallization accommodates dislocation creep and allows more H_2O to reside inside the grain boundary region (increased surface area by grain size reduction). The experiments simulate processes observed in natural rocks: Kilian et al. (2016) have documented decreasing intracrystalline H_2O contents during plastic deformation of quartz. This effect is observed in all of our deformed samples, too. In addition to plastic deformation, we observe microcracking. As both, plastic deformation and cracking occur simultaneously, their interplay may explain how H_2O is re-introduced from the grain boundary region into the grain interiors. Crack healing in the presence of H_2O has been demonstrated to generate dislocations that are necessary for the glide processes (Fitz Gerald et al., 1991; Tarantola et al., 2012; Stünitz et al., 2017). Thus, the cracking and healing processes may be directly connected to crystal plastic deformation.

The dependence on H_2O fugacity is shown by the mechanical data (flow stresses allowing m-exponent determination). A crucial parameter for fitting the fugacity exponent to the mechanical data is that the aggregate should be water-saturated in order to maintain an elevated f_{H2O}. This condition is satisfied by the H_2O being driven into the grain boundary region.

V.3. General perspectives

Relationship between experimental and natural deformation conditions

The temperature and strain rate conditions used in experimental deformation can be far away from those of the natural deformation, and it is important to ensure that the critical processes operating in experiment and nature are the same (e.g., Paterson, 1987). As strain rates in experiments are orders of magnitude higher than in nature, it is particularly important to pay attention to high stress/high strain rate microstructures such as cracks in experiments, because these could be features absent in natural low stress/low strain rate deformation. The cracks in our samples have formed at lower stresses than the Goetze criterion ($\Delta\sigma < \sigma_3$) and therefore

are inferred to have occurred in a regime, where plastic deformation prevails. In addition, some stresses in high pressure experiments have been very low, so that brittle deformation can be excluded as a dominant deformation mechanism. The cracks that have been forming have virtually no offsets, so that they do not contribute kinematically to the sample strain. From these observations, it is concluded that such cracks do not represent frictional deformation, and we can correlate the observed microstructures and their plastic deformation processes with plastically deformed natural ones.

Kilian et al. (2016) have made tantalizing observations of partially very low H_2O contents in amphibolite facies quartz crystals that are plastically deformed. This experimental study confirms that intracrystalline H_2O contents may decrease during crystal plastic deformation. However, it has been shown here that H_2O is stored in the grain boundary region and can be re-introduced into grains by cracking, whereby dislocations may be generated too (Fitz Gerald et al., 1991). Thus, H_2O recycling between grain interiors and grain boundary regions appears to be a continuing process during dislocation creep of quartz.

Therefore, measuring low intragranular H_2O content in naturally deformed rocks (after the deformation has ceased and rocks have been exhumed to the surface) does not necessarily indicate a high strength of the quartz, because the H_2O in the grain boundary region will have been lost in the process but may have been available during the deformation.

In order for the H_2O to be available for the deformation, it has to be maintained in the grain boundary region. This is one important condition for H_2O weakening. If the H_2O is removed, by, e.g., partial melting, where H_2O is partitioned into the melt and the melt is removed from the rock, the rock may effectively become very strong. This may be the case for granulites. So, one further great difference between the experiments and natural conditions is the fact that a natural system may not be closed, contrary to the experiments, where the sample and the H_2O are contained in the jacket.

Other minerals

The H_2O weakening in olivine has been studied extensively and the weakening has been attributed to point defects of H enhancing climb processes (Mei and Kohlstedt, 2000; Zhao et al., 2004). This weakening process is very different from what is observed in quartz, the olivine being able to deform by breaking Mg-O bonds whereas quartz has fully connected strong Si-O bonds in all directions.

According to this study, it is quite conceivable that similar processes may take place as those described in our quartz samples, because the number of slip systems active in olivine are also limited, suggesting that grain boundary accommodation processes may be important during deformation too. The solubility increase with pressure and temperature in olivine is similar as that in quartz (Manning, 1994). Most experiments on olivine have not been performed at high pressures but at low pressures in a gas apparatus, where the solubility increase due to pressure effects (and subsequent precipitation in dilatant sites) is less important. The same arguments of solution precipitation processes being important in grain boundary regions as accommodation processes may apply to other rock-forming minerals that are important for deformation, such as feldspars.

Polymineralic rocks

Quartz is one of the most important silica minerals occurring in large amounts in igneous, metamorphic and sedimentary rocks. However, the deformation of the continental crust does not only imply quartz rheological behaviour but also the one(s) of the other(s) mineral(s) that constitute the rock. Most natural rocks are polymineralic rocks, and their strengths depend on the rheology of the different minerals that compose them.

Thus, as there is a need to understand the deformation behaviour of single minerals, there is also a need to understand how mineral assemblies deform. The mechanical understanding of the different constituent phases is as important as that of the bulk rock. Especially, minerals that form a same rock are not expected to react the same way in monomineralic or polymineralic assemblies.

The strength of an aggregate depends on the proportion of the different minerals present, their mechanical behaviour (as a function of the conditions) but also on how they are placed relatively to each other.

In addition to the polymineralic aspect, metamorphic reactions taking place during the deformation may also have an important effect on the deformation (Mansard et al., 2020a, 2020b).

Continental crust

To model the rheological behaviour of the continental crust, quartz and feldspar assemblies are currently used. The feldspar is stronger than the quartz, especially at low temperature conditions (brittle-plastic transition for higher pressure-temperature conditions). So, the quartz is able to deform plastically at lower temperature conditions than feldspar and accommodate the deformation.

Moreover, at high pressure, the H_2O weakening will be much more enhanced for quartz than for feldspar, where the pressure dependence of H_2O weakening has not been documented (yet).

Implications at larger scale (geodynamics)

As many studies before (e.g., Jaoul et al., 1984; Tullis and Yund, 1989), this study has demonstrated that H_2O has a strong effect on the deformation of quartz, due to different processes, the most important ones being grain boundary processes and their effect on recrystallization and accommodation for plasticity. Only small concentrations of H_2O are required to cause a drastic reduction in strength. The strong pressure dependence of the weakening suggests that high pressure rocks will be especially affected by the weakening. Consequently, at great depth (high pressure), the plastic deformation of quartz is expected to proceed at very low stresses. The geodynamic sites, where these processes become very important, are subduction zones. Any type of model that tries to describe the rheology of subduction zones has to incorporate the H_2O-fugacity term to account for the increasing weakness of quartz with depth. The coupling and decoupling processes that are being discussed for the generation of earthquakes in subduction zones should take into account quartz rheologies dependent on H_2O and pressure.

Further work and perspectives

The results obtained in this study allow to identify some of the mechanisms that are active in the deformation of wet quartz aggregates. However, some questions are still unresolved and will need further research for a better understanding.

First, one of the major uncertainties is the characterization of the flow law parameters. Indeed, the strain rate stepping experiments performed here need to be repeated in order to obtain additional and better data allowing to characterize the n-exponent and verify whether the n-value varies systematically with pressure conditions or not. With n variations, the m-exponent and its potential change with pressure would need to be specified.

Then, other flow law parameters need to be determined. The most important term among these is the activation energy (Q), which so far shows a rather wide range of values (see a compilation in Richter et al., 2018). The variation in existing Q-values makes a reliable extrapolation of quartz rheology to geologically applicable strain rates very difficult at present. The same is true for the pre-exponential factor (A), of course, as this is required to complete the flow law. One way to improve the data base for determining these parameters would be new experiments performed at constant stress (instead of constant strain rate), as these will yield more reliable results at lower total strain.

Finally, it has to be determined if the dependence on H_2O concentration or speciation should be integrated into the flow low (C_{OH}^{p}) in addition to the H_2O fugacity term, the quantity of H_2O available being a crucial parameter, as already suggested by Stünitz et al. (2017). The results of the collaborative PhD at Charles University, Prague, will provide some important observations for this aspect.

For the H_2O contents and speciation, their evolution during deformation could be further studied by FTIR mapping. This precise technique could allow to determine how H_2O is redistributed between porphyroclasts, subgrains, recrystallized material and cracks. Further FTIR studies could also be performed at low temperature conditions to determine the form of H_2O in the sample (inclusions or clusters). The FTIR mapping should be coupled with cathodoluminescence images and EBSD maps in order to obtain a complete data set. However, one difficulty resides in the fact that porphyroclasts and small grains cannot be studied together as the resolution needed is not the same.

For the cathodoluminescence, it appears that the chemical characterization (major but also trace elements) of both starting and deformed samples should be conducted. The origin of the bright blue luminescence into the deformed samples would be an interesting parameter that will help to understand the exchange processes and chemical species (e.g., Ti may produce blue luminescence in quartz Bestmann and Pennacchioni, 2015) that happen within the small sized grains and at the boundary of the clasts during the deformation, these processes being fundamental in the pressure enhanced H_2O weakening mechanism.

The deformation mechanisms acting during sample deformation and especially the formation of the small grains need to be investigated in more detail, using TEM.

VI. References

Aasly, K., Malvik, T., Myrhaug, E.H., 2007. Advanced methods to characterize thermal properties of quartz. 12.

Aines, R.D., Rossman, G.R., 1984. Water in minerals? A peak in the infrared. Journal of Geophysical Research: Solid Earth 89, 4059–4071. https://doi.org/10.1029/JB089iB06p04059

Bachmann, F., Hielscher, R., Schaeben, H., 2011. Grain detection from 2d and 3d EBSD data—Specification of the MTEX algorithm. Ultramicroscopy 111, 1720–1733. https://doi.org/10.1016/j.ultramic.2011.08.002

Bailey, J.E., Hirsch, P.B., Mott, N.F., 1962. The recrystallization process in some polycrystalline metals. Proceedings of the Royal Society of London. Series A. Mathematical and Physical Sciences 267, 11–30. https://doi.org/10.1098/rspa.1962.0080

Barbin, V., Schvoerer, M., 1997. Cathodoluminescence and geosciences. Comptes Rendus de l`Academie des Sciences. Serie 2, Sciences de la Terre et des Planetes. https://doi.org/10.1016/S1251-8050(97)88284-5

Baron, M.A., Stalder, R., Konzett, J., Hauzenberger, C.A., 2015. OH-point defects in quartz in B- and Li-bearing systems and their application to pegmatites. Physics and Chemistry of Minerals 42, 53–62. https://doi.org/10.1007/s00269-014-0699-4

Beeler, N.M., Hirth, G., Thomas, A., Bürgmann, R., 2016. Effective stress, friction, and deep crustal faulting. Journal of Geophysical Research: Solid Earth 121, 1040–1059. https://doi.org/10.1002/2015JB012115

Bestmann, M., Pennacchioni, G., 2015. Ti distribution in quartz across a heterogeneous shear zone within a granodiorite: The effect of deformation mechanism and strain on Ti resetting. Lithos 227, 37–56. https://doi.org/10.1016/j.lithos.2015.03.009

Blacic, J.D., 1981. Water diffusion in quartz at high pressure: Tectonic implications. Geophysical Research Letters 8, 721–723. https://doi.org/10.1029/GL008i007p00721

Boggs, S., Krinsley, D.H., Goles, G.G., Seyedolali, A., Dypvik, H., 2001. Identification of shocked quartz by scanning cathodoluminescence imaging. Meteoritics & Planetary Science 36, 783–791. https://doi.org/10.1111/j.1945-5100.2001.tb01916.x

Bunge, H.J., 1982. Texture analysis in materials science–mathematical methods. Lst Edn 2–35.

Burgmann, R., Dresen, G., 2008. Rheology of the Lower Crust and Upper Mantle: Evidence from Rock Mechanics, Geodesy, and Field Observations. 48.

Byerlee, J.D., 1968. Brittle-ductile transition in rocks. Journal of Geophysical Research (1896-1977) 73, 4741–4750. https://doi.org/10.1029/JB073i014p04741

Chernak, L.J., Hirth, G., Selverstone, J., Tullis, J., 2009. Effect of aqueous and carbonic fluids on the dislocation creep strength of quartz. Journal of Geophysical Research: Solid Earth 114. https://doi.org/10.1029/2008JB005884

Cordier, P., Doukhan, J.-C., 1989. Water solubility in quartz and its influence on ductility. European Journal of Mineralogy 221–238. https://doi.org/10.1127/ejm/1/2/0221

den Brok, B., Meinecke, J., Röller, K., 1994. Fourier transform IR-determination of intragranular water content in quartzites experimentally deformed with and without added water in the ductile deformation field. Journal of Geophysical Research: Solid Earth 99, 19821–19828. https://doi.org/10.1029/94JB01473

den Brok, S.W.J. (Bas) den, 1998. Effect of microcracking on pressure-solution strain rate: The Gratz grain-boundary model. Geology 26, 915–918. https://doi.org/10.1130/0091-7613(1998)026<0915:EOMOPS>2.3.CO;2

den Brok, S.W.J., Spiers, C.J., 1991. Experimental evidence for water weakening of quartzite by microcracking plus solution–precipitation creep. Journal of the Geological Society 148, 541–548. https://doi.org/10.1144/gsjgs.148.3.0541

Farmer, V. t, Russell, J.D., 1964. The infra-red spectra of layer silicates. Spectrochimica Acta 20, 1149–1173.

Farver, J.R., Yund, R.A., 1992. Oxygen diffusion in a fine-grained quartz aggregate with wetted and nonwetted microstructures. Journal of Geophysical Research 97, 14017. https://doi.org/10.1029/92JB01206

Farver, J.R., Yund, R.A., 1991a. Measurement of oxygen grain boundary diffusion in natural, fine-grained, quartz aggregates. Geochimica et Cosmochimica Acta 55, 1597–1607. https://doi.org/10.1016/0016-7037(91)90131-N

Farver, J.R., Yund, R.A., 1991b. Oxygen diffusion in quartz: Dependence on temperature and water fugacity. Chemical Geology 90, 55–70. https://doi.org/10.1016/0009-2541(91)90033-N

Finch, M.A., Weinberg, R.F., Hunter, N.J.R., 2016. Water loss and the origin of thick ultramylonites. Geology 44, 599–602. https://doi.org/10.1130/G37972.1

Fitz Gerald, J.D., Boland, J.N., McLaren, A.C., Ord, A., Hobbs, B.E., 1991. Microstructures in water-weakened single crystals of quartz. Journal of Geophysical Research 96, 2139. https://doi.org/10.1029/90JB02190

Fukuda, J., Holyoke, C.W., Kronenberg, A.K., 2018. Deformation of Fine-Grained Quartz Aggregates by Mixed Diffusion and Dislocation Creep. Journal of Geophysical Research: Solid Earth 123, 4676–4696. https://doi.org/10.1029/2017JB015133

Fukuda, J., Shimizu, I., 2019. Water distribution in quartz schists of the Sanbagawa Metamorphic Belt, Japan: infrared spectroscopic mapping and comparison of the calibrations proposed for determining water contents. Earth, Planets and Space 71, 136. https://doi.org/10.1186/s40623-019-1117-4

Fusseis, F., Regenauer-Lieb, K., Liu, J., Hough, R.M., De Carlo, F., 2009. Creep cavitation can establish a dynamic granular fluid pump in ductile shear zones. Nature 459, 974–977. https://doi.org/10.1038/nature08051

Gerretsen, J., Paterson, M.S., McLaren, A.C., 1989. The uptake and solubility of water in quartz at elevated pressure and temperature. Physics and Chemistry of Minerals 16. https://doi.org/10.1007/BF00199553

Gleason, G.C., DeSisto, S., 2008. A natural example of crystal-plastic deformation enhancing the incorporation of water into quartz. Tectonophysics 446, 16–30. https://doi.org/10.1016/j.tecto.2007.09.006

Gleason, G.C., Tullis, J., 1995. A flow law for dislocation creep of quartz aggregates determined with the molten salt cell. 23.

Götze, J., Plötze, M., Habermann, D., 2001. Origin, spectral characteristics and practical applications of the cathodoluminescence (CL) of quartz - a review. Mineralogy and Petrology 71, 225–250. https://doi.org/10.1007/s007100170040

Götze, J., Schertl, H.-P., Neuser, R.D., Kempe, U., Hanchar, J.M., 2013. Optical microscope-cathodoluminescence (OM–CL) imaging as a powerful tool to reveal internal textures of minerals. Mineralogy and Petrology 107, 373–392. https://doi.org/10.1007/s00710-012-0256-0

Green, H.W., Borch, R.S., 1989. A new molten salt cell for precision stress measurement at high pressure. European Journal of Mineralogy 213–220. https://doi.org/10.1127/ejm/1/2/0213

Griggs, D., 1967. Hydrolytic Weakening of Quartz and Other Silicates. Geophysical Journal of the Royal Astronomical Society 14, 19–31. https://doi.org/10.1111/j.1365-246X.1967.tb06218.x

Griggs, D.T., Blacic, J.D., 1965. Quartz: Anomalous Weakness of Synthetic Crystals. Science 147, 292–295. https://doi.org/10.1126/science.147.3655.292

Gumez, L., 2010. Caractérisation des propriétés physico-chimiques du tendon altéré par l'absence du facteur de transcription TIEG1 (TGFβ inducible Early Gene 1). These de doctorat. Compiègne.

Hamers, M.F., Pennock, G.M., Drury, M.R., 2017. Scanning electron microscope cathodoluminescence imaging of subgrain boundaries, twins and planar deformation features in quartz. Physics and Chemistry of Minerals 44, 263–275.

Hamers, M.F., Pennock, G.M., Herwegh, M., Drury, M.R., 2016. Distinction between amorphous and healed planar deformation features in shocked quartz using composite color scanning electron microscope cathodoluminescence (SEM-CL) imaging. Meteoritics & Planetary Science 51, 1914–1931. https://doi.org/10.1111/maps.12711

Hansen, L.N., Zimmerman, M.E., Kohlstedt, D.L., 2012. The influence of microstructure on deformation of olivine in the grain-boundary sliding regime. Journal of Geophysical Research: Solid Earth 117. https://doi.org/10.1029/2012JB009305

Heilbronner, R., 2002. Analysis of bulk fabrics and microstructure variations using tesselations of autocorrelation functions. Computers & Geosciences 28, 447–455. https://doi.org/10.1016/S0098-3004(01)00088-7

Heilbronner, R., Barrett, S., 2013. Image Analysis in Earth Sciences: Microstructures and Textures of Earth Materials. Springer Science & Business Media.

Heilbronner, R., Tullis, J., 2002. The effect of static annealing on microstructures and crystallographic preferred orientations of quartzites experimentally deformed in axial compression and shear. Geological Society, London, Special Publications 200, 191–218. https://doi.org/10.1144/GSL.SP.2001.200.01.12

Hirth, G., Beeler, N.M., 2015. The role of fluid pressure on frictional behavior at the base of the seismogenic zone. Geology 43, 223–226. https://doi.org/10.1130/G36361.1

Hirth, G., Teyssier, C., Dunlap, J.W., 2001. An evaluation of quartzite flow laws based on comparisons between experimentally and naturally deformed rocks. International Journal of Earth Sciences 90, 77–87.

Hirth, G., Tullis, J., 1994. The brittle-plastic transition in experimentally deformed quartz aggregates. Journal of Geophysical Research: Solid Earth 99, 11731–11747. https://doi.org/10.1029/93JB02873

Hirth, G., Tullis, J., 1992. Dislocation creep regimes in quartz aggregates. Journal of Structural Geology 14, 145–159. https://doi.org/10.1016/0191-8141(92)90053-Y

Holyoke, C.W., Kronenberg, A.K., 2013. Reversible water weakening of quartz. Earth and Planetary Science Letters 374, 185–190. https://doi.org/10.1016/j.epsl.2013.05.039

Holyoke, C.W., Kronenberg, A.K., 2010. Accurate differential stress measurement using the molten salt cell and solid salt assemblies in the Griggs apparatus with applications to strength, piezometers and rheology. Tectonophysics 494, 17–31. https://doi.org/10.1016/j.tecto.2010.08.001

Ito, Y., Nakashima, S., 2002. Water distribution in low-grade siliceous metamorphic rocks by micro-FTIR and its relation to grain size: a case from the Kanto Mountain region, Japan. Chemical Geology 189, 1–18. https://doi.org/10.1016/S0009-2541(02)00022-0

Jaoul, O., Tullis, J., Kronenberg, A., 1984. The effect of varying water contents on the creep behavior of Heavitree quartzite. Journal of Geophysical Research: Solid Earth 89, 4298–4312. https://doi.org/10.1029/JB089iB06p04298

Jollands, M.C., Blanchard, M., Balan, E., 2020. Structure and theoretical infrared spectra of OH defects in quartz. European Journal of Mineralogy 32, 311–323. https://doi.org/10.5194/ejm-32-311-2020

Kats, A., 1962. Hydrogen in alpha-quartz. Philips Res. Rep. 17, 133-195,201-279.

Kekulawala, K., Paterson, M.S., Boland, J.N., 1981. An experimental study of the role of water in quartz deformation. Mechanical Behaviour of Crustal Rocks, Geophys. Monogr. Ser 24.

Kekulawala, K.R.S.S., Paterson, M.S., Boland, J.N., 1978. Hydrolytic weakening in quartz. Tectonophysics 46, T1–T6. https://doi.org/10.1016/0040-1951(78)90101-4

Kilian, R., Heilbronner, R., 2017. Analysis of crystallographic preferred orientations of experimentally deformed Black Hills Quartzite. Solid Earth 8, 1095.

Kilian, R., Heilbronner, R., Holyoke, C.W., Kronenberg, A.K., Stünitz, H., 2016. Dislocation creep of dry quartz. Journal of Geophysical Research: Solid Earth 121, 3278–3299. https://doi.org/10.1002/2015JB012771

Kohlstedt, D.L., Evans, B., Mackwell, S.J., 1995. Strength of the lithosphere: Constraints imposed by laboratory experiments. Journal of Geophysical Research: Solid Earth 100, 17587–17602.

Kronenberg, A.K., 1994. Chapter 4. HYDROGEN SPECIATION AND CHEMICAL WEAKENING OF QUARTZ, Silica. De Gruyter.

Kronenberg, A.K., Ashley, K.T., Francsis, M.K., Holyoke III, C.W., Jezek, L., Kronenberg, J.A., Law, R.D., Thomas, J.B., 2020. Water loss during dynamic recrystallization of Moine thrust quartzites, northwest Scotland. Geology 48, 557–561. https://doi.org/10.1130/G47041.1

Kronenberg, A.K., Hasnan, H.F.B., Holyoke III, C.W., Law, R.D., Liu, Z., Thomas, J.B., 2017. Synchrotron FTIR imaging of OH in quartz mylonites. Solid Earth 8, 1025–1045. https://doi.org/10.5194/se-8-1025-2017

Kronenberg, A.K., Kirby, S.H., Aines, R.D., Rossman, G.R., 1986. Solubility and diffusional uptake of hydrogen in quartz at high water pressures: Implications for hydrolytic weakening. Journal of Geophysical Research: Solid Earth 91, 12723–12741. https://doi.org/10.1029/JB091iB12p12723

Kronenberg, A.K., Segall, P., Wolf, G.H., 1990. Hydrolytic weakening and penetrative deformation within a natural shear zone. Geophysical Monograph 56, 21–36.

Kronenberg, A.K., Tullis, J., 1984. Flow strengths of quartz aggregates: grain size and pressure effects due to hydrolytic weakening. Journal of Geophysical Research: Solid Earth 89, 4281–4297.

Kronenberg, A.K., Wolf, G.H., 1990. Fourier transform infrared spectroscopy determinations of intragranular water content in quartz-bearing rocks: implications for hydrolytic weakening in the laboratory and within the earth. Tectonophysics 172, 255–271. https://doi.org/10.1016/0040-1951(90)90034-6

Larrieu, T.L., Ayers, J.C., 1997. Measurements of the pressure-volume-temperature properties of fluids to 20 kbar and 1000°C: A new approach demonstrated on H2O. Geochimica et Cosmochimica Acta 61, 3121–3134. https://doi.org/10.1016/S0016-7037(97)00155-5

Libowitzky, E., Rossman, G.R., 1997. An IR absorption calibration for water in minerals. American Mineralogist 82, 1111–1115.

Lu, L.X., Jiang, D., 2019. Quartz Flow Law Revisited: The Significance of Pressure Dependence of the Activation Enthalpy. Journal of Geophysical Research: Solid Earth 124, 241–256. https://doi.org/10.1029/2018JB016226

Luan, F.C., Paterson, M.S., 1992. Preparation and deformation of synthetic aggregates of quartz. Journal of Geophysical Research: Solid Earth 97, 301–320. https://doi.org/10.1029/91JB01748

Mainprice, D., Paterson, M., 2005. Experimental deformation of flint in axial compression. Geological Society, London, Special Publications 245, 251–276. https://doi.org/10.1144/GSL.SP.2005.245.01.12

Mainprice, D.H., 1981. The experimental deformation of quartz polycrystals. https://doi.org/10.25911/5d67b1e900b5b

Mainprice, D.H., Paterson, M.S., 1984. Experimental studies of the role of water in the plasticity of quartzites. Journal of Geophysical Research: Solid Earth 89, 4257–4269. https://doi.org/10.1029/JB089iB06p04257

Manning, C.E., 2018. Thermodynamic Modeling of Fluid-Rock Interaction at Mid-Crustal to Upper-Mantle Conditions. Thermodynamics of Geothermal Fluids 76, 135.

Manning, C.E., 1994. The solubility of quartz in H2O in the lower crust and upper mantle. Geochimica et Cosmochimica Acta 58, 4831–4839. https://doi.org/10.1016/0016-7037(94)90214-3

Mansard, N., Stünitz, H., Raimbourg, H., Précigout, J., 2020a. The role of deformation-reaction interactions to localize strain in polymineralic rocks: Insights from experimentally deformed plagioclase-pyroxene assemblages. Journal of Structural Geology 134, 104008. https://doi.org/10.1016/j.jsg.2020.104008

Mansard, N., Stünitz, H., Raimbourg, H., Précigout, J., Plunder, A., Nègre, L., 2020b. Relationship between microstructures and resistance in mafic assemblages that deform and transform. Solid Earth 11, 2141–2167. https://doi.org/10.5194/se-11-2141-2020

McLaren, A.C., 2005. Transmission Electron Microscopy of Minerals and Rocks. Cambridge University Press.

Mei, S., Kohlstedt, D.L., 2000. Influence of water on plastic deformation of olivine aggregates: 2. Dislocation creep regime. Journal of Geophysical Research: Solid Earth 105, 21471–21481. https://doi.org/10.1029/2000JB900180

Menegon, L., Fusseis, F., Stünitz, H., Xiao, X., 2015. Creep cavitation bands control porosity and fluid flow in lower crustal shear zones. Geology 43, 227–230. https://doi.org/10.1130/G36307.1

Müller, A., Koch-Müller, M., 2009. Hydrogen speciation and trace element contents of igneous, hydrothermal and metamorphic quartz from Norway. Mineralogical Magazine 73, 569–583. https://doi.org/10.1180/minmag.2009.073.4.569

Muto, J., Nagahama, H., Hashimoto, T., 2005. Water distribution in dynamically recrystallized quartz grains: cathodoluminescence and micro-infrared spectroscopic mapping. Geological Society, London, Special Publications 245, 397–407. https://doi.org/10.1144/GSL.SP.2005.245.01.19

Nakashima, S., 1995. Diffusivity of ions in pore water as a quantitative basis for rock deformation rate estimates. 19.

Nakashima, S., Matayoshi, H., Yuko, T., Michibayashi, K., Masuda, T., Kuroki, N., Yamagishi, H., Ito, Y., Nakamura, A., 1995. Infrared microspectroscopy analysis of water distribution in deformed and metamorphosed rocks. Tectonophysics 245, 263–276.

Negrini, M., Stunitz, H., Berger, A., Morales, L.F., 2014. The effect of deformation on the TitaniQ geothermobarometer: an experimental study. Contributions to Mineralogy and Petrology 167, 982.

Niimi, N., Aikawa, N., Shinoda, K., 1999. The infrared absorption band at 3596 cm of the recrystallized quartz from Mt. Takamiyama, southwest Japan.

Okazaki, K., Burdette, E., Hirth, G., 2021. Rheology of the Fluid Oversaturated Fault Zones at the Brittle-Plastic Transition. Journal of Geophysical Research: Solid Earth 126, e2020JB020804. https://doi.org/10.1029/2020JB020804

Okudaira, T., Jeřábek, P., Stünitz, H., Fusseis, F., 2015. High-temperature fracturing and subsequent grain-size-sensitive creep in lower crustal gabbros: Evidence for coseismic loading followed by creep during decaying stress in the lower crust? Journal of Geophysical Research: Solid Earth 120, 3119–3141. https://doi.org/10.1002/2014JB011708

Pagel, M., Barbin, V., Blanc, P., Ohnenstetter, D., 2000. Cathodoluminescence in Geosciences: An Introduction. In: Pagel, M., Barbin, V., Blanc, P., Ohnenstetter, D. (Eds.), Cathodoluminescence in Geosciences. Springer, Berlin, Heidelberg, 1–21. https://doi.org/10.1007/978-3-662-04086-7_1

Palazzin, G., Raimbourg, H., Stünitz, H., Heilbronner, R., Neufeld, K., Précigout, J., 2018. Evolution in H2O contents during deformation of polycrystalline quartz: An experimental study. Journal of Structural Geology 114, 95–110. https://doi.org/10.1016/j.jsg.2018.05.021

Panozzo, R., 1984. Two-dimensional strain from the orientation of lines in a plane. Journal of Structural Geology, Planar and Linear Fabrics of Deformed Rocks 6, 215–221. https://doi.org/10.1016/0191-8141(84)90098-1

Passchier, C.W., Trouw, R.A.J., 2005. Microtectonics. Springer Science & Business Media.

Paterson, M., 1982. The determination of hydroxyl by infrared absorption in quartz, silicate glasses and similar materials. Bulletin de Minéralogie 105, 20–29. https://doi.org/10.3406/bulmi.1982.7582

Paterson, M., Kekulawala, K.R.S.S., 1979. The role of water in quartz deformation. Bulletin de Minéralogie 102, 92–100. https://doi.org/10.3406/bulmi.1979.7261

Paterson, M.S., 2012. Materials Science for Structural Geology. Springer Science & Business Media.

Paterson, M.S., 1987. Problems in the extrapolation of laboratory rheological data. Tectonophysics 133, 33–43. https://doi.org/10.1016/0040-1951(87)90278-2

Paterson, M.S., Luan, F.C., 1990. Quartzite rheology under geological conditions. Geological Society, London, Special Publications 54, 299–307. https://doi.org/10.1144/GSL.SP.1990.054.01.26

Paterson, M.S., Wong, T. (Eds.), 2005. Evolution of Physical Properties during Brittle Failure. Experimental Rock Deformation — The Brittle Field. Springer, Berlin, Heidelberg, 59–114. https://doi.org/10.1007/3-540-26339-X_5

Pec, M., Stünitz, H., Heilbronner, R., Drury, M., 2016. Semi-brittle flow of granitoid fault rocks in experiments. Journal of Geophysical Research: Solid Earth 121, 1677–1705. https://doi.org/10.1002/2015JB012513

Pevik, J.A., 2015. Geological and Mineralogical Characterization of the Upper Part of the Gamasfjell Quartzite at the Vaggecearu Mountain.

Pirzer, M., Sawatzki, J., 2008. Method and device for correcting a spectrum. Google Patents.

Pitzer, K.S., Sterner, S.M., 1994. Equations of state valid continuously from zero to extreme pressures for H2O and CO2. The Journal of Chemical Physics 101, 3111–3116.

Post, A., Tullis, J., 1998. The rate of water penetration in experimentally deformed quartzite: implications for hydrolytic weakening. Tectonophysics 295, 117–137. https://doi.org/10.1016/S0040-1951(98)00145-0

Post, A.D., Tullis, J., Yund, R.A., 1996. Effects of chemical environment on dislocation creep of quartzite. Journal of Geophysical Research: Solid Earth 101, 22143–22155. https://doi.org/10.1029/96JB01926

Précigout, J., Prigent, C., Palasse, L., Pochon, A., 2017. Water pumping in mantle shear zones. Nature Communications 8, 15736. https://doi.org/10.1038/ncomms15736

Précigout, J., Stünitz, H., 2016. Evidence of phase nucleation during olivine diffusion creep: A new perspective for mantle strain localisation. Earth and Planetary Science Letters 455, 94–105. https://doi.org/10.1016/j.epsl.2016.09.029

Précigout, J., Stünitz, H., Pinquier, Y., Champallier, R., Schubnel, A., 2018. High-pressure, High-temperature Deformation Experiment Using the New Generation Griggs-type Apparatus. JoVE (Journal of Visualized Experiments) e56841. https://doi.org/10.3791/56841

Précigout, J., Stünitz, H., Villeneuve, J., 2019. Excess water storage induced by viscous strain localization during high-pressure shear experiment. Scientific Reports 9, 3463. https://doi.org/10.1038/s41598-019-40020-y

Ramseyer, K., Baumann, J., Matter, A., Mullis, J., 1988. Cathodoluminescence Colours of α-Quartz. Mineralogical Magazine 52, 669–677. https://doi.org/10.1180/minmag.1988.052.368.11

Richter, B., 2017. The brittle-to-viscous transition in experimentally deformed quartz gouge. Thesis. University_of_Basel. https://doi.org/10.5451/unibas-006774848

Richter, B., Stünitz, H., Heilbronner, R., 2018. The brittle-to-viscous transition in polycrystalline quartz: An experimental study. Journal of Structural Geology 114, 1–21. https://doi.org/10.1016/j.jsg.2018.06.005

Rossman, G.R., 2006. Analytical Methods for Measuring Water in Nominally Anhydrous Minerals. Reviews in Mineralogy and Geochemistry 62, 1–28. https://doi.org/10.2138/rmg.2006.62.1

Rovetta, M.R., Holloway, J.R., Blacic, J.D., 1986. Solubility of hydroxyl in natural quartz annealed in water at 900°C and 1.5 GPa. Geophysical Research Letters 13, 145–148. https://doi.org/10.1029/GL013i002p00145

Rutter, E. H, Brodie, K.H., 2004a. Experimental intracrystalline plastic flow in hot-pressed synthetic quartzite prepared from Brazilian quartz crystals. Journal of Structural Geology 26, 259–270. https://doi.org/10.1016/S0191-8141(03)00096-8

Rutter, E. H., Brodie, K.H., 2004b. Experimental grain size-sensitive flow of hot-pressed Brazilian quartz aggregates. Journal of Structural Geology 26, 2011–2023.

Rybacki, E., Renner, J., Konrad, K., Harbott, W., Rummel, F., Stöckhert, B., 1998. A Servohydraulically-controlled Deformation Apparatus for Rock Deformation under Conditions of Ultra-high Pressure Metamorphism. Pure and Applied Geophysics 152, 579–606. https://doi.org/10.1007/s000240050168

Schmid, S.M., 1982. Microfabric studies as indicators of deformation mechanisms and flow laws operative in mountain building. A= a 6, 4.

Skemer, P., Katayama, I., Jiang, Z., Karato, S., 2005. The misorientation index: Development of a new method for calculating the strength of lattice-preferred orientation. Tectonophysics 411, 157–167. https://doi.org/10.1016/j.tecto.2005.08.023

Spear, F.S., Wark, D.A., 2009. Cathodoluminescence imaging and titanium thermometry in metamorphic quartz. Journal of Metamorphic Geology 27, 187–205. https://doi.org/10.1111/j.1525-1314.2009.00813.x

Stalder, R., Konzett, J., 2012. OH defects in quartz in the system quartz–albite–water and granite–water between 5 and 25 kbar. Physics and Chemistry of Minerals 39, 817–827. https://doi.org/10.1007/s00269-012-0537-5

Stipp, M., Kunze, K., 2008. Dynamic recrystallization near the brittle-plastic transition in naturally and experimentally deformed quartz aggregates. Tectonophysics 448, 77–97. https://doi.org/10.1016/j.tecto.2007.11.041

Stipp, M., Stünitz, H., Heilbronner, R., Schmid, S.M., 2002a. The eastern Tonale fault zone: a 'natural laboratory' for crystal plastic deformation of quartz over a temperature range from 250 to 700°C. Journal of Structural Geology 24, 1861–1884. https://doi.org/10.1016/S0191-8141(02)00035-4

Stipp, M., Stünitz, H., Heilbronner, R., Schmid, S.M., 2002b. Dynamic recrystallization of quartz: correlation between natural and experimental conditions. Geological Society, London, Special Publications 200, 171–190. https://doi.org/10.1144/GSL.SP.2001.200.01.11

Stipp, M., Tullis, J., 2003. The recrystallized grain size piezometer for quartz. Geophysical Research Letters 30. https://doi.org/10.1029/2003GL018444

Stipp, M., Tullis, J., Behrens, H., 2006. Effect of water on the dislocation creep microstructure and flow stress of quartz and implications for the recrystallized grain size piezometer. Journal of Geophysical Research: Solid Earth 111. https://doi.org/10.1029/2005JB003852

Stöckhert, B., 2002. Stress and deformation in subduction zones: insight from the record of exhumed metamorphic rocks. Geological Society, London, Special Publications 200, 255–274.

Stöckhert, B., Massonne, H.-J., Ursula Nowlan, E., 1997. Low differential stress during high-pressure metamorphism: The microstructural record of a metapelite from the Eclogite Zone, Tauern Window, Eastern Alps. Lithos 41, 103–118. https://doi.org/10.1016/S0024-4937(97)82007-5

Stöckhert, B., Renner, J., 1998. Rheology of Crustal Rocks at Ultrahigh Pressure. In: Hacker, B.R., Liou, J.G. (Eds.), When Continents Collide: Geodynamics and Geochemistry of Ultrahigh-Pressure Rocks, Petrology and Structural Geology. Springer Netherlands, Dordrecht, 57–95. https://doi.org/10.1007/978-94-015-9050-1_3

Stöckhert, B., Wachmann, M., Küster, M., Bimmermann, S., 1999. Low effective viscosity during high pressure metamorphism due to dissolution precipitation creep: the record of HP–LT metamorphic carbonates and siliciclastic rocks from Crete. Tectonophysics 303, 299–319. https://doi.org/10.1016/S0040-1951(98)00262-5

Stünitz, H., Fitz Gerald, J.D., Tullis, J., 2003. Dislocation generation, slip systems, and dynamic recrystallization in experimentally deformed plagioclase single crystals. Tectonophysics 372, 215–233. https://doi.org/10.1016/S0040-1951(03)00241-5

Stünitz, Thust, A., Heilbronner, R., Behrens, H., Kilian, R., Tarantola, A., Gerald, J.D.F., 2017. Water redistribution in experimentally deformed natural milky quartz single crystals—Implications for H2O-weakening processes. Journal of Geophysical Research: Solid Earth 122, 866–894. https://doi.org/10.1002/2016JB013533

Tarantola, A., Diamond, L.W., Stünitz, H., 2010. Modification of fluid inclusions in quartz by deviatoric stress I: experimentally induced changes in inclusion shapes and microstructures. Contributions to Mineralogy and Petrology 160, 825–843. https://doi.org/10.1007/s00410-010-0509-z

Tarantola, A., Diamond, L.W., Stünitz, H., Thust, A., Pec, M., 2012. Modification of fluid inclusions in quartz by deviatoric stress. III: Influence of principal stresses on inclusion density and orientation. Contributions to Mineralogy and Petrology 164, 537–550. https://doi.org/10.1007/s00410-012-0749-1

Thomas, S.-M., Koch-Müller, M., Reichart, P., Rhede, D., Thomas, R., Wirth, R., Matsyuk, S., 2009. IR calibrations for water determination in olivine, r-GeO2, and SiO2 polymorphs. Physics and Chemistry of Minerals 36, 489–509. https://doi.org/10.1007/s00269-009-0295-1

Tokle, L., Hirth, G., Behr, W.M., 2019. Flow laws and fabric transitions in wet quartzite. Earth and Planetary Science Letters 505, 152–161.

Trépied, L., Doukhan, J.C., Paquet, J., 1980. Subgrain boundaries in quartz theoretical analysis and microscopic observations. Physics and Chemistry of Minerals 5, 201–218.

Trepmann, C.A., Stöckhert, B., 2003. Quartz microstructures developed during non-steady state plastic flow at rapidly decaying stress and strain rate. Journal of Structural Geology 25, 2035–2051. https://doi.org/10.1016/S0191-8141(03)00073-7

Tullis, J., Shelton, G.L., Yund, R.A., 1979. Pressure dependence of rock strength : implications for hydrolytic weakening. Bulletin de Minéralogie 102, 110–114. https://doi.org/10.3406/bulmi.1979.7263

Tullis, J., Yund, R.A., 1989. Hydrolytic weakening of quartz aggregates: The effects of water and pressure on recovery. Geophysical Research Letters 16, 1343–1346. https://doi.org/10.1029/GL016i011p01343

Tullis, J., Yund, R.A., 1985. Dynamic recrystallization of feldspar: A mechanism for ductile shear zone formation. Geology 13, 238–241. https://doi.org/10.1130/0091-7613(1985)13<238:DROFAM>2.0.CO;2

Tullis, T.E., Tullis, J., 1986. Experimental rock deformation techniques. Mineral and Rock Deformation: Laboratory Studies. American Geophysical Union Washington, DC, 297–324.

van Daalen, M., Heilbronner, R., Kunze, K., 1999. Orientation analysis of localized shear deformation in quartz fibres at the brittle–ductile transition. Tectonophysics 303, 83–107. https://doi.org/10.1016/S0040-1951(98)00264-9

Vernooij, M.G.C., den Brok, B., Kunze, K., 2006. Development of crystallographic preferred orientations by nucleation and growth of new grains in experimentally deformed quartz single crystals. Tectonophysics, Deformation Mechanisms, Microstructure and Rheology of Rocks in Nature and Experiment 427, 35–53. https://doi.org/10.1016/j.tecto.2006.06.008

Vityk, M.O., Bodnar, R.J., Doukhan, J.-C., 2000. Synthetic fluid inclusions. XV. TEM investigation of plastic flow associated with reequilibration of fluid inclusions in natural quartz. Contributions to Mineralogy and Petrology 139, 285–297. https://doi.org/10.1007/s004100000142

Wassmann, S., Stöckhert, B., 2013. Low stress deformation of garnet by incongruent dissolution precipitation creep. Journal of Structural Geology 46, 200–219. https://doi.org/10.1016/j.jsg.2012.09.002

Zhao, Y.-H., Ginsberg, S.B., Kohlstedt, D.L., 2004. Solubility of hydrogen in olivine: dependence on temperature and iron content. Contributions to Mineralogy and Petrology 147, 155–161. https://doi.org/10.1007/s00410-003-0524-4

VII. Appendix

This last chapter is here to precise different elements cited in the previous chapters of the thesis but for which a development in the main text was not necessary.

First, photos from the sample assembly manufacturing will be presented.

Then SEM cathodoluminescence images are compared with the corresponding EBSD maps.

The third part presents complementary data obtained from image analysis of both optical light and cathodoluminescence datasets with associated statistics as well as anisotropy study of the different samples.

Finally, additional data concerning Araldite contamination, H_2O contents and OH speciation are shown.

VII.1. The sample assembly

This first part shows some of the photographs taken during the different steps of the sample assembly fabrication.

VII.1.1. Sample

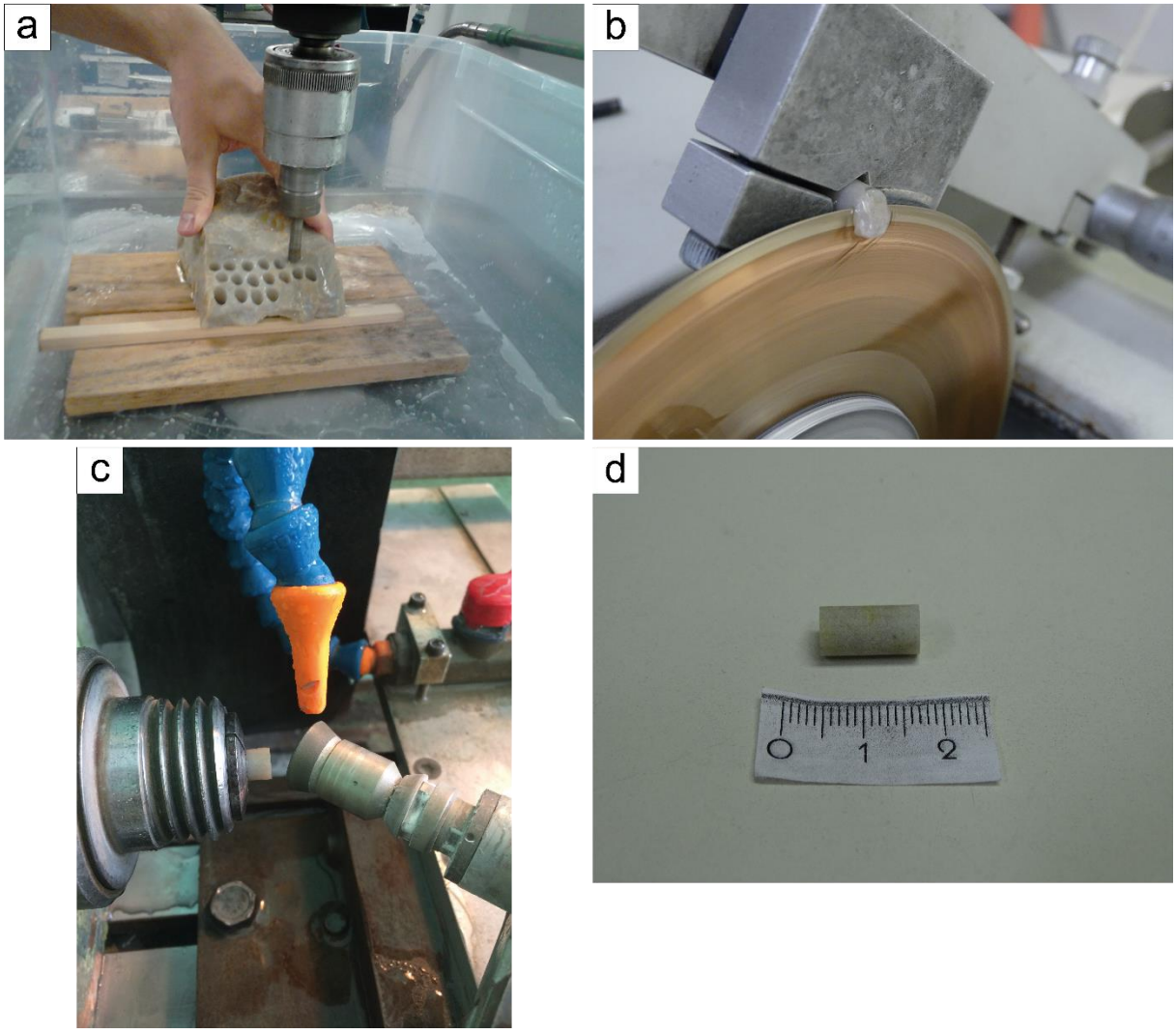

Figure VII.1. (a) Samples are cored into a Tana quartzite block using a drill press. (b) The samples ends are cut with a diamond saw (1-2 mm more than the desired final length). (c) The ends of the sample are then plane parallelized using the lathe machine and a diamond grinding tool with water as lubricant. (d) Final sample obtained.

VII.1.2. Jacket

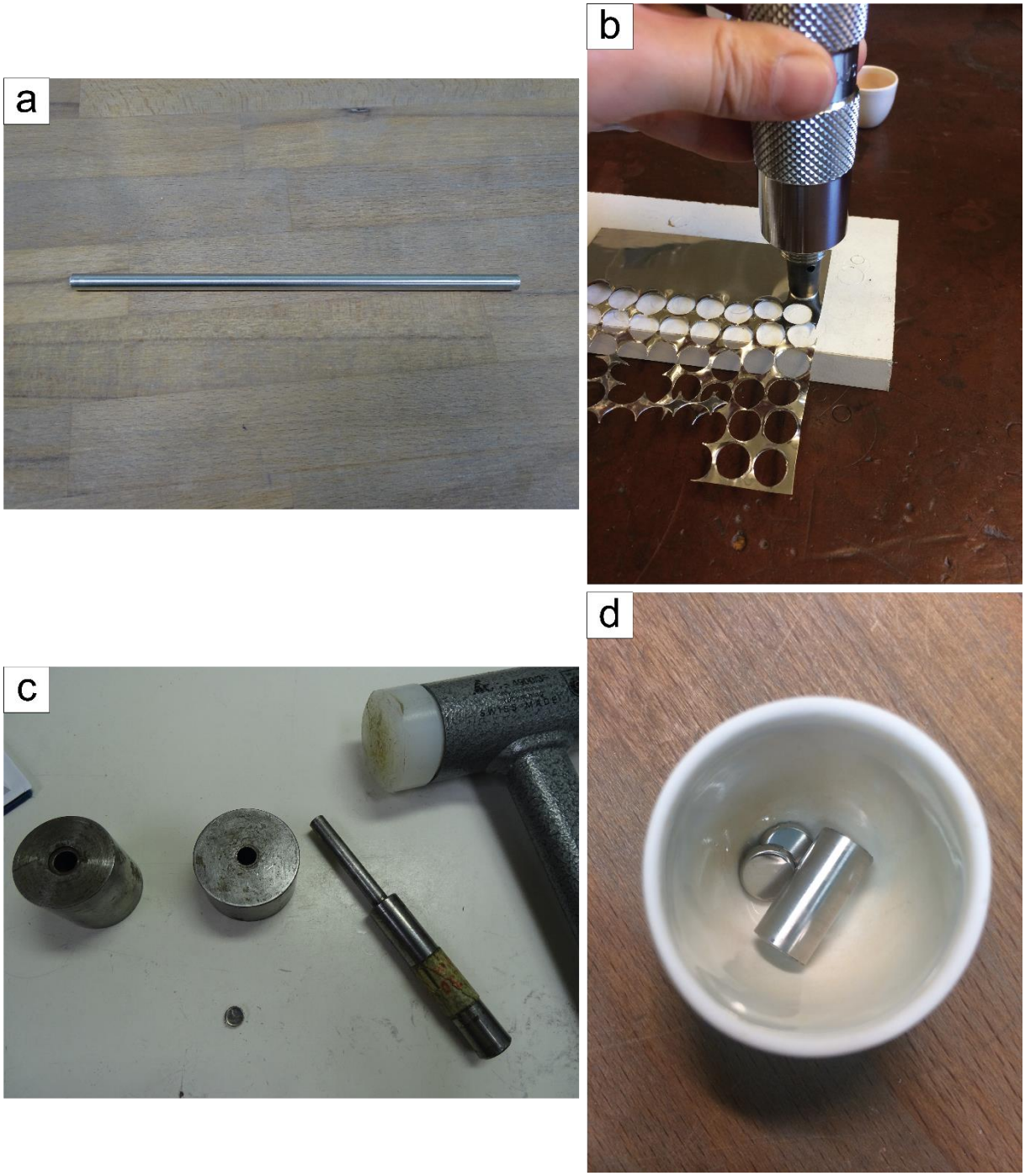

Figure VII.2. (a) Platinum tube from which the jacket is cut. (b) Two discs are cut in a platinum foil (0.15 mm) with a metal pincher (10 mm diameter). (c) The discs are then embossed with a special tool in order to form the cups. (d) The platinum tube and the two cups are then annealed at 900°C for at least 2 hours.

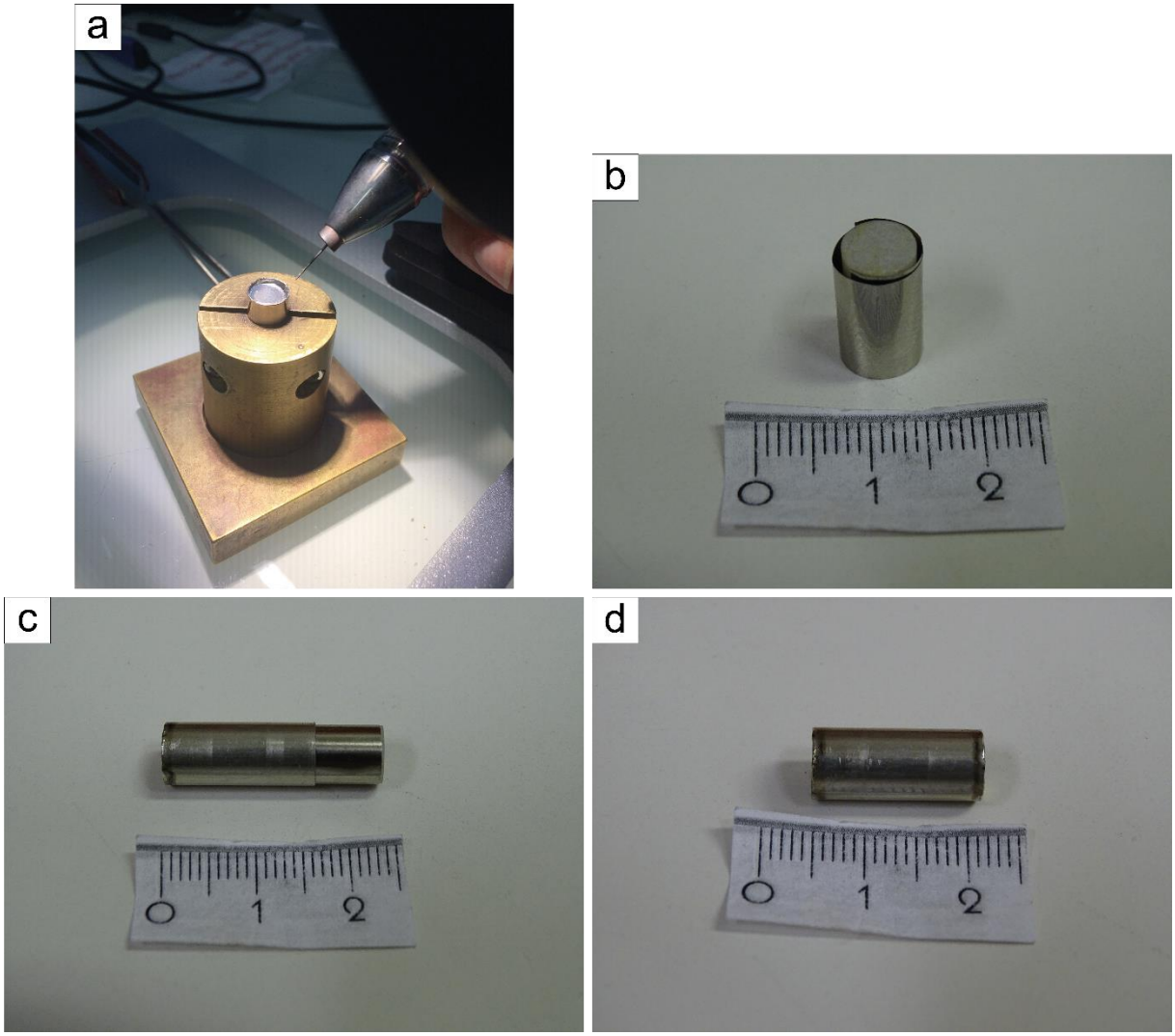

Figure VII.3. (a) One cup is first weld sealed at one extremity of the platinum tube using PUK welding machine. (b) The sample is twice wrapped into a Nickel foil. (c) The sample and the Ni foil are inserted into the half-welded jacket. The needed H_2O is added at the bottom before inserting them. (d) The second cup is weld sealed on the platinum tube. The jacket is ready.

VII.1.3. Thermocouples

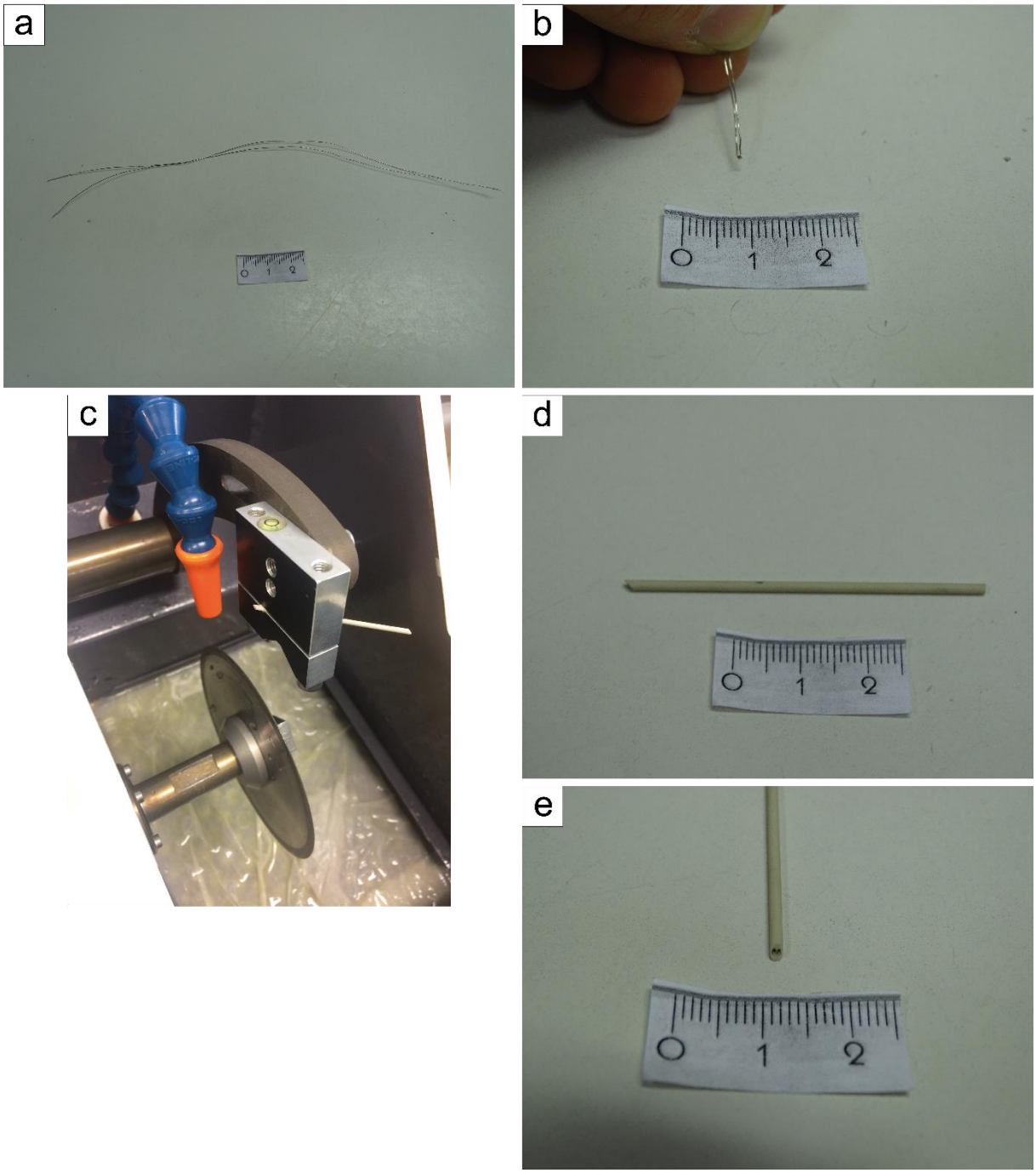

Figure VII.4. (a) For S-type thermocouples, two wires are cut: one made of Pt and the other of Pt-Rh. (b) The two wires are then welded together at one tip. The weld is then flattened and cut to a square shape. (c) The mullite tubes sheaths are cut at the right length with one end cut at 45° using the diamond saw and a special holder. (d) The longer mullite tube with one end at 45° and the other flat. (e) The mullite tubes contain two holes where the wires will be inserted. The holes need to be parallel to the 45° end.

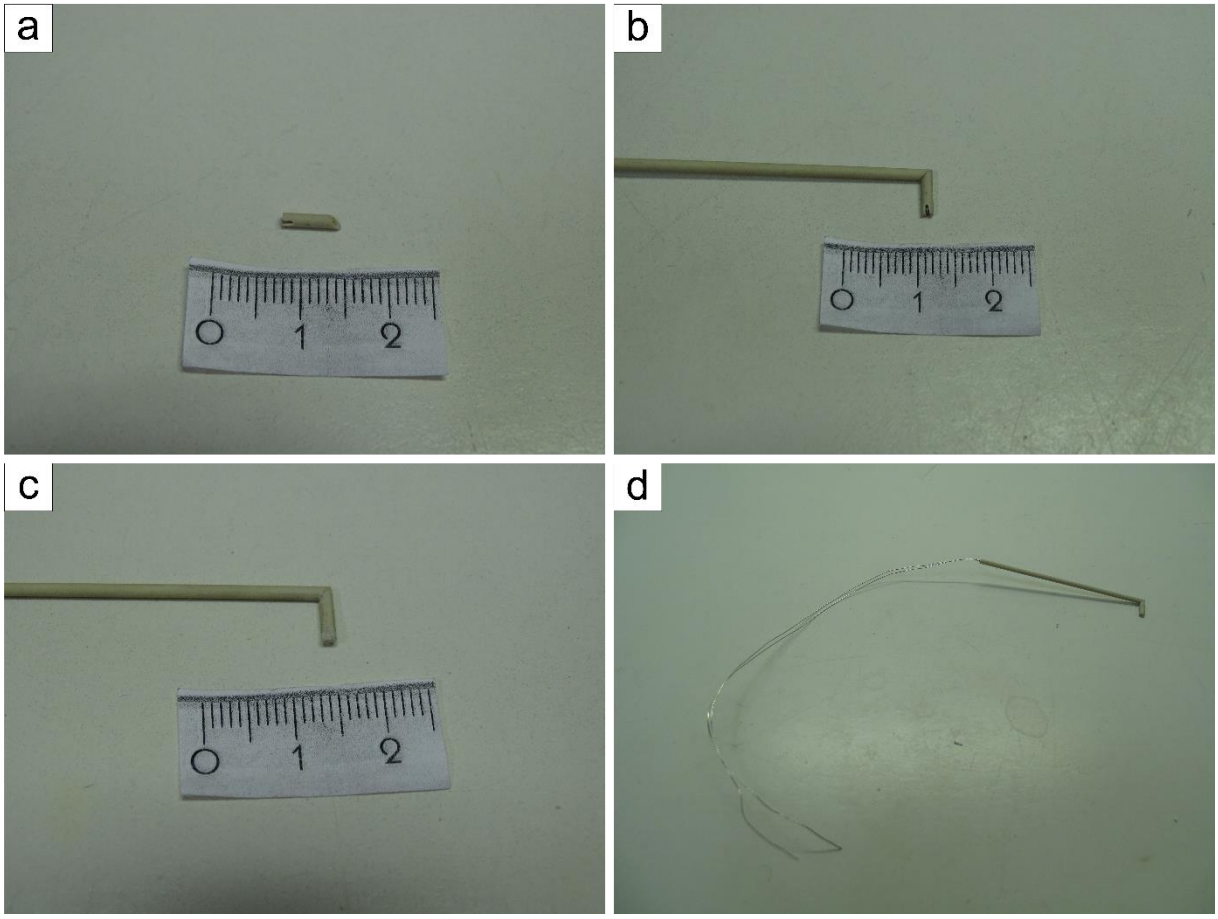

Figure VII.5. (a) A notch is made at the flat part of the smaller mullite tube. (b) The wires are then inserted into the two mullite tubes sheaths, the weld at the end of the wires fit into the notch made at the end of the smaller tube. The wires are bend in order to obtain a 90° angle between the two mullite tubes. (c) The mullite tubes are then glued together with ceramic glue and the notch is sealed with the same material. (d) The final thermocouple.

VII.1.4. Alumina pistons

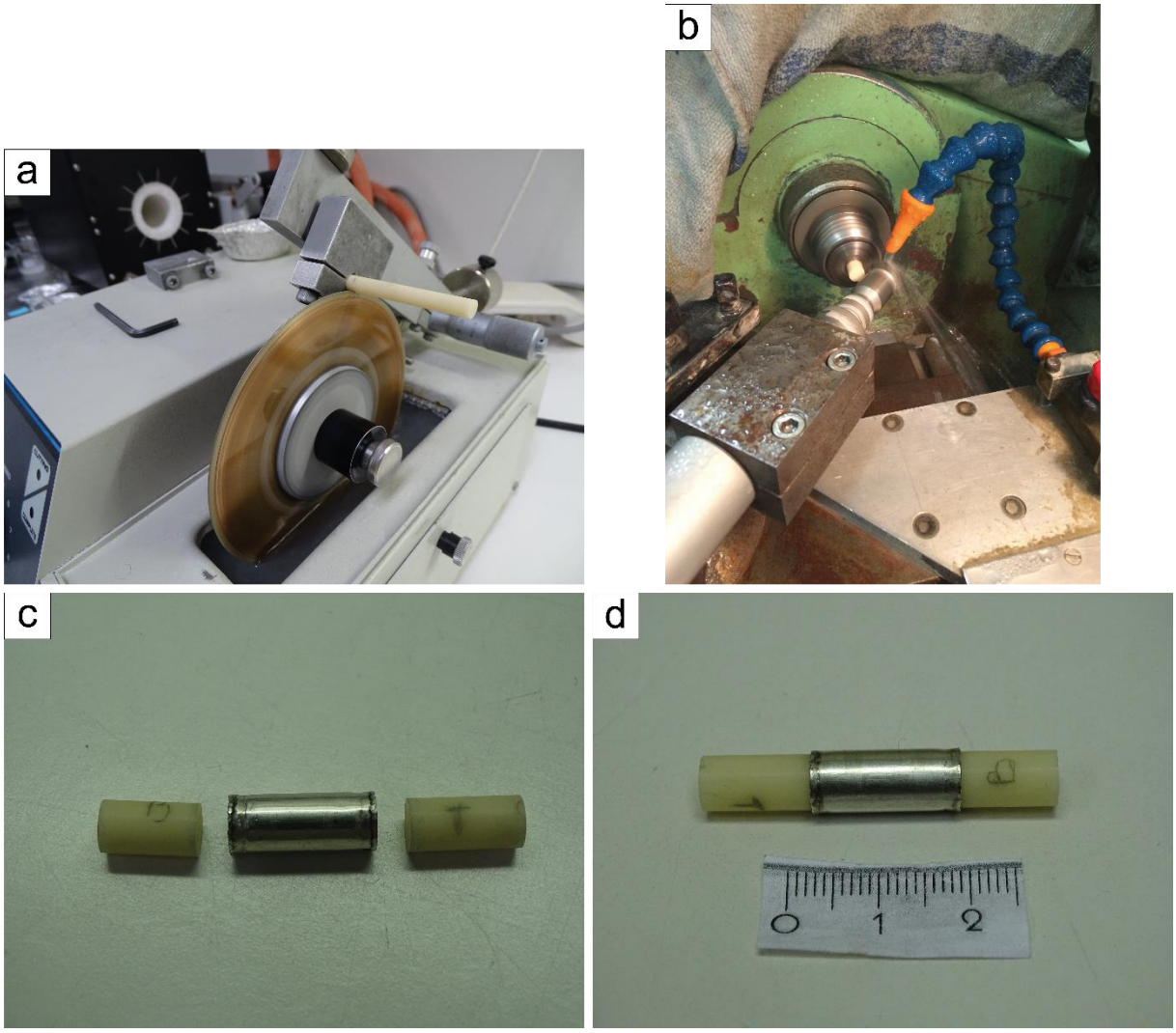

Figure VII.6. (a) The alumina pistons are cut with a diamond saw (1-2 mm more than the desired size). (b) The pistons ends are then plane parallelized and their length adjusted with the lathe machine equipped with a diamond grinding tool under water flow. (c) The two pistons are positioned at the ends of the jacket. They have to fit inside the two cups. (d) The pistons are inserted at the jacket ends.

VII.1.5. Salt pieces

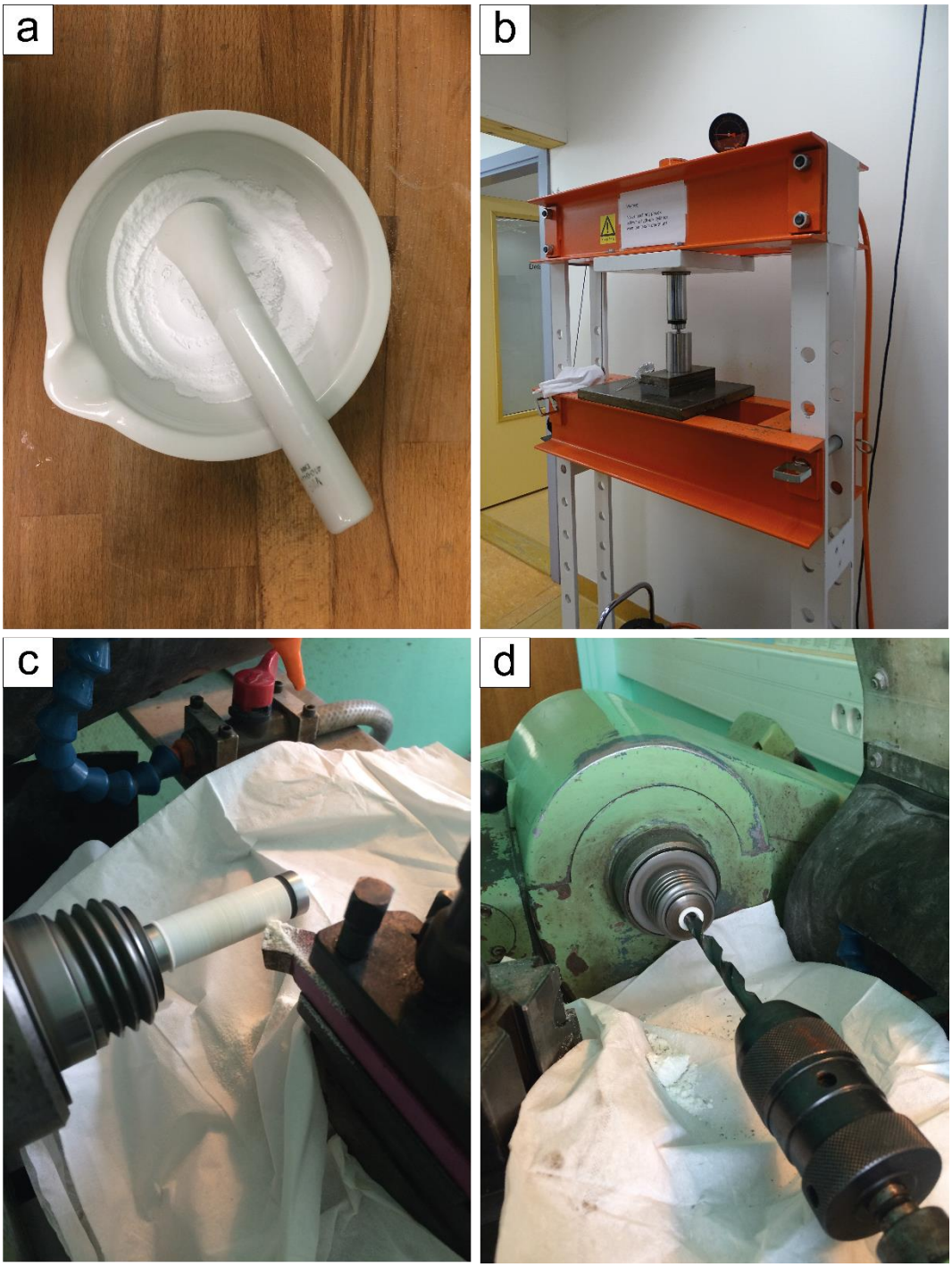

Figure VII.7. (a) NaCl is grinded into a ceramic mortar until it has the aspect of powdered sugar. (b) The salt is then cold pressed into special molds with 1-2 drops of distilled H2O to obtain the different pieces. (c) In Orléans, the external diameter of the salt pieces is adjusted using the lathe and a special blade. Here the external diameter of an inner salt piece is reduced in order to fit inside the furnace. (d) The inner diameter of the middle inner salt piece is also adjusted by drilling using the lathe machine. The inner diameter of the salt piece needs to be enlarged in order to fit the jacketed sample.

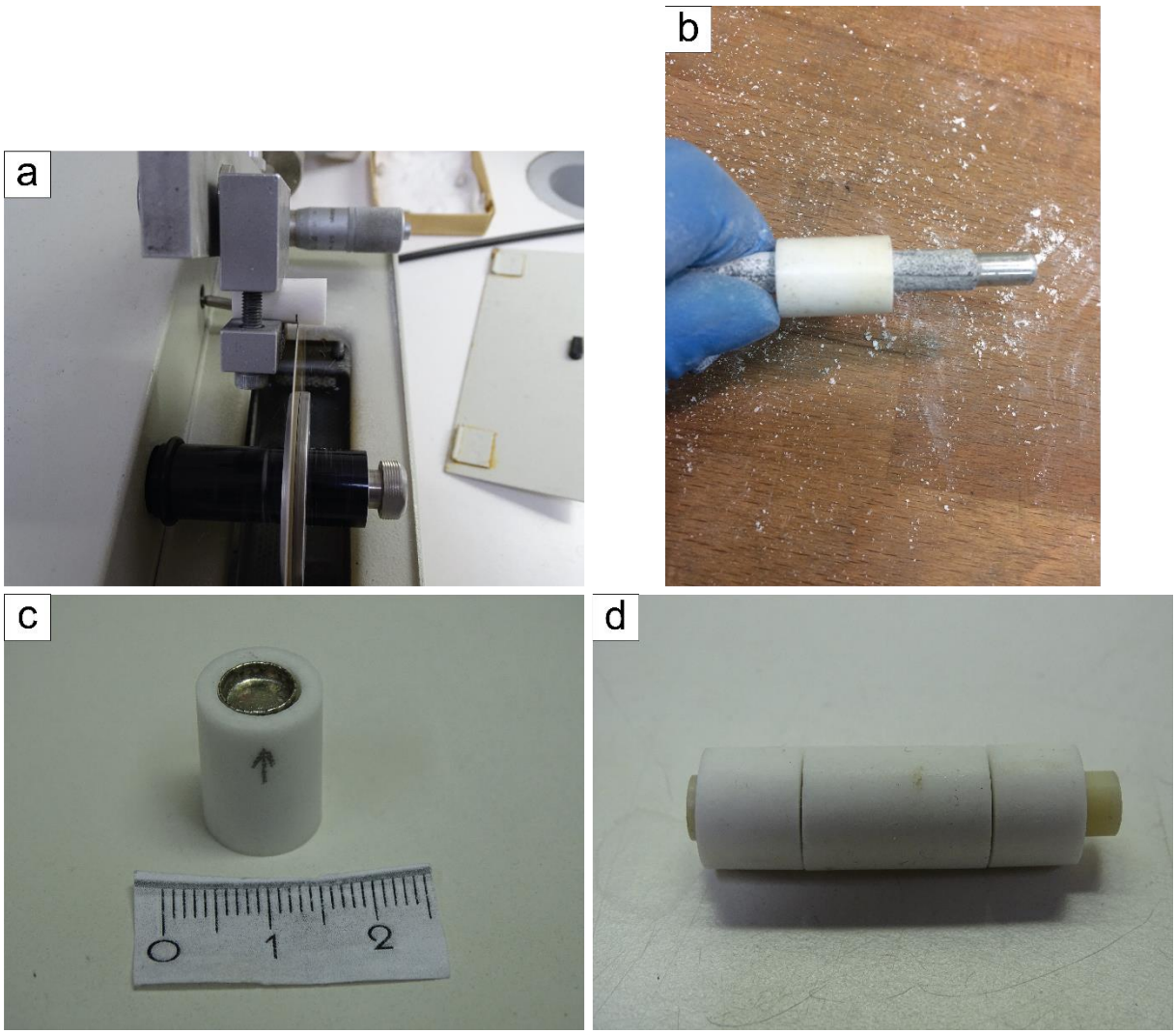

Figure VII.8. (a) The inner salt pieces are cut at the right dimensions using the diamond saw. Their length is then adjusted, and their ends plane parallelized with sandpaper. (b) Their inner diameter could be adjusted with a special grinding tool if needed. (c) The middle inner salt piece fit the jacket length. (d) The three inner salt pieces are put around the jacket and the pistons. The pistons are longer than the inner salt pieces in order to fit into the small Cu disc at the bottom (left on the image) and the big Cu disc and top lead piece at the top (right on the image).

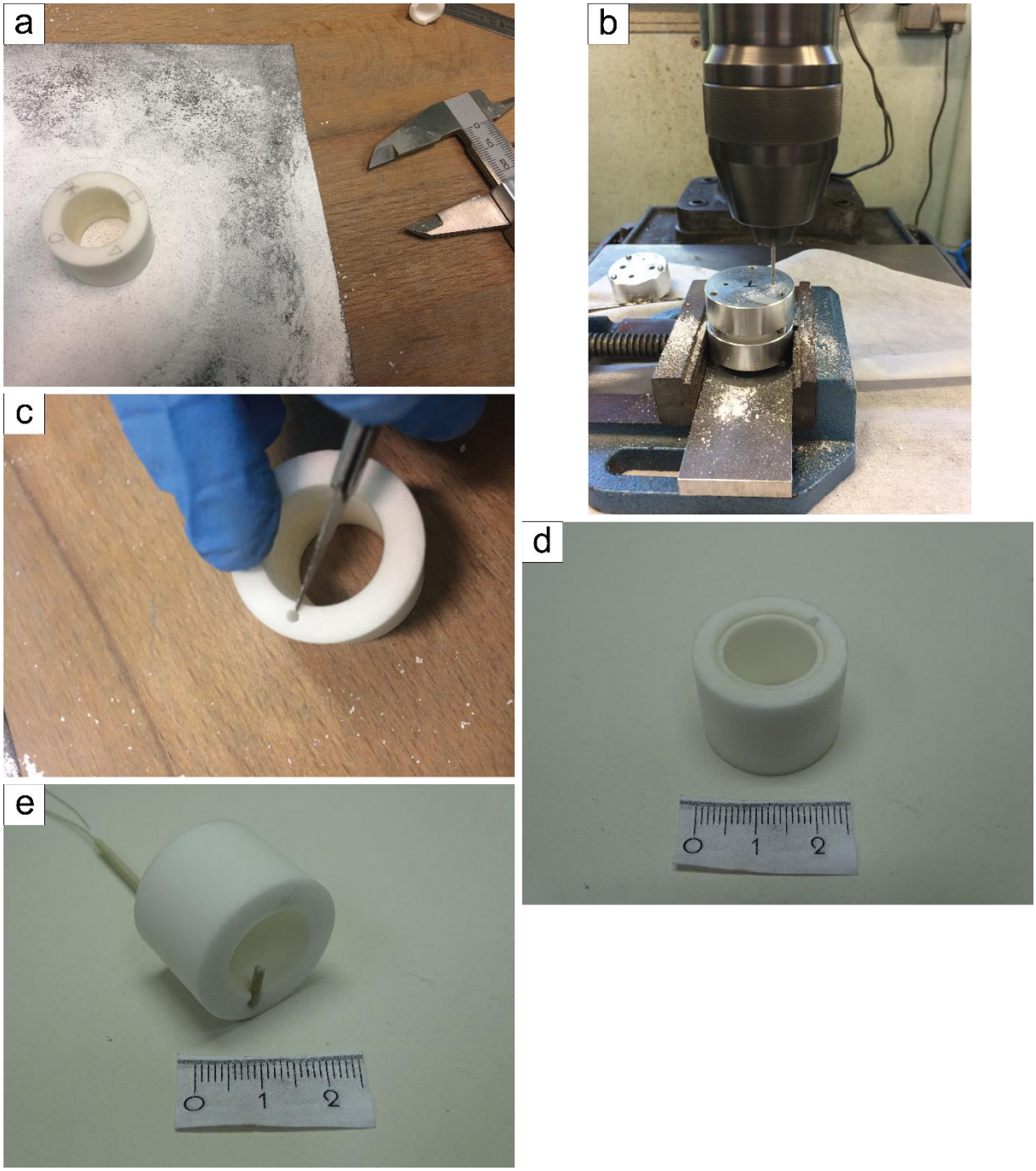

Figure VII.9. (a) The outer salt pieces are grinded with sandpaper to obtain the right length. (b) The bottom outer salt piece is drilled in order to pass the thermocouples inside. (c) The top part of the drill is dug with a scalpel to receive the 90° angle of the thermocouples. (d) At the bottom part of the bottom salt piece there is a special trench that will fit the small Cu disc. (e) The thermocouples should fit well inside the trench dug at the top part of the outer bottom salt piece.

VII.1.6. Furnace

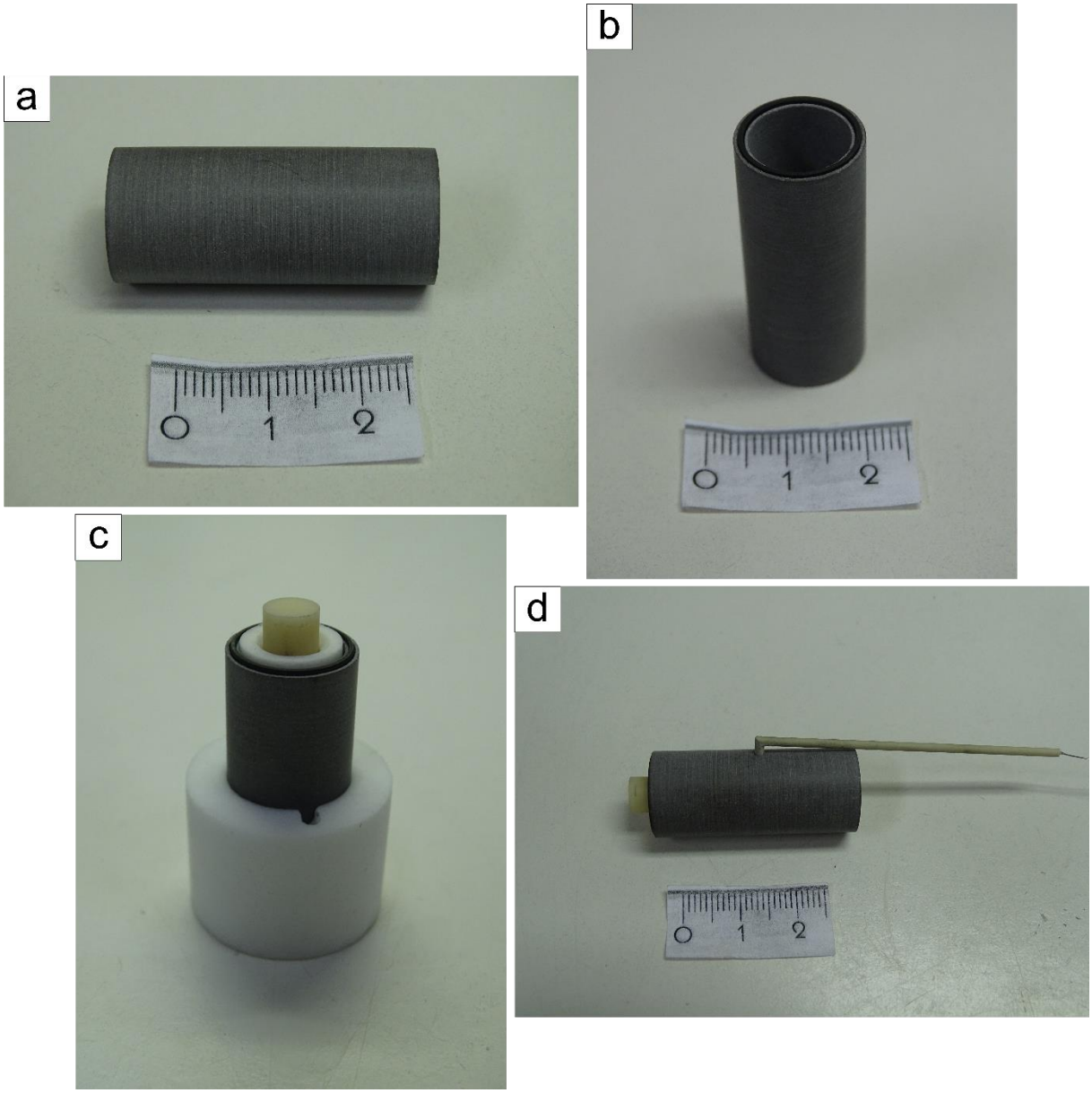

Figure VII.10. (a) and (b) The furnace is made of one graphite tube inserted into two pyrophyllite tubes, the graphite tube being slightly longer than the pyrophyllite ones. (c) The furnace is inserted into the outer salt pieces and inner salt pieces surrounding the sample and the pistons take place into it. The thermocouple will take place into the hole inside the outer bottom salt piece. (d) The thermocouple is inserted into the furnace and the inner salt pieces in order to be in contact with the sample's jacket.

VII.1.7. Lead piece

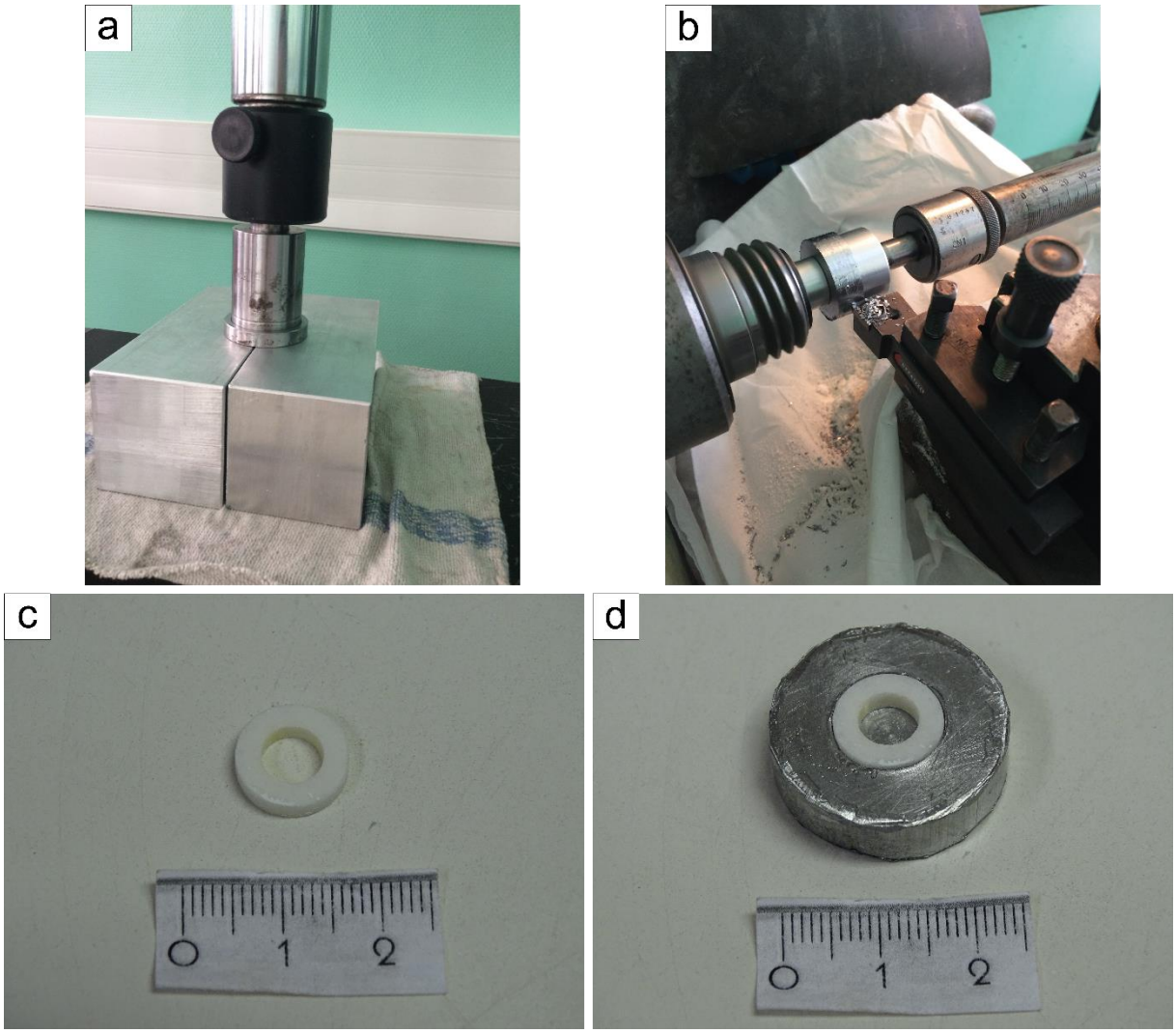

Figure VII.11. (a) The lead piece is made by pressing 50 g of melted lead at 4 tons during 30 seconds in a special mold. (b) The external diameter of the lead piece can be adjusted using the lathe machine and a special blade. (c) A salt ring is cut into an inner salt piece and is ground with sandpaper to the right thickness. (d) The salt ring is inserted at the bottom part of the lead piece. It will maintain the topmost part of the top piston in place.

VII.1.8. Pyrophyllite bottom piece

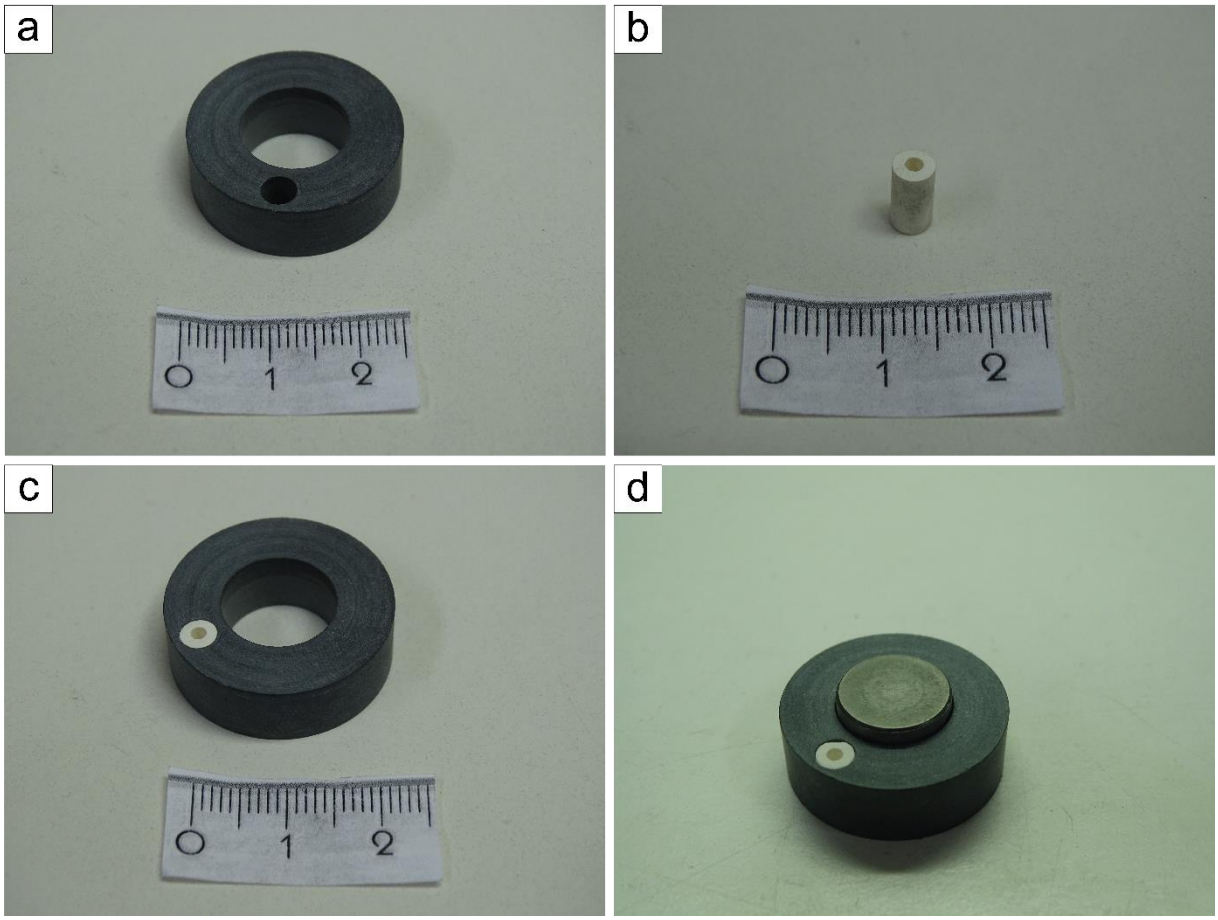

Figure VII.12. (a) Pyrophyllite bottom piece (drilled for one thermocouple configuration). (b) Crushable magnesia tube. (c) The crushable magnesia is inserted into the pyrophyllite piece in order to maintain the thermocouple (mullite tube). (d) The tungsten base plug should fit into the center hole of the pyrophyllite piece.

VII.1.9. Copper discs

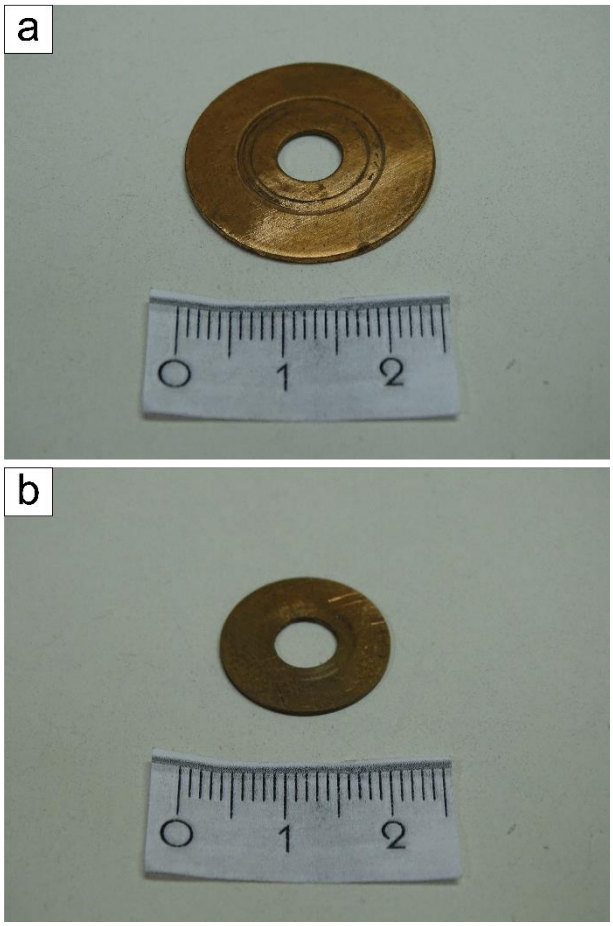

Figure VII.13. (a) Big Cu disc that will go at the top of the assembly (between the salt pieces and the lead piece). (b) Small Cu disc that will be inserted into the bottom outer salt piece. Both are in contact with the graphite furnace.

VII.1.10. Final steps

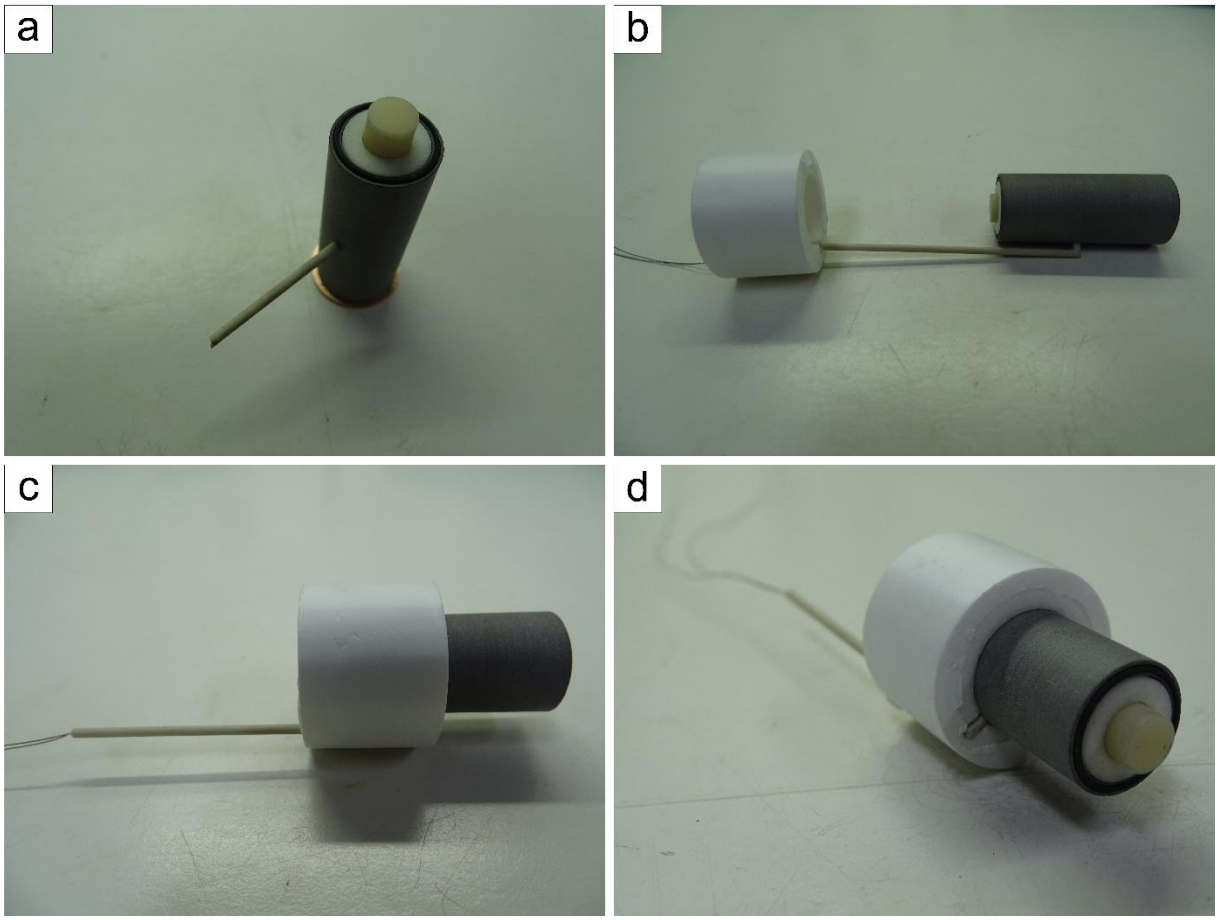

Figure VII.14. (a) The inner salt pieces around the jacketed sample and pistons are inserted into the graphite furnace. A stick allows the thermocouple holes to be maintained aligned. (b) The small thermocouple part is inserted into the graphite and inner middle salt piece. The long thermocouple part is inserted into the bottom outer salt piece. (c) & (d) The thermocouple in its final place.

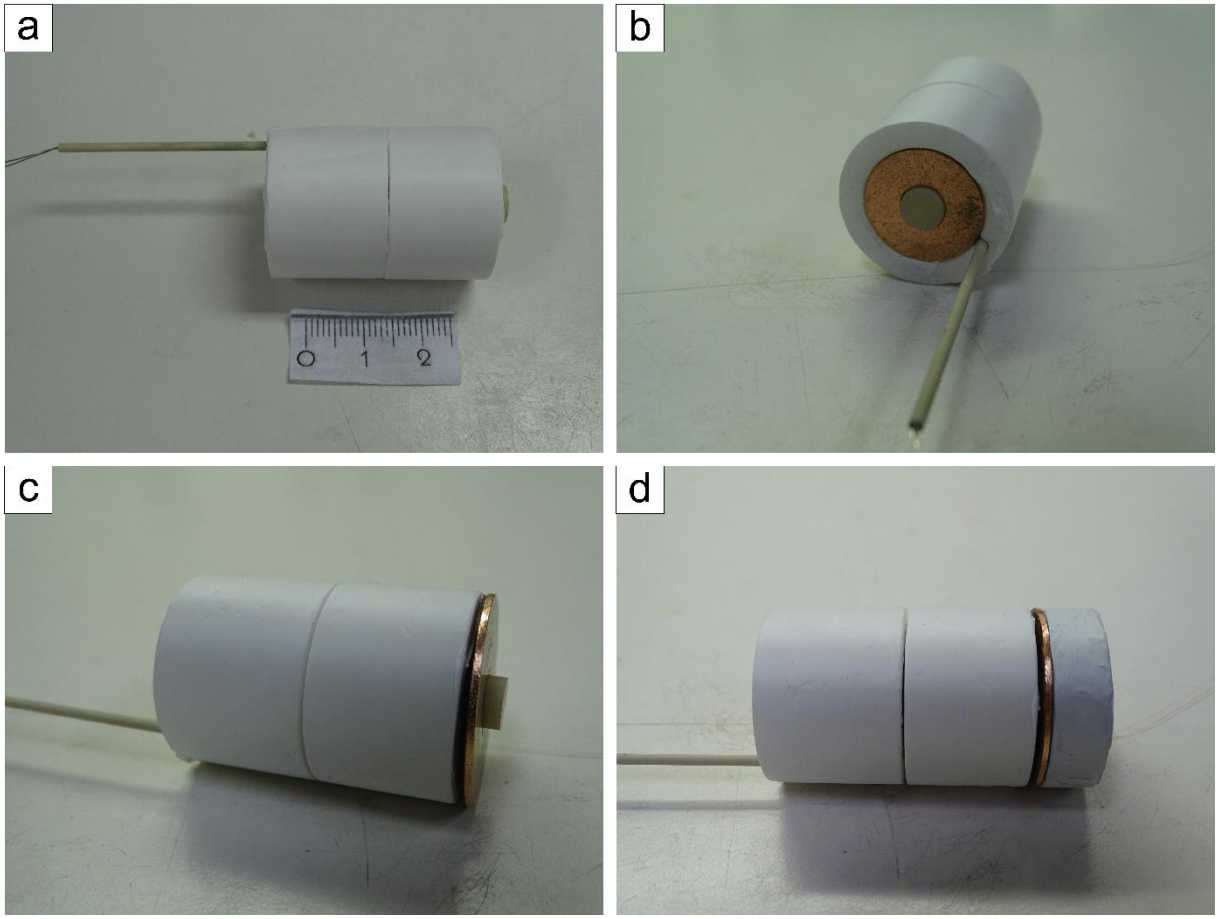

Figure VII.15. (a) The outer top salt piece is inserted around the furnace. (b) The small Cu ring is inserted at the bottom of the outer bottom salt piece. (c) The big Cu ring takes place at the top of the graphite furnace and top outer salt piece. (d) The lead piece (covered with Teflon tape) is put at the top of the assembly.

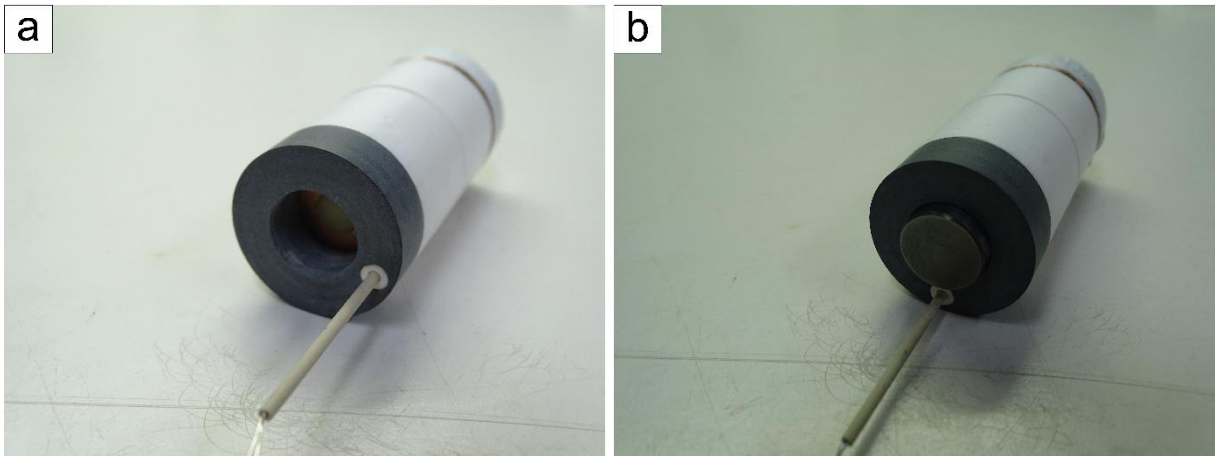

Figure VII.16. (a) The pyrophyllite bottom piece is put at the very bottom of the assembly. The thermocouple (mullite tube) being inserted into the crushable alumina. (b) The tungsten carbide plug is placed into the pyrophyllite piece.

VII.1.11. After the experiment

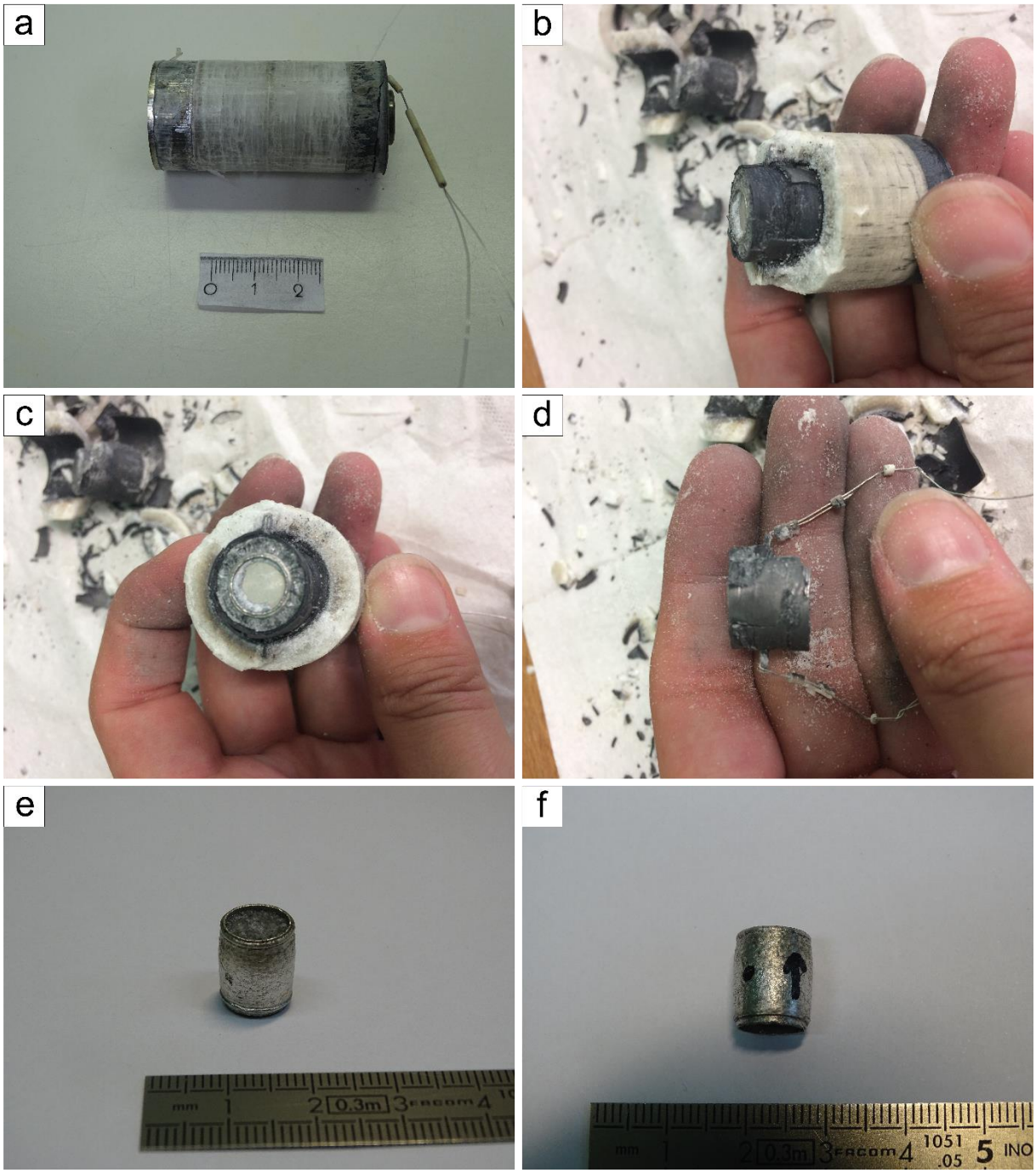

Figure VII.17. (a) The sample assembly after the experiment has been performed. (b) It is carefully destroyed in order to remove the sample. (c) & (d) During the destroying of the sample assembly it is important to keep the thermocouples as intact as possible to see their position relative to the sample at the end of the experiment. (e) & (f) The sample after the experiment. The emplacement of the thermocouples is marked, and the top indicated by an arrow. It will be cut to make the thin sections.

VII.2. Comparison between cathodoluminescence and EBSD

In this part, additional cathodoluminescence images are presented with the corresponding EBSD maps.

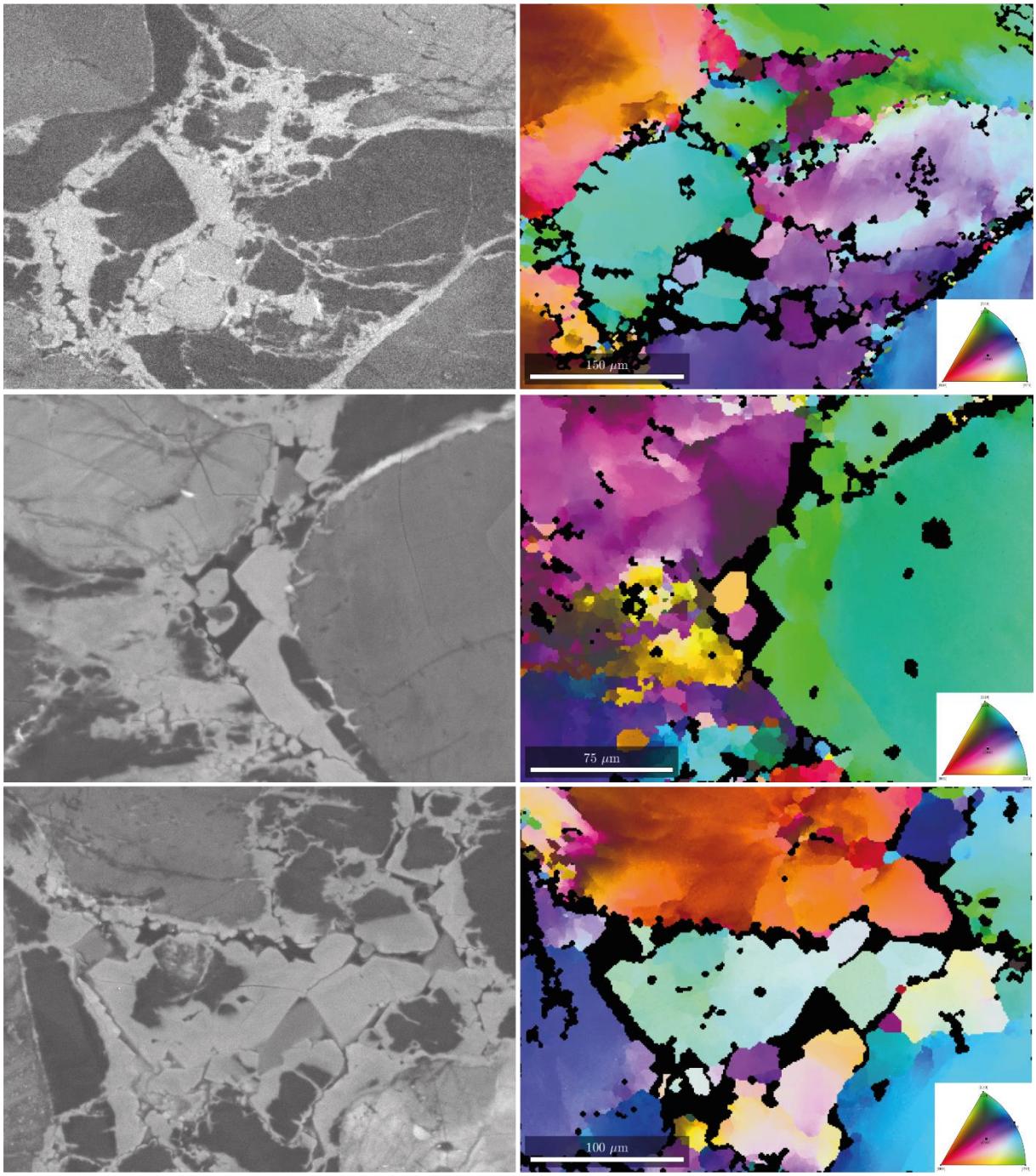

Figure VII.18. Cathodoluminescence (SEM-CL) images from 546LN sample deformed at 1000 MPa confining pressure and corresponding EBSD orientation maps. Crystal faces grow in continuity with the adjacent grain. Non-luminescent voids present at their edges are not indexed in EBSD maps, suggesting their amorphous nature.

VII.3. Image Analysis

This part of the appendix presents the results obtained from images analysis performed on both light and cathodoluminescence microscopy mosaic images. For each sample (starting material, deformed or hot-pressed) the left part of the figure corresponds to the segmented area. At the right side of the figure are displayed the grain parameter statistics (table) and histograms showing the repartition for grain sizes (equivalent diameter), aspect ratio and fit ellipse long axis orientation (with respect to the horizontal plane).

The results from the SURFOR analysis conducted on the same segmented images are also presented for some samples in order to compare the strain partition calculated from light and cathodoluminescence microscopy segmented images.

Light microscopy images

Image analysis have also been performed on segmented cross polarized light microscopy mosaic images of starting materials (TQ-1 and TQ-2) and deformed samples (OR52, OR33, OR42, 546LN, OR32, OR59, OR48 and 544LN). As explained before, the quartzite grains boundaries cannot be truly considered as passive markers as processes modify them (core and mantle structures, cracks, recrystallization …) contrary to the sand grains limits that are identifiable in cathodoluminescence images.

However, anisotropy analysis can nevertheless be performed on segmented light microscopy images, but will not completely reflect the real strain as processes occurring in the cement and at grain boundaries are undoubtedly taken into account.

Concerning the grain parameters, the equivalent diameter of grains is comparable in the starting material and in the deformed samples, with no variation due to experimental parameters (pressure or bulk strain). The aspect ratios of the two starting material thin sections studied (1.53 and 1.56) are equivalent to the hot-pressed sample OR59 one (1.58). The deformed samples aspect ratio are greater and vary from 1.92 for sample 546LN (1000 MPa) to 2.16 for sample OR32 (1000 MPa).

For all samples, the segmented images and corresponding statistics and histograms are presented in the following figures. On the whole, grain parameters data obtained from optical light microscopy are comparable to the ones obtained from light microscopy cathodoluminescence segmented images.

For the anisotropy characterization, the projection function curves obtained for all the samples segmented from light microscopy images are presented in the following SURFOR figures. The anisotropy of starting materials TQ-1 and TQ-2 as well as the hot-pressed sample OR59 are small (4.55, 3.40 and 5.33, respectively) and for OR59 not oriented in the shortening direction (min value at 150-155° instead of 90°). After deformation, the calculated strain is within the error percentage given by the starting material anisotropy compared to the measured bulk strain value except for the samples 546LN and OR32 (respectively underestimated and overestimated).

When comparing the values obtained from the light microscopy and from the light cathodoluminescence for the same samples (TQ-2, OR52, OR42, 546LN, OR32 and OR59), the

data obtained from light microscopy always slightly show more strain than cathodoluminescence images. But the difference is small and belongs to the uncertainty range.

VII.3.1. Starting material TQ-1

Light microscopy

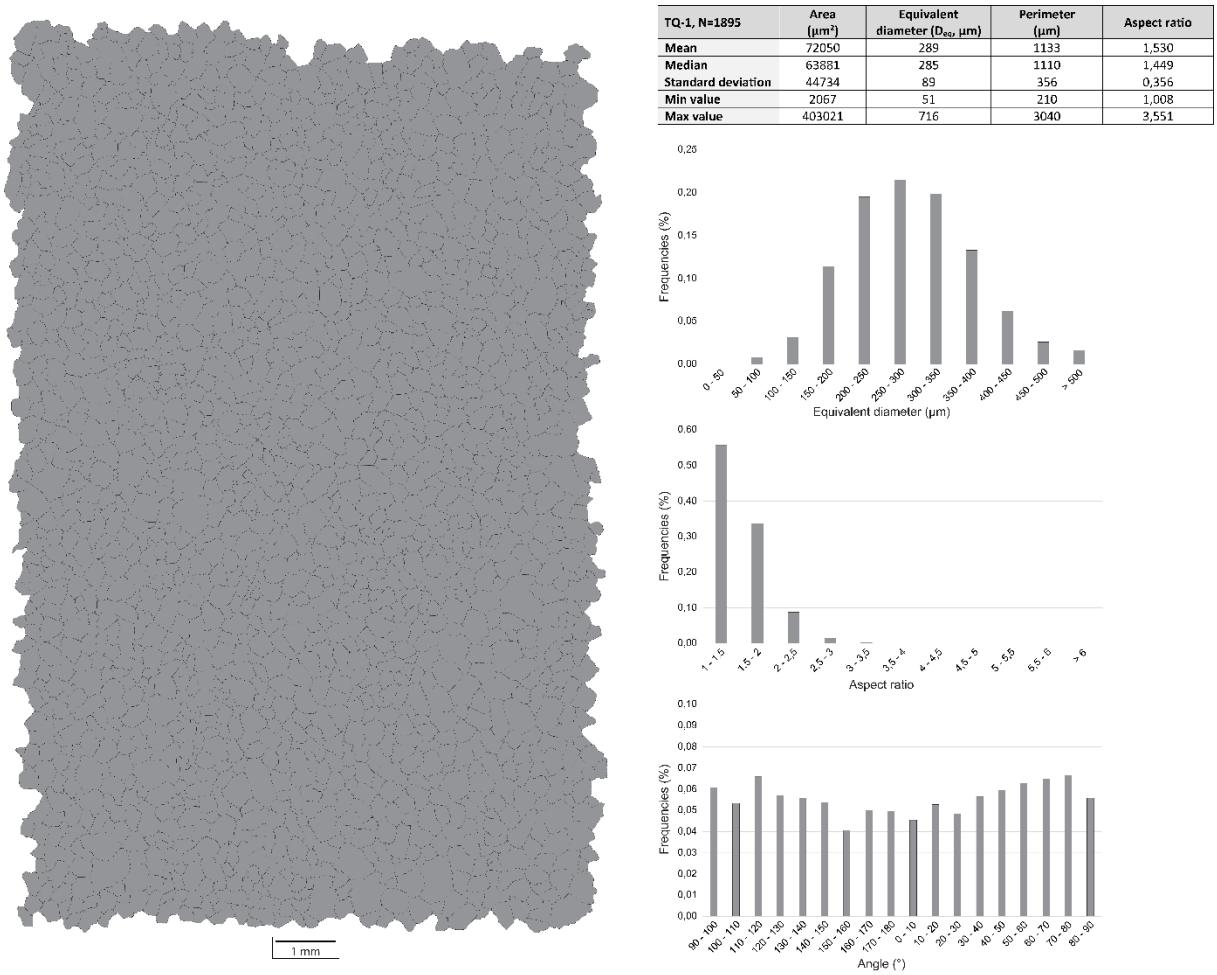

TQ-1, N=1895	Area (µm²)	Equivalent diameter (D_{eq}, µm)	Perimeter (µm)	Aspect ratio
Mean	72050	289	1133	1,530
Median	63881	285	1110	1,449
Standard deviation	44734	89	356	0,356
Min value	2057	51	210	1,008
Max value	403021	716	3040	3,551

Figure VII.19. Segmentation of optical light microscopy mosaic image of starting material TQ-1 and corresponding statistics for quartzite grain sizes, aspect ratio and major axis orientation.

VII.3.2. Starting material TQ-2

Light microscopy

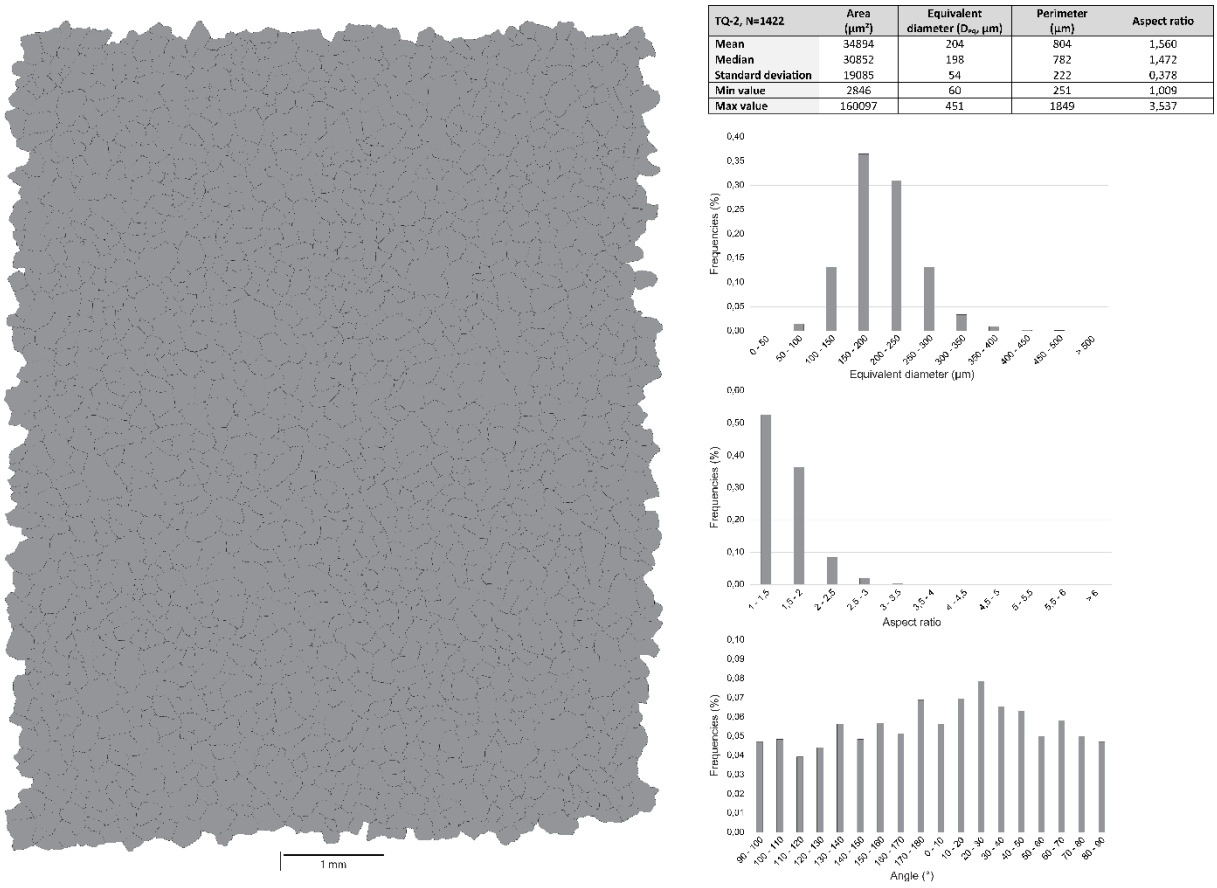

TQ-2, N=1422	Area (µm²)	Equivalent diameter (D_{eq}, µm)	Perimeter (µm)	Aspect ratio
Mean	34894	204	804	1,560
Median	30852	198	782	1,472
Standard deviation	19085	54	222	0,378
Min value	2846	60	251	1,009
Max value	160097	451	1849	3,537

Figure VII.20. Segmentation of optical light microscopy mosaic image of starting material TQ-2 and corresponding statistics for quartzite grain sizes, aspect ratio and major axis orientation.

Optical cathodoluminescence

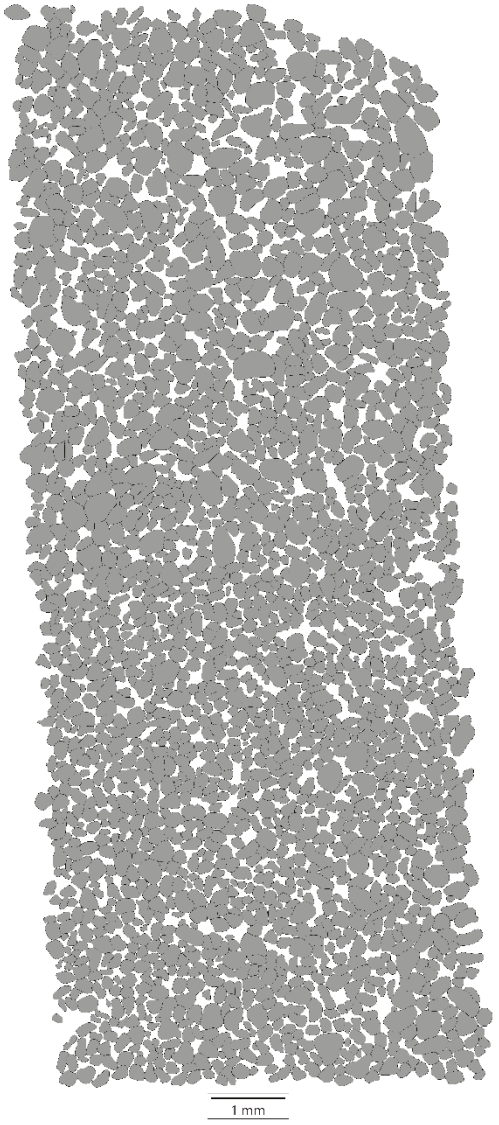

TQ-2, N=2103	Area (µm²)	Equivalent diameter (D_{eq}, µm)	Perimeter (µm)	Aspect ratio
Mean	30214	186	685	1,549
Median	25051	179	661	1,457
Standard deviation	21235	62	228	0,384
Min value	178173	476	1673	4,684
Max value	2594	57	200	1,014

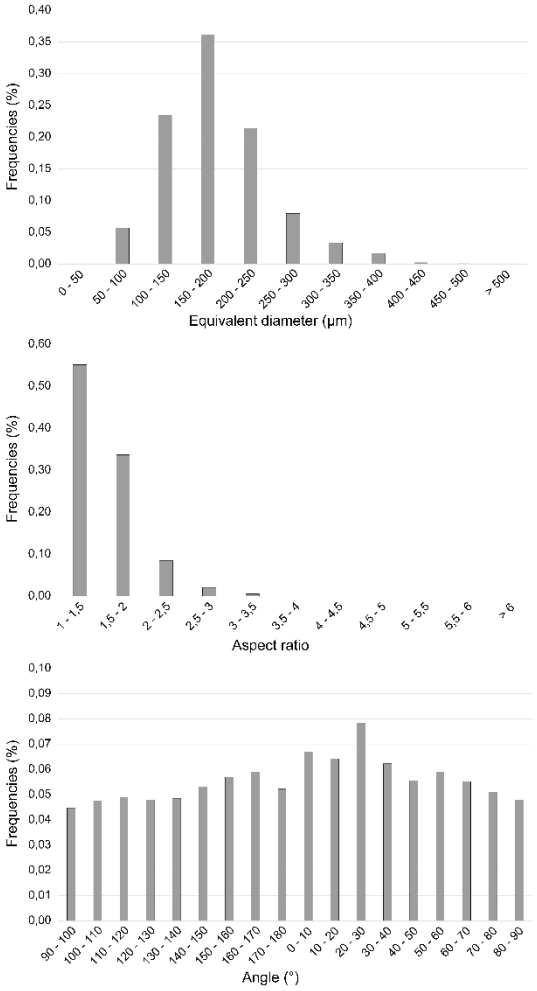

Figure VII.21. Segmentation of optical cathodoluminescence mosaic image of starting material TQ-2 and corresponding statistics for sand grain sizes, aspect ratio and major axis orientation.

SURFOR analysis

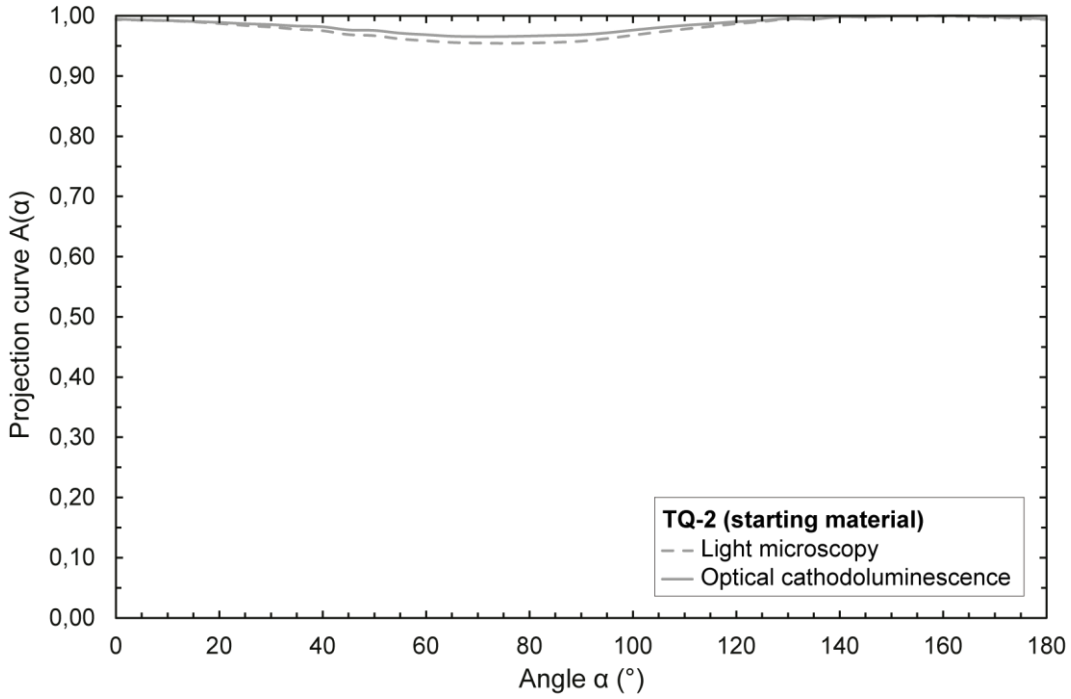

Figure VII.22. SURFOR projection curves for sample of starting material TQ-2. The sample presents a slight fabric anisotropy of 3.5% at 70° for sand grains (LM-CL) and 4.6% at 75° for quartzite grains (LM-LP).

VII.3.3. OR52 (700 MPa)

Light microscopy

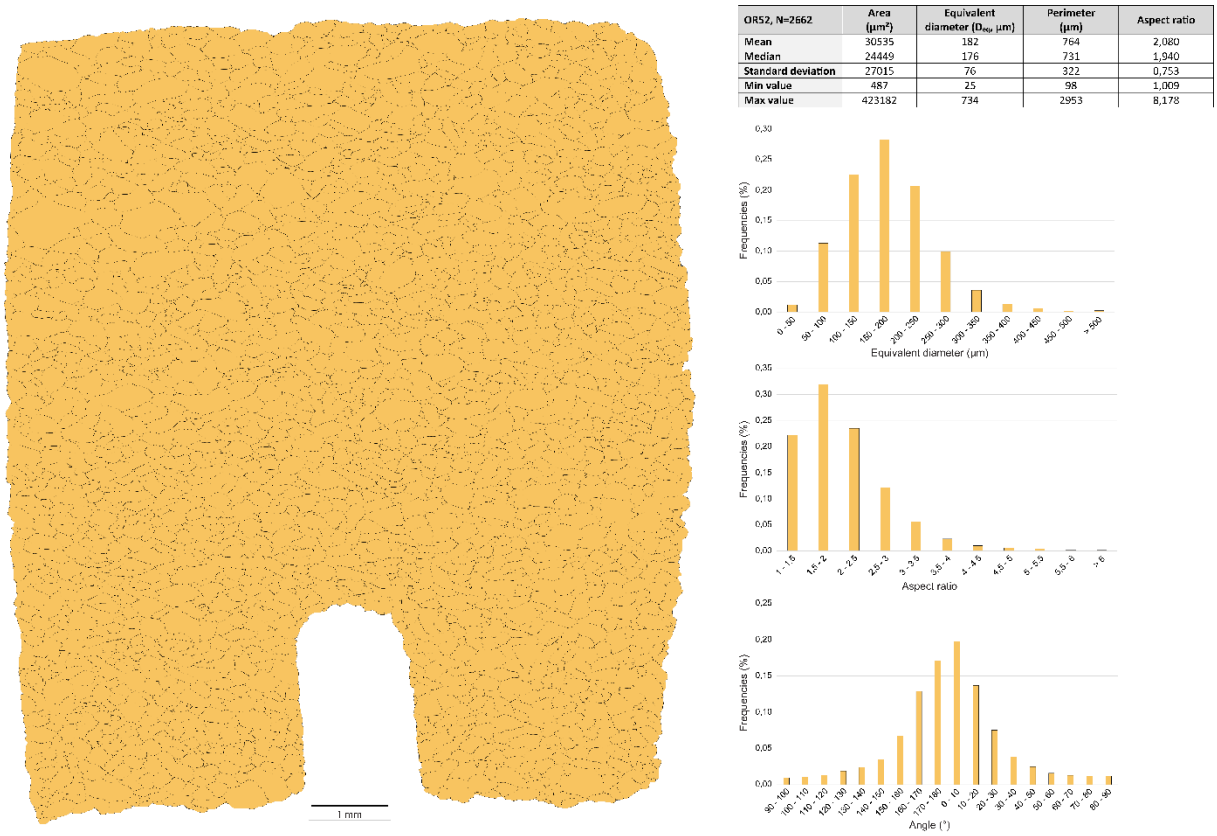

OR52, N=2662	Area (µm²)	Equivalent diameter (D_{eq}, µm)	Perimeter (µm)	Aspect ratio
Mean	30535	182	764	2,080
Median	24449	176	731	1,940
Standard deviation	27015	76	322	0,753
Min value	487	25	98	1,009
Max value	423182	734	2953	8,178

Figure VII.23. Segmentation of optical light microscopy mosaic image of deformed sample OR52 (700 MPa) and corresponding statistics for quartzite grain sizes, aspect ratio and major axis orientation.

Optical cathodoluminescence

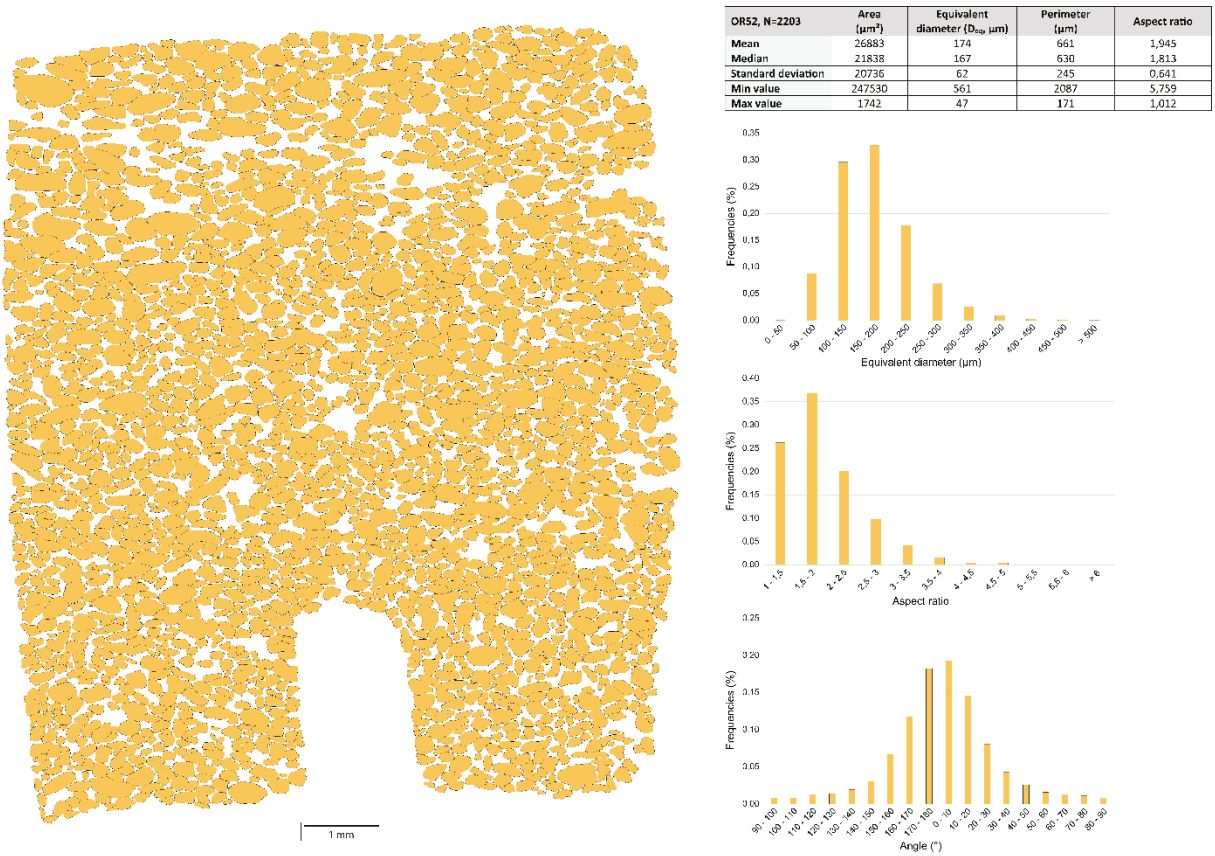

OR52, N=2203	Area (µm²)	Equivalent diameter (D_{eq}, µm)	Perimeter (µm)	Aspect ratio
Mean	26883	174	661	1,945
Median	21838	167	630	1,813
Standard deviation	20736	62	245	0,641
Min value	247530	561	2087	5,759
Max value	1742	47	171	1,012

Figure VII.24. Segmentation of optical cathodoluminescence mosaic image of deformed sample OR52 (700 MPa) and corresponding statistics for sand grain sizes, aspect ratio and major axis orientation.

SURFOR analysis

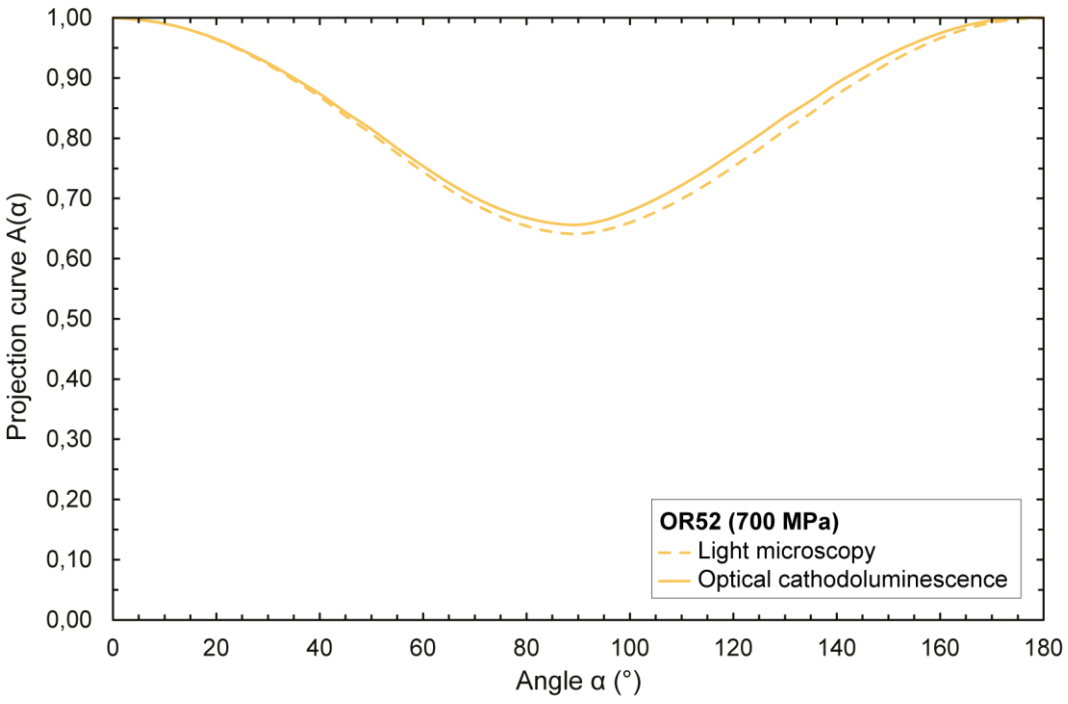

Figure VII.25. SURFOR projection curves for deformed sample OR52 (700 MPa). The sample presents a strain of 34.4% at 90° for sand grains (LM-CL) and 35.9% at 90° for quartzite grains (LM-LP).

VII.3.4. OR33 (800 MPa)

Light microscopy

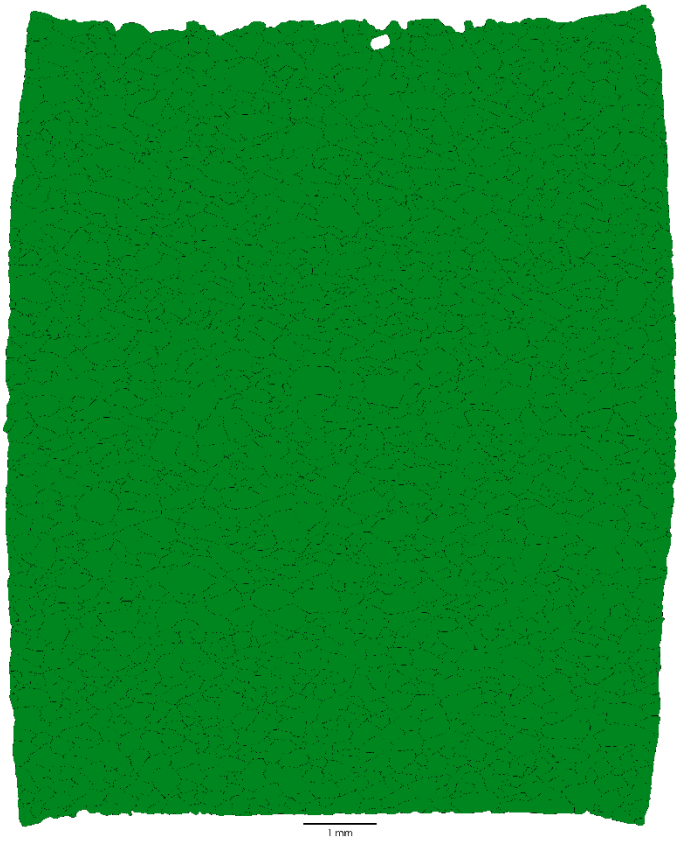

OR33, N=2485	Area (µm²)	Equivalent diameter (D_{eq}, µm)	Perimeter (µm)	Aspect ratio
Mean	37810	201	823	1,925
Median	29560	194	796	1,779
Standard deviation	32648	88	362	0,647
Min value	878	33	135	1,007
Max value	252600	567	2412	6,391

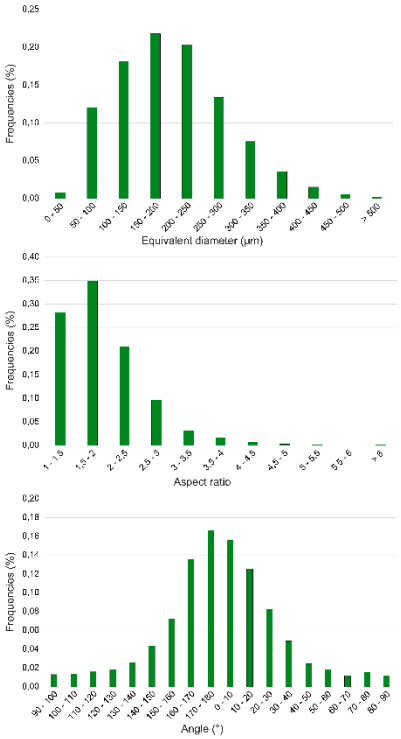

Figure VII.26. Segmentation of optical light microscopy mosaic image of deformed sample OR33 (800 MPa) and corresponding statistics for quartzite grain sizes, aspect ratio and major axis orientation.

VII.3.5. OR42 (800 MPa)

Light microscopy

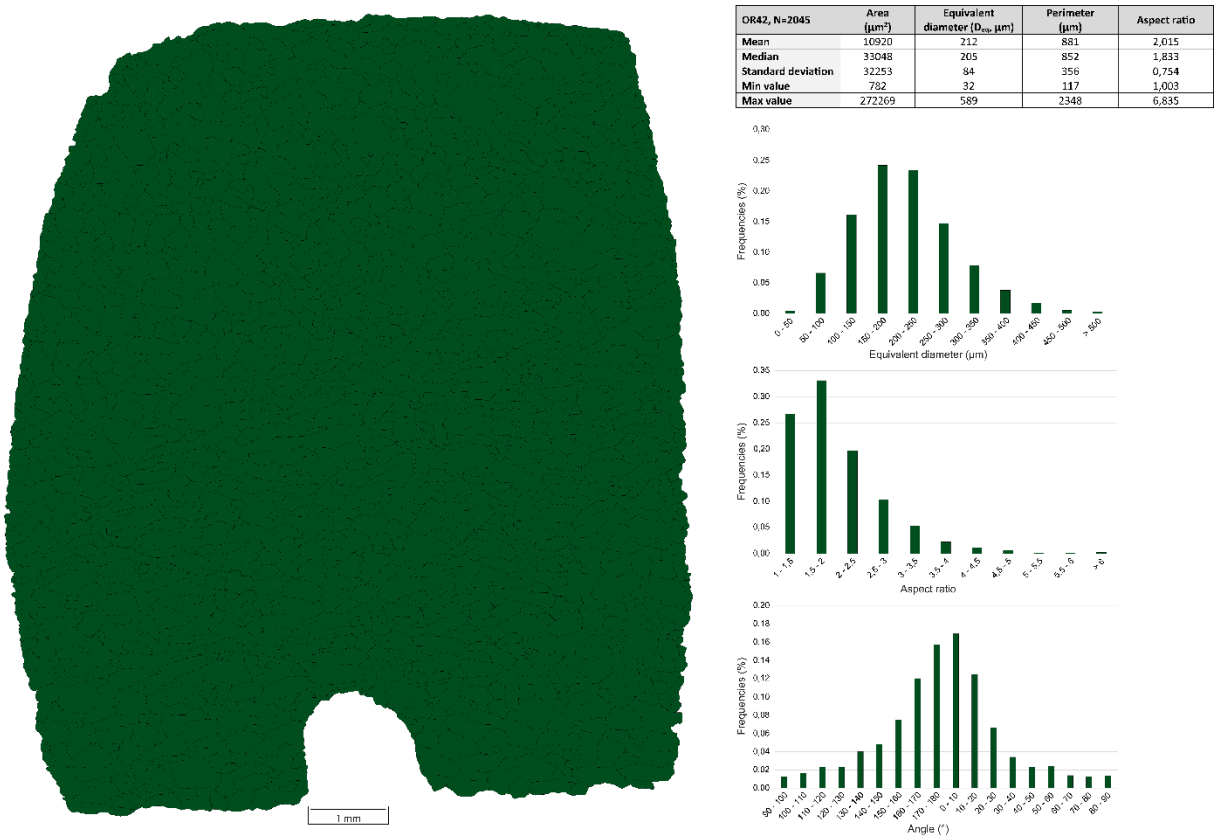

OR42, N=2045	Area (µm²)	Equivalent diameter (D_{eq}, µm)	Perimeter (µm)	Aspect ratio
Mean	10920	212	881	2,015
Median	33048	205	852	1,833
Standard deviation	32253	84	356	0,754
Min value	782	32	117	1,003
Max value	272269	589	2348	6,835

Figure VII.27. Segmentation of optical light microscopy mosaic image of deformed sample OR42 (800 MPa) and corresponding statistics for quartzite grain sizes, aspect ratio and major axis orientation.

Optical cathodoluminescence

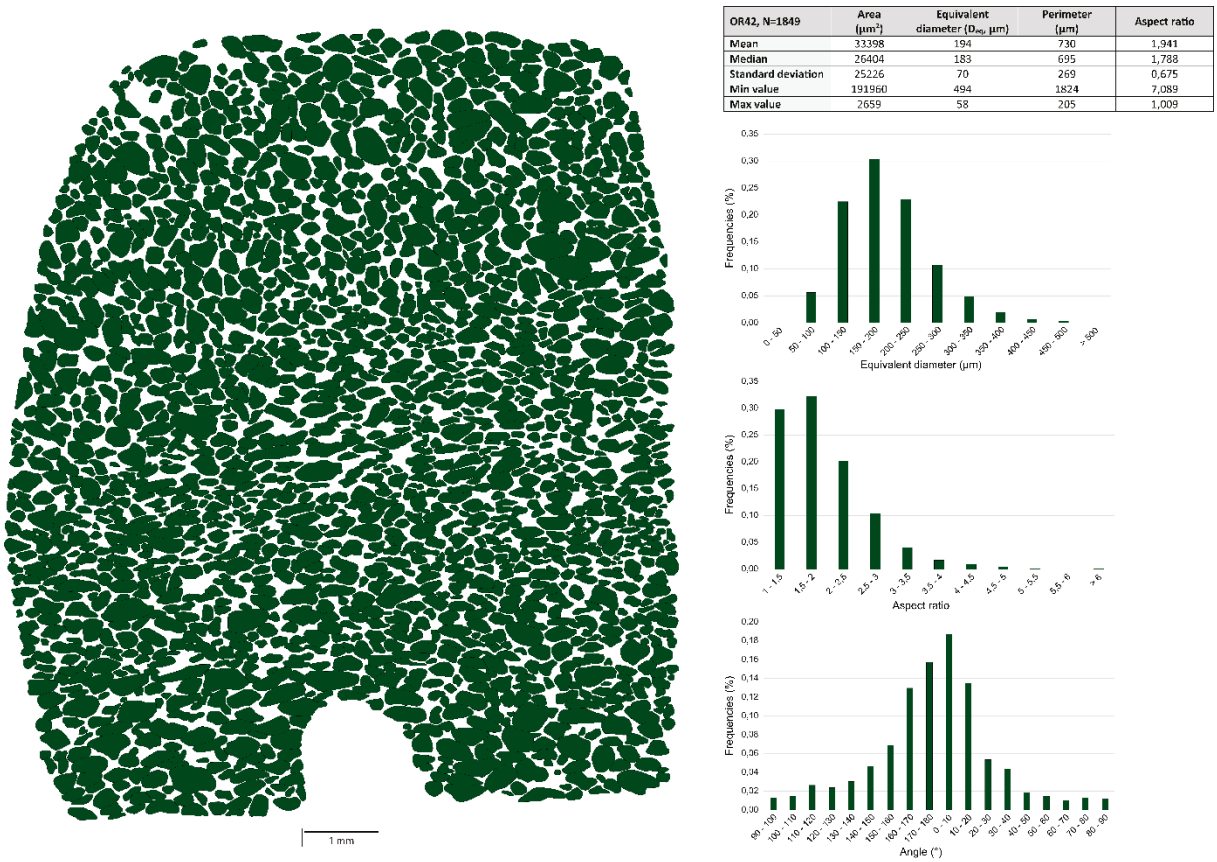

OR42, N=1849	Area (µm²)	Equivalent diameter (D_{eq}, µm)	Perimeter (µm)	Aspect ratio
Mean	33398	194	730	1,941
Median	26404	183	695	1,788
Standard deviation	25226	70	269	0,675
Min value	191960	494	1824	7,089
Max value	2659	58	205	1,009

Figure VII.28. Segmentation of optical cathodoluminescence mosaic image of deformed sample OR42 (800 MPa) and corresponding statistics for sand grain sizes, aspect ratio and major axis orientation.

SURFOR analysis

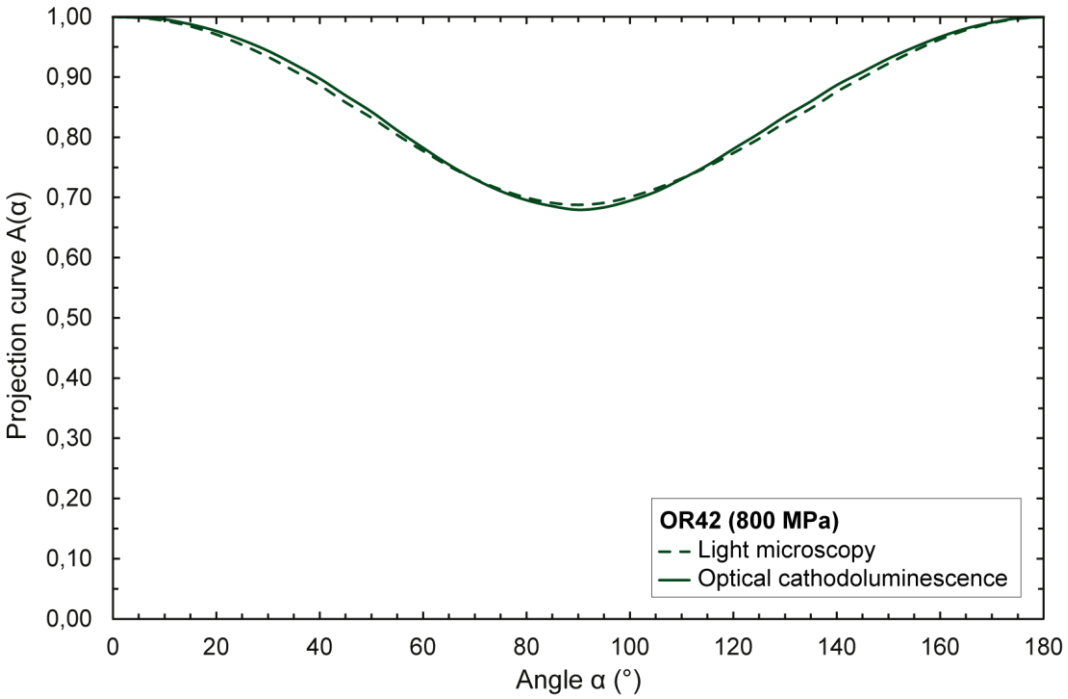

Figure VII.29. SURFOR projection curves for deformed sample OR42 (800 MPa). The sample presents a strain of 32.0% at 90° for sand grains (LM-CL) and 31.2% at 90° for quartzite grains (LM-LP).

VII.3.6. 546LN (1000 MPa)

Light microscopy

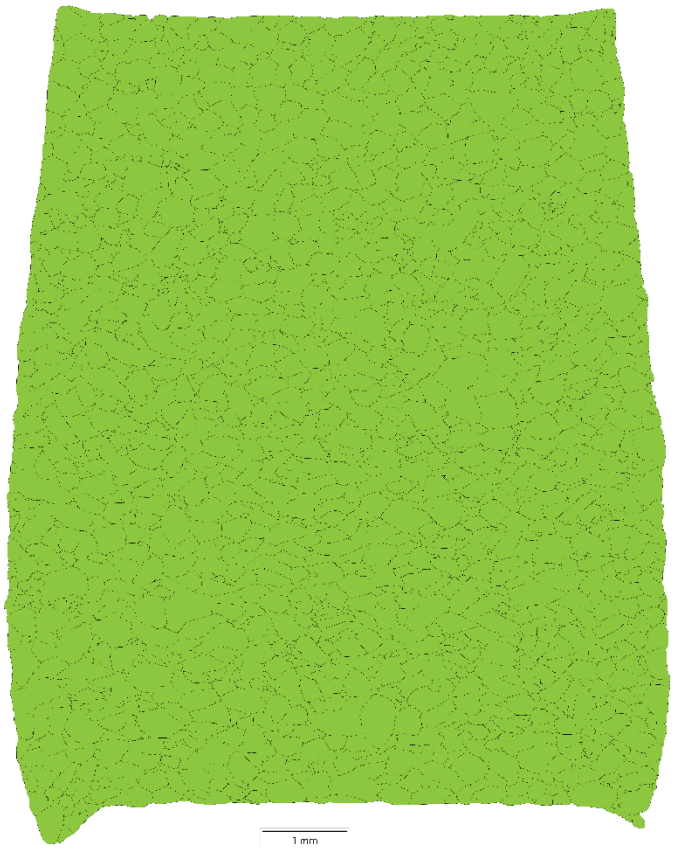

546LN, N=1970	Area (µm²)	Equivalent diameter (D_{eq} µm)	Perimeter (µm)	Aspect ratio
Mean	34745	186	769	1,917
Median	24605	177	741	1,739
Standard deviation	33120	98	401	0,725
Min value	503	25	109	1,017
Max value	207343	514	2473	7,957

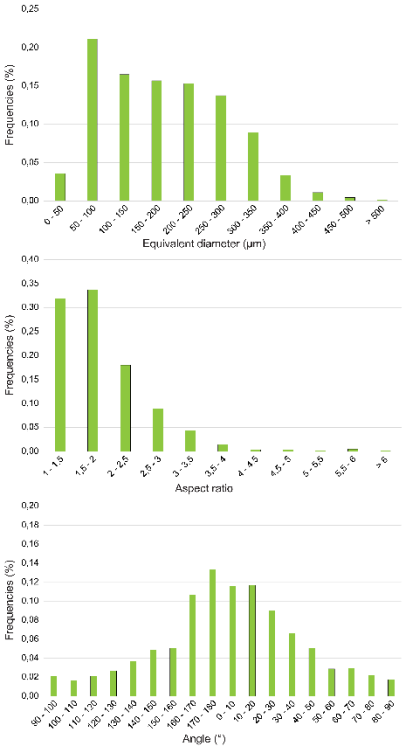

Figure VII.30. Segmentation of optical light microscopy mosaic image of deformed sample 546LN (1000 MPa) and corresponding statistics for quartzite grain sizes, aspect ratio and major axis orientation.

Optical cathodoluminescence

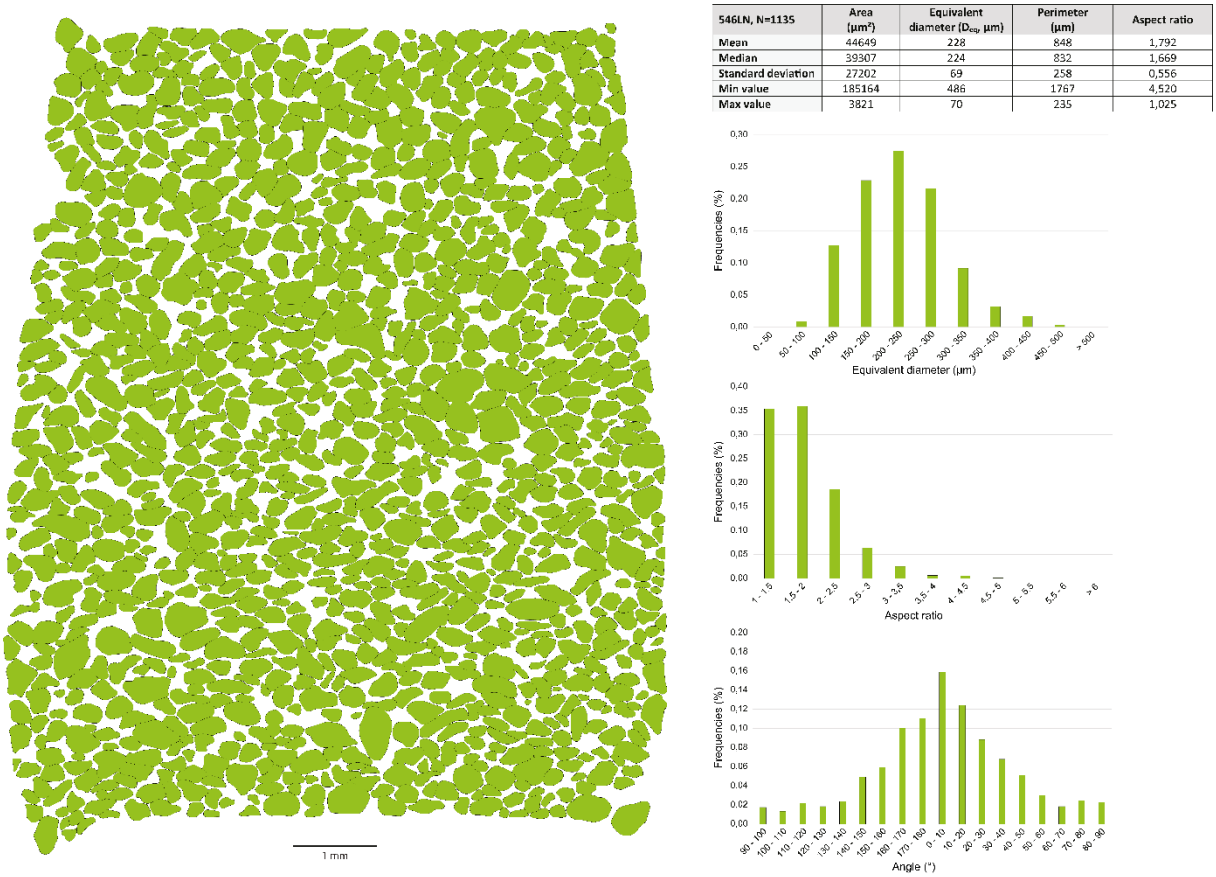

546LN, N=1135	Area (µm²)	Equivalent diameter (D_{eq}, µm)	Perimeter (µm)	Aspect ratio
Mean	44649	228	848	1,792
Median	39307	224	832	1,669
Standard deviation	27202	69	258	0,556
Min value	185164	486	1767	4,520
Max value	3821	70	235	1,025

Figure VII.31. Segmentation of optical cathodoluminescence mosaic image of deformed sample 546LN (1000 MPa) and corresponding statistics for sand grain sizes, aspect ratio and major axis orientation.

SURFOR analysis

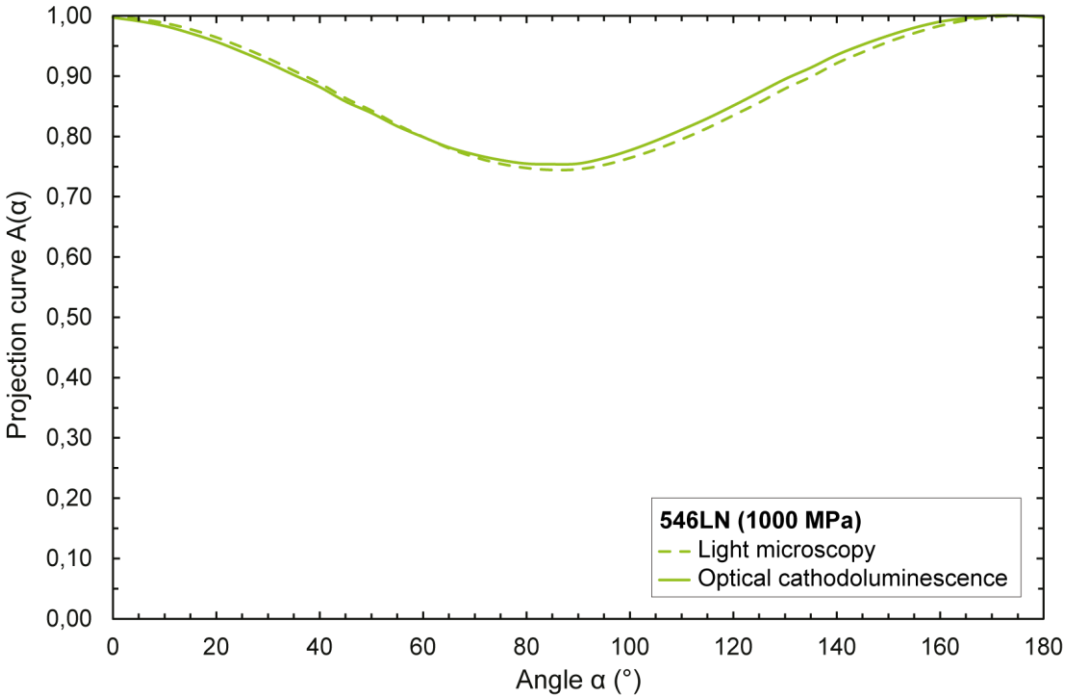

Figure VII.32. SURFOR projection curves for deformed sample 546LN (1000 MPa). The sample presents a strain of 24.6% at 85° for sand grains (LM-CL) and 25.5% at 85° for quartzite grains (LM-LP).

VII.3.7. OR32 (1000 MPa)

Light microscopy

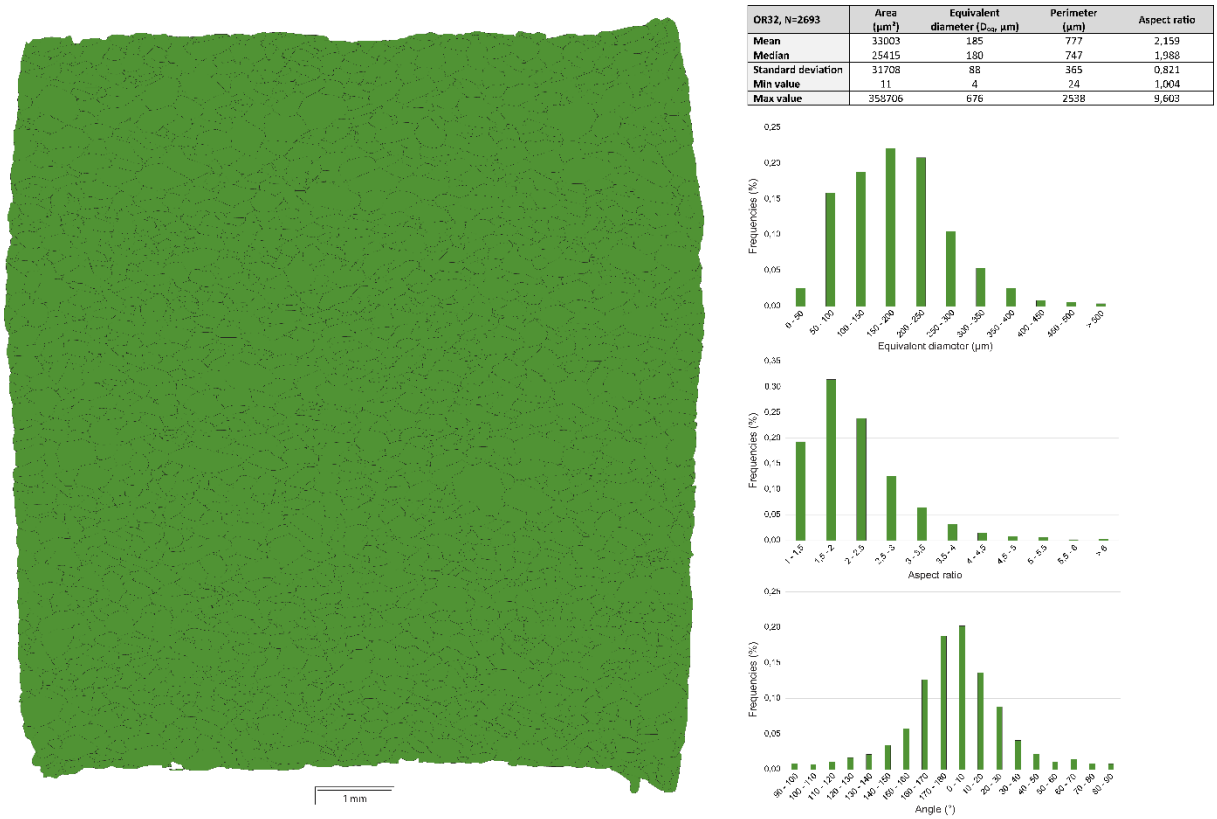

OR32, N=2693	Area (µm²)	Equivalent diameter (D_{eq}, µm)	Perimeter (µm)	Aspect ratio
Mean	33003	185	777	2,159
Median	25415	180	747	1,988
Standard deviation	31708	88	365	0,821
Min value	11	4	24	1,004
Max value	358706	676	2538	9,603

Figure VII.33. Segmentation of optical light microscopy mosaic image of deformed sample OR32 (1000 MPa) and corresponding statistics for quartzite grain sizes, aspect ratio and major axis orientation.

Optical cathodoluminescence

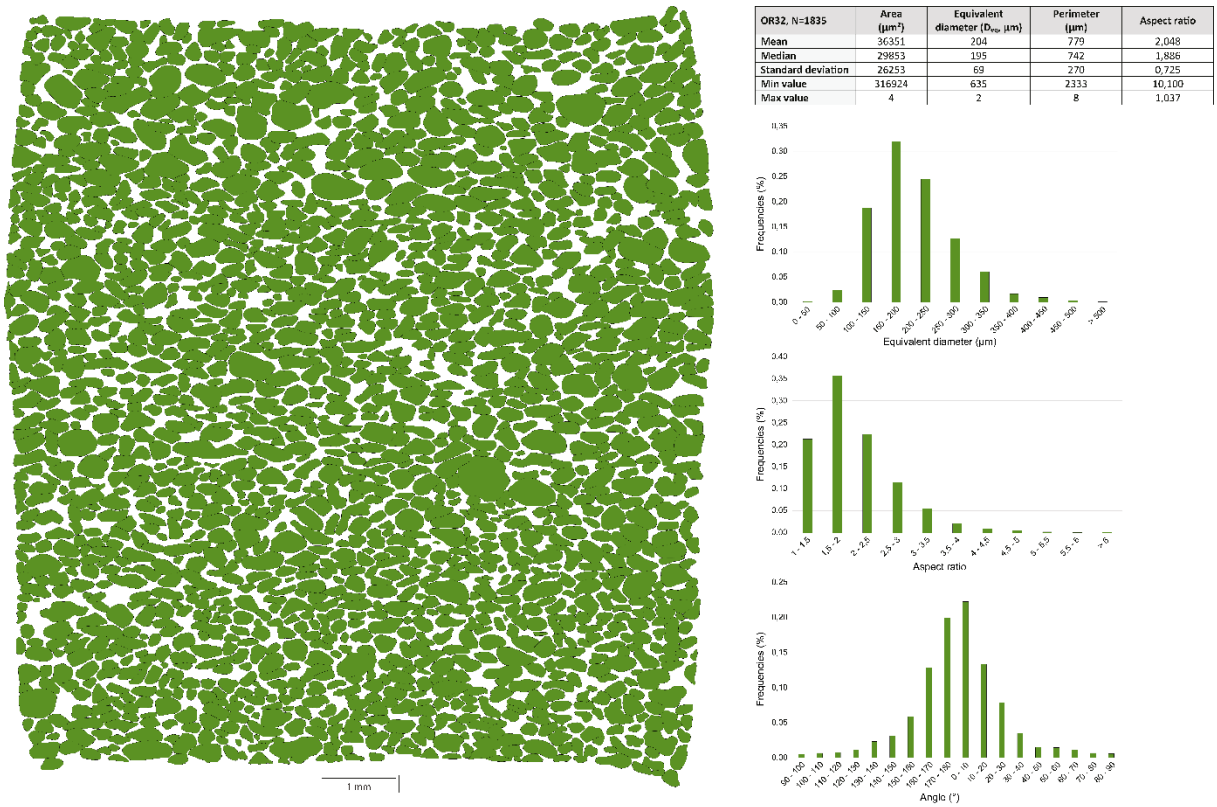

OR32, N=1835	Area (µm²)	Equivalent diameter (D_{eq}, µm)	Perimeter (µm)	Aspect ratio
Mean	36351	204	779	2,048
Median	29853	195	742	1,886
Standard deviation	26253	69	270	0,725
Min value	316924	635	2333	10,100
Max value	4	2	8	1,037

Figure VII.34. Segmentation of optical cathodoluminescence mosaic image of deformed sample OR32 (1000 MPa) and corresponding statistics for sand grain sizes, aspect ratio and major axis orientation.

SURFOR analysis

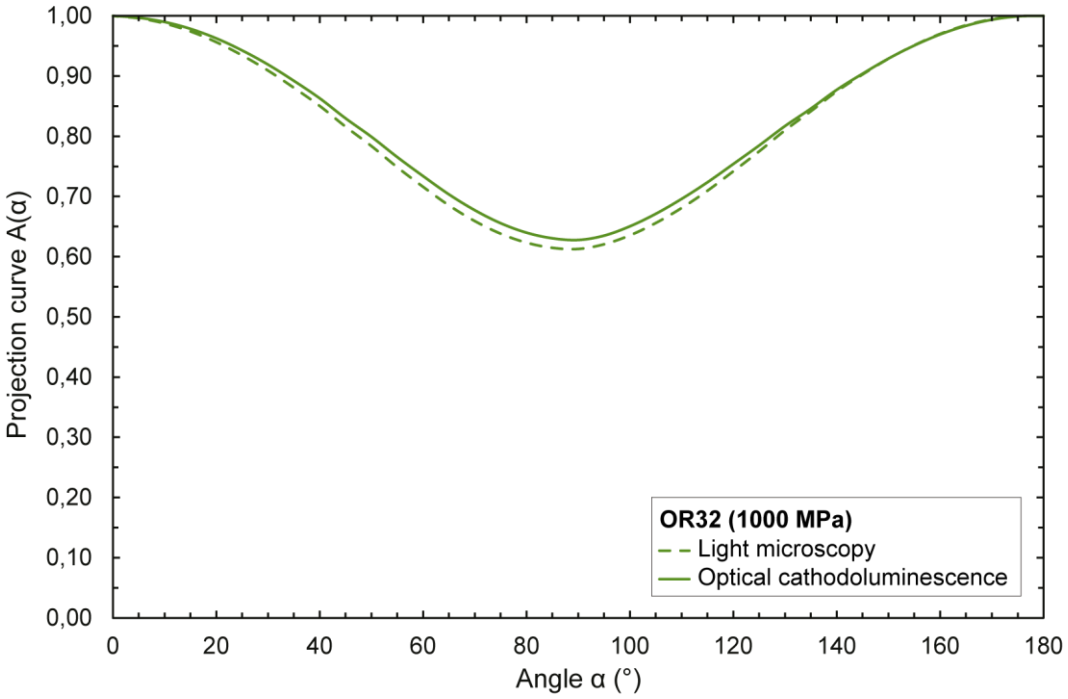

Figure VII.35. SURFOR projection curves for deformed sample OR32 (1000 MPa). The sample presents a strain of 37.2% at 90° for sand grains (LM-CL) and 38.7% at 90° for quartzite grains (LM-LP).

VII.3.8. OR59 (1000 MPa – hot-pressing)

Light microscopy

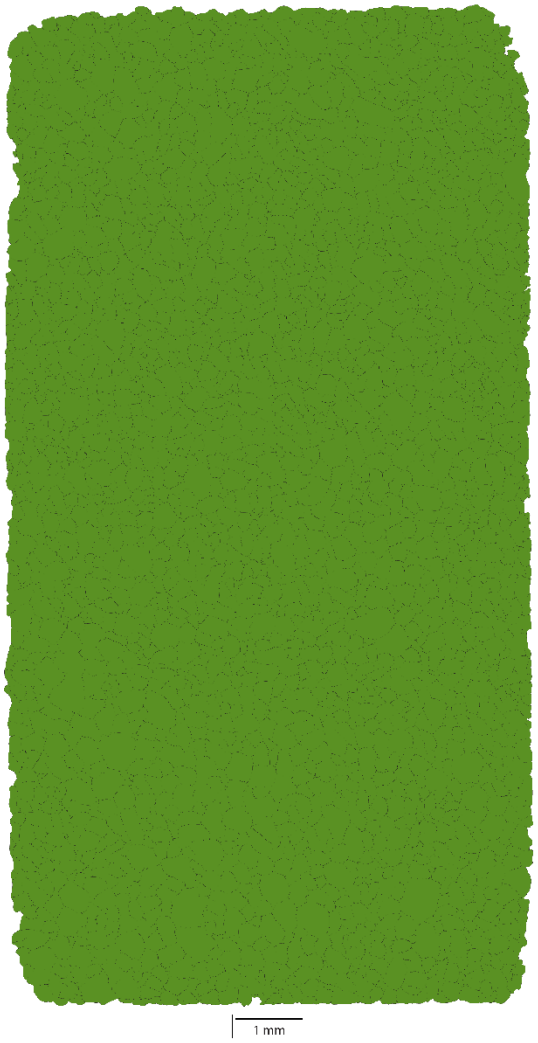

OR59, N=2820	Area (µm²)	Equivalent diameter (D_{eq}, µm)	Perimeter (µm)	Aspect ratio
Mean	40094	211	829	1,581
Median	33188	206	804	1,490
Standard deviation	31043	81	315	0,405
Min value	775	31	115	1,010
Max value	308852	627	2430	4,456

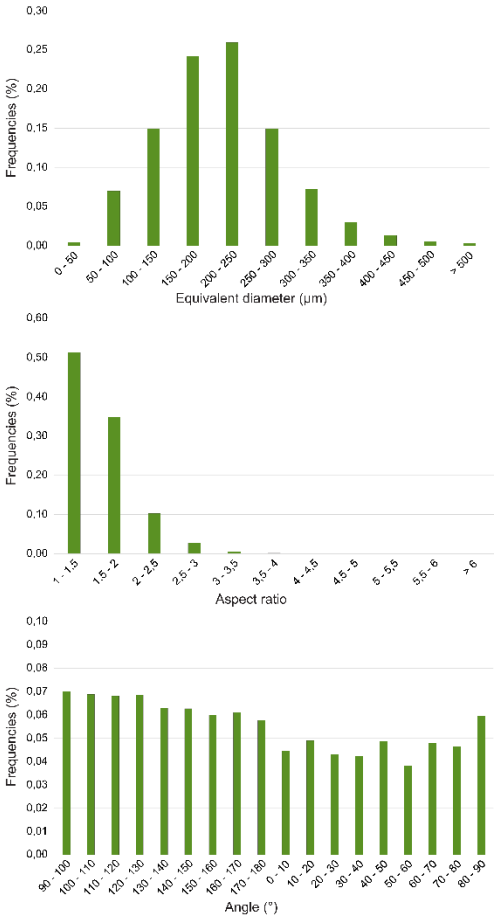

Figure VII.36. Segmentation of optical light microscopy mosaic image of hot-pressed sample OR59 (1000 MPa) and corresponding statistics for quartzite grain sizes, aspect ratio and major axis orientation.

Optical cathodoluminescence

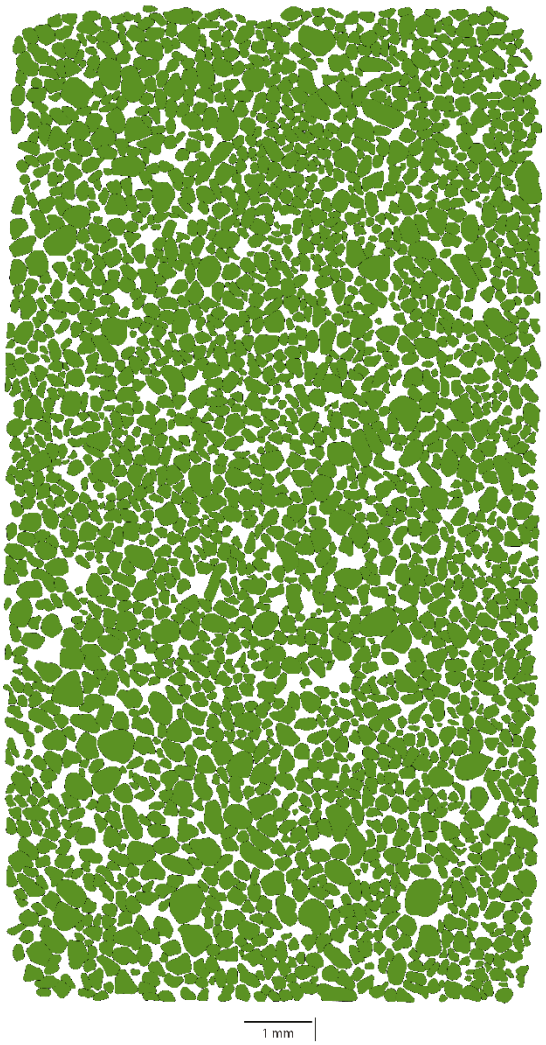

OR59, N=2343	Area (μm^2)	Equivalent diameter (D_{eq}, µm)	Perimeter (µm)	Aspect ratio
Mean	35754	202	732	1,560
Median	29054	192	699	1,483
Standard deviation	26115	68	247	0,383
Min value	249001	563	1915	3,912
Max value	3478	67	237	1,016

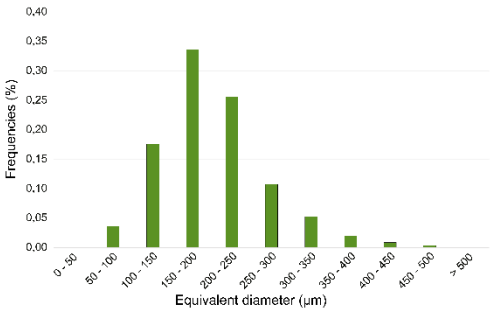

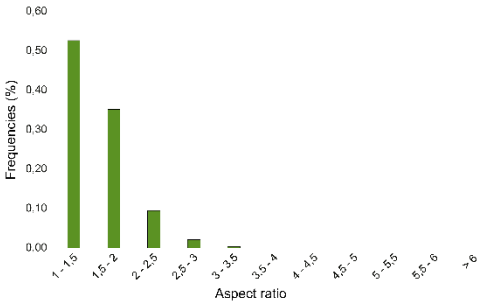

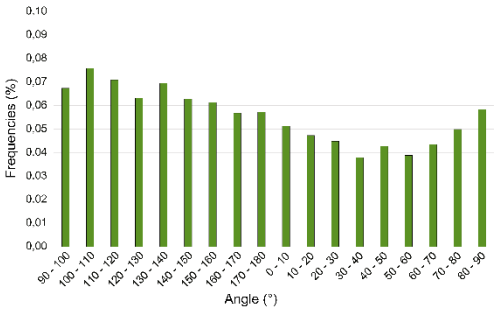

Figure VII.37. Segmentation of optical cathodoluminescence mosaic image of hot-pressed sample OR59 (1000 MPa) and corresponding statistics for sand grain sizes, aspect ratio and major axis orientation.

SURFOR analysis

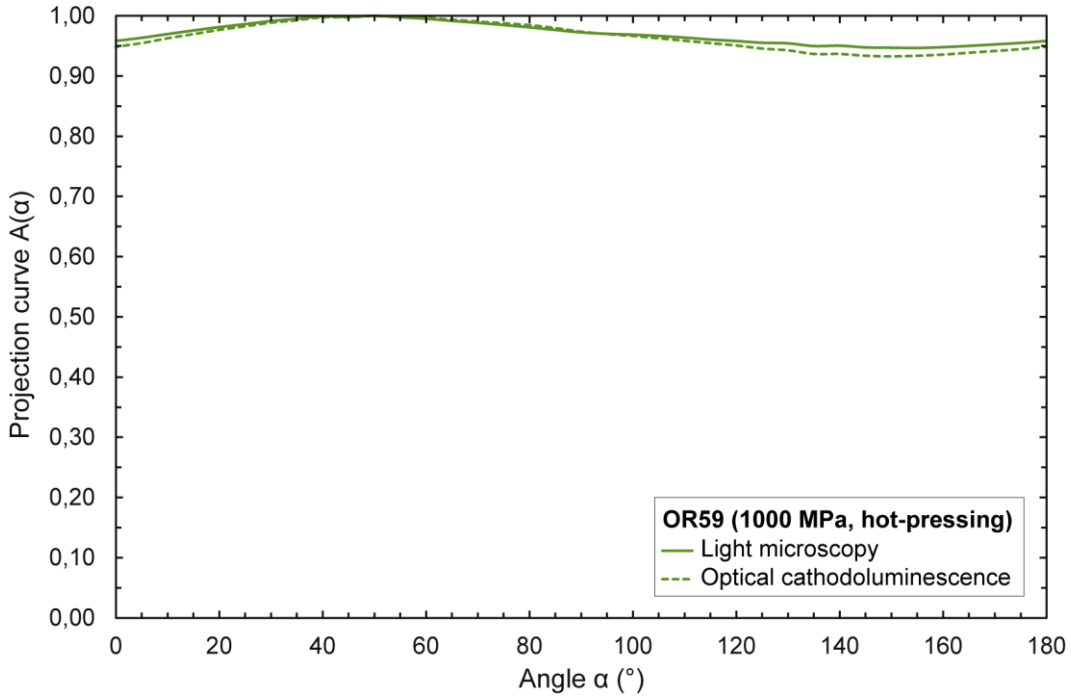

Figure VII.38. SURFOR projection curves for hot-pressed sample OR59 (1000 MPa). The sample presents a strain of 6.7% at 150° for sand grains (LM-CL) and 5.3% at 150-155° for quartzite grains (LM-LP).

VII.3.9. OR48 (1250 MPa)

Light microscopy

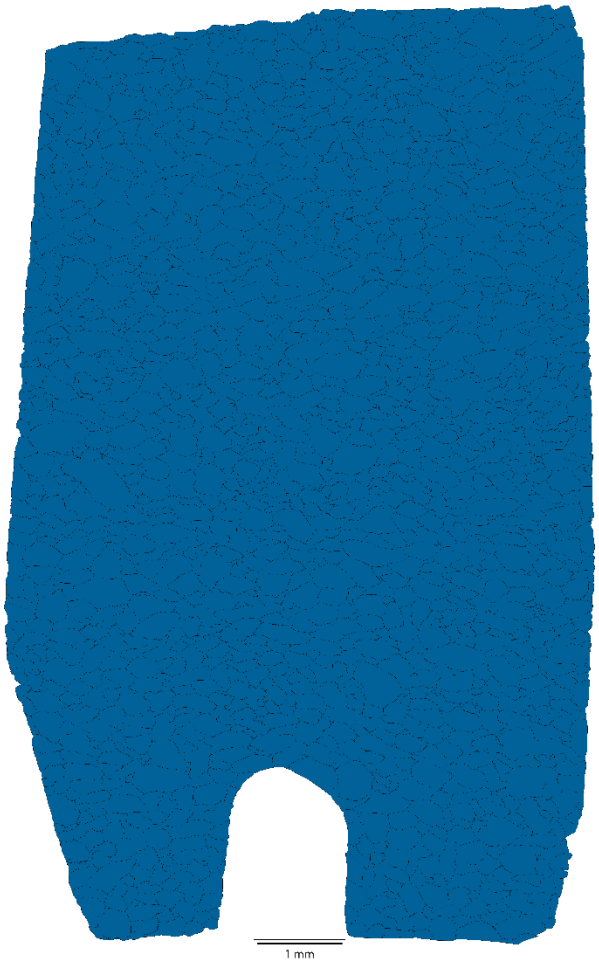

OR48, N=1903	Area (µm²)	Equivalent diameter (D_{eq}, µm)	Perimeter (µm)	Aspect ratio
Mean	34565	192	801	1,987
Median	27246	186	770	1,850
Standard deviation	29922	85	359	0,682
Min value	734	31	156	1,030
Max value	287900	605	2567	8,500

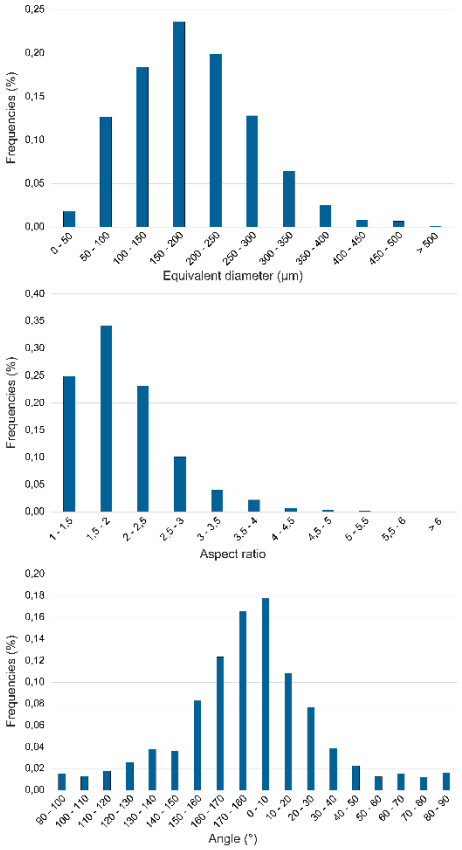

Figure VII.39. Segmentation of optical light microscopy mosaic image of deformed sample OR48 (1250 MPa) and corresponding statistics for quartzite grain sizes, aspect ratio and major axis orientation.

VII.3.10. 544LN (1500 MPa)

Light microscopy

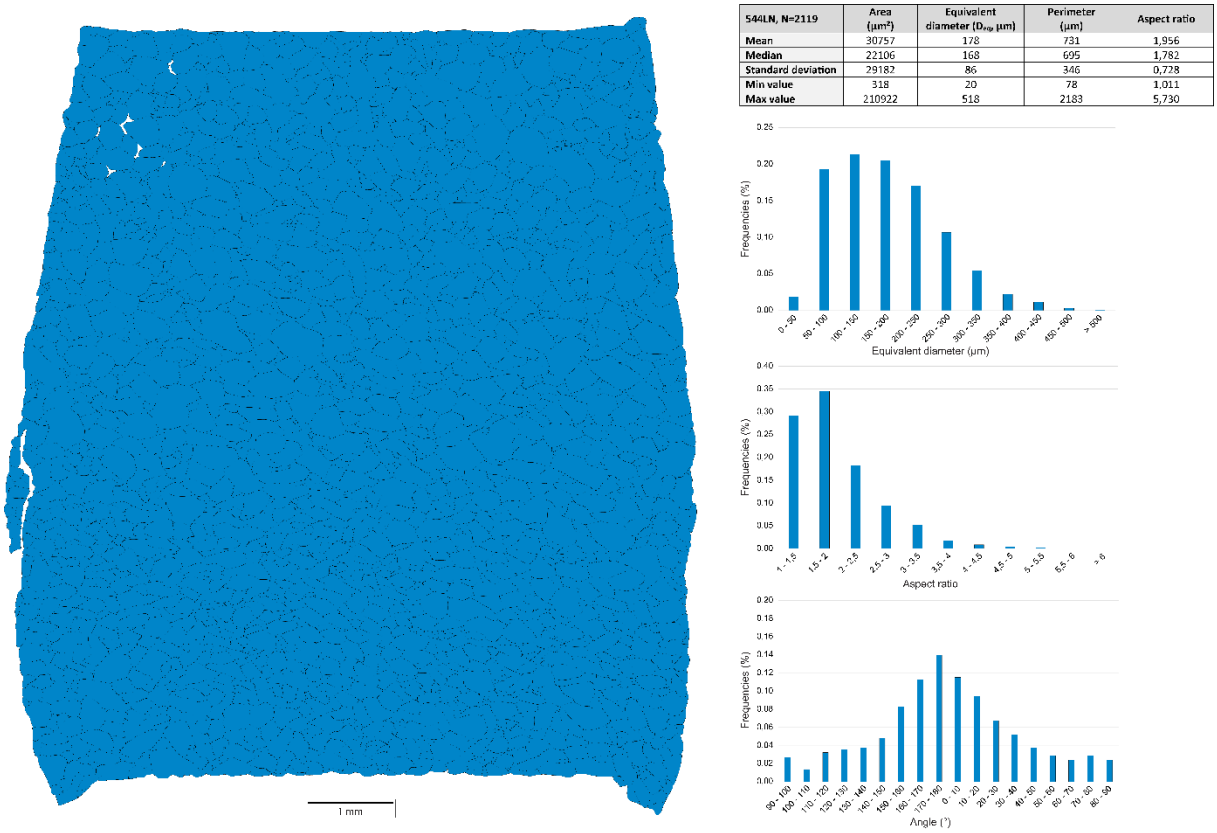

544LN, N=2119	Area (µm²)	Equivalent diameter (D_{eq}, µm)	Perimeter (µm)	Aspect ratio
Mean	30757	178	731	1,956
Median	22106	168	695	1,782
Standard deviation	29182	86	346	0,728
Min value	318	20	78	1,011
Max value	210922	518	2183	5,730

Figure VII.40. Segmentation of optical light microscopy mosaic image of deformed sample 544LN (1500 MPa) and corresponding statistics for quartzite grain sizes, aspect ratio and major axis orientation.

VII.3.11. OR64 (1500 MPa)

Optical cathodoluminescence

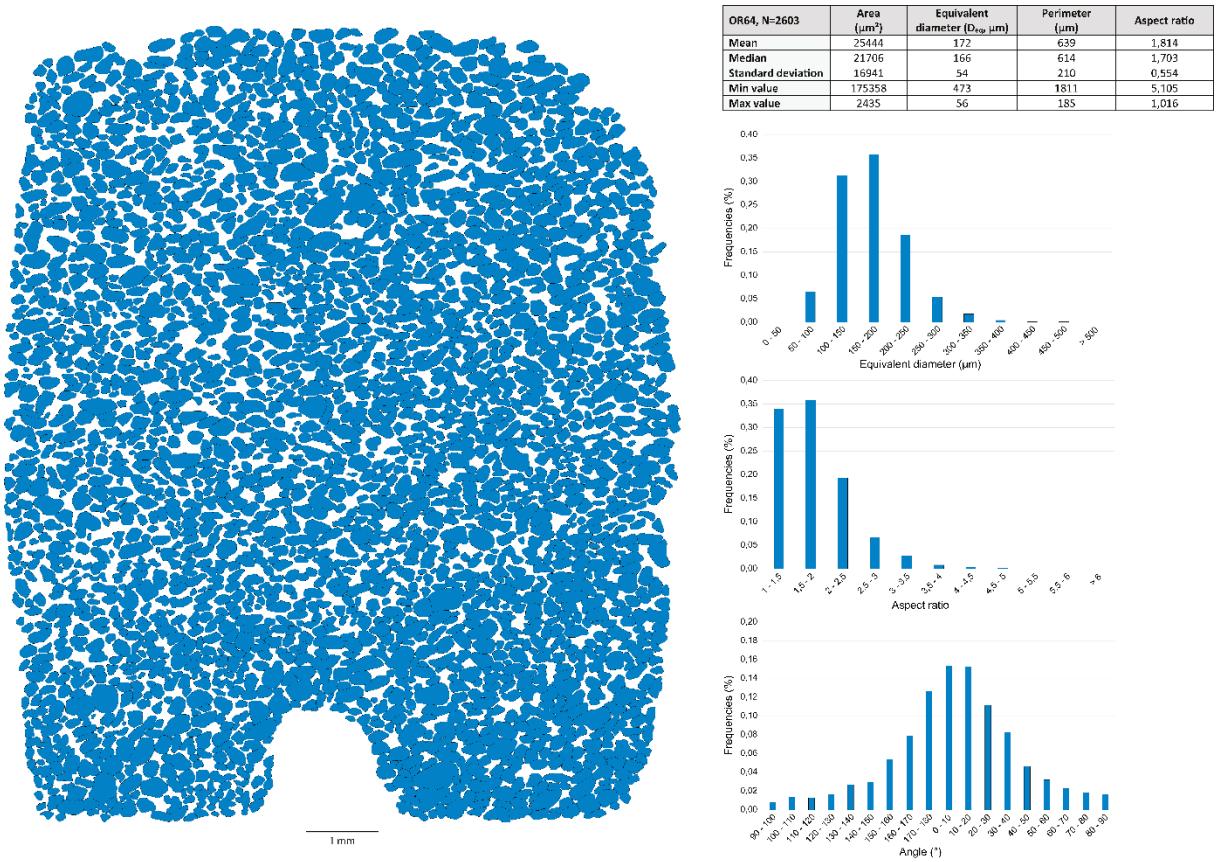

OR64, N=2603	Area (µm²)	Equivalent diameter (D_{eq} µm)	Perimeter (µm)	Aspect ratio
Mean	25444	172	639	1,814
Median	21706	166	614	1,703
Standard deviation	16941	54	210	0,554
Min value	175358	473	1811	5,105
Max value	2435	56	185	1,016

Figure VII.41. Segmentation of optical cathodoluminescence mosaic image of deformed sample OR64 (1500 MPa) and corresponding statistics for sand grain sizes, aspect ratio and major axis orientation.

VII.3.12. OR62 (2000 MPa)

Optical cathodoluminescence

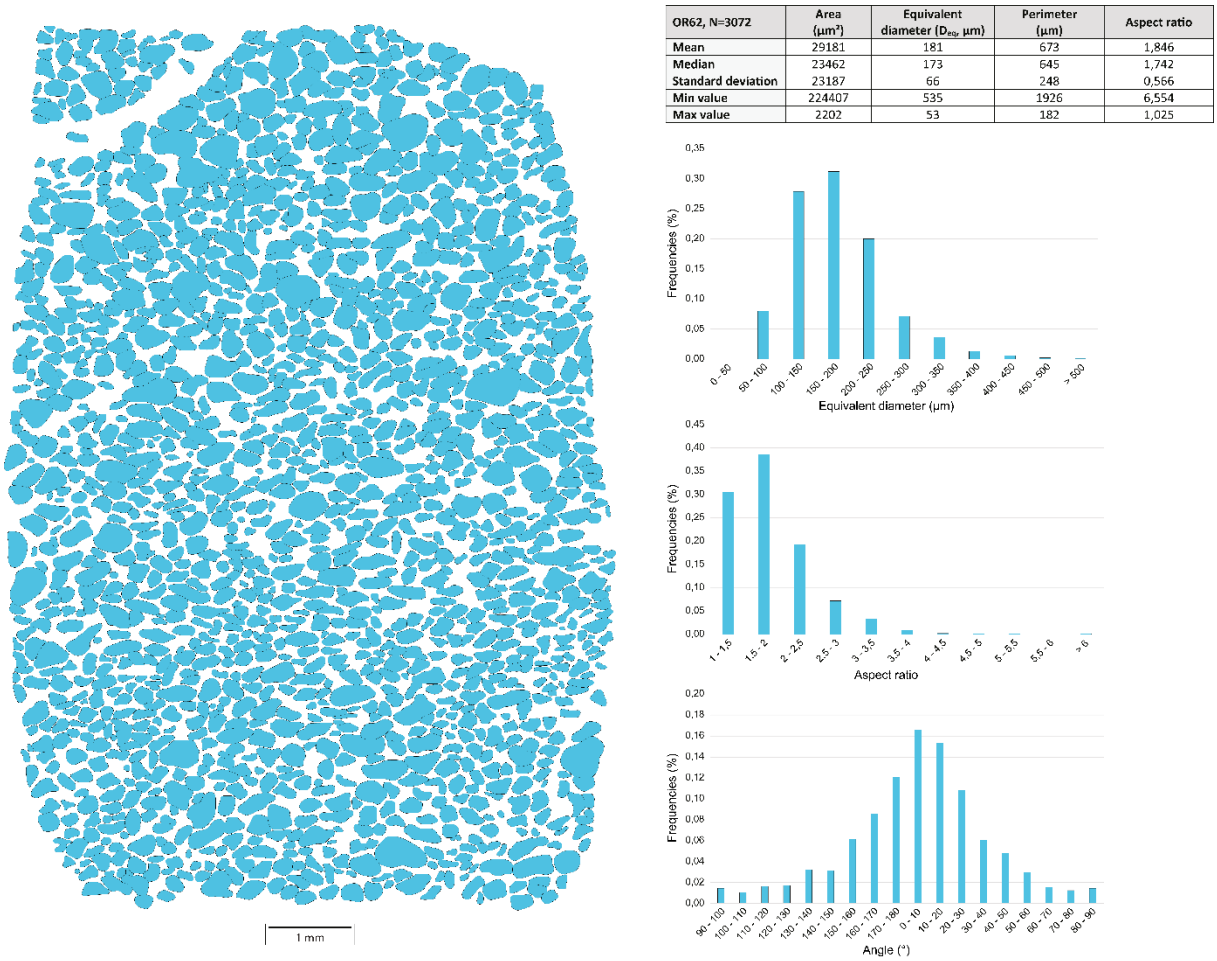

OR62, N=3072	Area (µm²)	Equivalent diameter (D_{eq}, µm)	Perimeter (µm)	Aspect ratio
Mean	29181	181	673	1,846
Median	23462	173	645	1,742
Standard deviation	23187	66	248	0,566
Min value	224407	535	1926	6,554
Max value	2202	53	182	1,025

Figure VII.42. Segmentation of optical cathodoluminescence mosaic image of deformed sample OR62 (2000 MPa) and corresponding statistics for sand grain sizes, aspect ratio and major axis orientation.

VII.3.13. SURFOR analysis: comparisons between samples and strain partitioning

VII.3.13.1. Light microscopy

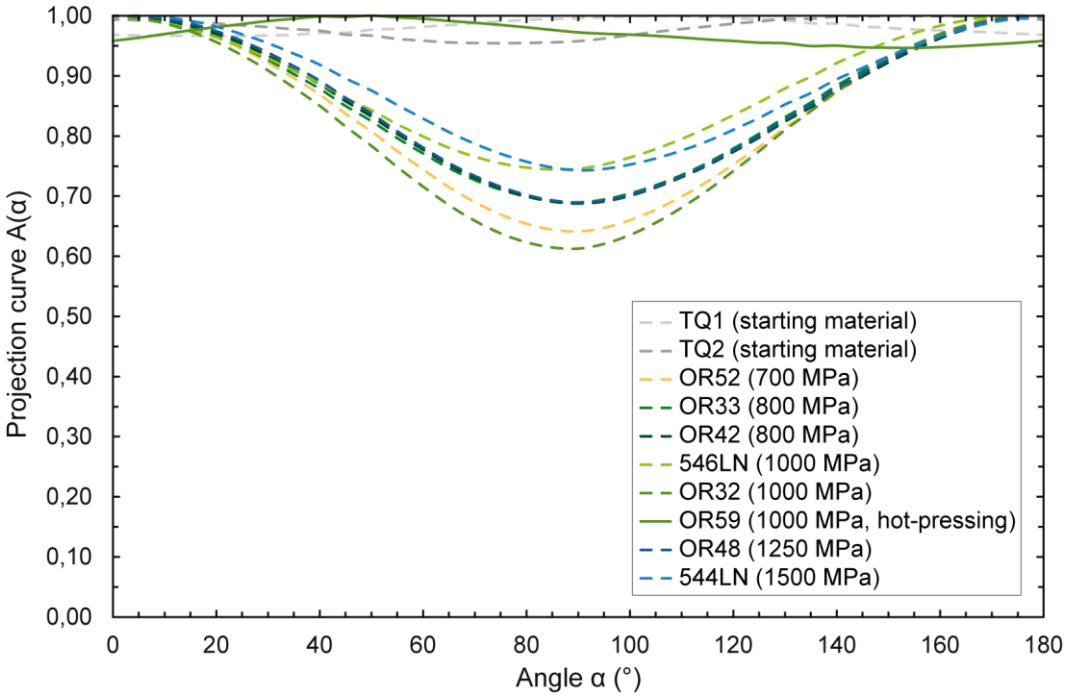

Figure VII.43. SURFOR projection curves for starting material, hot-pressed and deformed samples obtained from segmentation of quartzite grains from optical microscopy images. Starting materials TQ-1 and TQ-2 display a slight anisotropy (3.4% at 75° for TQ-1 and 4.6% at 20-25° for TQ-2). Hot-pressed sample OR59 displays a slight strain of 5.3% at 150-155°. Deformed samples display a strain comprised between 38.7% (OR32) and 25.5% (546LN) at 85-90°.

VII.3.13.2. Optical cathodoluminescence

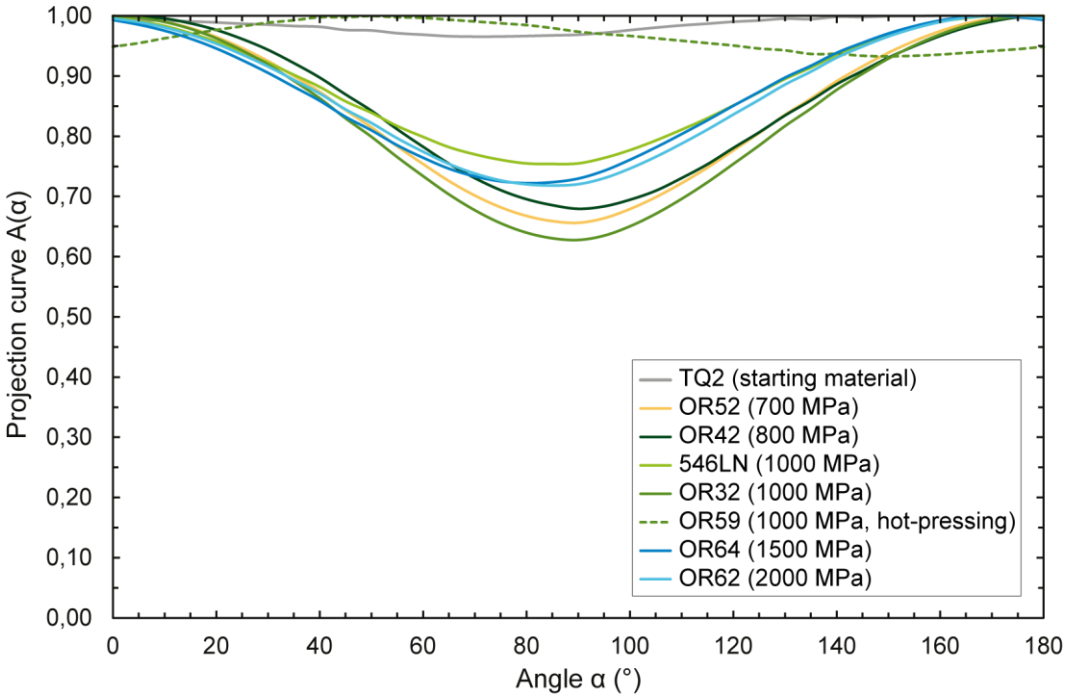

Figure VII.44. SURFOR projection curves for starting material, hot-pressed and deformed samples obtained from segmentation of sand grains from cathodoluminescence microscopy images. Starting material TQ-2 displays a slight anisotropy of 3.5% at 70°. Hot-pressed sample OR59 displays a slight strain of 6.7% at 150°. Deformed samples display a strain comprised between 37.2% (OR32) and 24.6% (546LN) at 80-90°.

VII.3.13.3. Strain partition

In order to characterize the strain partition (via anisotropy variations) inside the deformed samples, the segmented images were divided into four equal parts (from top to bottom) and the SURFOR analysis ran independently for each one. The results are presented below (Figure VII.45).

In the starting material, the fabric anisotropy slightly varies along the thin section but stays low (between 1.1 and 5.7%). The aspect ratio also shows little variations between 1.59 and 1.54 as well as the mean grain size (D_{eq} 170 – 214 µm). All these results indicate that some variations of the grain parameters are present at local scale.

For most of the deformed samples (except OR52), the highest fabric anisotropy is positioned at the middle part of the sample. The strain difference between the least and the most deformed parts is between 4.8% (OR32) and 24% (OR42). The mean anisotropy calculated from these values is consistent with the bulk strain previously determined on the whole sample.

Concerning the grain parameters, the aspect ratios values follow the same variations than the anisotropy with higher AR values for grains in the most deformed parts and smaller AR values in the least deformed parts. Moreover, the orientation of the fit ellipse long axes distribution is closer to the extension direction (perpendicular to the σ1 direction) in the parts where the strain is more pronounced.

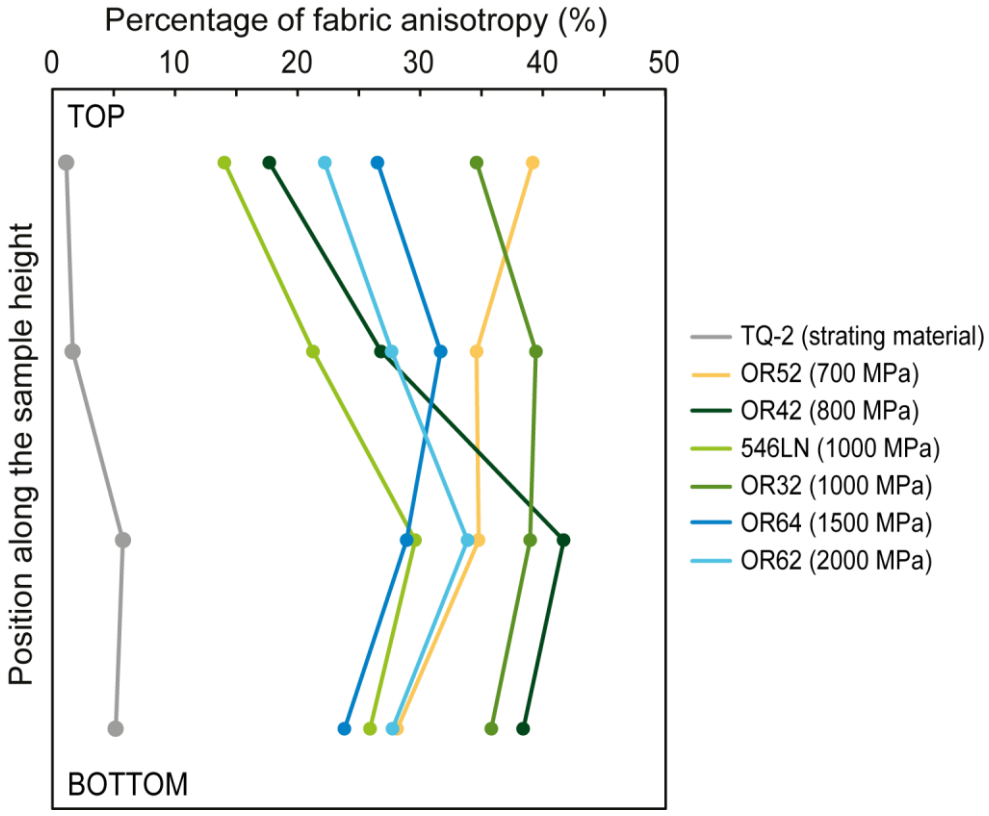

Figure VII.45. Partition of the fabric anisotropy along starting material and deformed samples. The starting material displays a low fabric anisotropy whereas deformed samples show higher strain with variations as a function of the position along the samples length. The higher strain part is at positioned the middle-bottom part for most of deformed samples (except OR52).

VII.4. H_2O contents and OH speciation

VII.4.1. Araldite® contamination

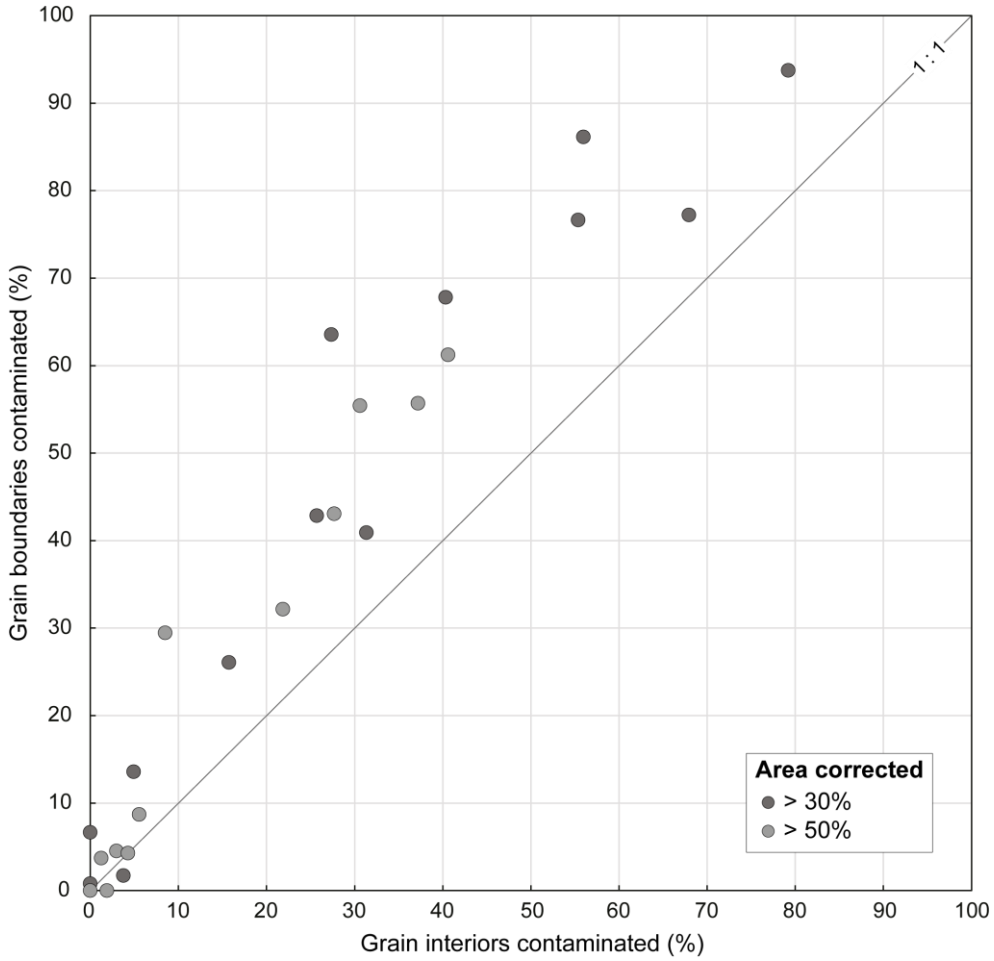

Figure VII.46. Percentage of grain boundaries contaminated as a function of the grain interiors contaminated (%). The grain boundaries are more contaminated than the grain interiors. The highest percentages of contamination always belong to the same sample.

Table VII.1. Mean H_2O contents ($H/10^6$ Si) for grain interiors and grain boundaries as a function of the percentage of area corrected due to Araldite contamination. The first line corresponds to the mean H_2O content and the second to the difference with the related percentage in parenthesis.

Sample	Mean H_2O content ($H/10^6$ Si)		Area corrected > 30%		Area corrected > 50%	
	Grain interiors	Grain boundaries	Grain interiors	Grain boundaries	Grain interiors	Grain boundaries
TQ-1	1659	2120	1659 0 (0%)	2213 -93 (-4.4%)	1659 0 (0%)	2120 0 (0%)
TQ-2	869	1579	947 -78 (-9.0%)	1772 -193 (-12.2%)	879 -9 (-1.1%)	1617 -37 (-2.4%)
542LN	1040	1297	1040 0 (0%)	1297 0 (0%)	1040 0 (0%)	1297 0 (0%)

OR60	991	1597	1638 -647 (-65.3%)	4502 -2905 (-181.9%)	1271 -280 (-28.2%)	2762 -1165 (-72.9%)
OR52	1006	1037	1258 -252 (-25.0%)	1266 -228 (-22.0%)	1145 -139 (-13.8%)	1204 -167 (-16.1%)
OR33	845	1260	942 -97 (-11.5%)	1689 -429 (-34.1%)	979 -134 (-15.8%)	1463 -203 -16.1%
OR42	805	1127	1066 -262 (-32.5%)	1549 -423 (-37.5%)	977 -172 (-21.4%)	1409 -282 (-25.1%)
OR73	1122	1403	1912 -790 (-70.4%)	2644 -1242 (-88.5%)	1465 -343 (-30.5%)	2066 -664 (-47.3%)
546LN	1468	1615	1484 -16 (-1.1%)	1722 -107 (-6.6%)	1468 0 (0%)	1615 0 (0%)
OR32	722	739	949 -228 (-31.6%)	1058 -319 (-43.2%)	838 -117 (-16.2%)	1004 -265 (-35.9%)
OR59	1228	2643	1253 -24 (-2%)	3269 -626 (-23.7%)	1250 -22 (-1.8%)	2728 -85 (-3.2%)
OR48	570	750	597 -27 (-4.7%)	1018 -268 (-35.7%)	592 -21 (-3.7%)	872 -122 (-16.2%)
544LN	978	1559	990 -12 (-1.2%)	1582 -22 (-1.4%)	978 0 (0%)	1559 0 (0%)
OR63	813	1227	822 -9 (-1.1%)	1317 -90 (-7.3%)	808 5 (+0.6%)	1253 -26 (-2.1%)
OR64	969	1187	1088 -119 (-12.3%)	1381 -194 (-16.3%)	1002 -33 (-3.4%)	1268 -81 (-6.8%)
OR57	1125	1151	1125 0 (0%)	1158 -7 (-0.6%)	1125 0 (0%)	1151 0 (0%)
OR62	1009	1133	1020 -12 (-1.2%)	1153 -20 (-1.8%)	1014 -5 (-0.5%)	1149 -16 (-1.5%)
OR54	759	894	775 -15 (-2.0%)	962 -68 (-7.6%)	763 -4 (-0.5%)	924 -30 (-3.4%)
OR50	552	540	552 0 (0%)	544 -4 (-0.8%)	552 0 (0%)	540 0 (0%)
OR56	1304	1500	1344 -39 (-3.0%)	1607 -107 (-7.1%)	1319 -15 (-1.2%)	1529 -29 (-1.9%)
OR66	880	1525	910 -30 (-3.5%)	1530 -5 (-0.4%)	895 -15 (-1.7%)	1525 0 (0%)

VII.4.2. H_2O contents in weight proportions (ppm)

VII.4.2.1. Starting materials

Table VII.2. H2O content (ppm) in grain interiors and grain boundaries for starting material sample TQ-1 and for grain interiors, grain boundaries, cement and triple junctions for starting material sample TQ-2.

Sample	Weight proportion (ppm)	Grain interiors	Grain boundaries	Cement	Triple junctions
TQ-1	**Number of data**	71	150		
	Mean	249	318		
	Median	211	295		
	Standard deviation	171	171		
	Min value	23	75		
	Max value	823	1135		
TQ-2	**Number of data**	67	66	69	69
	Mean	130	237	259	272
	Median	117	214	239	260
	Standard deviation	98	106	84	116
	Min value	11	69	91	65
	Max value	521	581	514	799

VII.4.2.2. Deformed samples

Table VII.3. H_2O content (ppm) in grain interiors, grain boundaries and recrystallized area for samples with no apparent strain partitioning between top and middle part.

Sample	Weight proportion (ppm)	Grain interiors	Grain boundaries	Recrystallized grains
542LN 600 MPa	Number of data	73	61	
	Mean	156	194	
	Median	114	159	
	Standard deviation	131	129	
	Min value	13	29	
	Max value	611	788	
OR52 700 MPa	Number of data	119	115	
	Mean	151	156	
	Median	119	144	
	Standard deviation	115	80	
	Min value	12	25	
	Max value	688	464	
OR33 800 MPa	Number of data	112	137	
	Mean	127	189	
	Median	101	160	
	Standard deviation	86	127	
	Min value	21	38	
	Max value	506	1042	

OR32 1000 MPa	Number of data	134	166	
	Mean	108	111	
	Median	82	79	
	Standard deviation	88	90	
	Min value	9	10	
	Max value	482	676	
OR59 1000 MPa Hot-pressing	Number of data	70		
	Mean	184		
	Median	170		
	Standard deviation	129		
	Min value	12		
	Max value	533		
OR48 1250 MPa	Number of data	106	129	
	Mean	86	113	
	Median	71	96	
	Standard deviation	60	89	
	Min value	18	15	
	Max value	332	745	
OR63 1500 MPa	Number of data	81	81	
	Mean	122	184	
	Median	91	142	
	Standard deviation	108	151	
	Min value	12	30	
	Max value	627	708	
OR64 1500 MPa	Number of data	108	115	
	Mean	145	178	
	Median	116	160	
	Standard deviation	127	125	
	Min value	14	11	
	Max value	812	698	
OR57 2000 MPa	Number of data	96	126	35
	Mean	169	173	241
	Median	142	136	216
	Standard deviation	119	156	112
	Min value	22	35	66
	Max value	632	1263	498
OR66 2000 MPa Hot-pressing	Number of data	53	58	
	Mean	132	229	
	Median	95	182	
	Standard deviation	124	152	
	Min value	13	26	
	Max value	650	676	

OR50 2000 MPa 52.38%	Number of data	106	50	66
	Mean	83	81	152
	Median	59	75	120
	Standard deviation	72	44	106
	Min value	18	19	30
	Max value	469	176	570
OR54 2000 MPa 39.75%	Number of data	124	61	69
	Mean	114	134	106
	Median	96	105	73
	Standard deviation	84	80	104
	Min value	21	23	12
	Max value	637	372	567
OR56 2000 MPa 74.43%	Number of data	71	41	52
	Mean	196	225	139
	Median	190	185	144
	Standard deviation	80	125	74
	Min value	32	42	14
	Max value	402	513	396

Table VII.4. H_2O contents (ppm) in grain interiors and grain boundaries in both least deformed and most deformed parts of samples for which a strain gradient between top and middle part is observed.

Sample	**Weight proportion (ppm)**	Grain interiors		Grain boundaries	
		Least deformed	Most deformed	Least deformed	Most deformed
OR42 800 MPa	Number of data	62	54	65	55
	Mean	175	59	194	139
	Median	122	51	158	102
	Standard deviation	143	40	128	122
	Min value	27	8	54	30
	Max value	785	170	696	753
546LN 1000 MPa	Number of data	70	70	73	68
	Mean	278	162	276	206
	Median	266	140	270	177
	Standard deviation	171	127	115	148
	Min value	29	19	36	42
	Max value	865	693	595	853
544LN 1500 MPa	Number of data	70	60	62	67
	Mean	167	123	272	199
	Median	114	87	248	161
	Standard deviation	185	101	144	131
	Min value	13	24	27	20
	Max value	885	506	882	640

OR62 2000 MPa	Number of data	56	49	67	53
	Mean	166	135	179	158
	Median	128	108	172	112
	Standard deviation	101	89	82	112
	Min value	48	20	34	43
	Max value	507	445	436	510

Lucille NEGRE

Relation entre les transferts d'eau et la déformation plastique : cas d'étude des quartzites

Résumé

Du fait de son abondance et de sa présence ubiquiste dans la croûte continentale, la rhéologie du quartz est un paramètre fondamental pour comprendre les processus géodynamiques. Malgré une longue histoire de recherche depuis la découverte précoce de l'effet de l'eau (H_2O) sur la rhéologie du quartz par Griggs et Blacic (1965), plusieurs aspects de l'affaiblissement par l'H_2O ne sont toujours pas résolus. Un de ces aspects est l'effet important de la pression sur l'affaiblissement du quartz par l'H_2O, dont les mécanismes ne sont pas compris. Dans cette étude, la dépendance à la pression de la résistance des agrégats de quartz a été revisitée en utilisant comme matériel de départ des échantillons naturels de quartzite d'une grande pureté et d'une taille de grains élevée de ~200 µm dans le but de diminuer le rôle des processus de fluage diffusion par rapport au fluage dislocation. Des expériences de déformation d'échantillons avec ajout d'H_2O (0.1 pds.%) ont été menées dans un appareil de type « Griggs » avec des pressions de confinement solide allant de 600 à 2000 MPa. Les données mécaniques montrent qu'aux conditions de déformation appliquées, la résistance du quartzite diminue systématiquement avec l'augmentation de pression. Les études microstructurales démontrent une accommodation de la déformation dominée par la déformation plastique cristalline des clastes de quartz (par fluage dislocation), à laquelle s'ajoutent des processus aux joints de grains où de nouveaux grains de petite taille sont formés. Les études mécaniques et microstructurales montrent toutes deux que les processus de microfracturation, dissolution-reprécipitation et transferts de matière aux joints de grains jouent également un rôle dans la déformation. L'effet majeur de la pression sur les mécanismes de déformation intervient au niveau des joints de grains : l'augmentation de la pression conduit à une augmentation significative de la génération de petits grains aux bordures des porphyroclastes originels. Ce processus est probablement celui qui contrôle l'effet adoucissant de la pression sur la résistance macroscopique de l'assemblage polycristallin. Un deuxième aspect de la dépendance du quartz à l'H_2O est lié à la quantité d'eau disponible pendant la déformation et la façon dont elle est utilisée. Pour explorer cette question, les intérieurs et les joints de grains ont été indépendamment mesurés par spectroscopie infrarouge à la fois dans le matériel de départ et dans les échantillons déformés. Il apparaît que pendant les expériences, les mécanismes de fluage dislocation ont contribué à la diminution du contenu en H_2O dans toutes les microstructures pendant la déformation, l'H_2O étant transférée depuis l'intérieur des grains vers la région des joints de grains. La distribution de l'H_2O et la déformation interagissent, le contenu en H_2O intracristallin favorisant la déformation (vitesse du fluage dislocation) tandis que la déformation accompagne le transport d'H_2O. Cette étude met en évidence la déformation du quartzite en présence de H_2O comme étant un système auto-suffisant avec l'H_2O qui accélère les taux de restauration et de recristallisation, et les micro-fractures qui permettraient à l'H_2O de pénétrer à nouveau dans les intérieurs de grains depuis les joints de grains. En effet, ces derniers jouent le rôle d'un site de stockage pour l'H_2O. Il convient de s'interroger sur la pérennité de ce stockage aux joints de grains pendant la déformation dans des conditions naturelles. Le drainage de ces sites conduirait potentiellement à durcir l'assemblage et à délocaliser la déformation.

Mots clés : quartz, eau (H_2O), déformation plastique, transferts

Relationship between water transfer and plastic deformation: the case study of quartzites

Summary

Due to its abundance and ubiquitous presence in the continental crust, the rheology of quartz is a fundamental parameter to understand geodynamic processes. Despite a long history of research since the early discovery of the effect of H_2O on quartz rheology by Griggs and Blacic (1965), many aspects of H_2O weakening of quartz are yet unresolved. One of these aspects is the enhancing effect of pressure on the H_2O weakening of quartz, whose mechanisms are not understood. In this study, the pressure dependence of the strength of quartz aggregates has been revisited using natural quartzite samples of high purity with a large grain size of ~200 µm as starting material in order to diminish the role of diffusion creep processes in comparison to dislocation creep. Experimental deformation of water-added (0.1 wt.%) samples was performed in a "Griggs" type solid medium apparatus at confining pressures ranging from 600 to 2000 MPa. Mechanical data show that at the deformation conditions applied, the quartzite strength decreases systematically with increasing confining pressure. Microstructural studies demonstrate an accommodation of the deformation dominated by crystal plastic deformation of quartz clasts (dislocation creep) supplemented by grain boundary processes where new small-sized grains formed. Both mechanical data and microstructural studies show that micro-cracking, dissolution-reprecipitation and material transfers at grain boundaries processes also play a part into deformation. The most prominent effect of pressure on bulk strength relies on grain boundary processes: pressure increase results in a large enhancement of the generation of small grains along the boundaries of the original large porphyroclasts. This effect is presumably the main cause for the weakening effect of pressure. One second aspect of the H_2O dependence of quartz is linked to the amount of water available during deformation and how it is used. To explore this point, infrared spectroscopy allowed to measure independently the grain interiors and boundaries, both on starting and experimental materials. It appears that through the experiments, dislocation creep mechanisms contributed to the decrease of the H_2O content in all microstructures during deformation, the H_2O being transferred from the grain interiors to the grain boundary region. H_20 distribution and deformation interact, with intracrystalline H_20 content enhancing the deformation (rate of dislocation creep) and deformation accompanying the transport of H_20. This study highlights the deformation of quartzite as being a self-sufficient system as H_20 accelerates the rates of recovery and recrystallization, and microcracks may allow H_20 to re-enter the interior of grains from the grain boundary region. The grain boundaries, act as a storage site for H_2O. For the deformation at natural conditions, it will be a critical parameter whether the H_2O will be preserved at these sites or whether it will be drained and thus potentially harden the assembly and relocate the deformation.

Keywords: quartz, water (H_2O), plastic deformation, transfers

Institut des Sciences de la Terre d'Orléans
1a rue de la Férollerie
45100 ORLEANS